ABSTRACT

Title of Dissertation:	ANALYSIS AND EXPERIMENTAL DEMONSTRATION OF CONFORMAL ADAPTIVE PHASE-LOCKED FIBER ARRAY FOR LASER COMMUNICATIONS AND BEAM PROJECTION APPLICATIONS
	Ling Liu, Doctor of Philosophy, 2008
Dissertation Directed By:	Professor Mikhail A. Vorontsov Institute for Systems Research and Department of Electrical and Computer Engineering, University of Maryland at College Park

The primary goal of this research is the analysis, development, and experimental demonstration of an adaptive phase-locked fiber array system for free-space optical communications and laser beam projection applications. To our knowledge, the developed adaptive phase-locked system composed of three fiber collimators (subapertures) with tip-tilt wavefront phase control at each subaperture represents the first reported fiber array system that implements both phase-locking control and adaptive wavefront tip-tilt control capabilities. This research has also resulted in the following innovations:

(a) The first experimental demonstration of a phase-locked fiber array with tip-tilt wavefront aberration compensation at each fiber collimator;

(b) Development and demonstration of the fastest currently reported stochastic parallel gradient descent (SPGD) system capable of operation at 180,000 iterations per second;

(c) The first experimental demonstration of a laser communication link based on a phase-locked fiber array;

(d) The first successful experimental demonstration of turbulence and jitter-induced phase distortion compensation in a phase-locked fiber array optical system;

(e) The first demonstration of laser beam projection onto an extended target with a randomly rough surface using a conformal adaptive fiber array system.

Fiber array optical systems, the subject of this study, can overcome some of the drawbacks of conventional monolithic large-aperture transmitter/receiver optical systems that are usually heavy, bulky, and expensive. The primary experimental challenges in the development of the adaptive phased-locked fiber-array included precise (<5 microrad) alignment of the fiber collimators and development of fast (100kHz-class) phase-locking and wavefront tip-tilt control systems. The precise alignment of the fiber collimator array is achieved through a specially developed initial coarse alignment tool based on high precision piezoelectric picomotors and a dynamic fine alignment mechanism implemented with specially designed and manufactured piezoelectric fiber positioners. Phase-locking of the fiber collimators is performed by controlling the phases of the output beams (beamlets) using integrated polarization-maintaining (PM) fiber-coupled $LiNbO_3$ phase shifters. The developed phase-locking controllers are based on either the SPGD algorithm or the multi-dithering technique. Subaperture wavefront phase tip-tilt control is realized using piezoelectric fiber positioners that are controlled using a computer-based SPGD controller.

Both coherent (phase-locked) and incoherent beam combining in the fiber array system are analyzed theoretically and experimentally. Two special fiber-based beam-combining testbeds have been built to demonstrate the technical feasibility of phase-locking compensation prior to free-space operation. In addition, the reciprocity of counter-propagating beams in a phase-locked fiber array system has been investigated.

Coherent beam combining in a phase-locking system with wavefront phase tip-tilt compensation at each subaperture is successfully demonstrated when laboratory-simulated turbulence and wavefront jitters are present in the propagation path of the beamlets. In addition, coherent beam combining with a non-cooperative extended target in the control loop is successfully demonstrated.

ANALYSIS AND EXPERIMENTAL DEMONSTRATION OF CONFORMAL ADAPTIVE PHASE-LOCKED FIBER ARRAY FOR LASER COMMUNICATIONS AND BEAM PROJECTION APPLICATIONS

By

Ling Liu

Dissertation submitted to the Faculty of the Graduate School of the
University of Maryland, College Park, in partial fulfillment
of the requirements for the degree of
Doctor of Philosophy
2008

Advisory Committee:
Professor Mikhail A. Vorontsov, Chair/Advisor
Professor Julius Goldhar
Professor Christopher C. Davis
Professor Eyad H. Abed
Professor Eun-Suk Seo, Dean's Representative

Acknowledgements

My thanks first go to my academic advisor, Prof. Mikhail A. Vorontsov, who brought me to his research group to start working in this new professional area five years ago. Without his supervision and support, I could not finish this dissertation. I am grateful to Prof. Julius Goldhar, Prof. Christopher C. Davis, Prof. Eyad H. Abed and Prof. Eun-Suk Seo for serving on my advisory committee.

I would like to show gratitude to my colleagues in Prof. Vorontsov's research group. Dr. Thomas Weyrauch and Dr. Ernst Polnau have helped me greatly in my experimental research efforts. Dr. Svetlana Lachinova discussed the results of her numerical analysis of similar research with me. Dr. Leonid Beresnev trained me to build and use the fiber positioners. Dr. Andrei Rostov helped me in the design and implementation of the microprocessor based SPGD controllers. Gary Carhart and Konley Aschenbach helped me in software programming.

I would also thank Dr. Dimitrios Loizos (JHU/UCSD) for his design and collaborative testing work on the VLSI multi-dithering controller and Dr. Walter Charczenko (EO-Space Inc.) for his help with the multi-channel fiber system.

Special thanks go to my wife, Yubing, for her consistent support in the past few years, especially during the difficult times we experienced together. My 4-year-old daughter, Amber, is also a good helper. She makes me laugh and get relaxed from my research work.

Table of Contents

List of Figures

List of Abbreviations

ADC, A/D:	analog-to-digital converter
AO:	adaptive optics
ARL:	Army Research Laboratory
ARM:	advanced RISC machines
AVR:	Alf (Egil Bogen) and Vegard (Wollan)'s RISC processor
BER:	bit error rate
CCD:	charge-coupled device
CPU:	central processing unit
DAC, D/A:	digital-to-analog converter
DE:	directed energy
DFB:	distributed feedback
DM:	deformable mirror
DOF:	degree of freedom
EO:	electro-optic
FC/APC:	fixed connection, angled physical contact
FC/UPC:	fixed connection, ultra physical contact
FFT:	fast Fourier transform
FWHM:	full-width-at-half-maximum
Gb/s:	giga-bits per second
GHz:	giga-hertz
HRL:	Hughes Research Laboratories
JHU:	Johns Hopkins University
kHz:	kilo-hertz
KΩ:	kilo-ohm
LADAR:	laser detection and ranging system
LC:	liquid crystal
LD:	laser diode
$LiNbO_3$:	lithium niobate crystal waveguide
LMA:	large mode area
LPF:	low pass filter

Mb/s:	mega-bits per second
MHz:	mega-hertz
MIT:	Massachusetts Institute of Technology
mm:	millimeter
ms:	millisecond
NA:	numerical aperture
nm:	nanometer
NRZ:	non-return-to-zero
OOK:	on-off keying
PC:	personal computer
PD:	photo detector
PER:	polarization extinction ratio
PIB:	power-in-the-bucket
PMF:	polarization maintaining fiber
PSF:	point spread function
RF:	radio frequency
RISC:	reduced instruction set computer
RMS:	root mean square
SBS:	stimulated Broullin scattering
SMF:	single mode fiber
SNR:	signal-to-noise ratio
SPGD:	stochastic parallel gradient descent
SR:	Strehl ratio
TE:	transverse electric
TIL:	target-in-the-loop
TM:	transverse magnetic
UCSD:	University of California, San Diego
UMD:	University of Maryland, College Park
VLSI:	very-large-scale integration
μm:	micrometer

Chapter 1 Introduction

This chapter is an introduction to the research on adaptive phase-locked fiber arrays. Section 1.1 describes the basic motivation for the research. Section 1.2 addresses the wavefront distortion compensation problem, which is an important issue for conformal optical systems. In Section 1.3, typical examples of system configuration based on an array of fiber collimators and feedback control systems are described. Section 1.4 addresses the related work in the development of optical systems. Section 1.5 describes the basic approach in this research.

1.1 Motivation for the research

In long-range free-space optical communications and laser beam projection applications (see Figure 1.1 for a simplified block diagram), an optical transmitter telescope (also called an optical antenna or beam director) with a large-size aperture (tens of centimeters or even larger in diameter) is usually required because the laser beam divergence angle and diffraction-limited focal spot size of an ideal (spatially coherent, quasi-monochromatic, and collimated) laser beam propagating in vacuum is inversely proportional to the optical aperture diameter (denoted by D) and hence can be potentially decreased by increasing the aperture size D. Therefore in a conventional beam transmitter/receiver telescope with a monolithic aperture, a large-aperture primary mirror is commonly used. In addition, the focal distance of the telescope's primary mirror (denoted by F) and the nominal length (denoted by H , which is defined as the distance between the vertices of the primary and secondary mirrors) become larger with increasing aperture size D (see Figure 1.2a). Both F and H typically exceed D by several times, which is a requirement to build a primary mirror with good optical quality. Consequently, a mono-

lithic large-aperture transmitter/receiver telescope is heavy, bulky, and expensive. Besides, a heavy and expensive gimbal system is usually required in order to point the beam toward its target.

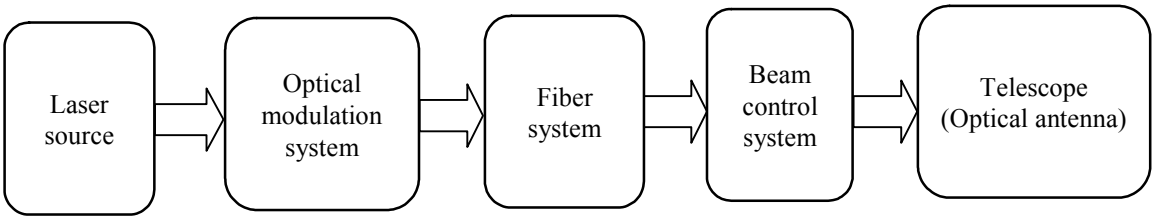

Figure 1.1: Diagram of a fiber-based optical transmitter for free-space laser communications and beam projection applications.

The laser source delivers optical power to the transmitter. In laser communication applications the laser beam is modulated to enter information into the transmitted beam. The fiber system routes light through fiber-coupled waveguides and necessary optical power amplification. Beam control system provides beam steering and wavefront control. The telescope is used to collimate the outgoing beam or does beam focus/defocus control.

The disadvantage of the monolithic large-aperture beam transmitter/receiver telescope stimulated recent development of a conformal adaptive phase-locked fiber array composed of multiple (denoted by N) identical small laser transmitter/receiver (subaperture) elements (see Figure 1.2b and Figure 1.2c for an example with seven subaperture elements). The fiber collimator lenses have much smaller optical aperture diameter (denoted by $d \ll D$) than the monolithic structure and correspondingly much shorter focal length (denoted by $f \ll F$). As shown in Figure 1.2c, the monolithic aperture diameter D is equal to the diameter of the smallest circle that encloses the N subapertures in the conformal optical system. Compared to the monolithic optical system, the conformal optical system is thus expected to be more compact and less expensive, which are important

advantages of the conformal optical systems. A third advantage of the conformal optical system architecture is its scalability of the optical power level. More optical elements can be added to the conformal system to achieve a higher total output optical power. A fourth advantage of the conformal optical system is its robustness to the subaperture element failures. If several elements fail to work properly, the conformal transmitter/receiver system will still be able to perform its functions with some performance degradation.

Figure 1.2a and Figure 1.2b show adaptive optics (AO) subsystems as components for both monolithic and conformal optical systems. They are used to compensate wavefront distortions from atmospheric turbulence or other dynamic aberrations in the optical propagation path. The relevance of adaptive optics for conformal optical system is addressed in the following section.

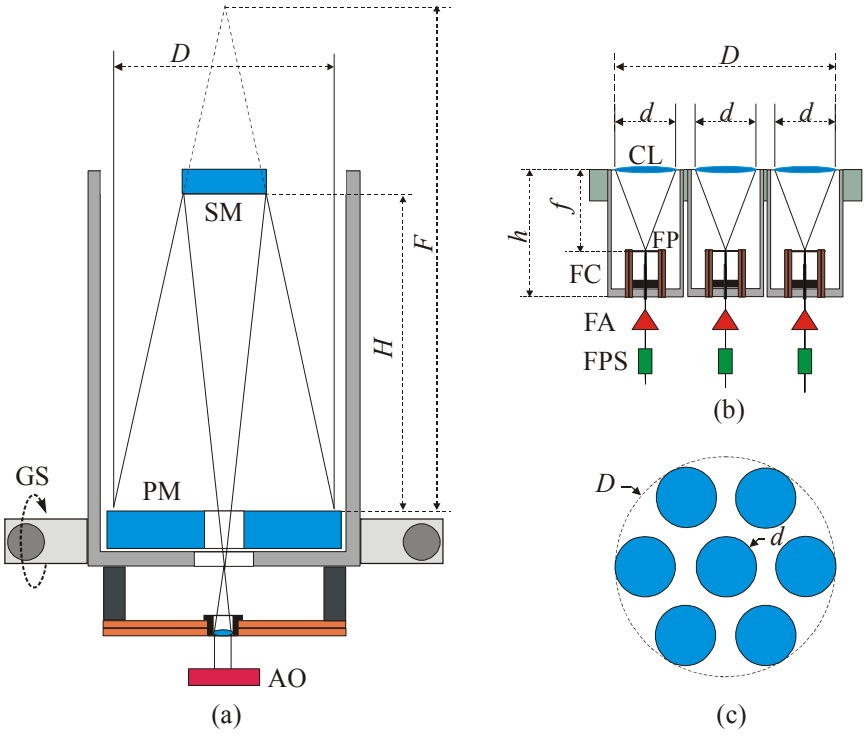

Figure 1.2: Monolithic vs. conformal optical systems: structure comparison

(a) Schematic of a typical beam transmitter/receiver telescope assembly with monolithic aperture (aperture diameter D , primary mirror focal distance F , telescope nominal length H), and adaptive optics (AO) system. (b) Conformal beam transmitter/receiver telescope assembly with $N=7$ identical subaperture fiber-coupled elements (subaperture diameter $d \ll D$, collimating lens focal length $f \ll F$, fiber collimator nominal length $h \ll H$), local adaptive optics system (FP), and phase-locking control system (FPS). (c) 2-D hexagonal array of seven identical subaperture elements. The conformal system has an equivalent aperture diameter D . Abbreviations are described as follows: GS - gimbal system, PM - primary mirror, SM - secondary mirror, AO - adaptive optics system, CL - collimating lens, FP - fiber positioner, FC - fiber collimator, FA - fiber amplifier, FPS - fiber phase shifter. The figures are adapted from [1].

1.2 Wavefront distortion compensation considerations

Laser beam propagation under atmospheric turbulence conditions can result in random fluctuations of both the beam intensity and the phase. In free-space optical communications or beam projection applications, the intensity and phase fluctuations can severely degrade the system performance. The adaptive optics technique that uses controllable mirrors with deformable surface (DM) can be applied to mitigate the effect of atmospheric turbulence and thus improve the overall system performance [2]. There are two major adaptive optics (AO) system types: the AO systems based on wavefront sensing and reconstruction referred to here as conventional AO systems [3, 4] and the AO systems based on system performance metric optimization also known as far-field adaptive optics [5-7]. The conventional AO technique is commonly used when the turbulence-induced intensity fluctuations (scintillations) are weak, e.g., in astronomical imaging systems. The metric-optimization based AO systems are especially efficient in laser communications and beam projection applications in which intensity fluctuations of laser beams are strong and wavefront aberrations are not easy to be sensed.

Application of AO techniques to a conformal optical system composed of an array of fiber collimators is not straightforward. Consider a subaperture element (fiber collimator) with diameter d as part of a fiber collimator array. The strength of the turbulence impact can be characterized by the ratio d/r_o , where r_o is the Fried parameter [8, 9]. Analysis [4, 10] of atmospheric turbulence effects on the optical system performance showed that if $d > r_o$, the outgoing laser beam divergence angle and the beam focal spot size on the receiver or target are determined by the Fried parameter r_o and are independent of d .

Under typical atmospheric conditions, the Fried parameter r_o ranges from <1cm for near-horizontal propagation paths in visible and infrared regions to >20cm for astronomical and airborne applications. Consequently, it is better to keep the diameter d of a subaperture element no larger than the Fried parameter r_o . For a fixed equivalent conformal beam diameter D , however, the selection of a small subaperture diameter d leads to a large number of subaperture elements

$$N \approx \left(\frac{D}{d} \right)^2 . \tag{1.1}$$

A large number of N is not desired since it leads to an increase of the system complexity and cost as well as it imposes additional difficulties in system integration. However, there exists a compromise between optical system performance, technical difficulties and budget for choosing an appropriate subaperture diameter d for a specific conformal optical system when a certain adaptive optics compensation system is implemented.

There are several considerations which can be taken into account while choosing the number of subapertures in conformal fiber array systems. To decrease the number of subapertures N , we can consider implementation of adaptive optics elements for wavefront phase distortion compensation at each subaperture. Note that in this approach the adaptive optics capabilities are distributed between N AO subsystems operating in parallel referred to here as local, on-subaperture AO systems.

Atmospheric turbulence-induced phase aberration can be expressed as an expansion of Zernike polynomials, known as classical Zernike aberrations (piston, wavefront tilts, defocus, astigmatisms, etc. from the lowest order to higher orders). From this viewpoint

adaptive optics compensation means cancellation (mitigation) of the corresponding Zernike aberrations.

Assume N phase-locked outgoing laser beams (beamlets) at the conformal system output. For adaptive optics compensation the system performance can be evaluated using the root mean square (RMS) residual wavefront phase error ε^2 or the Strehl ratio SR , where SR is characterized by the ratio of the on-axis value of either the aberrated point spread function (PSF) in an imaging system or the target focal spot intensity in a laser beam projection system to the corresponding value in absence of aberrations. If the RMS residual phase error $\varepsilon^2 \le \left(\frac{2\pi}{10}\right)^2 \approx 0.4\ \text{rad}^2$, then the Strehl ratio SR can be well-approximated by (see [11])

$$SR \approx \exp\left(-\varepsilon^2\right) . \tag{1.2}$$

The Marechal criterion (see [12]) states that an optical system can be regarded as well-corrected when the Strehl ratio $SR \ge 0.80$, which corresponds to a RMS residual phase error $\varepsilon^2 \le \left(\frac{2\pi}{14}\right)^2 \approx 0.2\ \text{rad}^2$. This criterion is used in the analysis for the conformal optical system discussed here.

For the classical Kolmogorov atmospheric turbulence model, the relations between residual phase error ε^2 , subaperture diameter d and the Fried parameter r_o are described as

$$\varepsilon_{Nz}{}^2 \approx \alpha_{Nz}\left(\frac{d}{r_o}\right)^{5/3} , \tag{1.3}$$

where N_z is the number of the lowest orders of Zernike aberrations that are corrected and α_{Nz} is the corresponding coefficient as listed in Table 1-1 for $N_z \le 20$.

N_Z	0	1	2	3	4	5	6
α_{Nz}	1.0299	0.5820	0.1340	0.1110	0.0880	0.0648	0.0587
N_Z	7	8	9	10	11	12	13
α_{Nz}	0.0525	0.0463	0.0401	0.0377	0.0352	0.0328	0.0304
N_Z	14	15	16	17	18	19	20
α_{Nz}	0.0279	0.0267	0.0255	0.0243	0.0232	0.0220	0.0208

Table 1-1: Residual RMS phase error coefficients vs. number of the lowest orders of corrected Zernike aberrations for the classical Kolmogorov atmospheric turbulence model (see Table IV in [13])

Consider four examples of AO compensation:

(1) Phase distortion compensation is performed using only a phase-locking system (piston-type aberration compensation). For this case, in accordance with Equation (1.3) and Table 1-1, we have

$$\varepsilon_{pl,0}{}^2 \approx 1.0299\left(\frac{d_{pl,0}}{r_o}\right)^{5/3}. \tag{1.4}$$

(2) Phase-locking and wavefront tip-tilt compensation are performed at each subaperture. In this case $N_z = 2$ and

$$\varepsilon_{pl,2}{}^2 \approx 0.1340\left(\frac{d_{pl,2}}{r_o}\right)^{5/3}. \tag{1.5}$$

(3) Phase-locking, tip-tilt and defocus compensation ($N_z = 3$) results in

$$\varepsilon_{pl,3}{}^2 \approx 0.1110\left(\frac{d_{pl,3}}{r_o}\right)^{5/3} . \tag{1.6}$$

(4) In the case of compensation of the first 20 lowest orders of Zernike aberrations (including piston) we finally have

$$\varepsilon_{pl,19}{}^2 \approx 0.0220\left(\frac{d_{pl,19}}{r_o}\right)^{5/3} . \tag{1.7}$$

In Equations (1.4), (1.5), (1.6), and (1.7), the "*pl*" indicates phase-locking (piston aberration) compensation and the number in the subscripts indicates how many lowest orders of Zernike aberrations are corrected. Then the total number (denoted by N_c) of control channels of the adaptive optics compensation system (including phase-locking) can be estimated as

$$N_c = N\left(N_z + 1\right) . \tag{1.8}$$

Consider an illustrative example in which the beam diameter $D = 50$ cm , the Fried parameter $r_o = 2$ cm and the residual phase error $\varepsilon^2 \approx 0.20$ rad^2 . Substituting these parameters into Equations (1.4), (1.5), (1.6) and (1.7), the required subaperture diameters are $d_{pl,0} \approx 0.75$ cm , $d_{pl,2} \approx 2.59$ cm , $d_{pl,3} \approx 2.86$ cm , and $d_{pl,19} \approx 7.52$ cm , respectively. Using Equation (1.1), the corresponding required total number of subaperture elements are $N_{pl,0} \approx 4483$, $N_{pl,2} \approx 372$, $N_{pl,3} \approx 305$, and $N_{pl,19} \approx 44$, respectively. Further using Equation (1.8), the corresponding total number of control channels are $N_c^{pl,0} = 4483$, $N_c^{pl,2} = 1116$, $N_c^{pl,3} = 1220$, and $N_c^{pl,19} = 880$, respectively. It can be seen from this simple estimation that the implementation of an adaptive optics system

with compensation of a few lowest orders of Zernike aberrations can greatly reduce the total number of subaperture elements and thus reduce the system structure complexity. In addition, the required control system can become less complicated in terms of the total number of control channels N_c .

In the adaptive phase-locked fiber array system described in this dissertation (see Figure 1.2b) phase-locking control is implemented using an integrated array of fiber-coupled phase shifters. To our knowledge, this system is the first reported conformal system that can perform both phase-locking and local on-subaperture wavefront tip-tilt aberration compensation [1]. The local on-subaperture wavefront phase tip-tilt control ($N_z = 2$) is implemented using an array of piezoelectric fiber positioners. An additional advantage of using phase tip-tilt control is the potential for using it to steer and direct the N beamlets to a desired focal point.

1.3 Typical configurations of conformal optical system

The conformal adaptive phase-locked fiber array as shown in Figure 1.2b can be potentially used in the following areas:

(1) Ground-based reconfigurable free-space laser communications [14];

(2) Satellite-to-satellite or to-aircraft crosslink, uplink and downlink [15];

(3) Beam projection applications including laser detection and ranging (LADAR) [16], laser pointing [17], active precision tracking for target stabilization [18, 19], directed energy (DE) applications [20-22].

In free-space laser communications, the objective is to establish a reliable and robust optical communication link and mitigate signal fadings. In beam projection applications, the objective is to increase brightness of the projected laser beam at a remote target in atmosphere.

Typical system configurations for free-space laser communications and beam projection applications using a conformal adaptive phase-locked fiber array are depicted in Figure 1.3 and Figure 1.4, respectively. In each of these configurations, there are N identical subaperture optical elements, but in the illustrations only three subapertures are shown. In Figure 1.3 or Figure 1.4a all beamlets originate from a single laser source and can be considered as coherent. Combining of these beamlets in the far field is referred to as coherent beam combining. In contrast, in Figure 1.4b, the beamlets originate from different laser sources, which corresponds to incoherent beam combining.

The major subsystems in Figure 1.3 or Figure 1.4 include a multi-channel fiber system, a conformal optical transmitter (or receiver), and feedback control systems. Coherent beam combining in the far field requires implementation of both phase-locking and local subaperture wavefront tip-tilt control. Incoherent beam combining requires only local subaperture wavefront tip-tilt control to make beamlets overlap with each other in the far field.

When the target is cooperative as shown in Figure 1.3 for the case of free-space communications, the metric signal can be directly measured and sent back through optical or radio frequency (RF) communication channel [6, 23, 24]. When the target is non-cooperative as shown in Figure 1.4, the metric signal can be obtained using the speckle field formed due to the outgoing beam being scattered off the target surface [25-29].

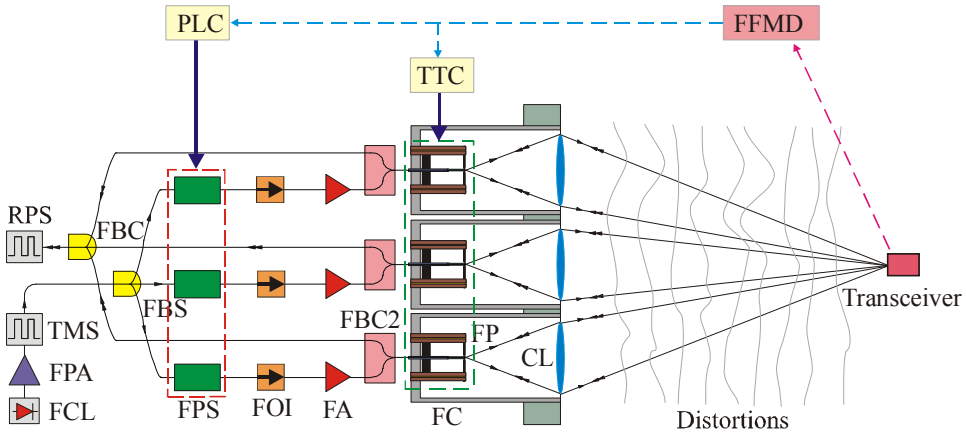

Figure 1.3: A typical system configuration of free-space laser communications using a conformal adaptive phase-locked fiber array.

Bidirectional propagation of light is shown by single-arrows and double-arrows, respectively. Abbreviations are described as follows: FCL - fiber-coupled laser, FPA - fiber preamplifier, TMS - transmitting modulation system, RPS- receiver processing system, FBS - fiber beam splitter, FBC - fiber beam combiner, FPS - fiber phase shifter, FOI - fiber optical isolator, FA - fiber amplifier, FBC2 - 2×1 fiber beam coupler, FP - fiber positioner, FC - fiber collimator, CL - collimating lens, PLC - phase-locking controller, TTC - tip-tilt controller, FFMD - far-field metric detector.

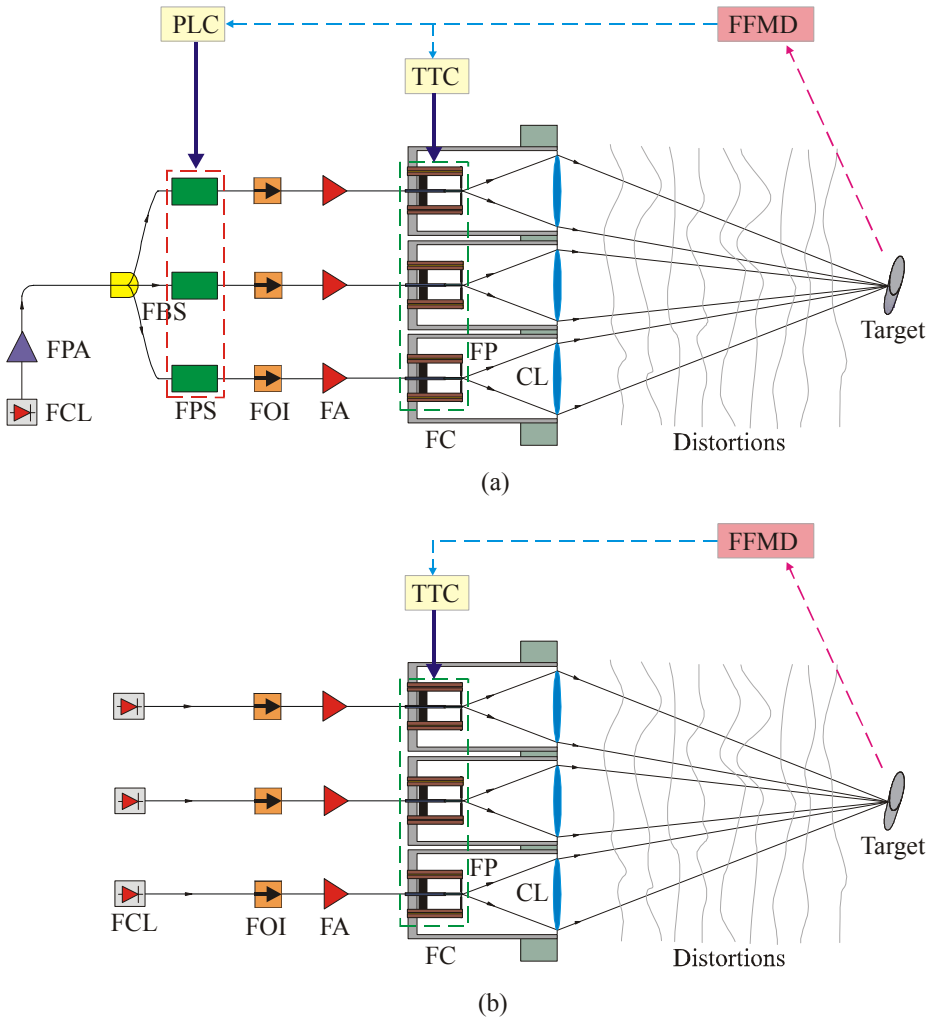

Figure 1.4: Typical system configurations for beam projection applications using a conformal adaptive phase-locked fiber array.

Here (a) is the system configuration with a single laser source, and (b) is the system configuration with beamlets originating from a laser source array. Abbreviations are the same as in Figure 1.3.

1.4 Related work

Coherent beam combining techniques can be classified into two categories: (1) passive coherent beam combining performed without external control of phase shifts in each fiber channel, and (2) active coherent beam combining with active modulations of phase shifts. Beam combining in multi-core fiber lasers [30-37], beam combining using passive fiber couplers in an all-fiber optical path [38-50] and beam combining of multiple tightly packed fiber laser bundle [50-57] belong to the passive coherent beam combining category. In these techniques, the differences of the lengths of the different optical paths are smaller than the coherence length of the used laser and no compensation for phase shifts is required. These systems can only operate in a special environment when there is no turbulence or acoustics or thermal effects which can randomly impact optical path differences in the multi-channel system.

Results from active coherent beam combining techniques in absence of both atmospheric turbulence and beam scattering off a remote target surface are reported in [58-66]. Coherent beam combining with compensation of atmospheric turbulence induced piston-type aberrations was first performed in 2004 in HRL Laboratories LLC, Malibu, California [55, 56, 67-69]. The authors demonstrated free-space phase-locking of a 70-mm-diameter aperture transceiver with a hexagonal closely packed array of seven 23-mm-diameter fiber collimator subapertures. The signal measured by the far-field receiver was maximized by modulating each subaperture's phase by adjusting the pump current to its amplifier's pump diode using multi-dithering control with lock-in amplifiers. The feedback signal was acquired from the photo detector at the target plane in the concave-mirror-converted far-field plane. In this system, compensation for weak and slow-varying atmospheric tur-

bulence effects was successfully demonstrated. The dither frequencies of the multi-dithering controller utilized were around 20kHz, which limits the phase distortion compensation bandwidth of phase-locking control. In [70, 71], coherent beam combining using stochastic parallel gradient descent (SPGD) algorithm through atmospheric turbulence performed at MIT Lincoln Laboratory in 2005 was reported. The optical outputs from 48 polarization-maintaining (PM) fibers in an 8×8 fiber array (only 48 were used) with 250μm pitch were collimated through an 8×8 lenslet array with the same pitch. The 48 collimated micro-beams were coherently combined through modulating individual in-line phase modulators (piezo-stretchers). The feedback signal was acquired from one of the photo detectors at the target plane in the lens focal plane. The perturbation rate of the SPGD controller was approximately 8kHz. This rate significantly limited the phase-locking compensation bandwidth. Another limitation of the system was the small size of the beamlet array, which is about 2mm×2mm. Besides the low perturbation/dither rate of the phase-locking controllers, both systems were also limited in the wavefront distortion compensation capabilities due to piston-only wavefront corrections.

Theoretical analysis and extensive numerical simulations [1, 72] of adaptive conformal optical system architectures recently performed at the Intelligent Optics Laboratory, U.S. Army Research Laboratory (ARL) / University of Maryland at College Park (UMD), for different numbers of subaperture elements, different geometrical parameters, different atmospheric turbulence strengths, showed that the system performance can be greately improved if both phase-locking control and tip-tilt control on each system subaperture can operate simultaneously. Due to the limitations in the modeling process such as the lack of knowledge of the actual characteristics of many physical components, the real-

time characteristics of the adaptive conformal system cannot be evaluated solely using numerical simulations but must be obtained experimentally.

1.5 Approach for the research

In the presented research the conformal adaptive phase-locked fiber array with both phase-locking control and local subaperture wavefront phase tip-tilt control is analyzed experimentally. This system is distinguished from the reported systems described in Section 1.4 (see [55, 56, 64-71]) where only phase-locking control was implemented. The following issues were addressed through both analysis and bench-top experiments:

(1) Literature search and review of the reported conformal fiber-based systems and the performance analysis results. Additional numerical simulations needed for better understanding of control issues and system parameter optimization.

(2) Experimental measurements of the actual characteristics of the key wavefront control components: the multi-channel fiber-coupled phase shifter array for phase-locking control and the piezoelectric fiber positioners for subaperture wavefront phase tip-tilt control.

(3) Analysis, optimization and hardware implementation of control algorithms and microprocessor based controllers for phase-locking and subaperture wavefront phase tip-tilt compensations. The following three SPGD controllers were designed, assembled and evaluated: (a) a PC-based SPGD controller with operational rate 16,000 iterations per second; (b) Atmel AVR microprocessor based controller with operational rate 95,000 iterations per second; (c) Atmel 32-bit ARM-based microcontroller AT91SAM9260 with operational rate 180,000 iterations per second. In addition, a multi-dithering controller

based on customized mixed-signal VLSI technology was developed in collaboration with Johns Hopkins University (JHU).

(4) Development of an all-fiber testbed for evaluation of phase-locking efficiency with different SPGD and multi-dithering controllers. In addition, the reciprocity principle of optical communication in a multi-channel all-fiber system with phase-locking control were analyzed using this testbed.

(5) Development of a free-space adaptive phase-locked system prototype with three subapertures (three fiber collimators with fiber positioners), integrated phase shifters and feedback controllers for phase-locking and subaperture tip-tilt compensation.

(6) Development of software for control and evaluation of the free-space adaptive phase-locked system prototype.

(7) Experimental analysis of the adaptive phase-locked fiber collimator array with laboratory-generated turbulence and jitter using a cooperative target (a pinhole with photo detector located at a lens focus).

(8) Experimental analysis of the adaptive phase-locked fiber collimator array with a non-cooperative extended target.

Chapter 2 Free-space laser beam combining: analysis

This chapter addresses basic principles for combining multiple beamlets in conformal optical systems. The discussion is based on relevant parts of [73-75] and Section 3.1 in [76]. In Section 2.1, propagation of a single truncated Gaussian beam is discussed. Section 2.2 addresses incoherent and coherent combining of multiple truncated Gaussian beamlets in conformal optical systems. In Section 2.3, the results from numerical simulations, which compare the properties of monolithic and conformal optical beam projection systems, are presented. In Section 2.4, the power scalability of a conformal optical system with coherent and incoherent beam combining is addressed. The simulation results are compared with theoretical results derived in Sections 2.1 and 2.2.

2.1 Propagation of single Gaussian beam

Consider a collimated laser beam with wavelength λ and vector electric field

$$\mathbf{E}_m(\mathbf{r}, z=0, t) = \hat{e}_m(t) M_m(\mathbf{r}) A_m(\mathbf{r}, z=0, t) e^{j\omega_0 t} \tag{2.1}$$

at the transmitter aperture pupil ($z=0$) propagating from a monolithic large-aperture transmitter with diameter D along the $+z$ direction to the far field. Here the subscript m indicates "monolithic", $\mathbf{r}=(x,y)$ is the transversal coordinate vector perpendicular to the z axis, t is time, $\hat{e}_m(t)$ is the unit vector describing the polarization state of the beam, $M_m(\mathbf{r})$ is the stepwise window function, which defines the aperture area Ω_m centered at $\mathbf{r}=\mathbf{0}$ with $M_m(\mathbf{r})=1$ inside Ω_m and zero otherwise. $A_m(\mathbf{r}, z=0, t)$ is the complex am-

plitude of the electric field, ω_0 is the optical carrier frequency of the beam and $j=\sqrt{-1}$. $A_m\left(\mathbf{r}, z=0, t\right)$ is considered to have a Gaussian profile

$$A_m\left(\mathbf{r}, z=0, t\right)=A_{0m}\exp\left(-\frac{\left|\mathbf{r}\right|^2}{w_{0m}^2}\right)\exp\left[j\varphi_m^{out}\left(\mathbf{r}, t\right)\right] , \tag{2.2}$$

where A_{0m} is a constant that depends on the total transmitted power P_T , w_{0m} is the waist radius of the Gaussian beam at the monolithic aperture pupil, and $\varphi_m^{out}\left(\mathbf{r}, t\right)$ is the outgoing beam phase aberration at the transmitter pupil. The Gaussian beam profile is used because it describes in good approximation the beam emerging from single-mode free-space coupled lasers as well as the lowest order mode, which propagates in an optical fiber waveguide. Higher-order modes are not considered because phase-locking requires, in general, only one mode to be present.

The monolithic aperture fill factor is defined as

$$\left(f_m\right)^2=\left(\frac{2w_{0m}}{D}\right)^2 . \tag{2.3}$$

It is reasonable to assume that the average phase aberration over the monolithic aperture vanishes, i.e.,

$$\overline{\varphi}_m^{out}\left(t\right)=\frac{1}{\pi\left(D/2\right)^2}\iint_{\Omega_m}\varphi_m^{out}\left(\mathbf{r}, t\right)d^2\mathbf{r}=0 . \tag{2.4}$$

The instantaneous pupil plane intensity is given by

$$I_m\left(\mathbf{r}, z=0, t\right) = M_m\left(\mathbf{r}\right)\left|A_{0m}\right|^2 \exp\left(-\frac{2\left|\mathbf{r}\right|^2}{w_{0m}^2}\right) \tag{2.5}$$

with the instantaneous pupil plane intensity at the aperture center $\left(\mathbf{r}=\mathbf{0}, z=0\right)$ being

$$I_m\left(\mathbf{r}=\mathbf{0}, z=0, t\right) = \left|A_{0m}\right|^2 \ . \tag{2.6}$$

The power of the truncated transmitted beam can be expressed as

$$\begin{aligned} P_m &= \iint_{\Omega_m} I_m\left(\mathbf{r}, z=0, t\right) d^2\mathbf{r} \\ &= \left[1-\exp\left(-\frac{2}{\left(f_m\right)^2}\right)\right]\frac{\pi\left(f_m\right)^2 D^2}{8}\left|A_{0m}\right|^2 \ , \\ &= \left[1-\exp\left(-\frac{2}{\left(f_m\right)^2}\right)\right] P_T \triangleq f_{cut} P_T \ , \end{aligned} \tag{2.7}$$

where

$$f_{cut} = 1-\exp\left(-\frac{2}{\left(f_m\right)^2}\right) \tag{2.8}$$

is referred to as the power cutoff coefficient of the monolithic aperture transmitter and

$$P_T = \frac{\pi\left(f_m\right)^2 D^2}{8}\left|A_{0m}\right|^2 \tag{2.9}$$

is the total output optical power before truncation by the limited aperture size. In optical systems $\left(f_m\right)^2$ is usually smaller than 1.0 and the transmitted power is thus

$$P_m \geq 0.865 P_T \ . \tag{2.10}$$

Thus, truncation does not impact the transmitted power significantly so that the cutoff effect of the finite size aperture is ignored in the following discussion until noted.

After propagation along the $+z$ direction to the target plane at $z = L$ within a medium that introduces phase distortions the vector electric field of the beam can be described by the following set of equations:

$$\mathbf{E}_m\left(\mathbf{r}, z = L, t\right) = \hat{e}_m\left(t\right) A_m\left(\mathbf{r}, z = L, t\right) e^{j\omega_0 t} \tag{2.11}$$

$$A_m\left(\mathbf{r}, z = L, t\right) \approx A_{0m} \frac{w_{0m}}{w_{Lm}} \exp\left(-\frac{|\mathbf{r}|^2}{w_{Lm}^2}\right) \exp\left[j\varphi_m^T\left(\mathbf{r}, t\right)\right] \tag{2.12}$$

$$w_{Lm} = w_{0m}\sqrt{1 + \left(\frac{L}{z_{om}}\right)^2} \tag{2.13}$$

Here $z_{om} = \dfrac{\pi\left(w_{0m}\right)^2}{\lambda}$ is the diffractive distance (also called the Rayleigh range for Gaussian beams), $\varphi_m^T\left(\mathbf{r}, t\right)$ is the beam phase at the target plane. Assuming that wavefront phase distortions are negligible (or compensated by an adaptive optics system at the transmitter), the instantaneous beam intensity at the target plane is given as

$$I_m\left(\mathbf{r}, z = L, t\right) \approx \left(\frac{w_{0m}}{w_{Lm}}\right)^2 \left|A_{0m}\right|^2 \exp\left(-\frac{2|\mathbf{r}|^2}{w_{Lm}^2}\right) \quad . \tag{2.14}$$

The target can be assumed to be in the far field if the propagation distance, L, exceeds the commonly used far field distance (see Equation 6.10 in [77])

$$L_{ff} = \frac{2D^2}{\lambda} \ , \tag{2.15}$$

where D is the diameter for a circular aperture, λ is the wavelength. (For instance, if the aperture diameter D=71mm and the wavelength λ=1064nm, then the above far field distance is $L_{ff} \approx 9.5$km.) With Equation (2.15) one can rewrite the Rayleigh range as

$$z_{om} = \frac{\pi \left(f_m \right)^2}{8} L_{ff} \ . \tag{2.16}$$

If $L \geq L_{ff}$ and $\left(f_m \right)^2 \approx (0.5 \sim 1.0)$, then

$$\left(z_{om} \right)^2 \approx \left(0.0386 \sim 0.1540 \right) \times \left(L_{ff} \right)^2 \leq 0.1540 L^2 \ . \tag{2.17}$$

Thus $\left(z_{om} \right)^2$ is generally small compared to L^2. Using Equations (2.12) and (2.13), the instantaneous intensity on the beam axis at the target plane $\left(\mathbf{r} = \mathbf{0}, z = L \right)$ can be described as

$$I_m \left(\mathbf{r} = \mathbf{0}, z = L, t \right) \approx \frac{z_{om}^2}{z_{om}^2 + L^2} \left| A_{0m} \right|^2 \ , \tag{2.18}$$

which can be approximated for $\left(z_{om} \right)^2 \ll L^2$ [Equation (2.17)] to

$$I_m \left(\mathbf{r} = \mathbf{0}, z = L, t \right) \approx \frac{z_{om}^2}{L^2} \left| A_{0m} \right|^2 = \frac{\pi^2 w_{0m}^4}{\lambda^2 L^2} \left| A_{0m} \right|^2 = \frac{\left(f_m \right)^4 \pi^2 D^4}{16 \lambda^2 L^2} \left| A_{0m} \right|^2 \tag{2.19}$$

The far field divergence angle (full solid angle, see Equation 3.1-20 in [76]) of the Gaussian laser beam is

$$\theta_m \approx \frac{2\lambda}{\pi w_{0m}} \approx \frac{2\lambda}{\pi \left(f_m \dfrac{D}{2} \right)} \approx \frac{4\lambda}{\pi D f_m} \ . \tag{2.20}$$

Equations (2.19) and (2.20) are the key results for propagation of a single Gaussian beam in free space. In the following section, Equation (2.19) will be compared with the corresponding results derived for coherent and incoherent beam combining of multiple beamlets from a conformal optical system.

2.2 Coherent and incoherent beam combining

In this section the beam intensities are analyzed for both coherent and incoherent combining of multiple beamlets transmitted by a conformal aperture system. The following convention is used throughout this section for simplicity without introducing confusion: $\{\bullet\}$ represents the ensemble of scalar or vector variables with the general indicator enclosed by $\{\ \}$. For example, $\mathbf{r}_i$ is a single vector while $\{\mathbf{r}_i\}$ indicates the ensemble $\mathbf{r}_1, \mathbf{r}_2, \cdots, \mathbf{r}_N$. Consider the system configurations as shown in Figure 1.4a and Figure 1.4b for beam projection applications. A new parameter, $(f_{con})^2$, referred to as conformal fill factor, is introduced here and is defined as the ratio of the total area of all subapertures to the area of the equivalent monolithic aperture, i.e.,

$$(f_{con})^2 = \frac{Nd^2}{D^2} \ , \tag{2.21}$$

where N is the number of subaperture elements, d is the subaperture diameter, D is the equivalent aperture diameter as shown in Figure 1.2c.

Similar to the monolithic case, for the conformal optical system the N beamlets are considered propagating along the $+z$ direction to the far field at $z = L$ and collimated at the transmitter. In addition, it is assumed that the beamlets are aligned in parallel to each

other and have the same wavelength λ . The vector electric fields at the transmitter subaperture pupils ($z = 0$) are given by

$$\mathbf{E}_i\left(\mathbf{r}, z=0, t\right) = \hat{e}_i\left(t\right) M\left(\mathbf{r}-\mathbf{r}_i\right) A_i\left(\mathbf{r}, z=0, t\right) e^{j\omega_0 t} \qquad i = 1, \cdots, N \ , \tag{2.22}$$

where $\mathbf{r}$ is the coordinate vector perpendicular to the z direction, $\left\{\mathbf{r}_i\right\}$ are the coordinate vectors at the subaperture pupil centers, t is time, $\left\{\hat{e}_i\left(t\right)\right\}$ are the unit vectors describing the polarization states of the respective beamlets, $\left\{M\left(\mathbf{r}-\mathbf{r}_i\right)\right\}$ are the stepwise window functions defining the subaperture areas $\left\{\Omega_i\right\}$ centered at $\left\{\mathbf{r}_i\right\}$ such that $\left\{M\left(\mathbf{r}-\mathbf{r}_i\right)=1\right\}$ inside the respective $\left\{\Omega_i\right\}$ and zero otherwise, $\left\{A_i\left(\mathbf{r}, z=0, t\right)\right\}$ are the respective complex electric field amplitudes for the N beamlets, ω_0 is the identical optical carrier frequency for all N beamlets, and $j = \sqrt{-1}$. It is assumed that the beamets 'amplitudes', $\left\{A_i\left(\mathbf{r}, z=0, t\right)\right\}$, have Gaussian profiles, i.e.,

$$\begin{aligned} A_i\left(\mathbf{r}, z=0, t\right) = A_{0i} \exp\left(-\frac{\left|\mathbf{r}-\mathbf{r}_i\right|^2}{w_0^2}\right) \qquad & i = 1, \cdots, N \ , \\ \times \exp\left[\, j\varphi_i^{out}\left(\mathbf{r}, t\right) + j\Delta_i^{out}\left(t\right)\right] & \end{aligned} \tag{2.23}$$

where $\left\{A_{0i}\right\}$ are constants which depend on the respective transmitted powers $\left\{P_{iT}\right\}$, w_0 is the common waist radius for all identical Gaussian beamlets at the respective subaperture pupils, $\left\{\varphi_i^{out}\left(\mathbf{r}, t\right)\right\}$ are the respective phase aberrations at the transmitter pupil plane for the N outgoing beamlets, and $\left\{\Delta_i^{out}\left(t\right)\right\}$ are the respective phase shifts of the beamlets at the transmitter pupils.

Similar to the definition of the monolithic aperture fill factor in Equation (2.3), the subaperture fill factor of a conformal optical system can be defined as

$$\left(f_{sub}\right)^2 = \left(\frac{2w_0}{d}\right)^2 \quad . \tag{2.24}$$

It is reasonable to assume zero averaged phase aberrations over each subaperture, i.e.,

$$\bar{\varphi}_i^{out}\left(t\right) = \frac{1}{\pi\left(d/2\right)^2}\iint_{\Omega_i}\varphi_i^{out}\left(\mathbf{r},t\right)d^2\mathbf{r} = 0 \qquad i = 1,\cdots,N \; . \tag{2.25}$$

The instantaneous intensities of the beamlets at the transmitter pupil plane are described by

$$I_i\left(\mathbf{r},z=0,t\right) = M\left(\mathbf{r}-\mathbf{r}_i\right)\left|A_{0i}\right|^2 \exp\left(-\frac{2\left|\mathbf{r}-\mathbf{r}_i\right|^2}{w_0^2}\right) \qquad i = 1,\cdots,N \; . \tag{2.26}$$

The power of a beamlet exiting its respective subaperture is given by

$$\begin{aligned} P_i &= \iint_{\Omega_i} I_i\left(\mathbf{r},z=0,t\right)d^2\mathbf{r} \\ &= \left[1-\exp\left(-\frac{2}{\left(f_{sub}\right)^2}\right)\right]\frac{\pi\left(f_{sub}\right)^2 d^2}{8}\left|A_{0i}\right|^2 \qquad i = 1,\cdots,N \; . \\ &= \left[1-\exp\left(-\frac{2}{\left(f_{sub}\right)^2}\right)\right]P_{iT} \end{aligned} \tag{2.27}$$

If the subaperture fill factor $\left(f_{sub}\right)^2$ in Equation (2.24) is assumed to be identical to the monolithic aperture fill factor $\left(f_m\right)^2$ in Equation (2.3), then the expressions for the cutoff coefficients for the subapertures in the conformal system and the monolithic aperture sys-

tem are the same. As in the case of the monolithic system above, the beam truncation effects are neglected in the following discussion for the conformal system.

At the target plane in the far field ($z = L$), the vector electric field of the combined beam is

$$\mathbf{E}\left(\mathbf{r}, z = L, t\right) = \sum_{i=1}^{N} \mathbf{E}_i\left(\mathbf{r}, z = L, t\right) \tag{2.28}$$

$$\mathbf{E}_i\left(\mathbf{r}, z = L, t\right) = \hat{e}_i\left(t\right) A_i\left(\mathbf{r}, z = L, t\right) e^{j\omega_0 t} \qquad i = 1, \cdots, N \tag{2.29}$$

$$\begin{aligned} A_i\left(\mathbf{r}, z = L, t\right) \approx A_{0i} \left(\frac{w_0}{w_L}\right) \exp\left(-\frac{|\mathbf{r}|^2}{w_L^2}\right) \qquad & i = 1, \cdots, N \\ \times \exp\left[j\varphi_i^T\left(\mathbf{r}, t\right) + j\Delta_i^T\left(t\right)\right] & \end{aligned} \tag{2.30}$$

$$w_L = w_0 \sqrt{1 + \left(\frac{L}{z_o}\right)^2} \tag{2.31}$$

Here $z_o = \dfrac{\pi\left(w_0\right)^2}{\lambda}$ is the diffractive distance (the Rayleigh range for Gaussian beamlets), $\left\{\varphi_i^T\left(\mathbf{r}, t\right)\right\}$ are the respective total beam phase aberrations at the target plane for each beamlet, $\left\{\Delta_i^T\left(t\right)\right\}$ are the respective differences of total phase shifts at the target plane for each beamlet.

If the total wavefront phase term for a beamlet at the target plane is denoted as

$$\Phi_i\left(\mathbf{r}, t\right) = \varphi_i^T\left(\mathbf{r}, t\right) + \Delta_i^T\left(t\right) \qquad i = 1, \cdots, N \ , \tag{2.32}$$

the instantaneous combined beam intensity at the target plane $(z = L)$ can be described as

$$I(\mathbf{r}, z = L, t) \approx \left(\frac{w_0}{w_L}\right)^2 \exp\left(-\frac{2|\mathbf{r}|^2}{w_L^2}\right) \times \left[\sum_{i=1}^{N} |A_{0i}|^2 + \underbrace{\sum_{1 \le i \ne s \le N} p_{i,s}(t)\left(A_{0i}^* \bullet A_{0s}\right)\cos\left(\Phi_i - \Phi_s\right)}_{N(N-1) \text{ terms in total}}\right] \tag{2.33}$$

where "*" indicates the complex conjugate and

$$p_{i,s}(t) = \hat{e}_i(t) \bullet \hat{e}_s(t) \qquad i, s = 1, \cdots, N \tag{2.34}$$

are the scalar products of the respective unit polarization vectors.

With Equations (2.21) and (2.15) one can express the Rayleigh range as

$$z_o = \frac{\pi (f_{sub})^2 (f_{con})^2}{8N} L_{ff} \ . \tag{2.35}$$

If $L \ge L_{ff}$, $(f_{sub})^2 \approx (0.5 \sim 1.0)$, $(f_{con})^2 \approx (0.3 \sim 1.0)$, and $N \ge 3$, then

$$(z_o)^2 \approx (0.0004 \sim 0.017) \times (L_{ff})^2 \le 0.017 L^2 \ . \tag{2.36}$$

Thus $(z_o)^2$ is small compared to L^2 and the instantaneous intensity at the target plane on the beam axis $(\mathbf{r} = \mathbf{0}, z = L)$, which is given by

$$I\left(\mathbf{r}=\mathbf{0},z=L,t\right)\approx\frac{z_o^2}{z_o^2+L^2}\left[\sum_{i=1}^{N}\left|A_{0i}\right|^2+\underbrace{\sum_{1\le i\ne s\le N}p_{i,s}\left(t\right)\left(A_{0i}^{*}\bullet A_{0s}\right)\cos\left(\Phi_i-\Phi_s\right)}_{N\left(N-1\right)\ \text{terms in total}}\right],\tag{2.37}$$

can be approximated by

$$I\left(\mathbf{r}=\mathbf{0},z=L,t\right)\approx\frac{\left(f_{sub}\right)^4\pi^2d^4}{16\lambda^2L^2}\left[\sum_{i=1}^{N}\left|A_{0i}\right|^2+\underbrace{\sum_{1\le i\ne s\le N}p_{i,s}\left(t\right)\left(A_{0i}^{*}\bullet A_{0s}\right)\cos\left(\Phi_i-\Phi_s\right)}_{N\left(N-1\right)\ \text{terms in total}}\right].\tag{2.38}$$

If the polarization states of the N beamlets are collinear at the target plane such that

$$p_{i,s}\left(t\right)=1\qquad i,s=1,\cdots,N\ ,\tag{2.39}$$

the subaperture wavefront phase distortions are negligible (or compensated completely for each beamlet with subaperture adaptive optics) and

$$\left[\Phi_i\left(\mathbf{r},t\right)-\Phi_s\left(\mathbf{r},t\right)\right]\bmod 2\pi=0\qquad i,s=1,\cdots,N\tag{2.40}$$

due to phase-locking control, then the N beamlets are said to be combined coherently at the target plane in the far field. In Equation (2.40), "mod" indicates modulo operation.

In order to compare the different systems, the total transmitted power in the conformal system needs to be approximately equal to the transmitted power in the monolithic aperture system discussed in Section 2.1 such that

$$\sum_{i=1}^{N}P_i\approx P_m\ .\tag{2.41}$$

Using Equations (2.7) and (2.27) it follows

$$d^2 \sum_{i=1}^{N} \left| A_{0i} \right|^2 \approx D^2 \left| A_{0m} \right|^2 \tag{2.42}$$

and from Equation (2.21), assuming that all subapertures transmit the same power

$$\left| A_{0i} \right|^2 \equiv \left| A_0 \right|^2 \approx \frac{\left| A_{0m} \right|^2}{\left(f_{con} \right)^2} \ . \tag{2.43}$$

With these assumptions for the coherent beam combining, the instantaneous intensity at the target plane on the beam axis $\left(\mathbf{r} = 0, z = L \right)$ can be written as

$$I^{coh} \left(\mathbf{r} = \mathbf{0}, z = L, t \right) \approx \frac{\left(f_{sub} \right)^4 \pi^2 \left(N d^2 \right)^2}{16 \lambda^2 L^2 \left(f_{con} \right)^2} \left| A_{0m} \right|^2 \ . \tag{2.44}$$

Comparing Equation (2.44) for coherent beam combining to Equation (2.19) for a single Gaussian beam in a monolithic optical system one can derive

$$I^{coh} \left(\mathbf{r} = \mathbf{0}, z = L, t \right) \approx \left(f_{con} \right)^2 I_m \left(\mathbf{r} = \mathbf{0}, z = L, t \right) \ . \tag{2.45}$$

Equations (2.44) and (2.45) are the most important results for coherent beam combining case in the conformal optical system as shown in Figure 1.4(a). These results show that the far-field intensity achievable with a monolithic optical system is the upper limit for conformal optical systems with coherent beam combining if they have the same aperture diameter D and the aperture fill factors $\left(f_{sub} \right)^2$, $\left(f_m \right)^2$ are equivalent.

Usually the optical detectors, receivers, or targets have a finitely fast response speed and must spend a certain amount of time τ to collect sufficient optical power and respond to

the incident optical signal. The measured intensity at the target plane on the beam axis is thus actually a temporal average given by

$$I\left(\mathbf{r}=\mathbf{0},z=L\right)=\left\langle I\left(\mathbf{r}=\mathbf{0},z=L,t\right)\right\rangle_{\tau}$$
$$\approx\frac{\left(f_{sub}\right)^{4}\pi^{2}d^{4}}{16\lambda^{2}L^{2}}\left[\sum_{i=1}^{N}\left|A_{0i}\right|^{2}+\underbrace{\sum_{1\le i\ne s\le N}p_{i,s}\left(t\right)\left(A_{0i}^{*}\cdot A_{0s}\right)\left\langle\cos\left(\Phi_{i}-\Phi_{s}\right)\right\rangle_{\tau}}_{N\left(N-1\right)\ \text{terms in total}}\right], \tag{2.46}$$

where $\left\langle\cdot\right\rangle_{\tau}$ indicates the average operation over the time interval τ. Typically τ is longer than the coherence time (1ns~1μs) of outgoing laser beamlets but much shorter than the characteristic update time (1ms~100ms) of atmospheric phase distortions. For a monolithic aperture transmitter with zero residual phase error or a conformal transmitter in the case of coherent beam combining, the average intensity over time τ is identical to the corresponding instantaneous intensity. Hence, we can rewrite the Equation (2.45) as

$$I^{coh}\left(\mathbf{r}=\mathbf{0},z=L\right)\approx\left(f_{con}\right)^{2}I_{m}\left(\mathbf{r}=\mathbf{0},z=L\right) \tag{2.47}$$

If, however, the phase differences $\left\{\Phi_{i}\left(\mathbf{r},t\right)\right\}$ for $1\le i\le N$ are scrambled enough to be considered random within the time averaging interval, the sum of interference terms in the expression of the on-axis intensity in the target plane vanishes, i.e.,

$$\left\langle\cos\left[\Phi_{i}\left(\mathbf{r},t\right)-\Phi_{s}\left(\mathbf{r},t\right)\right]\right\rangle_{\tau}=0\qquad 1\le i\ne s\le N\ , \tag{2.48}$$

and the average intensity in the target plane on the beam axis can be written as

$$I^{Incoh}\left(\mathbf{r}=\mathbf{0},z=L\right)\approx\frac{1}{N}\left(f_{con}\right)^{2}I_{m}\left(\mathbf{r}=\mathbf{0},z=L\right)\ . \tag{2.49}$$

In this case, the N beamlets are virtually independent to each other because their relative wavefront phases do not affect the average combined beam intensity in the target plane. Strictly speaking, this case may be referred to as pseudo-incoherent beam combining in the sense that the N beamlets originating from the same laser source with exactly identical wavelengths and wavelength variation dynamics but with sufficiently scrambled phases are not really incoherent. The genuine incoherent beams are usually generated by different laser sources with either same wavelengths or different wavelengths as shown in Figure 1.4(b). In this thesis the term "incoherent beams" is used for both pseudo-incoherent beams and genuine incoherent beams.

From substituting Equation (2.47) into Equation (2.49) follows

$$I^{coh}\left(\mathbf{r}=\mathbf{0}, z=L\right) \approx N \times I^{Incoh}\left(\mathbf{r}=\mathbf{0}, z=L\right) \ . \tag{2.50}$$

For incoherent beam combining, phase-locking control is not required. Therefore, it is easier to realize incoherent beam combining than to realize coherent beam combining. Moreover the optical output power level per beamlet can be higher mostly because the lower requirements on the coherence length or time, which allow for much broader laser linewidths (or even multiple lines). In addition, incoherent beamlets can propagate in multiple modes and the polarization states may be random.

Currently the power per subaperture for incoherent beam combining can be as high as six times the power level per subaperture for coherent beam combining [78]. Hence, it follows from Equation (2.50) that the maximum achievable on-axis intensity at the target for coherent beam combining can be up to $N/6$ times the corresponding value for incoherent

beam combining. Thus, if the number of subapertures is larger than six (i.e., $N \geq 7$), the maximum intensity on the target is higher for phase-locked coherently combined beams.

2.3 Comparison of conformal and monolithic optical systems: simulation

In this section conformal and monolithic optical systems are compared from a different point of view. Their performances are characterized by the far-field target plane peak intensity and the beam divergence angle obtained from numerical simulations. For conformal optical systems only the case of coherent beam combining is considered. As in the previous sections, each conformal optical system is considered to have N identical subapertures with diameter d. The aperture diameter of an equivalent monolithic system, D, is defined as the diameter of the smallest circle that can enclose all N subapertures. For the simulation of different conformal systems, d is adjusted in dependence on N, while the equivalent aperture diameter D, is kept constant.

The far-field complex electric field can be calculated as the two-dimensional spatial Fourier transform of the complex electric field in the aperture plane if the Fraunhoffer approximation for diffraction is valid [79]. This does not consider any phase distortions, e.g., from atmospheric turbulence; they are considered to be negligibly small or completely compensated by adaptive optics systems in the subapertures.

It is important at this point to select the appropriate value for the subaperture fill factor $\left(f_{sub}\right)^2$. In general, the subaperture fill factor $\left(f_{sub}\right)^2$ affects the system performance in the following manner for both laser communications and beam projection applications. Increasing $\left(f_{sub}\right)^2$ leads, on one hand, to outgoing beamlets with more uniform intensity distribution and thus increases the far-field on-axis intensity (i.e., reduces the beamlet's

divergence angle). On the other hand, more of the beamlet is cut off for larger $(f_{sub})^2$ due to truncation by the fiber-collimator subapertures, which reduces the transmitted power as indicated by the power cutoff coefficient f_{cut}. Increasing $(f_{sub})^2$ also leads to additional phase aberrations (induced by thermal effects, i.e., heating of collimator optics) in high energy systems. Numerical analysis in [80] shows that the subaperture fill factor of $(f_{sub})^2 \approx 0.89^2$ is close to the optimum for almost all relevant cases (especially in beam projection applications if zero-separation tightly packed hexagonal configuration is used). This value is used in all of the following simulations.

Two sets of simulations with two different conformal fill factors were performed. The first set, as shown in Figure 2.1, Figure 2.2, Figure 2.3, and Figure 2.4, includes nine cases: (a) a monolithic aperture with uniform intensity profile, (b) a Gaussian beam in a monolithic aperture, and (c-i) beamlets with Gaussian intensity profile in conformal systems with (c) three, (d) seven, (e) nineteen, (f) 37, (g) 61, (h) 91, and (i) 127 subapertures. For the conformal optical systems (c-i), tightly packed hexagonal configurations are considered, where the subaperture's diameter equals the distance between their centers. For all cases a uniform phase across the whole aperture is assumed. In Figure 2.1 the near-field intensity distributions for all cases are presented as grayscale images. Figure 2.2 shows the near-field intensity profiles along horizontal cross-section through the center of the respective aperture structure. The total transmitted power is the same for all nine cases, which requires that the near-field peak intensities are different, as can be seen from Figure 2.2. In Figure 2.3 the corresponding far-field intensity distributions (as calculated from the Fourier transformation of the respective near field) are shown. Figure 2.4 pro-

vides the corresponding far-field intensity profiles and derived beam divergence angles. The angular values for the abscissa are based on a diameter of $D = 33\,\text{cm}$ (13 inch) for the monolithic aperture or its equivalent for the conformal systems.

The second set of simulations, as shown in Figure 2.5, Figure 2.6, Figure 2.7, and Figure 2.8, was performed for nine similar cases with the difference that now for the conformal optical systems (c-i) less dense packed hexagonal configurations were considered, i.e., the subaperture diameter was reduced in comparison to the subaperture center distance by a factor of 0.80. The near-field intensity distributions and its cross-section (shown in Figure 2.5 and Figure 2.6, respectively) indicate that in comparison to the earlier configuration the near-field peak intensities are higher in order to obtain the same transmitted power. In Figure 2.7 and Figure 2.8 the corresponding far-field intensity distributions and their cross-sections are shown.

The results of the above numerical simulations verify the theoretical analysis in Sections 2.1 and 2.2.

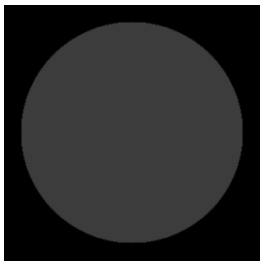

(a) monolithic aperture, uniform beam intensity

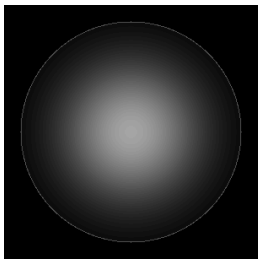

(b) monolithic aperture, Gaussian beam intensity

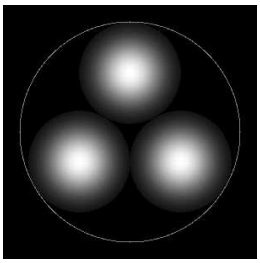

(c) three subapertures, Gaussian beam intensity

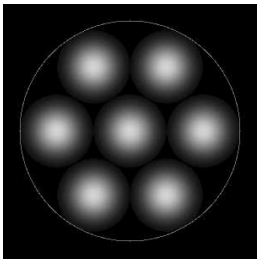

(d) seven subapertures, Gaussian beam intensity

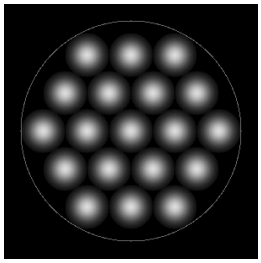

(e) nineteen subapertures, Gaussian beam intensity

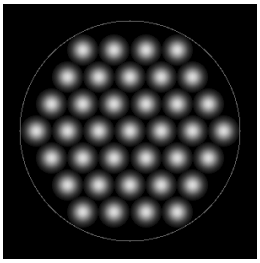

(f) 37 subapertures, Gaussian beam intensity

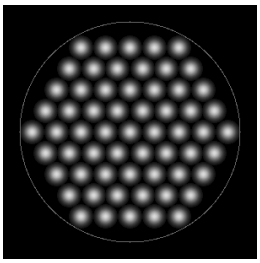

(g) 61 subapertures, Gaussian beam intensity

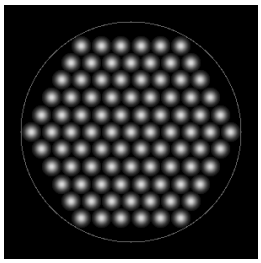

(h) 91 subapertures, Gaussian beam intensity

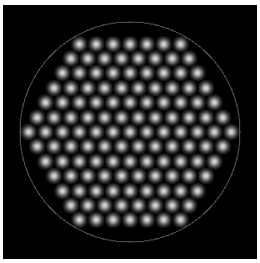

(i) 127 subapertures, Gaussian beam intensity

Figure 2.1: Near-field intensity distributions of densely packed beamlets with uniform outgoing phases. In each subfigure, the large gray circle outlines the monolithic aperture boundary or the equivalent aperture boundary for the conformal optical systems. The subaperture fill factor for the Gaussian profile is 0.89. Total outgoing powers for all cases are identical. For the conformal optical systems, all subapertures are packed tightly in a hexagonal pattern. Each subfigure stands for a 15" × 15" rectangle area.

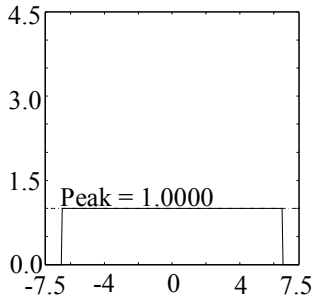

(a) monolithic aperture, uniform beam intensity

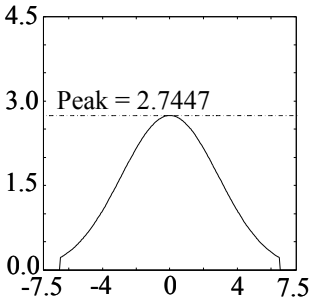

(b) monolithic aperture, Gaussian beam intensity

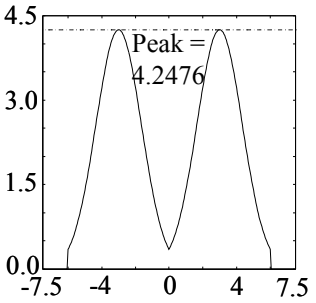

(c) three subapertures, Gaussian beam intensity

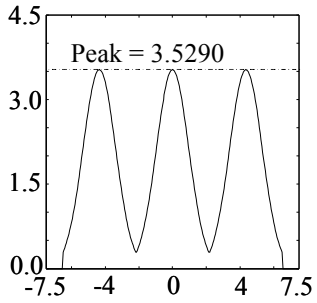

(d) seven subapertures, Gaussian beam intensity

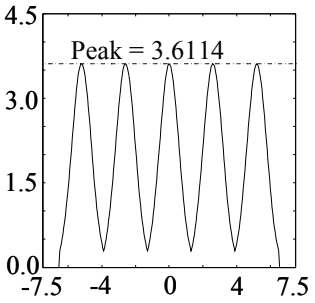

(e) nineteen subapertures, Gaussian beam intensity

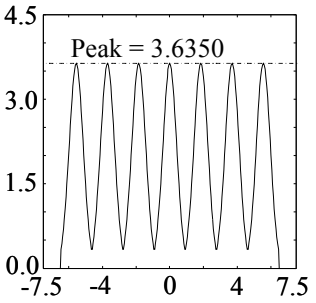

(f) 37 subapertures, Gaussian beam intensity

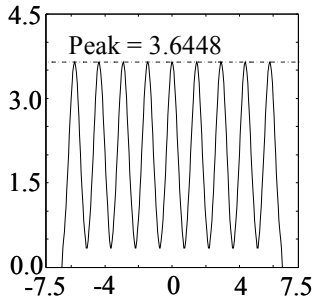

(g) 61 subapertures, Gaussian beam intensity

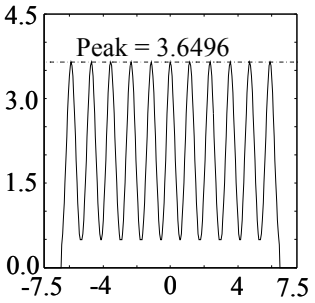

(h) 91 subapertures, Gaussian beam intensity

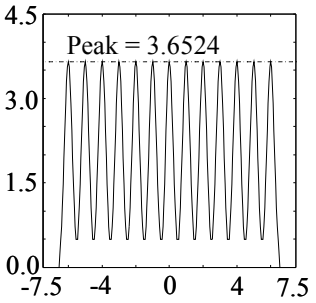

(i) 127 subapertures, Gaussian beam intensity

Figure 2.2: Near-field intensity distributions with uniform outgoing phases (sections along center horizontal lines of subfigures in Figure 2.1).

The exception is in subfigure (c), where the section passes through the centers of the two lower subapertures. The horizontal axis for each subfigure is labeled in inches. The normalized peak intensities as shown with respect to case (a) are used to keep the total outgoing powers identical to each other.

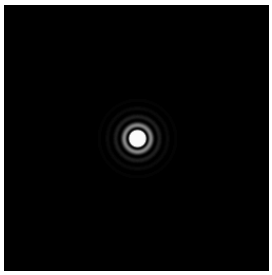

(a) monolithic aperture, uniform beam intensity

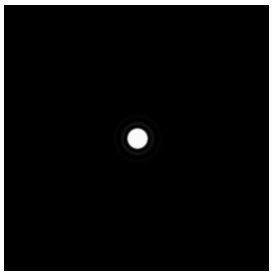

(b) monolithic aperture, Gaussian beam intensity

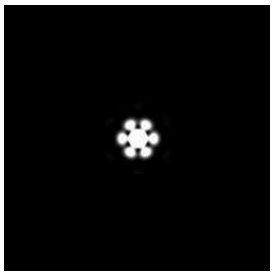

(c) three subapertures, Gaussian beam intensity

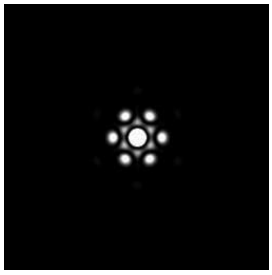

(d) seven subapertures, Gaussian beam intensity

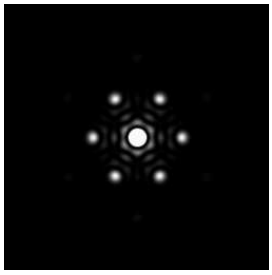

(e) nineteen subapertures, Gaussian beam intensity

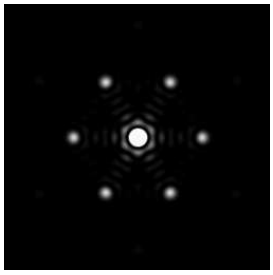

(f) 37 subapertures, Gaussian beam intensity

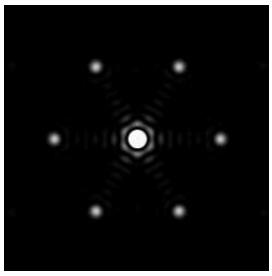

(g) 61 subapertures, Gaussian beam intensity

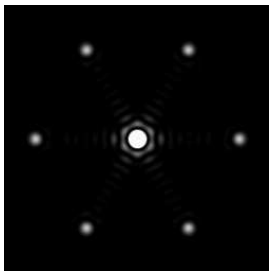

(h) 91 subapertures, Gaussian beam intensity

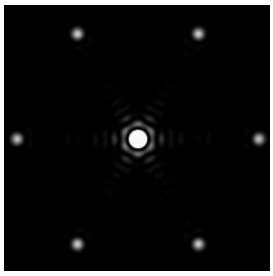

(i) 127 subapertures, Gaussian beam intensity

Figure 2.3: Far-field intensity distributions of the corresponding near-field intensity distributions as shown in Figure 2.1 and Figure 2.2.

Each subfigure stands for a 150μrad by 150μrad area in the far field around its beam axis.

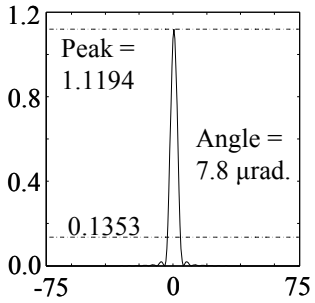

(a) monolithic aperture, uniform beam intensity

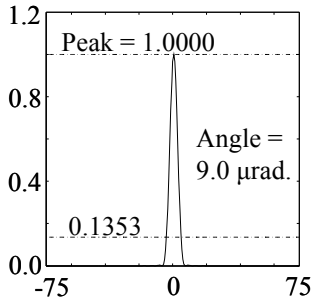

(b) monolithic aperture, Gaussian beam intensity

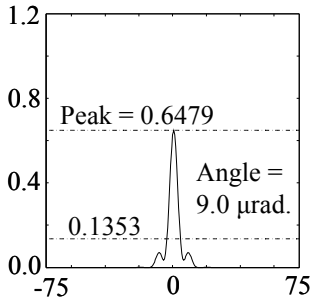

(c) three subapertures, Gaussian beam intensity

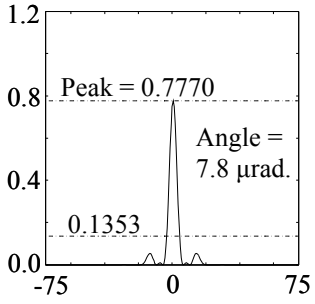

(d) seven subapertures, Gaussian beam intensity

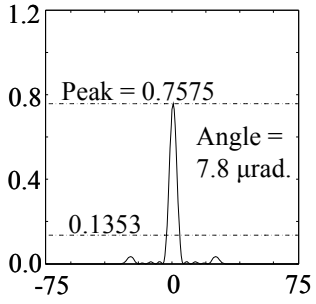

(e) nineteen subapertures, Gaussian beam intensity

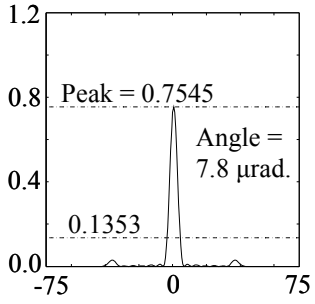

(f) 37 subapertures, Gaussian beam intensity

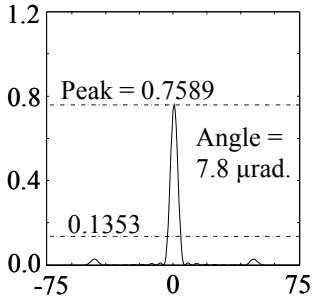

(g) 61 subapertures, Gaussian beam intensity

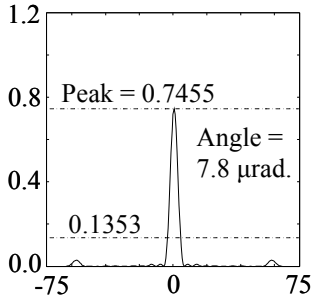

(h) 91 subapertures, Gaussian beam intensity

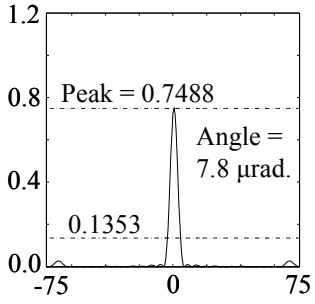

(i) 127 subapertures, Gaussian beam intensity

Figure 2.4:Far-field intensity distributions of the corresponding near-field intensity distributions (sections along center horizontal lines of subfigures in Figure 2.3) in Figure 2.1 and Figure 2.2. The horizontal axis for each subfigure is labeled in µrad.

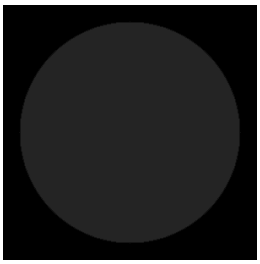

(a) monolithic aperture, uniform beam intensity

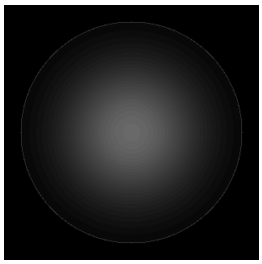

(b) monolithic aperture, Gaussian beam intensity

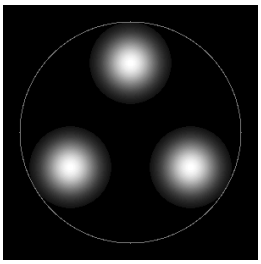

(c) three subapertures, Gaussian beam intensity

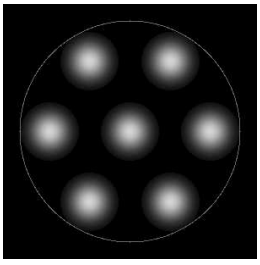

(d) seven subapertures, Gaussian beam intensity

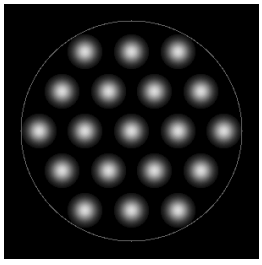

(e) nineteen subapertures, Gaussian beam intensity

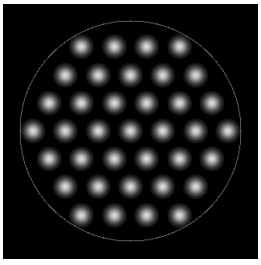

(f) 37 subapertures, Gaussian beam intensity

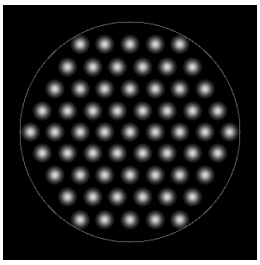

(g) 61 subapertures, Gaussian beam intensity

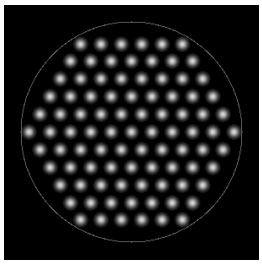

(h) 91 subapertures, Gaussian beam intensity

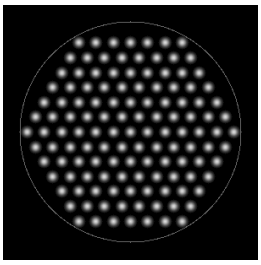

(i) 127 subapertures, Gaussian beam intensity

Figure 2.5: Near-field intensity distributions of tightly packed beamlets with uniform outgoing phases. In each subfigure, the large gray circle outlines the monolithic aperture boundary or the equivalent aperture boundary for the conformal optical systems. The subaperture fill factor for Gaussian profile is 0.89. Total outgoing powers for all cases are identical. For the conformal optical systems, all subapertures are packed in a hexagonal pattern. The subaperture diameter for each conformal system, however, is shrunk to 0.80 times of the subaperture diameter in the corresponding case in Figure 2.1. Each subfigure stands for a 15" × 15" rectangle area.

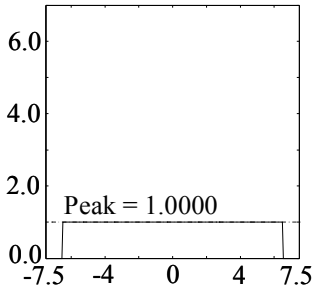

(a) monolithic aperture, uniform beam intensity

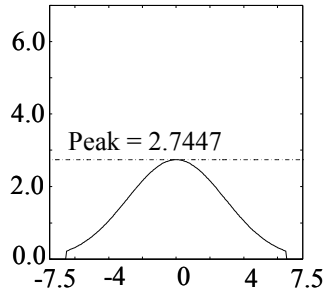

(b) monolithic aperture, Gaussian beam intensity

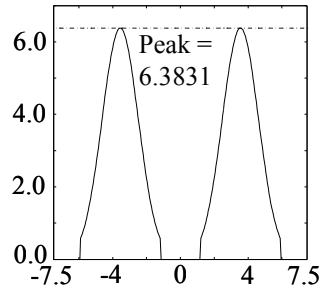

(c) three subapertures, Gaussian beam intensity

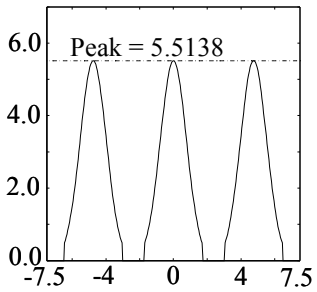

(d) seven subapertures, Gaussian beam intensity

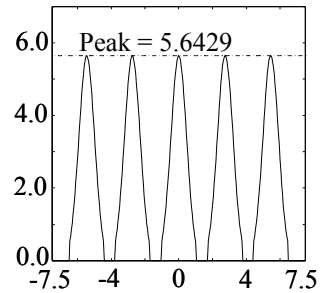

(e) nineteen subapertures, Gaussian beam intensity

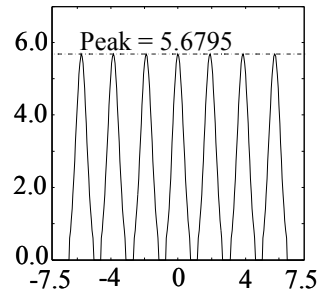

(f) 37 subapertures, Gaussian beam intensity

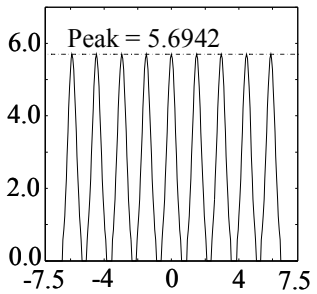

(g) 61 subapertures, Gaussian beam intensity

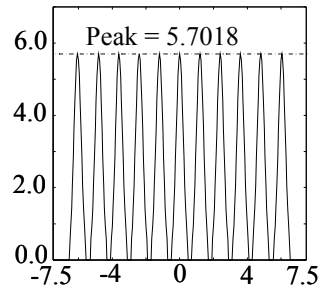

(h) 91 subapertures, Gaussian beam intensity

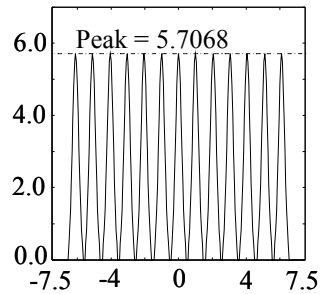

(i) 127 subapertures, Gaussian beam intensity

Figure 2.6: Near-field intensity distributions with uniform outgoing phases (sections along center horizontal lines of subfigures in Figure 2.5).

The exception is in subfigure (c), where the section passes through the centers of the two lower subapertures. The horizontal axis for each subfigure is labeled in inches. The normalized peak intensities as shown with respect to case (a) are used to keep the total outgoing powers identical to each other.

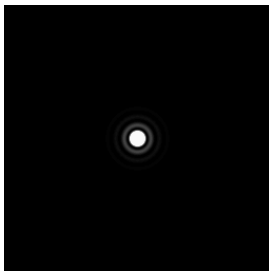

(a) monolithic aperture, uniform beam intensity

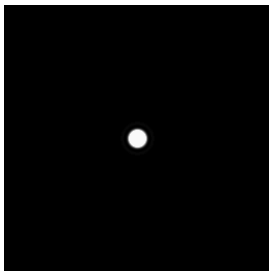

(b) monolithic aperture, Gaussian beam intensity

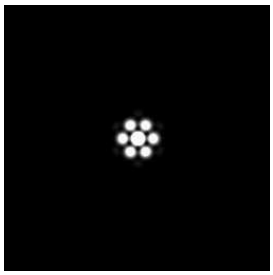

(c) three subapertures, Gaussian beam intensity

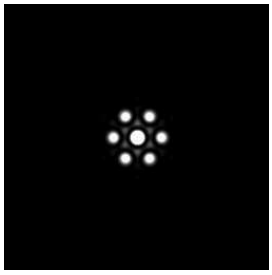

(d) seven subapertures, Gaussian beam intensity

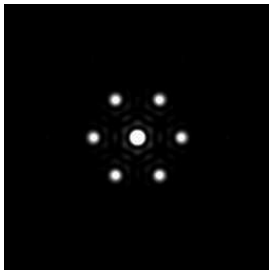

(e) nineteen subapertures, Gaussian beam intensity

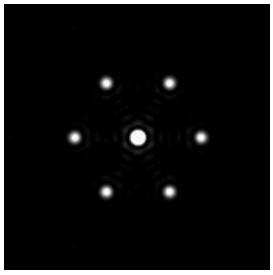

(f) 37 subapertures, Gaussian beam intensity

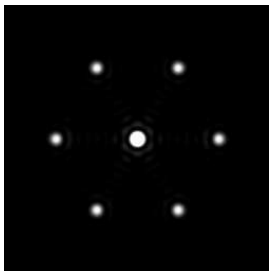

(g) 61 subapertures, Gaussian beam intensity

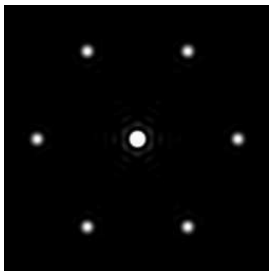

(h) 91 subapertures, Gaussian beam intensity

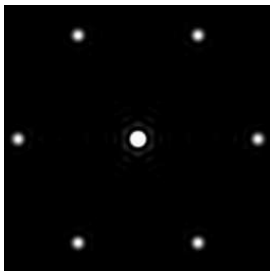

(i) 127 subapertures, Gaussian beam intensity

Figure 2.7: Far-field intensity distributions of the corresponding near-field intensity distributions as shown in Figure 2.5 and Figure 2.6.

Each subfigure stands for a 150μrad by 150μrad area in the far field around its beam axis.

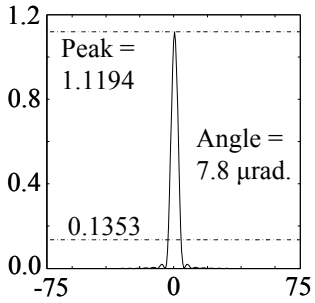

(a) monolithic aperture, uniform beam intensity

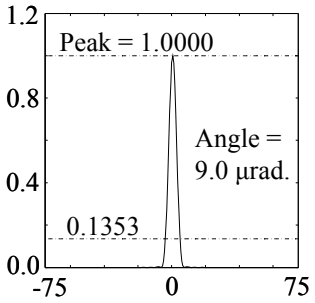

(b) monolithic aperture, Gaussian beam intensity

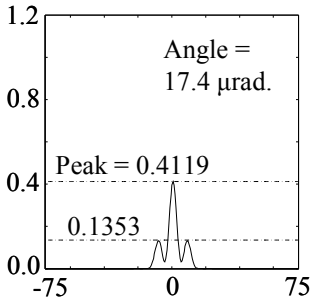

(c) three subapertures, Gaussian beam intensity

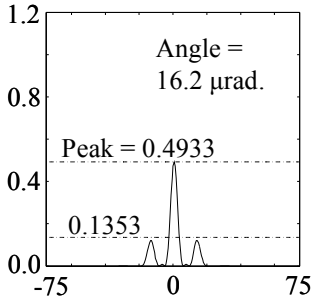

(d) seven subapertures, Gaussian beam intensity

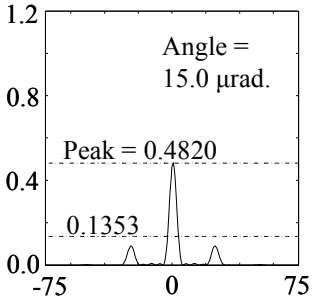

(e) nineteen subapertures, Gaussian beam intensity

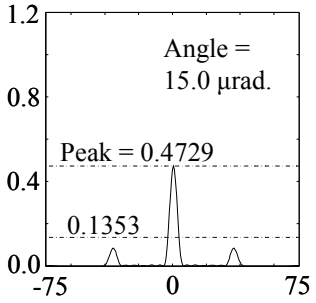

(f) 37 subapertures, Gaussian beam intensity

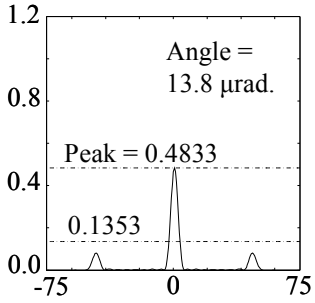

(g) 61 subapertures, Gaussian beam intensity

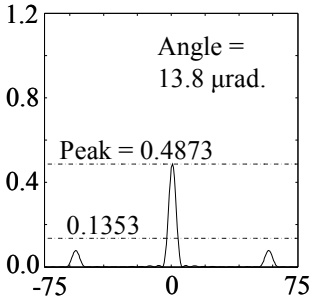

(h) 91 subapertures, Gaussian beam intensity

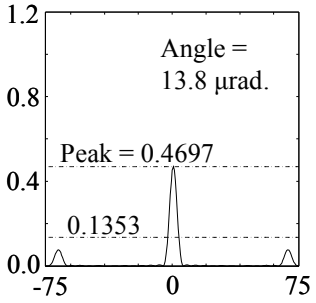

(i) 127 subapertures, Gaussian beam intensity

Figure 2.8: Far-field intensity distributions of corresponding near-field intensity distributions (sections along center horizontal lines of subfigures in Figure 2.7) in Figure 2.5 and Figure 2.6.

The horizontal axis is labeled in μrad. The normalized peak intensities as shown with respect to case (b) are used to keep the total outgoing powers identical to each other.

2.4 Power scalability of coherent vs. incoherent beam combining: simulation

In this section, the power scalability of conformal optical systems is evaluated. In contrast to the previous section, incoherent and coherent beam combining are considered, the size of individual subapertures is kept constant and, thus the size of the conformal aperture increases with the number of beamlets *N*. Assuming that the complex electric vector fields of the N beamlets is described by

$$E_i\left(\mathbf{r}_{nf}\right) = M\left(\mathbf{r}_{nf} - \mathbf{r}_i\right) A_i\left(\mathbf{r}_{nf}\right) \qquad i = 1, \cdots, N \tag{2.51}$$

and the beamlets have identical polarization states (the time variable t and position $z = 0$ are omitted here without loss of generality; $\mathbf{r}_{nf}$ instead of $\mathbf{r}$ is used to represent transversal coordinates in the near field), then the far-field intensity distributions [i.e., for $\mathbf{r}$ and $z \geq L_{ff}$, see Equation (2.15)] for coherent and incoherent beam combining can be calculated using

$$I^{Coh}\left(\frac{\mathbf{r}}{z}\right) = \left\| FFT2\left(\sum_{i=1}^{N} E_i\left(\mathbf{r}_{nf}\right)\right)\right\|^2 \tag{2.52}$$

and

$$I^{Incoh}\left(\frac{\mathbf{r}}{z}\right) = \sum_{i=1}^{N}\left(\left\| FFT2\left(E_i\left(\mathbf{r}_{nf}\right)\right)\right\|^2\right) , \tag{2.53}$$

respectively. Here $FFT2(\bullet)$ is the two-dimensional spatial Fourier transform as shown in Equation 2.1 of [79], $\|\bullet\|^2$ is the intensity operation by squaring the combined field complex amplitude, and $\frac{\mathbf{r}}{z}$ indicates the far-field spatial frequency.

Figure 2.9 shows the seven configurations with 1, 7, 19, 37, 61, 91, 127 subaperture elements, respectively, that were considered. Subaperture elements are identical and transmit the same power, i.e., the total outgoing power is proportional to the number of subaperture elements, N . Figure 2.10 shows the far-field target plane peak intensity values calculated for coherent beam combining in dependence on N. The peak intensity is quadratic to the number of subaperture elements, N . Figure 2.11 shows the corresponding results for incoherent beam combining. In this case, the target plane peak intensity is linear to N . The far-field target plane peak intensity gain, G , defined as the ratio of the far-field target plane peak intensities of coherent and incoherent beam combining, i.e.,

$$G = \frac{I^{Coh}\left(\mathbf{r}=\mathbf{0}\right)}{I^{Incoh}\left(\mathbf{r}=\mathbf{0}\right)} \tag{2.54}$$

is linear to the number of subaperture elements N in accordance with Equation (2.50).

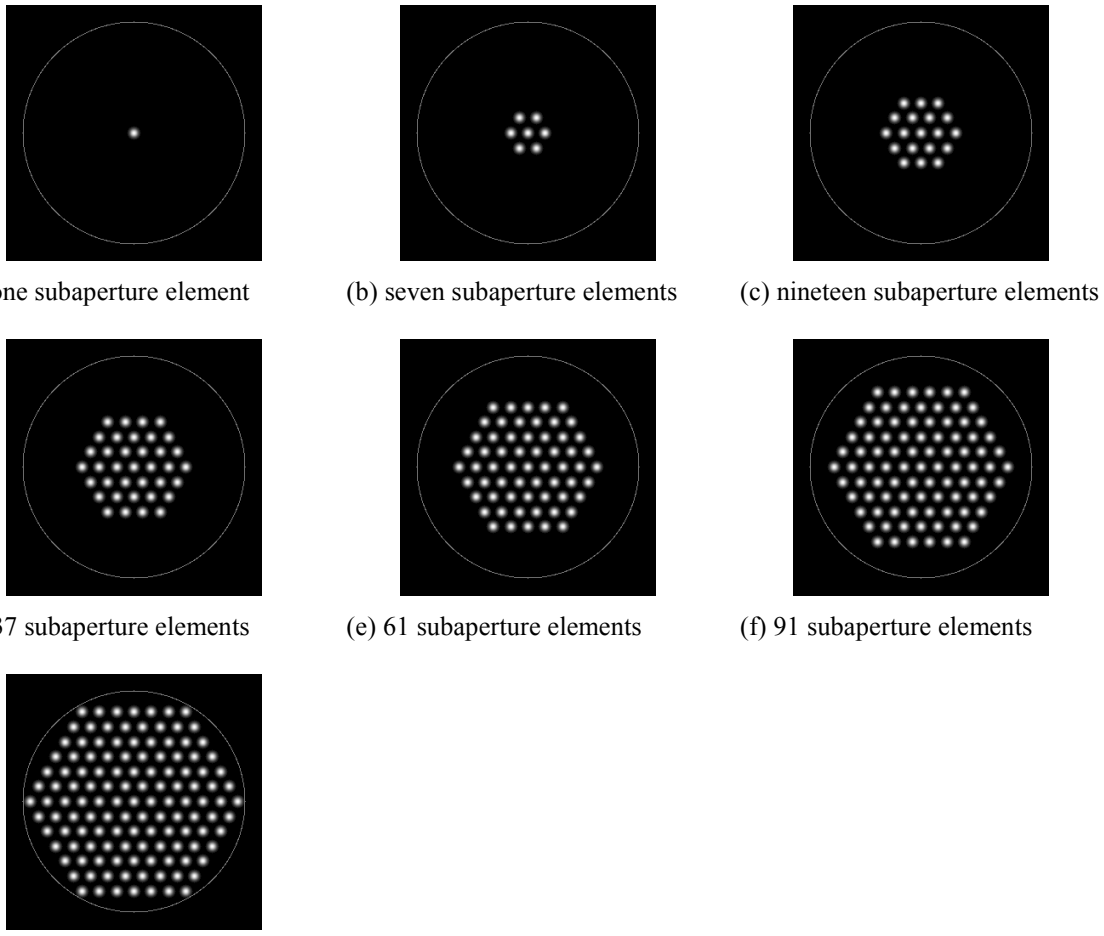

(a) one subaperture element (b) seven subaperture elements (c) nineteen subaperture elements

(d) 37 subaperture elements (e) 61 subaperture elements (f) 91 subaperture elements

(g) 127 subaperture elements

Figure 2.9: Near-field intensity distributions of the conformal optical systems with uniform outgoing phases as shown in Figure 2.5(i) but with different number of subaperture elements used.

In each subfigure (g), the large gray circle outlines the equivalent aperture boundary of the conformal optical system. In the other subfigures, the large gray circles serve as geometrical reference. Each subaperture beamlet has Gaussian profile.

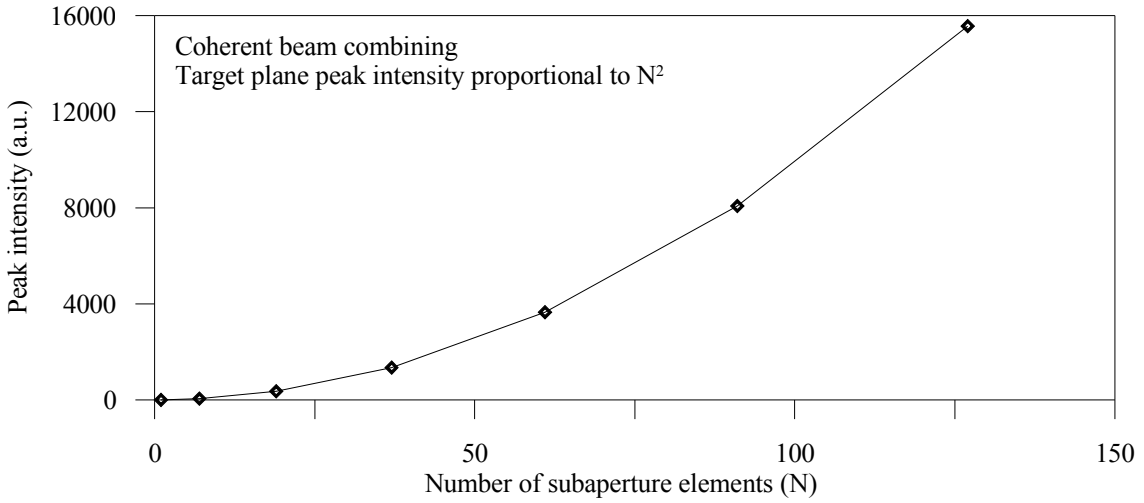

Figure 2.10: Target plane peak intensity with arbitrary unit vs. number of subaperture elements for coherent beam combining.

For all cases as shown in Figure 2.9(a-g), the peak intensities are normalized to case (a) where only single subaperture is used.

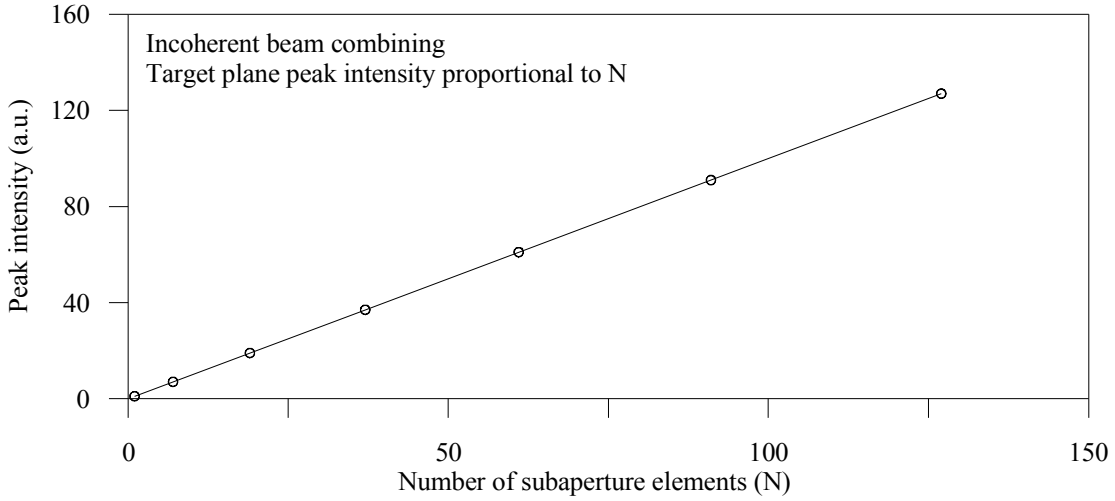

Figure 2.11: Target plane peak intensity with arbitrary unit vs. number of subaperture elements for incoherent beam combining.

For all cases as shown in Figure 2.9(a-g), the peak intensities are normalized to case (a) where only single subaperture is used.

Chapter 3 Conformal adaptive phase-locked fiber array

In this chapter, the system architecture and key subsystems of the conformal adaptive phase-locked fiber collimator arrays are addressed. Section 3.1 describes the general system architecture. In Section 3.2, spatial configurations of a conformal optical transmitter and/or receiver system with multiple identical subaperture elements are addressed. The next Section 3.3 discusses piezoelectric fiber positioners for subaperture wavefront phase tip-tilt control. Section 3.4 discusses a multi-channel fiber system and Section 3.5 addresses the phase shifting elements based on $LiNbO_3$ waveguide technology. In the final Section 3.6, the metric signal selection and acquisition of wavefront correction feedback control system are addressed.

3.1 System architecture

Conformal adaptive phase-locked fiber arrays can be used in a variety of applications. Among these potential applications are free-space laser communication and low- and high-power beam projection applications as stated already in Section 1.3. The adaptive phase-locked fiber arrays share a common general system architecture [1], although the implementations for different applications differ in some specific details. This general system architecture is composed of the following key subsystems:

(1) a conformal optical transmitter/receiver system which consists of multiple identical subaperture elements and provides light coupling capability from the fiber system to free space or vice versa.

(2) a local adaptive optics (AO) compensation system at each subaperture element which provides capabilities of compensating certain lowest orders of Zernike aberrations, for instance tip-tilt, in each beamlet.

(3) a multi-channel fiber system. This fiber system includes passive beam routing parts such as beam splitter/combiner and optical isolators, and active optical parts. The active optical parts are fiber-coupled laser sources, fiber preamplifiers/amplifiers, fiber-coupled beam intensity controllers, phase controllers, polarization controllers and optical communication modulators.

(4) global and local feedback control systems. The global feedback system controls the phase-locking of the phases of the beamlets from the different subapertures and the local feedback systems provide control for the adaptive compensation within each subaperture.

(5) wavefront control algorithms such as the stochastic parallel gradient descent (SPGD) algorithm and the multi-dithering algorithm.

In a laser communication system the above described system architecture can be used on the optical transmitter side, on the optical receiver side or on both sides. A simplified conformal optical transmitter system is shown in Figure 3.1.

The outgoing laser originates from a seed laser unit which usually contains an internal optical isolator to eliminate the backreflection and is fed into a fiber preamplifier which amplifies the optical power to an appropriate intermediate level if necessary. Then the output beam from the fiber preamplifier is fed to a $1\times N$ fiber-coupled phase shifter array. After passing through the $1\times N$ phase shifter array, the single input beam is split into

N phase-correlated beamlets with identical power for each beamlet. The relative phases of these N output beamlets are preshifted through the electrical modulations from the N-output phase-locking controller. The N phase-shifted beamlets are then fed to an $N \times N$ fiber amplifier array with which the N beamlets are boosted to the required power level. Then the power-amplified N beamlets are collimated and sent into free space by a conformal optical transmitter with N identical subaperture elements. On each of these subaperture elements, there are adaptive optical components like, e.g., a tip-tilt modulator that might be implemented using a variety of techniques. Techniques available are for instance piezoelectric fiber positioners [81], piezoelectric deformable pocket mirrors [82], rotating Risley prisms [83, 84] and liquid crystal (LC) based beam deflectors [85].

As discussed before, the global phase-locking control and the on-subaperture local adaptive optics control are required to realize coherent combining of the N beamlets. Propagation of the beamlets through free space where wavefront aberrations caused by turbulent air can introduce phase aberrations. The phase-locking controller can be implemented through a variety of algorithms such as the stochastic parallel gradient descent (SPGD) algorithm and the multi-dithering algorithm. The electrical phase-locking modulation signals are used to control the $1 \times N$ phase shifter array to introduce phase shift compensation. At the same time the phase-locking control is running, the individual beamlets are actively steered.

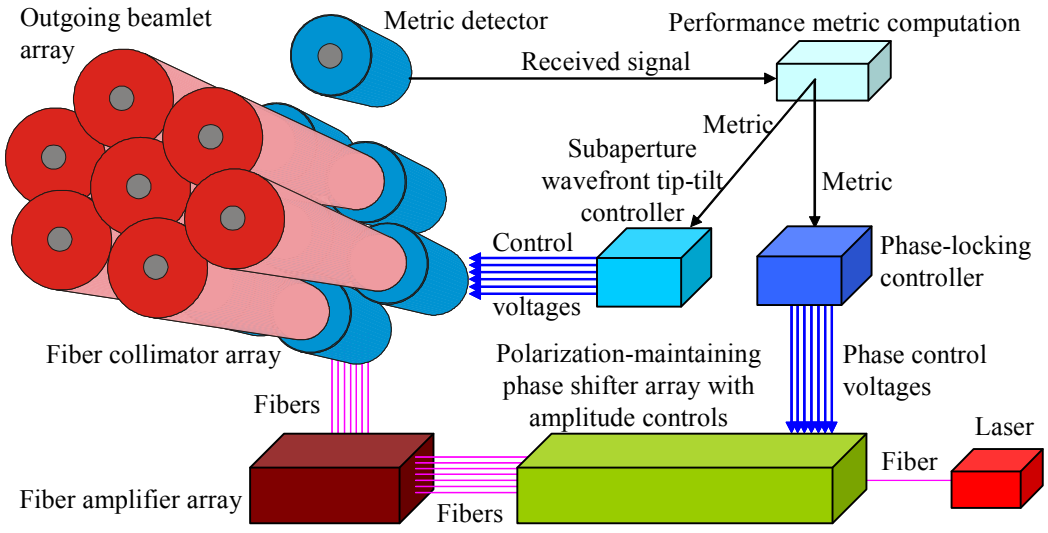

Figure 3.1: System architecture and key subsystems of a conformal adaptive phase-locked fiber system. Key subsystems include: a conformal optical transmitter/receiver system with multiple identical subaperture elements; a multi-channel fiber-based network for beam routing, power amplifications, beam phase, intensity, polarization controls; a local on-subaperture element adaptive optics (AO) compensation system; electrical driving systems for phase-locking and local adaptive optics compensation; efficient control algorithms such as the stochastic parallel gradient descent (SPGD) or the multi-dithering techniques implemented in the feedback control systems. All fiber-based optical elements are polarization-maintaining (PM). The polarization states of beamlets are linearly polarized and are aligned with the slow axis of the PM fiber elements.

3.2 Conformal optical transmitter/receiver system

As seen in Section 1.3, a conformal adaptive phase-locked fiber collimator array can be used in a variety of applications. For different applications, the conformal optical transmitter/receiver system can have different configurations, which are designed and utilized to meet different primary purposes correspondingly. This section reviews a few possibilities of spatial configurations for multiple identical subaperture elements [1]. Then a three-subaperture conformal optical transmitter system is described.

For beam projection applications, especially for high-power directed energy systems, a higher target plane peak intensity and a smaller beam divergence angle are desired. This requires that the conformal fill factor $\left(f_{con}\right)^2$ defined in Equation (2.21) is as close to unity as possible. In Figure 3.2, a hexagonal spatial configuration of subaperture elements is given. When the identical fiber collimators are arranged in this configuration, the conformal fill factor $\left(f_{con}\right)^2$ is close to 0.75. One of the difficulties for configuration as shown in Figure 3.2, however, is the inconvenience to physically add more subaperture elements if needed. If the clustered configuration as shown in Figure 3.3 is used, the conformal fill factor is close to 0.58, and it becomes more convenient to add more clusters containing seven-subaperture elements per cluster.

In free-space laser communications, a lower bit error rate (BER) is a much more important objective. The spatial configuration of the subaperture elements as shown in Figure 3.4 offers spatial diversity. Spatial diversity indicates that wavefront phase distortions related to atmospheric turbulence for received communication signals at individual subapertures can be considered statistically independent if the separation between

subapertures is much larger than the Fried parameter. With this configuration, there exist high probabilities that all signals do not fade simultaneously and the deepest fades can be avoided.

For the experiments described in this thesis, a conformal optical transmitter system with three fiber beam collimators as shown in Figure 3.5 has been built. This system is used to demonstrate that coherent beam combining can be achieved with phase-locking and subaperture wavefront phase tip-tilt control.

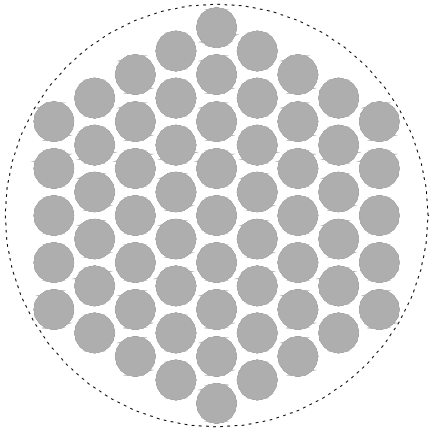

Figure 3.2: Hexagonal spatial configuration of a conformal optical transmitter system for beam projection applications.

The large dashed circle indicates the equivalent conformal aperture. Each gray-shaded disc indicates a subaperture element.

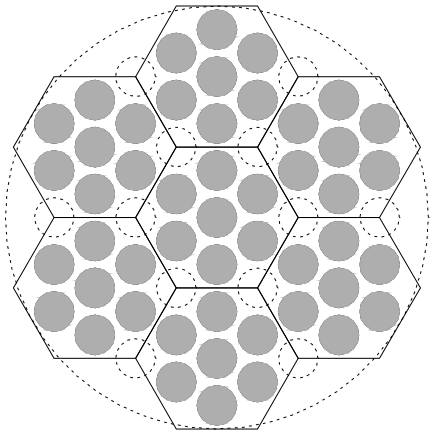

Figure 3.3: Clustered spatial configuration of a conformal optical transmitter system for beam projection applications.

The large dashed circle indicates the equivalent conformal aperture. Each hexagon indicates the boundary of a cluster containing seven subaperture elements. Each gray-shaded disc indicates a subaperture element. Each small dashed circle indicates a missing subaperture element.

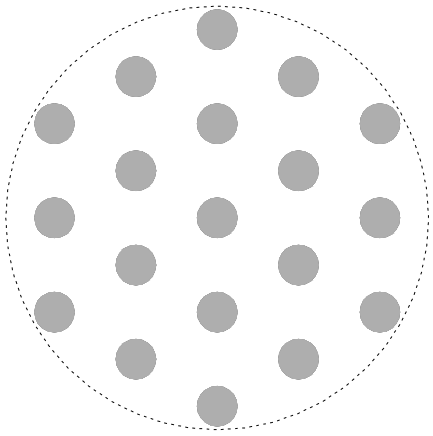

Figure 3.4: Hexagonal spatial configuration of a conformal optical transmitter system for free-space laser communications.

The large dashed circle indicates the equivalent conformal aperture. Each gray-shaded disc indicates a subaperture element. When the separation between subaperture elements is much larger than the Fried parameter r_o [8, 9], spatial diversity is introduced into the communication link.

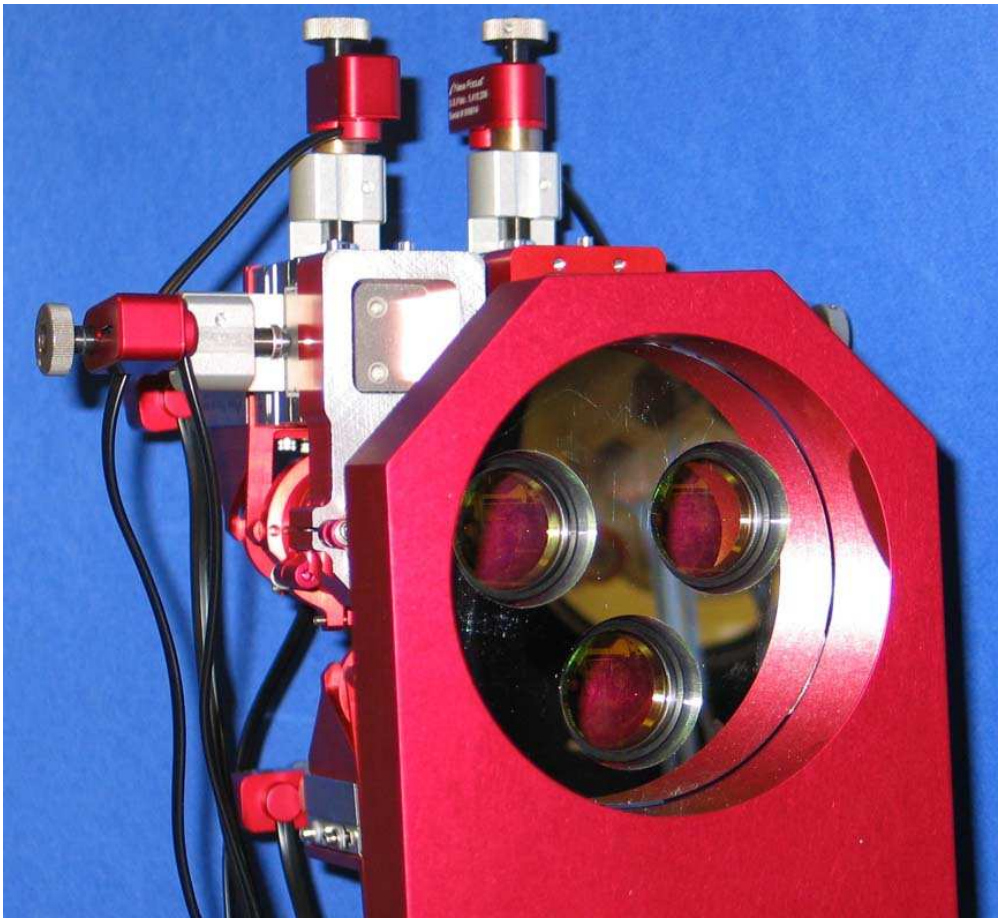

Figure 3.5: Conformal optical transmitter with three subaperture elements.

Equivalent conformal aperture diameter $D \approx 71\text{mm}$. Subaperture lens diameter $d = 25.4\text{mm}$. Subaperture lens focal length $f = 107\text{mm}$. Distance between lens centers $l = 40\text{mm}$. Design wavelength $\lambda = 1064\text{nm}$. Whole conformal fill factor $(f_{con})^2 \approx 0.37$. Subaperture fill factor $(f_{sub})^2 \approx 0.75$. The diamond-cut mirror surface on the mount of the subaperture elements is used as a beamlet prealignment reference. For convenience of beamlet identification purpose in later chapters, the upper-right subaperture (beamlet) is identified as #1, the upper-left subaperture (beamlet) is identified as #2, and the bottom subaperture (beamlet) is identified as #3. The attached motorized screws are for the purpose of beamlet prealignment.

3.3 Subaperture beam collimator with wavefront phase tip-tilt compensation using piezoelectric fiber positioner

Subaperture beam collimators are critical elements of a conformal optical transmitter as shown in Figure 3.5. This section describes a subaperture beam collimator that includes a piezoelectric fiber positioner [81] as an adaptive optical component to provide tip-tilt control. This combination of fiber collimator and tip-tilt controller was used in the experiments described in this work. The working mechanism of a fiber positioner is shown in Figure 3.6. The fiber positioner is based on piezoelectric ceramic technology.

The basic principle is based on the observation that the length of a thin rectangular piezoceramic plate changes when a voltage is applied. Two identical such piezo ceramic plates can be used to form a double-layer piezo assembly by glueing them tightly face to face that the two ceramic plates have identical electrical polarities. When a control voltage is applied to them, the two ceramic plates observe opposite polarities for the same control voltage. One ceramic plate expands in length while the other shrinks in length. The piezoceramic assembly will bend accordingly. This piezoceramic assembly is here referred to as a piezoelectric actuator as shown in the left part of Figure 3.6. In the right part of Figure 3.6, two pairs of piezoelectric actuators are mounted on a plexiglass base in an orthogonal manner. With this configuration, either non-neighboring pair of piezoelectric actuators can convert the bending motion into a linear motion. A 2-dimensional transversal motion is available for the stainless steel cross sitting on tips of the four actuators. A tiny protection tube with a fiber inside is further driven by the steel cross transversally to introduce fiber tip deviation.

Pictures of a fiber positioner without and with protection mount tube are given in the left part and right part of Figure 3.7, respectively. Damping material is located in between the four piezo actuators to suppress the effect of hysteresis. The measured response characteristic of the fiber tip deviation vs. the applied control voltage for a fiber positioner is given in Figure 3.8. In the measurement, sinusoidal voltages with amplitude ±100 volts and variable frequencies are applied to the two pairs of piezoelectric fiber actuators. The device bandwidth is around 2.0kHz. The device has a larger sensitivity when a very low frequency voltage is applied due to its capacitive load nature. The response curve peaks at around 1.6kHz due to the first resonance and the damping effect applied to the actuators.

Figure 3.9 shows the schematic of a fiber collimator. If no voltage is applied, the situation is shown in solid lines. The fiber tip is located at the focal point of the collimating lens. The axis of the outgoing beamlet is aligned with the axis of the fiber collimator. If a voltage is applied to the actuators, the fiber tip shows a transversal deviation $\Delta r(t)$ from the focal point of the collimator lens. The angle $\Delta\varphi(t)$ between the axis of outgoing beamlet and the axis of the fiber collimator is in this case given by

$$\Delta\varphi(t) \approx \frac{\Delta r(t)}{f} \ . \tag{3.1}$$

The wavefront of this outgoing beamlet varies with the same angle. Consequently, the wavefront of the combined beam in the far field is actively modulated by multiple fiber positioners. This can be used to compensate for wavefront tilts due to atmospheric phase

distortions and/or jitters along the beam propagation path, as well as to steer the beamlets to focus at a specific point.

The fiber beam collimator assembly is shown in Figure 3.10. Each fiber beam collimator is mainly composed of a beam collimating lens, a cylindrical enclosure, and a piezoelectric fiber positioner for wavefront tip-tilt control, all of which are designed and developed at the ARL in collaboration with UMD (2007). There are six adjustable degrees of freedom for the specific beamlet or the fiber tip. The outgoing beam polarization state can be adjusted by rotating the protection mount tube of the fiber positioner. The polarization angle mismatch between the three beamlets is controlled within ±0.5°. The focus/defocus adjustment along the beam axis is performed through a picomotor. Adjustments of the other four degrees of freedom of the fiber tip, including the fiber tip orientation angles and the fiber tip transversal deviations from the focal point of the collimating lens, are coupled due to the specific fiber collimator structure. They must be adjusted together in an iterative manner. The fiber tip orientation angles can be adjusted through four screws. The static fiber tip transversal deviations are adjusted through the corresponding picomotors. The linear resolution of picomotor is ~30 nm per step if electrically driven by driver from NewFocus Inc. The dynamic range of the beam steering angle for this fiber collimator with a fiber positioner is ±300μrad.

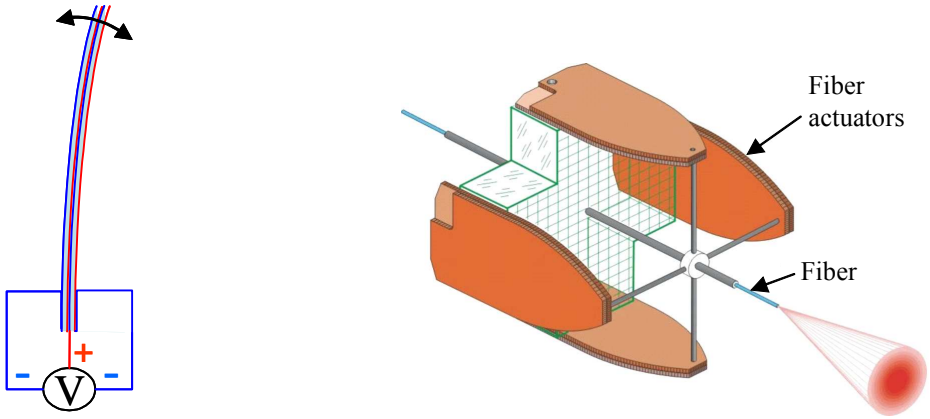

Figure 3.6: Illustrations of a fiber positioner with two pairs of piezoelectric fiber actuators.

Left: a fiber actuator composed of a pair of piezoelectric ceramic plates with appropriate dimensions. Right: a fiber positioner with pairs of fiber actuators mounted on a plexiglass base (courtesy of Dr. Beresnev). A steel cross sits on the tips of four fiber actuators. The fiber tip is actuated by the fiber actuators through the steel cross when control voltages are applied.

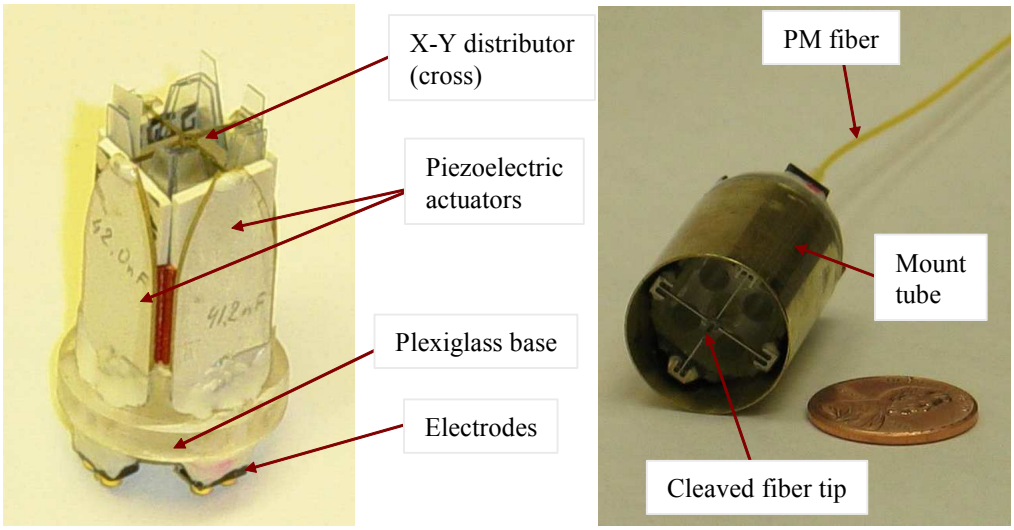

Figure 3.7: Piezoelectric fiber positioner developed at ARL (2005-2007).

The picture on the left is a fiber positioner without the protection mount tube. The picture on the right is a fiber positioner with the protection mount tube and fiber connected. Damping material is put between the four fiber actuators to suppress the effect of hysteresis.

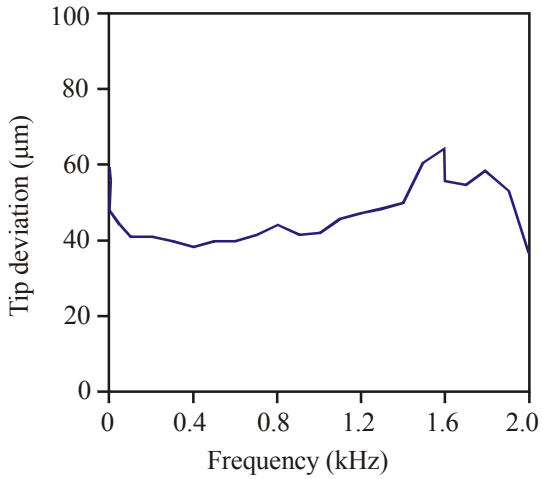

Figure 3.8: Measured voltage-deviation response characteristics of a piezoelectric fiber positioner.

Due to the capacitive load nature of fiber actuators, the tip deviation peaks at very low frequency modulations.

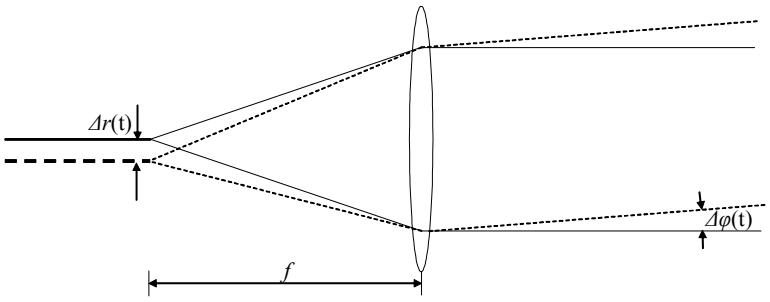

Figure 3.9: Schematic of a fiber beam collimator.

The fiber positioner is not shown here. The fiber tip is located in the vicinity of the collimating lens focal point.

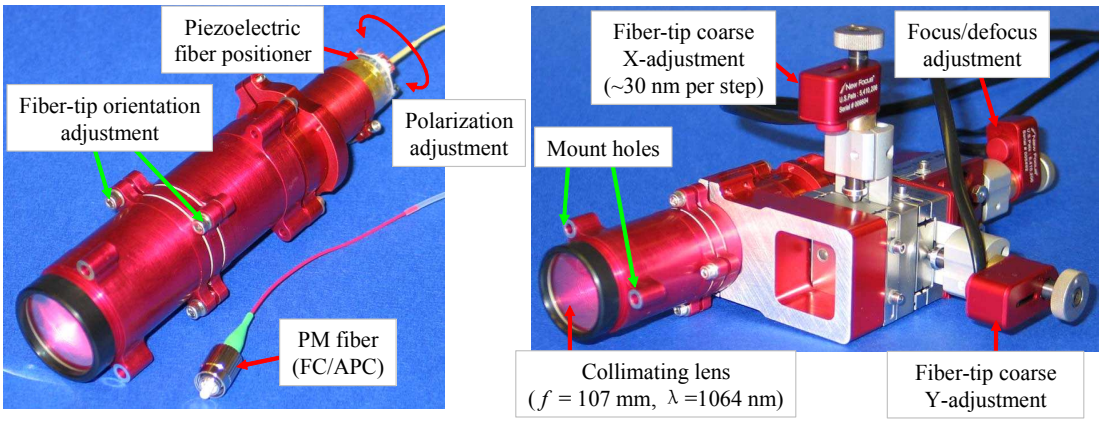

Figure 3.10: Fiber beam collimator developed at ARL in collaboration with UMD (2007).

The outgoing beam polarization state can be adjusted by rotating the protection mount tube of the fiber collimator. The focus/defocus adjustment along the beam axis is performed through the corresponding picomotor. Adjustments of the other four degrees of freedom of the fiber tip, including the fiber tip orientation angles and the fiber tip transversal deviations from the focal point of the collimator lens, are coupled due to the specific fiber collimator structure. They must be adjusted together in an iterative manner. Dynamic range of beam steering angle is ±300μrad for this beam collimator.

3.4 Multi-channel fiber system

The multi-channel fiber system is an important part of the conformal optical system. The multi-channel fiber system affords capabilities for beam routing, active wavefront phase modulation, intensity modulation and polarization control, and optical power amplifications.

The multi-channel fiber system for the conformal adaptive phase-locked fiber array is shown in Figure 3.11. The linearly polarized single-mode optical output from the laser source is split into N linearly polarized single-moded beamlets, which are coupled into free space through N fiber beam collimators. Here, the beamlets take Gaussian beam profiles due to the single mode nature of the chosen polarization-maintaining optical fibers. For convenience, these fiber optical components are connected through fiber mating sleeves instead of optical splicing.

Beamlet phase shifting can be realized through different techniques such as pump current modulation of a diode optical amplifier for each beamlet [55, 56, 67-69], a piezoelectric fiber stretcher [70, 71], and a fiber-coupled electro-optical phase shifter based on $LiNbO_3$ technology [86]. In our system, a $LiNbO_3$-based phase shifter is used due to its fast response characteristic. Polarization-maintaining fibers are used in the system to keep the polarization states of the multiple beamlets unchanged for convenience of demonstration purpose. In reality, the polarization states of the different beamlets can be maintained unchanged with ordinary single mode fibers and additional in-line fiber-coupled polarization controllers [87, 88]. Large mode area (LMA) single-mode fiber instead of ordinary

single mode fiber (SMF) or polarization-maintaining fiber (PMF) can be used when the optical power is high [89].

The multi-channel fiber network as shown in Figure 3.11 can introduce much noise into optical beamlets after the light goes from the laser source, through the optical isolator, the fiber preamplifier, the fiber beam splitter network with built-in phase modulations and amplitude controls, and the necessary fiber amplifiers, to free space. Consider the temporal coherence characteristics of the N beamlets. In order to coherently combine the N beamlets, the smallest temporal coherence length of the N beamlets must be longer than the largest difference of the N optical path lengths that extends from the laser source to the target in the far field. By referring to Table 10.1-1 and Equation 10.1-16 in [76], the coherence length l_c for a Gaussian beam can be approximately expressed as

$$l_c \approx \frac{0.66c}{\Delta\nu_{FWHM}}, \tag{3.2}$$

where $\Delta\nu_{FWHM}$ is the full-width-at-half-maximum (FWHM) spectral linewidth of the Gaussian beam, and c is the speed of light in vacuum.

The Equation (3.2) shows that the narrower the linewidth is, the longer the coherence length is. In general, the respective linewidths of the N beamlets are identical to each other and are determined by the single laser source in use. As seen in Figure 3.11, however, if high power fiber amplifiers are inserted in-line in the fiber system, the power level of each beamlet is increased. In the high power region, a large mode area (LMA) fiber with low numerical aperture (NA) is usually used to accommodate high laser power while keeping the single mode nature and a narrow linewidth by mitigating stimulated

Brillouin scattering (SBS) effect [90]. This kind of noise due to the finite beam spectral linewidths varies fast (100.0MHz~10.0GHz). It is usually referred to as fast phase noise.

A second kind of noise for each beamlet is due to the backreflections occurring at the fiber ends in fiber mating sleeves and at the fiber ends in the piezoelectric fiber positioners. This kind of noise can be reduced by using FC/APC fiber connectors to connect fibers or by splicing the fibers together. The backreflection occurring at terminating fiber ends in fiber positioners can be reduced by using angled cleaving.

A third kind of noise is due to the polarization crosstalk. Each beamlet is supposed to be linearly polarized. In practice, however, the beamlets are never completely linearly polarized. We consider the optical energy in the orthogonal polarization mode other than the chosen polarization mode as the polarization noise. Polarization crosstalk can happen in the following situations. First, the polarization angles of the polarization-maintaining fiber connectors are not oriented in exactly the same direction in the fiber mating sleeves. Second, in the $LiNbO_3$ waveguides for the fiber beam splitter network with integrated fiber phase shifters and amplitude controls, the modulations introduce polarization crosstalks. Twisting and bending of polarization-maintaining (PM) fibers can also introduce polarization crosstalks. Polarization noise is usually characterized by the polarization extinction ratio (PER), which is defined as the ratio of the power in the chosen polarization mode to the power in the unwanted orthogonal polarization mode. 20dB is taken as a reasonable lower limit of the polarization extinction ratio in this thesis for free-space laser communications and beam projection applications.

In the physical implementation of the integrated fiber beam splitter with built-in phase shifters and amplitude controls, there are many $LiNbO_3$ waveguides that are close to each other. The beamlets crosstalk to each other through evanescent mode coupling. This is the optical crosstalk of the beamlets. At the same time, the chosen control voltages $U_1 \cdots U_N$ for phase shifts and $A_1 \cdots A_N$ for amplitude controls for the N beamlets do not really modulate their respective beamlets separately. The control voltages for a specific beamlet also slightly modulates neighboring beamlets. This is the beamlet crosstalk due to modulation electric field coupling. The crosstalks between the beamlets can be mitigated with careful design and fabrication of the integrated fiber beam splitter network.

The photorefractive effect is another possible source of optical noise in a multi-channel fiber system. Each waveguide made of photorefractive material $LiNbO_3$ [91, 92] for phase control behaves like a cavity with weak reflection coefficients at its two facets. When the optical power level is high and the optical linewidth is narrow, it is possible for standing optical waves to exist in this cavity. Through charge carrier displacement, this standing wave introduces an optical grating along the waveguide. This optical grating in the $LiNbO_3$ waveguide will transmit less optical power and back reflect some optical power.

In the laser and the fiber system of a conformal fiber optical system, the dispersion noise is assumed to be negligibly small because the fiber length in each channel is not very long (<10m). We assume the glass optical fiber has a constant refractive index for the design optical wavelength everywhere in the system.

Another important kind of noise is due to variations in the lengths of the fiber optical paths. Temperature fluctuations and mechanical deformations (acoustic vibrations) can result in slow variations (<1.0kHz) in the fiber lengths. This is referred to as slow phase noise.

Two kinds of noise, fast phase noise and slow phase noise, are addressed further as follows. $\left\{\Delta_i^{out}(t)\right\}$ in the analysis of Section 2.2 are referred to as phase noise in the multi-channel fiber system. When optical devices of the multi-channel fiber system are well designed, fabricated and integrated, the phase noise is mainly caused by the fluctuation of the optical carrier frequency related to the finite linewidth of the used laser source and fiber amplifiers, and by variations in optical fiber lengths. For a given channel, the phase noise can be described as (see [74])

$$\Delta_i^{out}(t) \approx \frac{nl_i(t)\omega_i(t)}{c} \approx \frac{nl_i(t)\omega_0}{c} + \frac{nl_i(t)\Delta\omega_i(t)}{c} \quad , \tag{3.3}$$

where n (roughly constant) is the refractive index of the optical fiber for the design wavelength, $l_i(t)$ is the time-varying fiber length for the specific channel, ω_0 is the nominal laser optical carrier frequency, $\Delta\omega_i(t)$ is the laser frequency deviation from its nominal value and c is the speed of light in vacuum. Rewrite Equation (3.3) as

$$\Delta_i^{out}(t) \approx \Delta_i^{slow}(t) + \Delta_i^{fast}(t) \tag{3.4}$$

$$\Delta_i^{slow}(t) = \frac{nl_i(t)\omega_0}{c} \tag{3.5}$$

$$\Delta_i^{fast}(t) = \frac{nl_i(t)\Delta\omega_i(t)}{c} = \frac{nl_i\Delta\omega_i(t)}{c} + \underbrace{\frac{n\Delta l_i(t)\Delta\omega_i(t)}{c}}_{\text{small term}} \approx \frac{nl_i\Delta\omega_i(t)}{c} \tag{3.6}$$

where l_i is the nominal length of the specific optical fiber path. $\{\Delta_i^{slow}(t)\}$ and $\{\Delta_i^{fast}(t)\}$ are the aforementioned slow phase noise and fast phase noise, respectively. Slow phase noise can be compensated through phase-locking techniques using fiber-coupled phase shifters [86]. Active compensation of fast phase noise caused by optical carrier frequency fluctuations and drifts is commonly referred to as frequency locking [93, 94]. Direct optical frequency locking using external controls is at present due to the absence of sufficiently fast controller and frequency modulators a challenging task. However, the fast phase noise components $\{\Delta_i^{fast}(t)\}$ can be automatically balanced between different optical fiber channels when all beamlets are generated from a single seed laser and the lengths of optical fiber paths are roughly equal.

As an important part of the multi-channel fiber system, a fiber-coupled phase shifter array based on $LiNbO_3$ technology will be exclusively discussed in the following section.

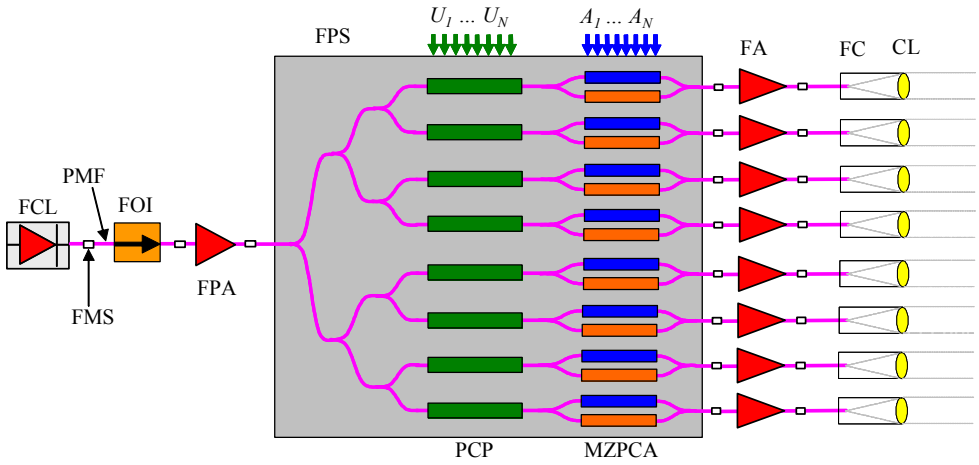

Figure 3.11: Schematic of a multi-channel fiber system

Abbreviations are described as follows: FCL - fiber-coupled laser, FMS - fiber mating sleeve, PMF – polarization-maintaining fiber, FOI - fiber optical isolator, FPA - fiber preamplifier, FPS - fiber phase shifters, PCP - electro-optic Pockel's cell for phase shifting, MZPCA - Mach-Zehnder interferometer pair of electro-optic Pockel's cells for amplitude control, $U_1 \cdots U_N$ - respective modulating voltages for the phase shifts for the N beamlets, $A_1 \cdots A_N$ - respective modulating voltages for the amplitude controls for the N beamlets, FA - fiber amplifier, FC - fiber collimator, CL - collimating lens.

3.5 Fiber-coupled phase shifter array

The working mechanism of fiber-coupled waveguide phase shifters is based upon the electro-optic (EO) effects [95] for specific kinds of crystals. When these crystals are placed within an electric field, their refractive index tensor undergoes small variations. When an optical beam passes through a crystal in such a situation, the beam experiences a phase shift that depends on the strength of the electric field. In the commonly used lithium niobate ($LiNbO_3$) crystal, Pockel's effect (linear electro-optic effect) dominates. A conceptual fiber phase shifter in a specific format is discussed as an example.

Figure 3.12 shows the schematic of this conceptual fiber phase shifter based on lithium niobate technology. The substrate is made of lithium niobate. The waveguide is made of lithium niobate doped with a dopant such as magnesium oxide. The coordinate z-axis is defined along the optical axis of the used lithium niobate crystal. The lithium niobate crystal is uniaxial and has one optical axis. The optical axis of a crystal has the following characteristic. When light propagates along the optical axis of a crystal, the propagation speed of light in this crystal is independent of its polarization state. If the light propagates along any direction other than along the optical axis, its polarization state will change. If linearly polarized light propagates along the x-axis and its polarization vector (electric field vector) is within either the xz-plane or the xy-plane, then its polarization state is maintained unchanged before and after passing through the phase shifter [95].

When the polarization vector is within the xz-plane, the phase shift is [96]

$$\Delta\Psi_z(t) \approx -\frac{\pi n_e^3 r_{33} L_{ps} \Gamma_z}{\lambda w} V(t) \ . \tag{3.7}$$

When the polarization vector is within the xy-plane, the phase shift is [96]

$$\Delta\Psi_y(t) \approx -\frac{\pi n_o^3 r_{13} L_{ps} \Gamma_y}{\lambda w} V(t) \ . \tag{3.8}$$

In the above two equations for calculation of the phase shifts, n_e and n_o are the extraordinary and ordinary refractive index of lithium niobate, respectively. $n_e = 2.08 \sim 2.29$, $n_o = 2.15 \sim 2.39$ and $n_e < n_o$ in near infrared to visible regions. r_{33} and r_{13} are two of the electro-optic coefficients of lithium niobate crystal. $r_{33} \approx 30.8$ pm/V. $r_{13} \approx 9.6$ pm/V when the control voltage $V(t)$ modulates in dc to audio range; $r_{13} \approx 8.6$ pm/V when the control voltage $V(t)$ modulates in higher frequencies up to 1.0MHz. $V(t)$ is the external control voltage for phase modulation. L_{ps} is the length of the light propagation path within the phase shifter waveguide. Γ_z and Γ_y are the geometry-dependent electro-optic overlap integral factors [97]. For this specific configuration like a parallel capacitor, the electro-optic overlap integral factors Γ_z and Γ_y are approximately unity. λ is the design wavelength of light for this device. w is the thickness of the Pockel's cell.

In the derivation of Equations (3.7) and (3.8), crosstalks between the two orthogonal polarization states of input light were assumed negligibly small. The derivation procedure also neglected the fringe effects of the parallel capacitor to the modulation electric field. Note that when the above phase shifter is built physically, only the control voltage $V(t)$ can be tuned in a large dynamic range (±40V). The wavelength λ can be tuned only in a small range (±10nm away from the design wavelength) without introducing large noise into the multi-channel fiber system.

When the phase shift in either Equation (3.7) or Equation (3.8) is π radians, the corresponding control voltage is referred to as the halfwave voltage V_π^z or V_π^y for respective light launch mode with the input polarization direction within the xz-plane or the xy-plane. The halfwave voltages for the two launch modes can be written as

$$V_\pi^z \approx -\frac{\lambda w}{n_e^3 r_{33} L_{ps} \Gamma_z} \tag{3.9}$$

$$V_\pi^y \approx -\frac{\lambda w}{n_o^3 r_{13} L_{ps} \Gamma_y} \tag{3.10}$$

Substitute Equation (3.9) into Equation (3.10)

$$V_\pi^y \approx \frac{n_e^3 r_{33} \Gamma_z}{n_o^3 r_{13} \Gamma_y} V_\pi^z \tag{3.11}$$

With appropriate design parameters, the halfwave voltage V_π^z can be implemented as low as a couple of volts [96]. For example, at room temperature (25°C), for the design wavelength λ=1064nm, $n_e \approx 2.17$, $n_o \approx 2.25$, $\Gamma_z \approx \Gamma_y \approx 1.0$, w=60μm, L_{ps}=100mm. We have $V_\pi^z \approx 2.0$V. Also

$$V_\pi^y \approx (2.9 \sim 3.2) V_\pi^z \tag{3.12}$$

for modulating control frequency ranging from dc to megahertz. The above formula indicates that the two launch modes with orthogonal polarization states experience different phase-shift sensitivities. In general, the launch mode with the polarization vector lying in the xz-plane is preferred in most applications because of the smaller halfwave control voltage. This mode is usually referred to as TM mode for the fiber phase shifter. The polarization of the TM mode is usually aligned with the slow axis of the polarization-

larization of the TM mode is usually aligned with the slow axis of the polarization-maintaining fiber.

Figure 3.13 shows the schematic of the 1×8 polarization-maintaining phase shifters with amplitude controls used in our conformal optical system. For each channel, the amplitude control is implemented through a Mach-Zehnder interferometer formed with two additional phase shifting elements. One element in this Mach-Zehnder interferometer has a fixed control voltage, while the other has a variable control voltage to tune the intensity of the combined beam.

The halfwave voltage is an important parameter of a optical phase modulator and can be measured experimentally as shown in Figure 3.14. Two identical $LiNbO_3$ phase shifter elements form a Mach-Zehnder interferometer. The control voltage of one phase shifter is tied to ground. For the second phase shifter, the control voltage change introduces relative phase delay according to Equation (3.7). By increasing monotonically the second control voltage in a sufficiently large range, transition of the received signal at optical power sensor from maxima to adjacent minima or from minima to adjacent maxima indicates control voltage changing by halfwave voltage. As shown in Figure 3.15, the halfwave voltage is ~1.55V. The phase shift is roughly linear to the applied control voltage. For all eight phase shifter elements, the halfwave voltages are roughly equal.

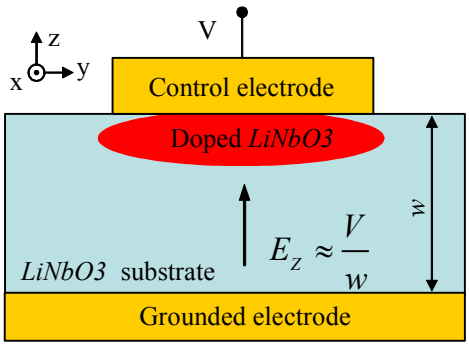

Figure 3.12: Schematic of a $LiNbO_3$ fiber phase shifter element.

The substrate is made of $LiNbO_3$. The waveguide is made of $LiNbO_3$ doped with MgO. The z-axis is defined along the optical axis of the $LiNbO_3$ crystal. Linearly polarized light propagates along the x-axis. The beam polarization can be either within the xz-plane or within the xy-plane in order to maintain the polarization state.

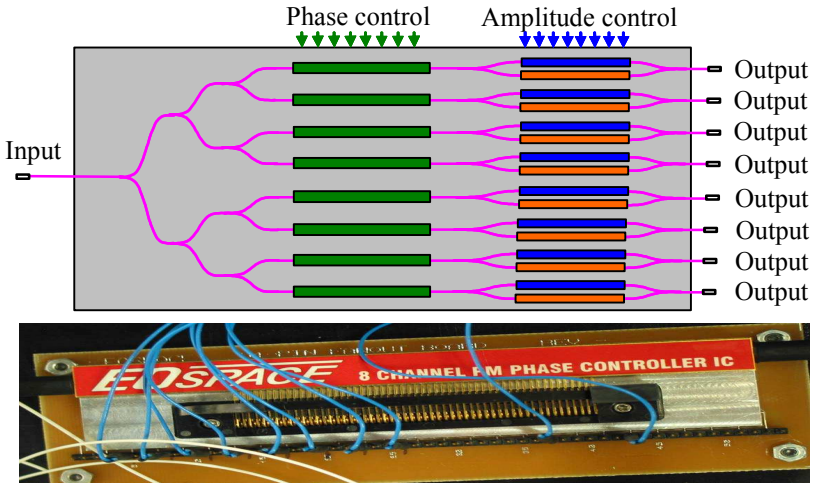

Figure 3.13: 1X8 polarization maintaining fiber phase shifters with amplitude controls developed at EO-Space, Inc. 2007.

Waveguides in green are for phase controls. Waveguides in blue and orange form Mach-Zehnder interferometers for amplitude controls. For TM launch mode, the halfwave voltage for phase control is ~1.55V. The halfwave voltage for amplitude control is ~4.1V.

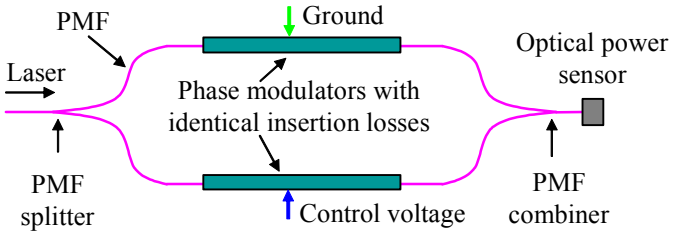

Figure 3.14: Schematic of the halfwave voltage measurement for a phase shifter element.

By increasing monotonically the second control voltage in a sufficiently large range, transition of the received signal at optical power sensor from maxima to adjacent minima or from minima to adjacent maxima indicates the control voltage changing by the halfwave voltage.

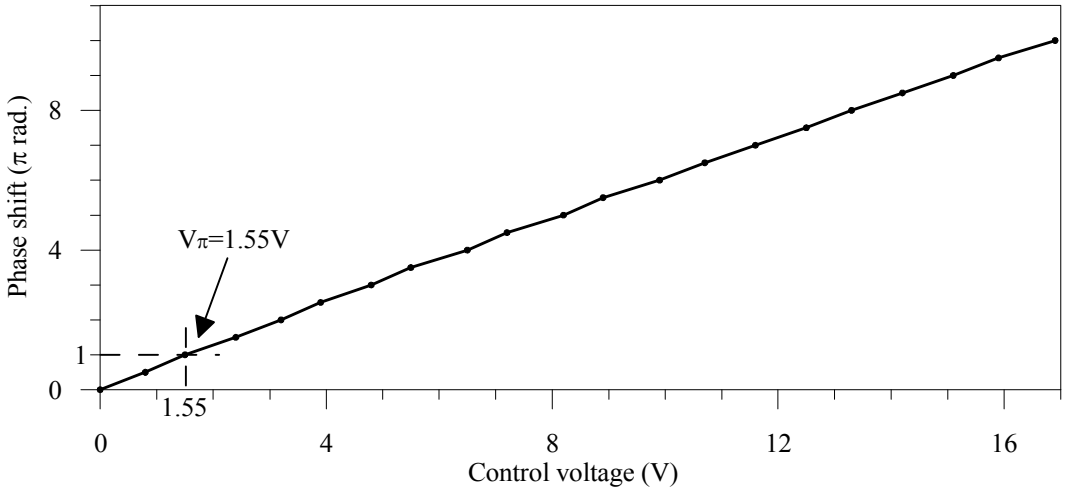

Figure 3.15: Response curve of a $LiNbO_3$ phase shifter element.

The measurement used experimental setup in Figure 3.14.The halfwave voltage is ~1.55V. The phase shift is roughly linear to the applied control voltage.

3.6 Feedback control systems: metric signal feedback mechanism

Feedback control systems of the system architecture as shown in Figure 3.1 include a fiber-coupled phase shifter array for phase-locking control as described in Section 3.5, piezoelectric tip-tilt fiber positioners for subaperture wavefront corrections as described in Section 3.3, algorithms and controller implementations for phase-locking and subaperture wavefront tip-tilt compensations as described in Chapter 4, and selection and acquisition of the feedback system metric signal as described in this section.

In free-space laser communications and beam projection applications, adaptive optics compensation can be performed through optimization of one or multiple simultaneous far-field system metric signals [5-7] instead of wavefront sensing and conjugation (conventional adaptive optics approach) [3, 4]. This is due to the difficulties in wavefront aberration measurements resulted from strong atmospheric turbulence-induced intensity scintillations. Commonly used metrics are the collected power or the beam focal spot size at the far-field receiver or the target. Technologies for transferring the far-field metric signal to the adaptive optics compensation system are discussed for different applications below.

In applications with a cooperative far-field target such as free-space laser communications, an radio frequency (RF) wireless communication link can be used [6, 23, 24] to transmit the signal to the controller unit. This RF link needs to be fast enough such that the adaptive optics compensation system in the near field does not experience delay waiting for the metric signal. Compared to gigabits per second data capacity in optical communications, the data capacity of this RF link can be as low as 10MHz that is still fast

enough to meet the requirements of the state-of-the-art feedback controllers addressed in Chapter 4. Because this RF link only transports averaged received optical power which does not contain confidential data, this metric signal feedback mechanism is secure. Due to its long wavelength nature compared to an optical beam, this RF link experience much less performance degradation effect due to atmospheric turbulence and does not have additional alignment problem.

Besides the RF link, counter-propagating optical beam originating from the far field can also be utilized to obtain the system metric signal for the adaptive optics feedback compensation system at the transmitter side in the near field. The principle of this method can be briefly described as follows. From the viewpoint in the near field, there are two optical beams, the transmitting beam and the receiving beam, which counter propagate through the same optical path and experience similar wavefront phase distortions. Consequently, the collected optical powers on both sides of the laser communication link fluctuate in the same manner. The necessary information for our adaptive optics feedback compensation system is the variation of the collected optical power. The collected optical powers on both sides are equivalent as a system metric signal for feedback control system. When the collected optical power in the near field is maximized, the collected optical power in the far field is simultaneously maximized. This is referred to as the reciprocity principle. With the reciprocity principle applied, the adaptive optics compensation system can be localized in either the near field or the far field while maintaining the target-in-the-loop configuration.

In beam projection applications where there is no cooperative target or object, wireless RF link or the reciprocity principle cannot be used to acquire the far-field metric signal

for the adaptive optics compensation system at the transmitter side. What can be used as a feedback metric signal is the reflected or scattered light from the far-field target. Non-cooperative targets in these applications can be generally classified into two categories: unresolved targets and resolved targets. When an illuminated object in the far field is smaller than the diffraction limited beam size, it can be treated as an unresolved scattering point source. Scattering radiation intensity of an unresolved target at any point in its scattering field is approximately proportional to the incident beam intensity. The dc signal of the collected power through photo detector located in the scattering radiation field of unresolved target can be used as a system metric signal. This metric is referred to as power-in-the-bucket (PIB) metric. In this case, when the incident beam size is reduced, the energy concentration on the target is higher and the scattering radiation intensity received by the photo detector is also higher.

When the illuminated target size is larger than the diffraction limited incident beam size, it must be treated as a resolved scattering extended object comprising a large amount of scattering point sources. At any point in the scattering field of the resolved target, scattering radiation intensity depends upon the interference of scattering radiations from all these point sources. The scattering radiation field of the resolved target illuminated with a coherent beam is referred to as speckle field. Speckles generally exist in a wide range. The scattering radiant intensity is proportional to the cosine of the angle between the observer's line of sight and the target surface normal. This is referred to as Lambet′s cosine law. When the spot size on target is larger, the mean speckle size is smaller; when the spot size on target is smaller, the mean speckle size is larger [28, 98, 99]. If the extended object is stationary relative to the incident beam, a lens can be used to image the focal

spot on target of the illuminating beam onto a photo detector. With a correct pinhole immediately in front of the photo detector, the metric level depends on how well the beam is focused on the target. When the collected power is maximized, the illuminating beam is focused on the extended object.

If the extended object is not stationary relative to the illuminating beam, the speckle field is time-varying and the collected by the photo detector scattered power in the speckle field fluctuates. The strength and therefore the power spectrum of these scattered power fluctuations depend on the beam spot size on the extended object. The better the illuminating beam is focused onto the target, the smaller the focal spot size is, the larger the collected scattered power fluctuations are, and the higher the frequency components present in the power spectrum. The distributed parallel time-varying speckle field for the moving resolved extended target can be used to generate system metric signals for the adaptive optics feedback compensation systems [25-29].

Chapter 4 Phase-locking and subaperture wavefront tip-tilt control algorithms and controller implementations

In this chapter, control algorithms and controller implementations for phase-locking control and subaperture wavefront tip-tilt compensation in a conformal adaptive phase-locked fiber array are addressed as an important extension of the feedback control systems described in Section 3.6. In Section 4.1, general considerations for efficient wavefront control algorithms are discussed. In Section 4.2, general principles of the stochastic parallel gradient descent (SPGD) algorithm are addressed. In Section 4.3, considerations of adaptive control parameters for the SPGD algorithm are discussed. In Section 4.4, software and hardware implementations of the SPGD controllers are presented. In Section 4.5, general principles of the multi-dithering algorithm are discussed. In Section 4.6, the effect of dither amplitude in phase-locking control using the multi-dithering algorithm is discussed. In Section 4.7, the hardware controller implementing the multi-dithering algorithm is presented. In Section 4.8, the SPGD and multi-dithering techniques are compared.

For description convenience, the following convention is used throughout this chapter. $\{\cdot\}$ represents the ensemble of variables with a general indicator enclosed by $\{\ \}$. For example, $u_i(t)$ is a specific continuous-time control voltage, while $\{u_i(t)\}$ indicates the ensemble $u_1(t)\cdots u_N(t)$ or in discrete-time format, for a given index of time $n=0,1,2,\cdots$, $u_i^{(n)}$ is a specific control voltage, while $\{u_i^{(n)}\}$ indicates the ensemble $u_1^{(n)}\cdots u_N^{(n)}$.

4.1 General considerations for wavefront control algorithms

In free-space laser communications and beam projection systems with either a cooperative or non-cooperative far-field target, the final goal of feedback control systems is to fully precompensate the outgoing wavefront such that the target plane intensity distribution is focused to a diffraction-limited point. Due to strong intensity scintillations induced by long path propagation through atmospheric turbulence and the difficulty of direct wavefront sensing, the feedback control system is implemented to fulfill this goal approximately through optimization of a far-field system metric [5-7]. As discussed in Section 3.6, this metric can be any simply measurable and efficient cost-function directly related to the far-field target plane peak intensity or the far-field beam divergence angle. Cost-function selection depends mostly on the expected computational complexity associated with optimization and on projected accuracy in practical implementation. At the same time, cost-function sensing must turn out a high signal-to-noise ratio (SNR) and a high convergence speed.

In applications using the conformal adaptive phase-locked fiber array, controllable variables in feedback control systems include N control voltages for phase-locking compensation and $2N$ control voltages for subaperture wavefront tip-tilt compensations, where N is the total number of beamlets. In total, there are $N_c = 3N$ control voltages. For convenience of description and without loss of generality, a specific control voltage for phase-locking control will be denoted by $u_i(t)$, where $i = 1 \cdots N$, and a detailed description of only the phase-locking controller will be given. The control algorithm for subaperture wavefront tip-tilt compensation is generally the same when the $2N$ control voltages

for subaperture wavefront tip-tilt compensation are considered. The selected far-field metric signal, denoted by $J(t)$, generally depends on controllable voltages $\{u_i(t)\}$ and a variety of phase noise sources including atmospheric turbulence. For all cases considered in Section 3.6, no matter what control algorithm is used, the phase precompensation goal is to find optimal control voltages $\{u_i(t)\}$ for the N transmitted beamlets for given phase noise. These optimal control voltages correspond to the optimal phase status of these beamlets that further corresponds to the maximum value of the target-plane metric $J(t)$. Given the continuously changing phase noise including atmospheric turbulence, the optimal control voltages $\{u_i(t)\}$ can only be obtained if the control system can run much faster than the noise changes. A characteristic time for atmospheric turbulence $\tau_{at} \approx 10^{-3} \sim 10^{-2}$ seconds which is usually faster than the different slow-varying phase noise described in Section 3.4. Thus characteristic turbulence time τ_{at} is taken as characteristic phase noise time. The convergence time of a feedback control system based on a specific control algorithm, denoted by τ_{conv}, must be much shorter than the characteristic turbulence time τ_{at}. Otherwise, before the feedback control system converges, a new atmospheric turbulence pattern forms. With the assumption of "frozen" turbulence or "frozen" phase noise such that $\tau_{conv} \ll \tau_{at}$, the selected far-field system performance metric signal $J(t)$ can be described as a function of control voltages $\{u_i(t)\}$

$$J(t) = J\left(\{u_i(t)\}\right) \tag{4.1}$$

The most commonly used algorithms for optimizing the above cost function, such as a hill-climbing algorithm, either discretely or continuously, update control voltages $\{u_i(t)\}$ in such a way that the cost function $J(t)$ increases to a (local) maximum for maximizing optimization or decreases to a (local) minimum for minimizing optimization.

For a discrete-time control algorithm, the method of updating control voltages $\{u_i(t)\}$ can be described as

$$\operatorname{sgn}\left(u_i^{(n+1)} - u_i^{(n)}\right) = \pm \operatorname{sgn}\left(\frac{J\left(u_1^{(n+1)} \cdots u_N^{(n+1)}\right) - J\left(u_1^{(n)} \cdots u_N^{(n)}\right)}{u_i^{(n+1)} - u_i^{(n)}}\right) \tag{4.2}$$

where $\operatorname{sgn}(\bullet)$ is a sign function of real numbers, $\pm$ corresponds to maximizing/minimizing optimization, $n = 0,1,2,\cdots$ is the index of time, and $i = 1 \cdots N$. A control algorithm implementing the method as shown in Equation (4.2) is usually referred to as gradient descent (ascent) algorithm. For a continuous-time control algorithm, the method of updating control voltages $\{u_i(t)\}$ can be similarly described as

$$\operatorname{sgn}\left(\frac{du_i}{dt}\right) = \pm \operatorname{sgn}\left(\frac{\partial J\left(u_1 \cdots u_N\right)}{\partial u_i}\right) \tag{4.3}$$

A control algorithm implementing the method as shown in Equation (4.3) is usually referred to as a gradient flow algorithm. The occurrences of $\operatorname{sgn}(\bullet)$ in Equations (4.2) and (4.3) allow for different implementations of these algorithms.

4.2 Stochastic parallel gradient descent algorithm: general principles

Section 4.1 addresses general considerations for different wavefront control algorithms: discrete-time and continuous-time techniques. Among a variety of discrete-time techniques, the stochastic parallel gradient descent (SPGD) algorithm [100, 101] is commonly used. In this section, general principles of the SPGD algorithm are addressed. Section 4.3 will address some SPGD advanced features such as adaptive control parameters and correlated perturbations. Section 4.4 will describe a few implementations of SPGD controllers for wavefront distortion compensations.

Equation (4.1) in discrete-time format can be written as

$$J^{(n)} = J\left[\left\{u_i^{(n)}\right\}\right] . \tag{4.4}$$

In order to optimize the cost function as shown in Equation (4.4), the control voltages need be updated with their gradients estimated in a certain manner. The basic idea of estimating control voltage gradients is to apply different control voltage perturbations twice to the control system, then to measure the corresponding system cost function perturbation and then to approximate control voltage gradient with both control voltage perturbations and system cost function perturbation following Equation (4.2). SPGD control algorithm generally performs the following update rule for the control voltages

$$u_i^{(n+1)} = u_i^{(n)} + \eta\, \gamma_i^{(n)}\, \delta u_i^{(n)}\, \Delta J^{(n)} , \tag{4.5}$$

where $i = 1 \cdots N$ is the control voltage index, $n = 0,1,2,\cdots$ is the time index, $\left\{u_i^{(n)}\right\}$ are the control voltages, η is the optimizing mode parameter with $\eta = +1$ for maximizing

optimization, $\eta = -1$ for minimizing optimization and $\eta = 0$ for optimization off status, $\left\{\gamma_i^{(n)}\right\}$ are respective fixed or adaptive, update coefficients for control voltages $\left\{u_i^{(n)}\right\}$, $\left\{\delta u_i^{(n)}\right\}$ are respective fixed or adaptive, zero-mean, statistically independent or correlated following a certain rule, perturbations of control voltages $\left\{u_i^{(n)}\right\}$, and $\Delta J^{(n)}$ is the measured metric perturbation corresponding to control voltage perturbations $\left\{\delta u_i^{(n)}\right\}$ and is calculated as the difference between measured metric values $J_+^{(n)}$ after application of "positive" perturbations $\left\{u_i^{(n)} + \delta u_i^{(n)}\right\}$ and $J_-^{(n)}$ after application of "negative" perturbations $\left\{u_i^{(n)} - \delta u_i^{(n)}\right\}$) such that

$$\Delta J^{(n)} = J_+^{(n)} - J_-^{(n)} \tag{4.6}$$

$$J_+^{(n)} = J\left[\left\{u_i^{(n)} + \delta u_i^{(n)}\right\}\right] \qquad \text{and} \qquad J_-^{(n)} = J\left[\left\{u_i^{(n)} - \delta u_i^{(n)}\right\}\right] \tag{4.7}$$

Equations (4.6) and (4.7) implement bipolar control voltage perturbations. A method with unipolar control perturbations can be also applied such that

$$\Delta J^{(n)} = J^{(n)} - J_-^{(n)} \tag{4.8}$$

$$J^{(n)} = J\left[\left\{u_i^{(n)}\right\}\right] \qquad \text{and} \qquad J_-^{(n)} = J\left[\left\{u_i^{(n)} - \delta u_i^{(n)}\right\}\right] \tag{4.9}$$

Partial derivative approximations of the cost function with respective control voltages $\left\{\frac{J\left(u_1^{(n+1)}\cdots u_N^{(n+1)}\right)-J\left(u_1^{(n)}\cdots u_N^{(n)}\right)}{u_i^{(n+1)}-u_i^{(n)}}\right\}$ in Equation (4.2) are estimated in Equation (4.5) by $\left\{\delta u_i^{(n)}\,\Delta J^{(n)}\right\}$. This method with generated control voltage perturbations $\left\{\delta u_i^{(n)}\right\}$ and measured metric perturbation $\Delta J^{(n)}$ avoids dividing operation and is advantageous when one or more $\left\{\delta u_i^{(n)}\right\}$ are very small numbers.

From the above descriptions, it can be seen that SPGD works in an iterative manner. The metric cost function of the control system could converge with properly selected control parameters such as control voltage perturbations and update coefficients after a certain number of iterations with "frozen" atmospheric turbulence assumption. For convenience, maximizing optimization is considered only until the end of this section. Each SPGD iteration include generation of random control voltage perturbations, application of control voltage perturbations, measurement of the metric cost function, and update of the control voltages. Random control voltage perturbations can be generated using pseudo-random number generators. The sequence of random control voltage perturbations does not have to be infinitely long but have to be longer than the required number of SPGD iterations for metric cost function to converge. For bipolar perturbations as shown in Equations (4.6) and (4.7), perturbations need be applied twice in each iteration. For unipolar perturbations as shown in Equations (4.8) and (4.9), perturbations need be applied once in each iteration. Metric cost function must be measured twice per iteration as shown in Equations (4.6) and (4.8) for either bipolar perturbations or unipolar perturbations. Explicit update of control voltages following Equation (4.5) can be performed by the end of the

current iteration. Implicit update of control voltages can also be performed in combination with control voltage perturbations of the following iteration. Stochastic parallel gradient descent timing diagrams of an arbitrary selected control voltage $u_i(t)$ and metric cost function $J(t)$ are given in Figure 4.1 for four different cases: (a) with bipolar perturbations and explicit update period of control voltages (Figure 4.1a), (b) with bipolar perturbations and implicit update period of control voltages (Figure 4.1b), (c) with unipolar perturbations and explicit update period of control voltages (Figure 4.1c), (d) with unipolar perturbations and implicit update period of control voltages (Figure 4.1d). In general, the method with implicit update period of control voltages is preferred because of shorter time elapse per iteration and therefore faster convergence speed, which can be seen by comparison of Figure 4.1(b,d) and Figure 4.1(a,c). The method with bipolar control voltage perturbations is also generally preferred based on the following signal-to-noise ratio (*SNR*) analysis. Numerical simulations show that system performance metric J usually converges within 5~30 iterations per channel depending on selection of control parameters.

In a SPGD iteration with either bipolar perturbations or unipolar perturbation of control voltages, metric cost function is measured twice in order to calculate metric perturbation $\Delta J^{(n)}$. Two sources contribute to metric perturbation $\Delta J^{(n)}$: control voltage perturbations and wavefront phase distortions due to different kinds of noise though atmospheric turbulence is assumed to be "frozen". Denote as $\left\langle \Delta J^{(n)} \right\rangle_{Signal}$ the standard deviation of the calculated metric perturbation $\Delta J^{(n)}$ when control voltage perturbations are present. Denote

as $\left\langle \Delta J^{(n)} \right\rangle_{Noise}$ the standard deviation of calculated metric perturbation $\Delta J^{(n)}$ due to background phase noise when control voltage perturbations are not present. Signal-to-noise ratio (*SNR*) of SPGD algorithm can be defined as

$$SNR = \frac{\left\langle \Delta J^{(n)} \right\rangle_{Signal}}{\left\langle \Delta J^{(n)} \right\rangle_{Noise}} \tag{4.10}$$

SNR must be larger than a threshold value (~7dB observed in this work) otherwise SPGD algorithm will stop working successfully. On average, *SNR* is larger when bipolar control voltage perturbations instead of unipolar perturbations are applied in SPGD iterations.

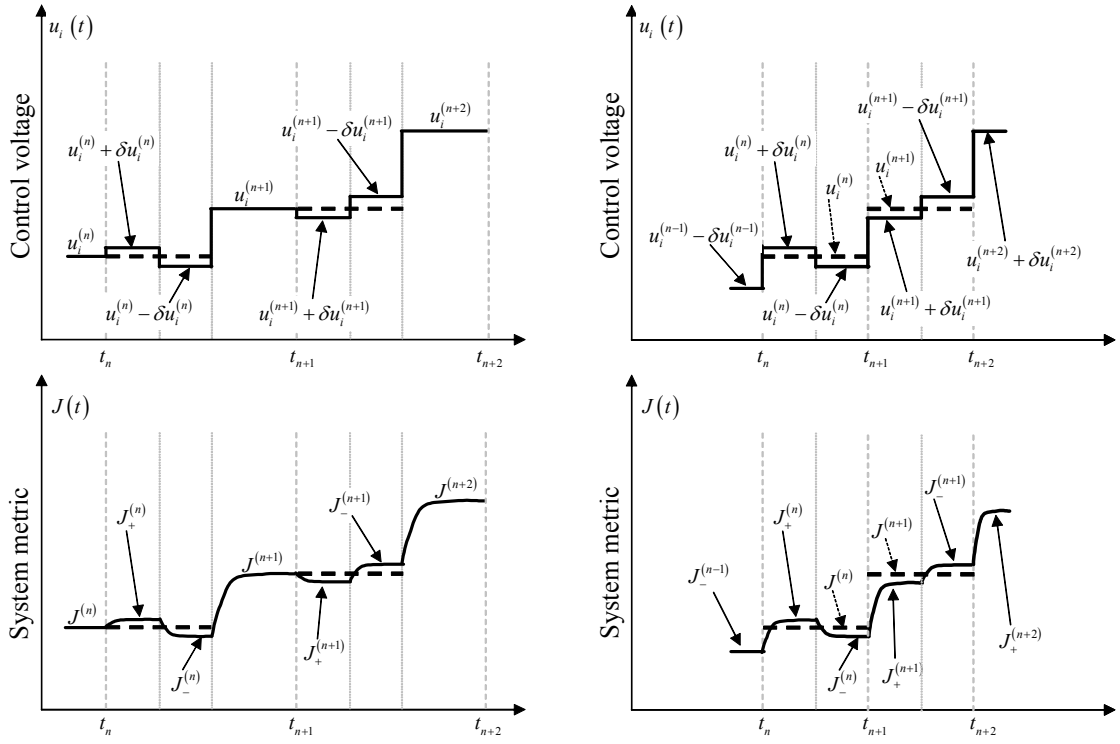

(a) bipolar perturbations, explicit update period

(b) bipolar perturbations, implicit update period

(c) unipolar perturbations, explicit update period

(d) unipolar perturbations, implicit update period

Figure 4.1: Timing diagrams of the stochastic parallel gradient descent (SPGD) algorithm

4.3 Stochastic parallel gradient descent algorithm: adaptive parameters

This section reviews the techniques using adaptive control parameters in the SPGD algorithm [102, 103]. In Equation (4.5), both positive control voltage update coefficients $\left\{\gamma_i^{(n)}\right\}$ and control voltage perturbations $\left\{\delta u_i^{(n)}\right\}$ can be fixed numbers or adapted numbers depending on the level of metric cost function $J^{(n)}$. With relatively larger values for $\left\{\gamma_i^{(n)}\right\}$ and $\left\{\delta u_i^{(n)}\right\}$, the absolute value of gradient $\frac{dJ(t)}{dt}$ would be larger and hence the metric cost function $J(t)$ would converge relatively faster. The stability of feedback control system, however, generally degrades more or less as the absolute value of gradient $\frac{dJ(t)}{dt}$ becomes large. There exists a tradeoff between the convergence speed and the system stability for using fixed values for control voltage update coefficients $\left\{\gamma_i^{(n)}\right\}$ and control voltage perturbations $\left\{\delta u_i^{(n)}\right\}$. If adaptive values for $\left\{\gamma_i^{(n)}\right\}$ and $\left\{\delta u_i^{(n)}\right\}$ are used, both fast convergence speed and good control system stability can be obtained simultaneously. The basic idea behind this is to use relatively large absolute values for $\left\{\gamma_i^{(n)}\right\}$ and $\left\{\delta u_i^{(n)}\right\}$ in order to increase convergence speed when the absolute value of the metric cost function is small or away from its optimal value, and to use relatively small absolute values for $\left\{\gamma_i^{(n)}\right\}$ and $\left\{\delta u_i^{(n)}\right\}$ in order to keep good stability or small variation in the vicinity near the optimal value of the metric signal. Upon convergence, however, absolute values of $\left\{\delta u_i^{(n)}\right\}$ must be large enough to introduce sufficient metric perturbation for the

SPGD algorithm to run properly with background noise present. In the following, adaptive techniques for control parameters $\left\{\gamma_i^{(n)}\right\}$ and $\left\{\delta u_i^{(n)}\right\}$ are discussed for maximizing optimization mode. Different profiles can be used to adapt these parameters as long as these profiles meet the requirements for fast convergence speed and good system stability. We will focus on the profile implemented in our SPGD controller.

The adaptation of control voltage update gains $\left\{\gamma_i^{(n)}\right\}$ is addressed first. $\left\{\gamma_i^{(n)}\right\}$ are adapted depending on the level of the metric values following the rule

$$\gamma_i^{(n)} = \gamma_i^{\max}\ \alpha\left(J^{(n-1)}\right) \tag{4.11}$$

where $\left\{\gamma_i^{\max}\right\}$ are user-specified parameters which can be set upon initialization and updated on demand, $\alpha\left(J^{(n-1)}\right)$ is an adaptive function following a designed profile, and $J^{(n-1)}$ is the unperturbed metric value described in Equation (4.4) with unipolar perturbations described by Equations (4.8) and (4.9) or the equivalently unperturbed metric value with bipolar perturbations described by Equations (4.6) and (4.7) can be calculated as

$$J^{(n-1)} = \frac{J_+^{(n-1)} + J_-^{(n-1)}}{2} \tag{4.12}$$

The adaptive profile function $\alpha\left(J^{(n-1)}\right)$ varies, usually for convenience, between zero and one and is defined in our SPGD controller as

$$\alpha\left(J^{(n-1)}\right)=\left[\frac{J_{\text{opt}}-J^{(n-1)}}{J_{\text{opt}}+J^{(n-1)}}\right]^{p} \tag{4.13}$$

where J_{opt} is the optimal goal metric value and p is a positive exponent. Both J_{opt} and p are user-specified parameters. The function $\alpha\left(J^{(n-1)}\right)$ may be implemented in either of the two following ways. $\alpha\left(J^{(n-1)}\right)$ can be calculated directly by the controller using parameters J_{opt} and p in each SPGD iteration. This method is convenient when SPGD controller is implemented through PC, but is not preferred because this controller on PC usually running MS Windows is not generally a real-time system and has low SPGD iteration rate using commercially available analog-to-digital and digital-to-analog converter boards. The second method is used for real-time SPGD controllers based on dedicated microprocessors. A supervisory PC can be used to generate a look-up table for $\alpha\left(J^{(n-1)}\right)$ which is uploaded to the controller microprocessors during initialization. If the user wants to change one of the parameters, J_{opt} or p, the look-up table is recalculated and the updated table is uploaded to the controller. The second method is generally preferred because it takes advantage of simple redefinition of the adaptive profile $\alpha\left(J^{(n-1)}\right)$ and the SPGD controller can be a real-time system and usually has a larger iteration rate. A single adaptive profile is used for all control channels. With different parameters $\left\{\gamma_i^{\max}\right\}$ applied for different channels, all control channels do not have to take the same update gains.

Similarly, the magnitudes of metric perturbations $\left\{\delta u_i^{(n)}\right\}$ can be adapted with respect to the metric value level according to the following rule

$$\delta u_i^{(n)} = \kappa_i^{(n)} \beta\left(J^{(n-1)}\right) \tag{4.14}$$

where $\left\{\kappa_i^{(n)}\right\}$ are statistically independent or correlated perturbation parameters, $\beta\left(J^{(n-1)}\right)$ is an adaptive profile function and can be defined as

$$\beta\left(J^{(n-1)}\right) = \left[\frac{J_{\text{opt}} - J^{(n-1)}}{J_{\text{opt}} + J^{(n-1)}}\right]^q \tag{4.15}$$

with J_{opt} and q as user-specified parameters. $\beta\left(J^{(n-1)}\right)$ may be implemented in a similar way as $\alpha\left(J^{(n-1)}\right)$. As mentioned above, $\left\{\kappa_i^{(n)}\right\}$ can be either statistically independent or correlated to each other for a given time index n in each SPGD iteration. In general, $\left\{\kappa_i^{(n)}\right\}$ need to be statistically independent to each other in the SPGD algorithm. For certain applications such as compensation for classical Kolmogorov atmospheric turbulence, $\left\{\kappa_i^{(n)}\right\}$ can be made correlated for each channel in order to further increase the control system convergence speed due to the fixed relative strengths of impact from different Zernike aberrations described by Equation (1.3) and Table 1-1. Perturbation coefficients $\left\{\kappa_i^{(n)}\right\}$ are proportional to either a set of uncorrelated perturbations $\left\{v_i^{(n)}\right\}$ or correlated

perturbations $\left\{w_i^{(n)}\right\}$. The choice between $\left\{v_i^{(n)}\right\}$ and $\left\{w_i^{(n)}\right\}$ is made depending on the metric level as follows

$$\kappa_i^{(n)} = \begin{cases} c_i\, v_i^{(n)} & \text{if } J^{(n-1)} > J_{\text{th}} \\ d_i\, w_i^{(n)} & \text{if } J^{(n-1)} \le J_{\text{th}} \end{cases} \tag{4.16}$$

where $\{c_i\}$, $\{d_i\}$ and J_{th} are user-specified parameters. Uncorrelated and correlated perturbations can be respectively predefined as follows

$$\mathbf{V} = \{V_{ik}\} = \begin{Bmatrix} V_{11} & \cdots & V_{1k} & \cdots & V_{1K} \\ \vdots & & \vdots & & \vdots \\ V_{i1} & \cdots & V_{ik} & \cdots & V_{iK} \\ \vdots & & \vdots & & \vdots \\ V_{N1} & \cdots & V_{Nk} & \cdots & V_{NK} \end{Bmatrix} \tag{4.17}$$

$$\mathbf{W} = \{W_{im}\} = \begin{Bmatrix} W_{11} & \cdots & W_{1m} & \cdots & W_{1M} \\ \vdots & & \vdots & & \vdots \\ W_{i1} & \cdots & W_{im} & \cdots & W_{iM} \\ \vdots & & \vdots & & \vdots \\ W_{N1} & \cdots & W_{Nm} & \cdots & W_{NM} \end{Bmatrix} \tag{4.18}$$

where $i = 1 \cdots N$, $k = 1 \cdots K$, $m = 1 \cdots M$, N is the total number of control channels, K and M are two positive integers which must be larger than their corresponding minimum numbers of the required SPGD iterations for convergence.

By using an appropriate threshold value J_{th}, control voltage perturbation parameters $\left\{\kappa_i^{(n)}\right\}$ and thus $\left\{\delta u_i^{(n)}\right\}$ can be statistically independent or correlated to each other. If J_{th} is smaller than the possible minimum metric value which is usually zero, then the

statistically independent perturbation parameters are used. If J_{th} is larger than the optimal goal metric value J_{opt}, then the correlated perturbation parameters are used. For other threshold value $0 < J_{\text{th}} < J_{\text{opt}}$, either statistically independent or correlated perturbation parameters are used depending on metric value $J^{(n-1)}$ as shown in Equation (4.16) . The respective column indices $k^{(n)}$ and $m^{(n)}$ for matrices **V** and **W** can be taken either randomly or sequentially in a loop manner within their own ranges $1 \le k^{(n)} \le K$ and $1 \le m^{(n)} \le M$. K and M need be larger if $k^{(n)}$ and $m^{(n)}$ are selected sequentially than the corresponding values K and M if $k^{(n)}$ and $m^{(n)}$ are selected randomly.

4.4 Stochastic parallel gradient descent algorithm: controller implementations

In this section, implementations of three different SPGD controllers for either phase-locking or subaperture wavefront tip-tilt compensations are addressed. For description convenience, only maximizing optimization of the metric cost function is considered here. As mentioned in Section 4.1, the SPGD algorithm can be used to find a local maximum for metric cost function. In general, this local maximum is not the global maximum. Our optimization goal of feedback control systems, however, is to find the global maximum. This problem can be resolved in most cases with following considerations. If phase-locking compensation is used only, then all local maxima of metric cost function are identical. If subaperture wavefront tip-tilt compensations are used as well, the unique global maximum corresponding to a flat wavefront of the metric cost function can be obtained by limiting control voltages within an appropriate vicinity of the global maximum. If physically implemented SPGD controllers in use are not fast enough, uncompensated

fast wavefront phase distortions can prevent feedback control systems from being stuck at a certain local maximum.

Another problem in the controller implementation is that a physical controller can only have limited dynamic ranges of output control voltages. If a control voltage reaches either its top rail voltage or bottom rail voltage and has an update gradient to go beyond the rail, it will be stuck at the rail. In this case, this control voltage will be reset to some value in the middle of its dynamic range. The destination voltage must be selected such that the introduced metric degradation is as small as possible. By referring to Section 2.2 and Section 3.5, a conclusion can be drawn as follows. The far-field metric signal $J(t) = J\left(\{u_i(t)\}\right)$ as shown in Equation (4.1) is a periodic function for each control voltage $u_i(t)$ in phase-locking system. The reason behind this is that each control voltage $u_i(t)$ is approximately proportional to phase shift introduced by the corresponding fiber-coupled phase shifter as shown in Equations (3.7) and (3.8). The period for each control voltage $u_i(t)$ can be taken as double of corresponding halfwave voltage for that channel as shown in Equations (3.9) and (3.10). Halfwave voltages denoted by $\{V_{\pi,i}\}$ for different channels are approximately equal. When an output control voltage $u_i(t)$ reaches its top (or bottom) rail, it can be reset by subtracting (or adding) a voltage offset in multiples of $2V_{\pi,i}$ corresponding to a phase shift in multiples of 2π radians. This process is referred to as 2π-reset. In theory, there is no additional phase noise introduced to the system if 2π-reset process happens in extremely short time. In reality, implementations of different SPGD controllers include digital-to-analog converter circuits and operational amplifi-

ers that have finite slew rates. During 2π -reset process, the control voltage experiences a continuous evolution from its rail value to its predefined destination value. In between, there is at least one voltage value which corresponding to a π -radian phase shift. The metric cost function will experience one or multiple very short but severe degradations depending on how many multiples of $2V_{\pi,i}$ voltage it experiences. The unexpected metric degradations should not be reflected into calculations for metric perturbations through exception handling mechanism such as bypassing one or more explicit or implicit control voltage update periods as shown in Figure 4.1. After necessary 2π -reset, this specific control voltage can still be actively updated. The accurate values of halfwave voltages $\{V_{\pi,i}\}$ are usually not known. Therefore, 2π -reset of control voltages will introduce additional small phase noise. Large dynamic ranges for control voltages are preferred to reduce the occurrences of 2π -reset process although a dynamic range up to $2V_{\pi,i}$ is sufficient in theory. 2π -reset process is only good for phase-locking control. For subaperture wavefront tip-tilt compensation, a control voltage is simply set to its middle value (usually zero volts) when it touches its rail voltage. In the physical implementations of SPGD controllers, it is noticed that the control voltages may drift from their lower rail voltage to upper rail voltage or vice versa continuously due to nonsymmetrical rounding errors in resolution-limited hardware-based calculations even though the controller works properly. For instance, if an output control voltage is represented with 12-bit resolution by an integer ranging from 0 to 4095, the average rounding error is +0.5 due to complete ceiling rounding method, where the number +0.5 corresponds to half least significant bit of this control voltage. This control voltage is likely to drift from its lower rail to upper rail as the SPGD algorithm runs. Control voltage drift can be mitigated by subtracting one

from the integer representation of this control voltage in every other SPGD iteration. Similar technique but with opposite polarity can be applied to mitigate control voltage drift due to complete floor rounding method. There is another useful technique which can be used to mitigate control voltage drifts thus to reduce the occurrences of output control voltages at their rail values. Equation (4.5) can be modified as follows

$$\begin{cases} w_i^{(n+1)} = u_i^{(n)} + \eta\, \gamma_i^{(n)}\, \delta u_i^{(n)}\, \Delta J^{(n)} \\ u_i^{(n+1)} = w_i^{(n+1)} - \dfrac{1}{N}\sum_{i=1}^{N} w_i^{(n+1)} \end{cases} \tag{4.19}$$

such that

$$\frac{1}{N}\sum_{i=1}^{N} u_i^{(n+1)} \equiv 0 \tag{4.20}$$

where $\left\{u_i^{(n)}\right\}$ are still the control voltages, and $\left\{w_i^{(n)}\right\}$ are intermediate variables. This technique is referred to as zero averaging of control voltages. Zero averaging of control voltages can be implemented either through direct software programming as shown in Equation (4.19), or through the ordinary SPGD technique as shown in Equation (4.5) and parallel electronic circuits to perform calculations as shown in the second line of Equation (4.19). The second method is preferred generally due to iteration rate concern.

For phase-locking control, three SPGD controllers were implemented: one PC-based controller with analog-to-digital and digital-to-analog converter boards, and two different microprocessor-based controllers. The PC-based SPGD phase-locking controller include a personal computer and an analog-to-digital converter card PCI-DAS1602 and a digital-to-analog converter card PCI-DDA08/12 which are available at Measurement Comput-

ing, Inc. With programming using high-level language such as C++ on PC, implementation of SPGD algorithm as described in Sections 4.2 and 4.3 is rather straightforward. Advanced features of SPGD algorithm such as adaptive control parameters can be realized easily and studied carefully. Due to the limiting A/D conversion speed of most commercially available data acquisition boards including PCI-DAS1602, this PC-based SPGD controller does not have a high iteration rate (~16,000 iterations per second) or a large compensation bandwidth. For subaperture wavefront phase tip-tilt control using piezoelectric fiber positioners with measured characteristic response curve as shown in Figure 3.8 in Section 3.3, the PC-based SPGD controller with iteration rate slowed down to ~950 iterations per second is considered sufficiently fast. The beamlets in our conformal system are likely to be steered in similar manners simultaneously. The control voltages applied to piezoelectric fiber positioners for all beamlets can be grouped into two sets: horizontal control voltages and vertical control voltages. Each set of control voltages are more or less correlated to each other. Thus partially correlated control parameters can be applied to calculating control voltages.

Analysis of feedback control strategies for conformal adaptive phase-locked fiber array in [72] showed that subaperture wavefront phase tip-tilt control must be applied before or at the same time when phase-locking control is applied. The multiple beamlets need to be steered to focus to the same point or at least partially overlap onto each other before they can be phase-locked. Care needs to be taken when both phase-locking control and subaperture wavefront phase tip-tilt control run simultaneously. On one hand, they cooperate in maximizing system metric $J(t)$. On the other hand, for either phase-locking control loop or subaperture wavefront phase tip-tilt control loop, metric perturbation due

to the other control loop is virtually noise. They need to compensate virtual noise due to each other. This problem is resolved in our control systems by utilizing much faster phase-locking controllers based on either SPGD technique or multi-dithering technique described in Sections 4.5, 4.6, 4.7 and 4.8, and relatively slow PC-based SPGD controller for subaperture wavefront phase tip-tilt compensation. Phase-locking control system and subaperture wavefront phase tip-tilt control system cooperate to maximize metric signal by taking different temporal bandwidths. For phase-locking control, relatively slow metric perturbation due to subaperture wavefront phase tip-tilt control is "frozen". For subaperture wavefront phase tip-tilt control, the much faster metric perturbation due to phase-locking control is invisible when a lowpass filter (LPF) with an appropriate cutoff frequency in between the two working bandwidths is applied to the metric signal $J(t)$ before it is fed to the subaperture wavefront phase tip-tilt controller.

Atmospheric turbulence in free-space optical communications or laser beam projection applications with near horizontal propagation paths is commonly thought to contain frequency components up to ~1,000 Hz. Most of the energy of turbulence is contained in frequency components no more than ~150 Hz. Frequency components from ~150Hz to ~1,000Hz do not contribute much to atmospheric turbulence strength. Two phase-locking SPGD controllers using different microprocessors were built for our conformal optical system. Both SPGD controllers implement bipolar control voltage perturbations and implicit control voltage update periods as shown in Figure 4.1(b). The first hardware SPGD controller for phase-locking compensation is an eight-channel controller based on Atmel AVR 8-bit RISC microprocessors as shown in Figure 4.2. This SPGD controller has iteration rate ~95,000 iterations per second. 2π -reset feature is implemented in this con-

troller. As the first prototype of microprocessor-based SPGD controllers, this controller does not use adaptive control parameters.

In order to further investigate phase-locking control using SPGD algorithm, a second eight-channel hardware SPGD controller as shown in Figure 4.3 based on Atmel 32-bit ARM-based microcontroller AT91SAM9260 has been built. The controller has an operational rate <180,000 iterations per second. 2π -reset feature is implemented in this controller. Adaptive control update gain coefficients and adaptive control voltage perturbations are implemented.

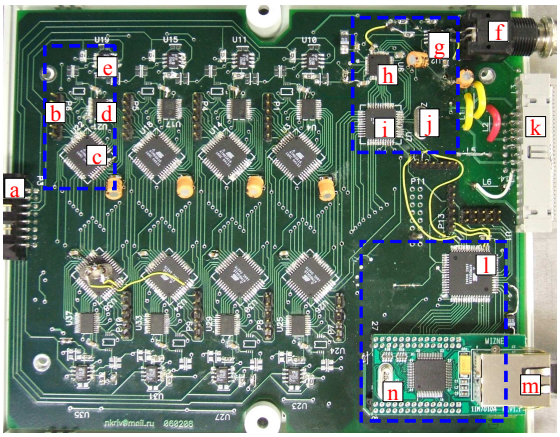

Figure 4.2: Eight-channel Atmel AVR 8-bit RISC microprocessor-based SPGD controller, developed at UMD (2006).

Channel output update rate: ~95,000 iterations/sec, channel output dynamic range: ±15V (±6πrad. phase shift). Control parameters of all eight channels can be tuned (hot programming) independently while running. 2π -reset feature is implemented in this controller. The upper-left dashed blue rectangle outlines one of the eight control channels. The upper-right dashed blue rectangle outlines the metric perturbation computation unit. The bottom-right dashed blue rectangle outlines the coordination unit. Notes: (a) output connector with eight analog outputs to phase modulators for compensation, (b) eight connectors for serial processor initialization, (c) eight microprocessors (ATMEGA16A) for calculations of control voltages, (d) eight DACs (TLW5639) for channel outputs, (e) eight voltage amplifiers (OP37) for channel outputs, (f) analog metric input from photo sensor, (g) preamplifier (INA129) for metric input, (h) ADC (ADS7881) for metric input, (i) microprocessor (ATMEGA16A) for metric perturbation computation, (j) crystal oscillator (16.0MHz) for SPGD controller clocking, (k) power supplies (±15V, +5V), (l) microprocessor (ATMEGA128) for SPGD controller coordination, (m) Ethernet interface (WIZnet-NM7010A) for exchanging control commands and parameters with supervisory PC, (n) crystal oscillator (25.0MHz) for controller coordination.

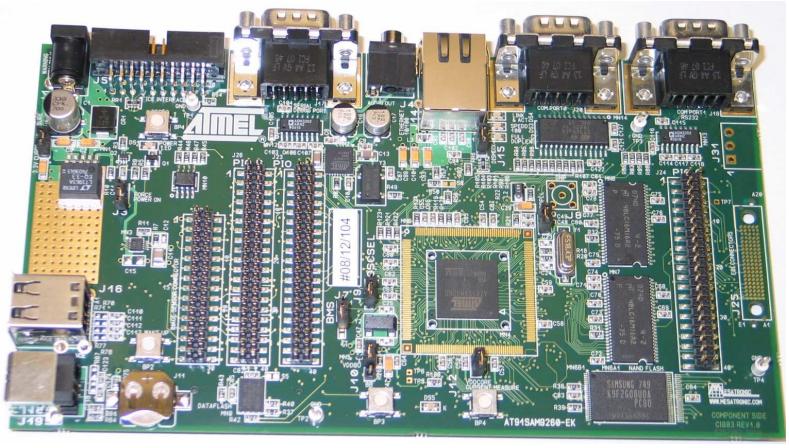

Evaluation kit AT91SAM9260-EK hosting 32-bit ARM-based microcontroller AT91SAM9260.

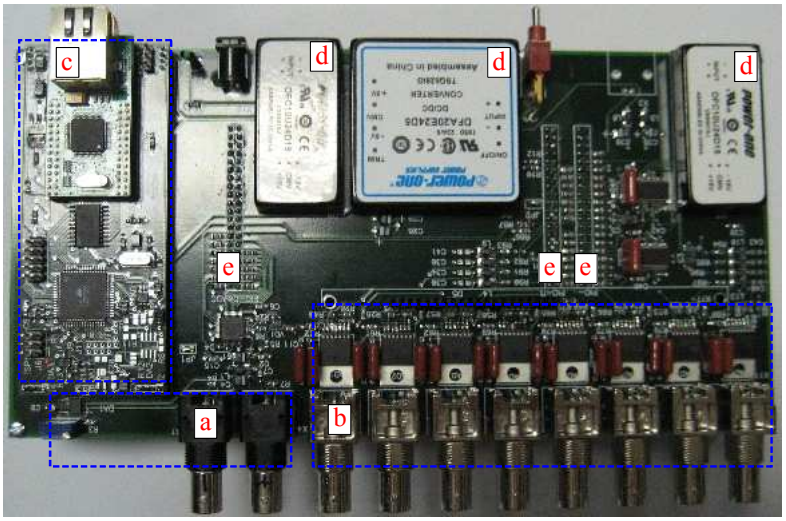

Board hosting ADC for metric input and DACs and amplifiers for output control voltages. (a): differential metric inputs, (b): eight analog outputs, (c): Ethernet-based interface board between supervisory PC and controller, (d): dc/dc power converters (DFA20E24D5, DFC10U24D15), (e) interfacing connectors between this board and microcontroller evaluation kit AT91SAM9260-EK board as shown above.

Figure 4.3: Eight-channel SPGD controller based on Atmel 32-bit ARM-based microcontroller AT91SAM9260, developed at UMD (2008).

Channel output update rate: ~180,000 iterations per second, channel output dynamic range: ±25V (±10πrad. phase shift). 2π -reset feature is implemented in this controller. Adaptive control parameters as described in Section 4.3 are used.

4.5 Multi-dithering algorithm: general principles

The multi-dithering technique for adaptive optics was first reported by O'Meara [104-106] and Hardy [11]. In the past thirty years, the multi-dithering technique was not extensively used due to lack of sufficiently fast hardware controllers. With sufficiently fast hardware, the multi-dithering technique can be used for wavefront phase compensation. The very challenging frequency-locking problem as mentioned in Section 3.4 might be resolved with this technique. The stochastic parallel gradient descent (SPGD) algorithm described in previous sections is the primary wavefront compensation technique in this work. As tentative research efforts, general principles of the multi-dithering technique are addressed in this section. Dither amplitude considerations are discussed in Section 4.6. A hardware multi-dithering controller based on VLSI technology is described in Section 4.7.

Phase-locking control using the multi-dithering technique can be realized by updating the control voltages $\{u_i(t)\}$ continuously while estimating their gradients in the following manner for $i = 1 \cdots N$ as a special implementation of Equation (4.3),

$$\frac{du_i}{dt} \propto \frac{\partial J\left(u_1 \cdots u_N\right)}{\partial u_i} \tag{4.21}$$

where $J(t) = J\left(u_1 \cdots u_N\right)$ is the system metric. $\left\{\frac{\partial J\left(u_1 \cdots u_N\right)}{\partial u_i}\right\}$ and thus $\left\{\frac{du_i}{dt}\right\}$ in Equation (4.21) are evaluated in parallel by applying dithered control voltages $\{\tilde{u}_i(t)\}$

with appropriately selected dither frequencies $\{\omega_i\}$ and a common dither amplitude α to the beam projection system as follows,

$$\tilde{u}_i(t) = u_i(t) + \alpha \sin(\omega_i t) \tag{4.22}$$

and for the i th ($i = 1 \cdots N$) channel, multiplying the detected metric signal $J(\tilde{u}_1 \cdots \tilde{u}_N)$ and the same sinusoidal dither signal $\sin(\omega_i t)$, and then passing the product $J(\tilde{u}_1 \cdots \tilde{u}_N)\sin(\omega_i t)$ through a low pass filter (LPF) with appropriately selected common cutoff frequency ω_{cut}. This process is shown in Figure 4.4.

The feasibility of Equation (4.21) can be shown in the following derivation. Using Taylor's expansion, the dithered system metric can be written as

$$\begin{aligned} J(\{\tilde{u}_i(t)\}) &= J(\{u_i(t) + \alpha \sin(\omega_i t)\}) \\ &= J(\{u_i(t)\}) + \sum_{i=1}^{N} \alpha \frac{\partial J}{\partial u_i} \sin(\omega_i t) + o(\alpha) \end{aligned} \tag{4.23}$$

where $o(\alpha)$ indicates higher (≥ 2) order terms of α. The dc part of $o(\alpha)$ is thought to be small under certain conditions and the ac part can be filtered out in the multi-dithering algorithm. For the i th ($i = 1 \cdots N$) channel,

$$J(\{\tilde{u}_j(t)\})\sin(\omega_i t) \approx \left[J(\{u_j(t)\}) + \sum_{j=1}^{N} \alpha \frac{\partial J}{\partial u_j} \sin(\omega_j t) + o(\alpha) \right] \sin(\omega_i t) \tag{4.24}$$

The low pass operation with cutoff frequency

$$\omega_{cut} < \min(\{\omega_i\}, \{|\omega_i - \omega_j|\}) \qquad (1 \cdots i \neq j \cdots N) \tag{4.25}$$

gives

$$\left\langle J\left(\left\{\tilde{u}_j(t)\right\}\right)\sin\left(\omega_i t\right)\right\rangle_{\omega_{cut}} \approx \frac{\alpha}{2}\frac{\partial J}{\partial u_i} \tag{4.26}$$

where $\langle\bullet\rangle_{\omega_{cut}}$ indicates the low pass operation with cutoff frequency ω_{cut}, $''\approx''$ indicates omission of higher order terms $o(\alpha)$. As shown in Figure 4.4, undithered control voltage $u_i(t)$ is the integration of the term in Equation (4.26) such that

$$\frac{du_i(t)}{dt} \approx \frac{1}{2}\gamma\alpha\frac{\partial J}{\partial u_i} \tag{4.27}$$

where γ is the common update gain coefficient for all N control voltages. We have

$$\frac{dJ(t)}{dt} = \frac{dJ\left(\left\{u_i(t)\right\}\right)}{dt} = \sum_{i=1}^{N}\frac{\partial J}{\partial u_i}\frac{du_i(t)}{dt} \approx \frac{1}{2}\gamma\alpha\sum_{i=1}^{N}\left(\frac{\partial J}{\partial u_i}\right)^2 \tag{4.28}$$

Assume update gain coefficient γ and small dither amplitude α are positive. This makes $\frac{dJ(t)}{dt} \geq 0$, which indicates a (locally) maximizing process for the system metric $J(t)$. The absolute value of $\frac{dJ(t)}{dt}$ determines the convergence speed of the system metric $J(t)$. $\frac{dJ(t)}{dt}$ is linearly proportional to the update gain coefficient γ and an implicit function $\alpha\sum_{i=1}^{N}\left(\frac{\partial J}{\partial u_i}\right)^2$ of the dither amplitude α. It is straightforward to conclude that increasing magnitude of update gain γ would increase convergence speed of metric $J(t)$

as long as the control system is in a stable working condition. Dependence of $\frac{dJ(t)}{dt}$ on the dither amplitude α is rather complicated and will be discussed separately in Section 4.6.

As shown in Section 4.1, the ″frozen″ turbulence assumption with characteristic atmospheric turbulence frequency parameter $1/\tau_{at}$ is taken, where τ_{at} is the characteristic atmospheric turbulence time parameter. For atmospheric phase distortion compensation, it is desired that the smallest selected dithering frequency far exceeds the characteristic atmospheric turbulence frequency parameter such that

$$\omega_{\min} = \min\left(\{\omega_i\}\right) \gg 1/\tau_{at} \tag{4.29}$$

because a certain number of dithering cycles with frequency $\omega_{\min}$ are generally required to phase-lock all N beamlets with initial relative phase differences. All N control voltages are dithered at different frequencies $\{\omega_i\}$ simultaneously and in parallel. Equations (4.25) and (4.29) show that dithering frequencies $\{\omega_i\}$ and the low pass cutoff frequency ω_{cut} can be selected in the following manner. The characteristic atmospheric turbulence frequency time parameter $\tau_{at} \approx 10^{-3} \sim 10^{-2}$ seconds need be estimated first. Then choose the low pass cutoff frequency

$$\omega_{cut} = \frac{(50 \sim 200)}{\tau_{at}} \tag{4.30}$$

depending on convergence speed. After ω_{cut} is selected, the smallest dither frequency and dither frequency separations can be selected such that

$$\min\left(\{\omega_i\}, \left\{\left|\omega_i - \omega_j\right|\right\}\right) > (2 \sim 3)\omega_{cut} \qquad (1 \cdots i \neq j \cdots N) \tag{4.31}$$

to prevent crosstalk between channels by using low pass filter operations. At the same time, all dither frequencies $\{\omega_i\}$ must be within the compensation bandwidth of the wavefront corrector denoted by ω_{comp}, which can be described as

$$\max\left(\{\omega_i\}\right) < \omega_{comp} \tag{4.32}$$

The above description of the multi-dithering algorithm assumes synchronous detection of metric signal $J(t)$, which means that the effect of dithered control voltages $\{\tilde{u}_i(t)\}$ is reflected in metric signal $J(t)$ immediately and can be sensed simultaneously by the lumped multi-dithering controller. Physical beam projection systems, however, are always distributed in a relatively large spatial scale. The dither of the metric signal $J(t)$ due to dithered control voltages $\{\tilde{u}_i(t)\}$ applied to the phase modulators in the beam projection system can be only detected at a later time. The nonsynchronous detection in our multi-dithering controller implementation is addressed in Section 4.7.

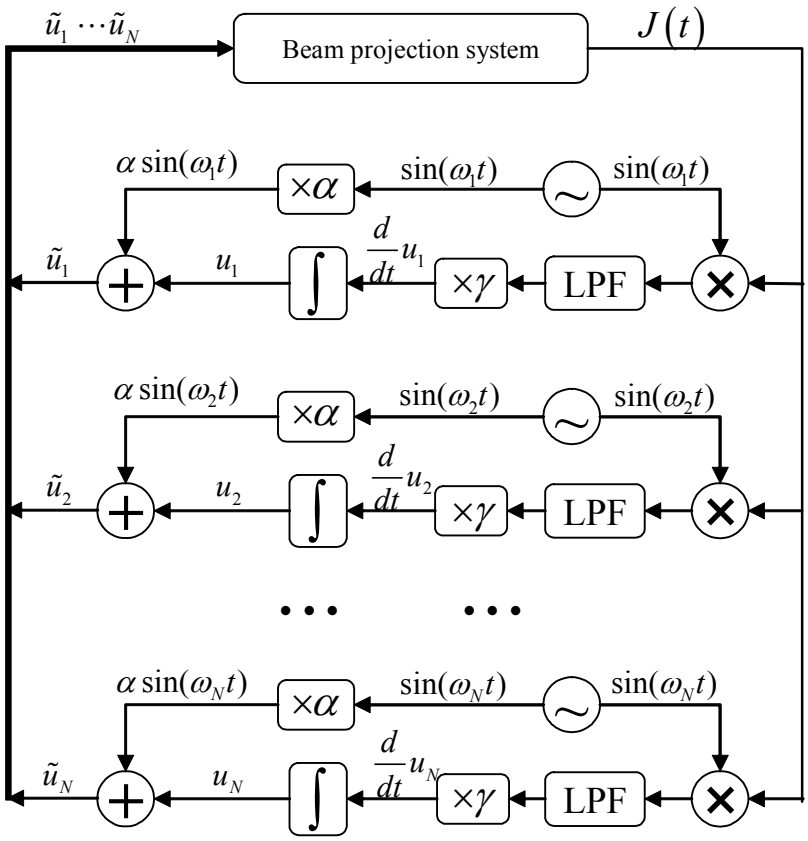

Figure 4.4: Schematic of the phase-locking controller based on the multi-dithering algorithm.

The synchronous detection of the metric signal $J(t)$ is assumed here for description convenience. For the i th ($i = 1 \cdots N$) channel, signal $\sin(\omega_i t)$ or $\alpha \sin(\omega_i t)$ to the left of sinusoidal generator is taken as dither signal while signal $\sin(\omega_i t)$ to the right of sinusoidal generator is taken as de-modulation signal.

4.6 Multi-dithering algorithm: dither amplitude considerations

As shown in Equation (4.28), $\frac{dJ(t)}{dt}$ is roughly proportional to $\alpha\sum_{i=1}^{N}\left(\frac{\partial J}{\partial u_i}\right)^2$, which is an implicit function of the dither amplitude α. In this section, a discussion of the effect of the dither amplitude α on the metric signal $J(t)$ is reviewed [7] for the following explicit, a simplified version of metric signal as shown in Equation (2.33)

$$J(t) = A_0^2\left(N + \sum_{1\le i\ne k\le N}\cos\left[\Phi_i(t) - \Phi_k(t)\right]\right) \tag{4.33}$$

where A_0 is the identical complex amplitude for all N outgoing beamlets and $\{\Phi_i(t)\}$ are relative phases of beamlets such that

$$\Phi_i(t) = \Delta_i(t) + u_i(t) + \alpha\sin(\omega_i t) \tag{4.34}$$

where $\{\Delta_i(t)\}$ are the respective propagation medium induced slow-varying phase shifts of all N beamlets, and $\{u_i(t) + \alpha\sin(\omega_i t)\}$ are phase modulations due to dithered control voltages as shown in Equation (4.22). For simplicity, here dithered control voltages are used to directly represent phase modulations by referring to Section 3.5. For the ith ($i = 1\cdots N$) channel, the residual uncompensated phase shift can be written as

$$\varepsilon_i(t) = \Delta_i(t) + u_i(t) \tag{4.35}$$

Term $\cos\left[\Phi_i(t) - \Phi_k(t)\right]$ in Equation (4.33) can be written as

$$\begin{aligned}\cos\left[\Phi_i(t)-\Phi_k(t)\right] &= \cos\left[\varepsilon_i(t)-\varepsilon_k(t)\right]\cos\left[\alpha\sin(\omega_i t)-\alpha\sin(\omega_k t)\right] \\ &\quad -\sin\left[\varepsilon_i(t)-\varepsilon_k(t)\right]\sin\left[\alpha\sin(\omega_i t)-\alpha\sin(\omega_k t)\right] \\ &= \cos\left[\varepsilon_i(t)-\varepsilon_k(t)\right]\cos\left[\alpha\sin(\omega_i t)\right]\cos\left[\alpha\sin(\omega_k t)\right] \\ &\quad +\cos\left[\varepsilon_i(t)-\varepsilon_k(t)\right]\sin\left[\alpha\sin(\omega_i t)\right]\sin\left[\alpha\sin(\omega_k t)\right] \\ &\quad -\sin\left[\varepsilon_i(t)-\varepsilon_k(t)\right]\sin\left[\alpha\sin(\omega_i t)\right]\cos\left[\alpha\sin(\omega_k t)\right] \\ &\quad +\sin\left[\varepsilon_i(t)-\varepsilon_k(t)\right]\cos\left[\alpha\sin(\omega_i t)\right]\sin\left[\alpha\sin(\omega_k t)\right]\end{aligned} \tag{4.36}$$

With the following two identities

$$\begin{cases}\sin\left[\alpha\sin(\omega_i t)\right] = 2\sum_{n=1}^{\infty} J_{(2n-1)}(\alpha)\sin\left[(2n-1)\omega_i t\right] \\ \cos\left[\alpha\sin(\omega_i t)\right] = J_0(\alpha)+2\sum_{n=1}^{\infty} J_{2n}(\alpha)\cos(2n\omega_i t)\end{cases} \tag{4.37}$$

where $J_0(\alpha)$, $J_1(\alpha)$, $J_2(\alpha)$ and etc. are Bessel functions of the first kind, the metric signal in Equation (4.33) can be written as

$$J(t) = \langle J\rangle^{dc} + \sum_{i=1}^{N} B_i \sin(\omega_i t) + o.t. \tag{4.38}$$

after a little algebra, where the dc part of metric signal is

$$\langle J\rangle^{dc} = A_0^2\left(N + J_0^2(\alpha)\sum_{1\le i\ne k\le N}\cos\left[\varepsilon_i(t)-\varepsilon_k(t)\right]\right) \tag{4.39}$$

and the coefficient of ac terms $\sin(\omega_i t)$ is

$$B_i = -4A_0^2 J_0(\alpha)J_1(\alpha)\sum_{k=1}^{N}\sin\left[\varepsilon_i(t)-\varepsilon_k(t)\right] \tag{4.40}$$

and "o.t." represents other terms of the ac part which can be filtered out in multi-dithering algorithm and are omitted. The dc part of dithered metric signal can achieve its maximum value

$$\left\langle J\right\rangle_{\max}^{dc}\left(\alpha\right)=A_0^2N\left[1+\left(N-1\right)J_0^2\left(\alpha\right)\right] \tag{4.41}$$

when all N beamlets have residual uncompensated phases $\left\{\varepsilon_i\left(t\right)\right\}=\mathbf{0}$. With very small dither amplitude α, the dc part of dithered metric signal approaches its limit in ideal coherent combining situation

$$\lim_{\alpha\to 0}\left\langle J\right\rangle_{\max}^{dc}\left(\alpha\right)=\left(A_0N\right)^2 \tag{4.42}$$

The ratio of $\left\langle J\right\rangle_{\max}^{dc}\left(\alpha\right)$ over $\lim_{\alpha\to 0}\left\langle J\right\rangle_{\max}^{dc}\left(\alpha\right)$

$$\eta\left(\alpha\right)=\frac{\left\langle J\right\rangle_{\max}^{dc}\left(\alpha\right)}{\lim_{\alpha\to 0}\left\langle J\right\rangle_{\max}^{dc}\left(\alpha\right)}=\frac{1}{N}\left[1+\left(N-1\right)J_0^2\left(\alpha\right)\right] \tag{4.43}$$

can be used to evaluate the effect of the dither amplitude on the normalized metric. It can be verified that for $\alpha\in\left[0,2.4\right]$ in radians, $\eta\left(N,\alpha\right)$ is a monotonically decreasing function of α for a given N.

Hence it is desired to use as a small dither amplitude α as possible in the multi-dithering algorithm. This statement is only valid for working conditions with relatively weak background noise. Dither amplitude α must be large enough to keep sufficiently large signal-to-noise ratio (SNR) to properly run the multi-dithering algorithm. By equating the right side of Equation (4.23) and the right side of Equation (4.38), it can be seen that

$$B_i \equiv \alpha \frac{\partial J}{\partial u_i} \tag{4.44}$$

Then Equation (4.28) becomes

$$\begin{aligned} \frac{dJ(t)}{dt} &\approx \frac{1}{2}\gamma\alpha \sum_{i=1}^{N}\left(\frac{B_i}{\alpha}\right)^2 \\ &= A_0^4 \gamma \left[\frac{8J_0^2(\alpha)J_1^2(\alpha)}{\alpha}\right] \sum_{i=1}^{N}\left(\sum_{k=1}^{N}\sin\left[\varepsilon_i(t)-\varepsilon_k(t)\right]\right)^2 \end{aligned} \tag{4.45}$$

The above expression shows that the convergence speed of the metric signal $J(t)$ depends on the total outgoing power due to term A_0^4, the control voltage update gain γ, the dither amplitude α due to term

$$\xi(\alpha) = \frac{8J_0^2(\alpha)J_1^2(\alpha)}{\alpha} \tag{4.46}$$

which monotonically increases for $\alpha \in [0, 0.791]$ and decreases for $\alpha \in [0.791, 2.4]$, and residual uncompensated phases $\{\varepsilon_i(t)\}$ due to term $\sum_{i=1}^{N}\left(\sum_{k=1}^{N}\sin\left[\varepsilon_i(t)-\varepsilon_k(t)\right]\right)^2$ that indicates coupling between different control channels. Convergence speed must tuned carefully with the above factors.

In the following, the effect of the dither amplitude α on signal-to-noise ratio (SNR) of an individual control channel is discussed. For the i th ($i = 1 \cdots N$) control channel as shown in Figure 4.4 and Figure 4.6, the signal denoted by $\langle \tilde{J}_i \rangle_{signal}$ can be estimated by the standard deviation of output current of the photo detector for detecting metric modulation due to the i th dither signal $\alpha \sin(\omega_i t)$ such that

$$\left\langle \tilde{J}_i \right\rangle_{signal} = \chi \left| B_i \right| = 4\chi A_0^2 J_0(\alpha) J_1(\alpha) \left| \sum_{k=1}^{N} \sin\left[\varepsilon_i(t) - \varepsilon_k(t) \right] \right| \tag{4.47}$$

where χ is the photo detector sensitivity with respect to the input power. The signal term $\left\langle \tilde{J}_i \right\rangle_{signal}$ includes background noise contribution. The noise $\left\langle \tilde{J} \right\rangle_{noise}$ can be estimated by the standard deviation of the output current of the photo detector for detecting dithered metric $\langle J \rangle_{\max}^{dc}(\alpha)$ [see Equation (4.41)] affected by background noise in phase-locked condition such that

$$\left\langle \tilde{J} \right\rangle_{noise} = \chi \varsigma \langle J \rangle_{\max}^{dc}(\alpha) = \chi \varsigma A_0^2 N \left[1 + (N-1) J_0^2(\alpha) \right] \tag{4.48}$$

where ς is the amplitude of the stray modulation due to background noise. The signal-to-noise ratio (SNR) of the i th ($i = 1 \cdots N$) control channel can be written as

$$SNR_i = \frac{\left\langle \tilde{J}_i \right\rangle_{signal}}{\left\langle \tilde{J} \right\rangle_{noise}} = \frac{4}{\varsigma} \left(\frac{J_0(\alpha) J_1(\alpha)}{N\left[1 + (N-1) J_0^2(\alpha) \right]} \right) \left| \sum_{k=1}^{N} \sin\left[\varepsilon_i(t) - \varepsilon_k(t) \right] \right| \tag{4.49}$$

It can be seen that the signal-to-noise ratios for all control channels have the same dependence on the dither amplitude α with the dependence factor

$$\zeta(\alpha) = \frac{J_0(\alpha) J_1(\alpha)}{N\left[1 + (N-1) J_0^2(\alpha) \right]} \tag{4.50}$$

For a N-channel phase-locking control system even with known total output optical power, known couplings between channels, known background noise level and spectrum and hence known selected frequencies of dither signals, selection of dither amplitude α is still a tradeoff between different concerns such as normalized metric, convergence

speed and signal-to-noise ratio. In experimental work using the multi-dithering controller, the dither amplitude can be tuned to an appropriate value with the considerations in this section.

4.7 Multi-dithering algorithm: controller implementation

In the previous two sections, general principles of the multi-dithering control algorithm as well as selection criteria for appropriate dither amplitudes were described. In this section, some aspects of the implementation of multi-dithering control in an eight-channel controller based on mixed signal VLSI technology are discussed. Photographs of the hardware, which was developed in cooperation with JHU/ARL [107-109]. are shown in Figure 4.5. In this controller, a 2π-reset feature (similar to the one described in Section 4.4 for the SPGD controllers) was implemented to mitigate problems due to the finite dynamic range of the output control voltages. The controller does not exactly implement the control voltage update rule presented in Equation (4.27): The partial derivative of the metric with respect to the i th control channel, $\frac{\partial J}{\partial u_i}$, is replaced by its sign, $\mathrm{sgn}\left(\frac{\partial J}{\partial u_i}\right)$, which was more favorable for the circuit realization.

As already briefly discussed at the end of Section 4.5, the multi-dithering controller must work with nonsynchronous detection, because of the time delay (denoted as T) between the instant at which dithered control voltages $\{\tilde{u}_i\}$ are applied and the instant at which the metric J is picked up by the controller. (Note that T includes not only the optical beam propagation time but also delays related to control voltage application and the metric signal processing time.) Thus, the metric measured at time t is actually a function of the control voltages applied at time $t-T$, i.e.,

$$J(t) = J\left[u_1(t-T)\cdots u_N(t-T)\right] \tag{4.51}$$

In order to compensate for the delay *T*, the controller introduces phase shifts ψ_i between the sinusoidal dither signals and the modulation signal before multiplication with the dithered metric signal (see Figure 4.4 and Figure 4.6). Thus, in Equation (4.24), the term $J\left(\left\{\tilde{u}_j(t)\right\}\right)$ is replaced by $J\left(\left\{\tilde{u}_j(t-T)\right\}\right)$ and the term $\sin(\omega_i t)$ is replaced by $\sin(\omega_i t+\psi_i)$. Taking into account all these considerations, the behavior of the realized multi-dithering controller can be described by the following two equations [compare to Equation (4.27) and Equation (4.28)]:

$$\frac{du_i(t)}{dt}=\frac{1}{2}\gamma\alpha\,\mathrm{sgn}\left(\frac{\partial J}{\partial u_i}\right)\sin(\omega_i T-\psi_i) \tag{4.52}$$

$$\frac{dJ(t)}{dt}=\frac{1}{2}\gamma\alpha\sum_{i=1}^{N}\left|\frac{\partial J}{\partial u_i}\right|\sin(\omega_i T-\psi_i) \tag{4.53}$$

In Equations (4.52) and (4.53), the term $\sin(\omega_i T-\psi_i)$ must be positive in order to assure that $\frac{dJ(t)}{dt}\geq 0$ and thus metric maximization is achieved. If the delay time, *T*, is known with sufficient accuracy, then the phase delays $\{\psi_i\}$ can be chosen deterministically in order to fulfill this demand. In reality, T, is most likely not known (it may even vary, e.g., because of a changing propagation distance) and the controller (or the operator) has to search for appropriate values for $\{\psi_i\}$.

The realized multi-dither controller uses a trial-and-error method to select the phase delays $\{\psi_i\}$ from a set of discrete values. If each ψ_i is chosen out of a set of *B* evenly spaced values within the interval $[0,2\pi)$, it is not difficult to verify that at least five dis-

crete values are required to cover all possibilities that allow metric maximization for any time delay T. $\{\psi_i\}$ may take, e.g., values from $\psi_i = \{0,\ \frac{2\pi}{5},\ \frac{4\pi}{5},\ \frac{6\pi}{5},\ \frac{8\pi}{5}\}$, or $\psi_i = \{0,\ \frac{\pi}{3},\ \frac{2\pi}{3},\ \pi,\ \frac{4\pi}{3},\ \frac{5\pi}{3}\}$ or $B = 5$ and $B = 6$, respectively. There are totally B^N combinations $\psi_1, \ldots \psi_N$ for a system with N control channels (beamlets), potentially resulting in a lengthy search phase especially for conformal optical system with a large number of subapertures. This problem can be mitigated by starting the trial-and-error method with just two beamlets to select ψ_1 and ψ_2. At most B^2 combinations need to be tried in this case. Then add one more beamlet to select ψ_3, which requires trial of at most B combinations when ψ_1 and ψ_2 are already selected. The same maximum number of combinations needs to be tried for any other beamlet added to the beam until all N beamlets are included. This way, a good set of $\{\psi_i\}$ would be found after trying at most $B^2 + B(N-2)$ combinations. For example, for $N = 7$ and $B = 6$ (this is the value realized in the multi-dithering controller, because of an easier circuit realization), the second method requires at most 66 trials in comparison to $B^N = 279936$ for the first method. (Note that a beamlet can simply be added or removed from the system using the amplitude controls implemented through in-line fiber-coupled Mach-Zehnder interferometers as shown in Figure 3.11.) It is immediately evident that this trial-and-error method can only be successful if the round trip delay T does not change significantly during the search period. However, because of the discrete values for $\{\psi_i\}$ the multi-dithering control system can afford certain variations in the round trip delay T within a range in the

order of $\frac{2\pi}{\omega_i B}$. Thus, this multi-dithering control approach is viable for laser communication or beam projection applications with stationary or slowly moving transceivers.

The trial-and-error method could be further improved using lock-in amplifier technique in the following way . The block labeled with "lock-in amplifiers" in Figure 4.6c takes for each channel *i* the demodulation signal $\sin(\omega_i t)$ and generates an orthogonal demodulation signal $\cos(\omega_i t)$ Then it performs analog lock-in amplifier operations

$$\begin{cases} \left\langle J(t)\sin(\omega_i t)\right\rangle_{\omega_{lcut}} \equiv \left\langle J\left(\left\{\tilde{u}_j(t+T)\right\}\right)\sin(\omega_i t)\right\rangle_{\omega_{lcut}} = \dfrac{\alpha}{2}\dfrac{\partial J}{\partial u_i}\cos(\omega_i T) \\ \left\langle J(t)\cos(\omega_i t)\right\rangle_{\omega_{lcut}} \equiv \left\langle J\left(\left\{\tilde{u}_j(t+T)\right\}\right)\cos(\omega_i t)\right\rangle_{\omega_{lcut}} = \dfrac{\alpha}{2}\dfrac{\partial J}{\partial u_i}\sin(\omega_i T) \end{cases} \tag{4.54}$$

where ω_{lcut} is the common cutoff frequency of low pass filters in the lock-in amplifier pairs for all N channels. ω_{lcut} is usually selected to be smaller than ω_{cut} as given in Equation (4.25), but larger than $1/T$. By combining the two formulae in Equation (4.54) we have

$$\omega_i T = k\pi + \tan^{-1}\frac{\left\langle J(t)\cos(\omega_i t)\right\rangle_{\omega_{lcut}}}{\left\langle J(t)\sin(\omega_i t)\right\rangle_{\omega_{lcut}}} \quad \text{for} \quad k = 0,1,2,\cdots \tag{4.55}$$

Then additional phase shift for demodulation signal for this channel can be selected as

$$\psi_i = (\omega_i T) \bmod (2\pi) \tag{4.56}$$

where "mod" indicates modulo operation. ψ_i is not yet unambiguous and can take either of two values that differ by π. The use of one of these two values result in metric maxi-

mization. The correct values for $\{\psi_i\}$ can be determined by a trial-and-error method, which requires only a maximum of $2N$ trials for a system with N beamlets. This method can speed up the phase search significantly. Using lock-in amplifiers, however, would increase the complexity of circuit implementation and has not yet been realized.

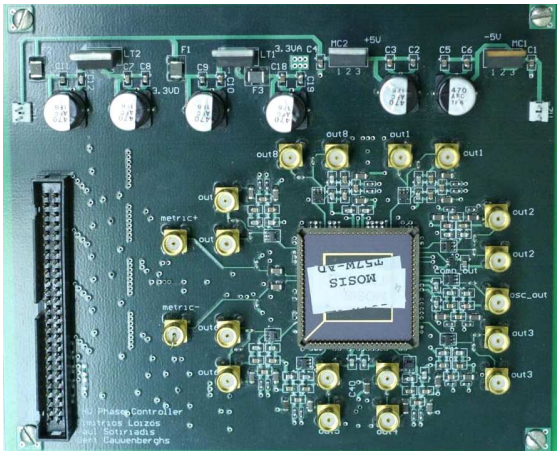

(a) Eight-channel multi-dithering controller based on customized mixed signal VLSI chip

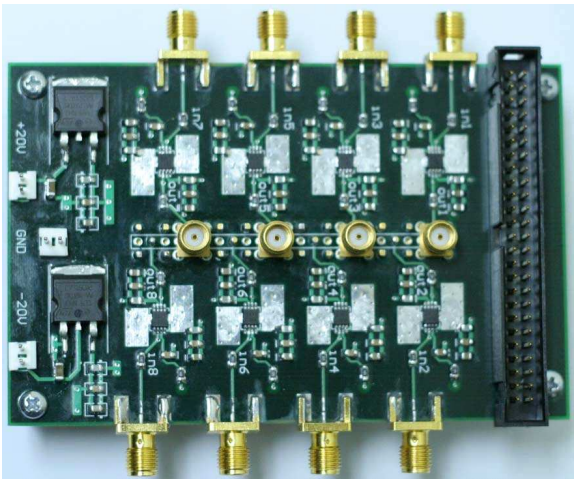

(b) Eight-channel voltage buffer (THS3001, 420MHz bandwidth) for control output voltages

Figure 4.5: Mixed signal VLSI multi-dithering controller developed at the Johns Hopkins University (2006).

Dither frequencies range: 100Hz~200MHz. Direct channel output dynamic range: 0.5~2.5V. Output dynamic range after amplification: ±15V. 2π-reset feature is implemented in this controller. Notes: (a) IDC50 connector is for interfacing to PC card (PCI-DAC6703). Power supplies are ±7V. Each output channel has two output terminals with 50Ω output impedance. There are two differential metric inputs terminals with 50Ω input impedance. (b) IDC50 connector is for interfacing to PC card (PCI-DDA08/12). All terminals have 50Ω impedance.

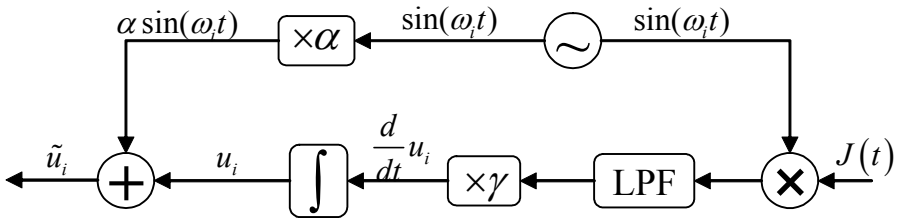

(a) Control channel implementation with synchronous detection

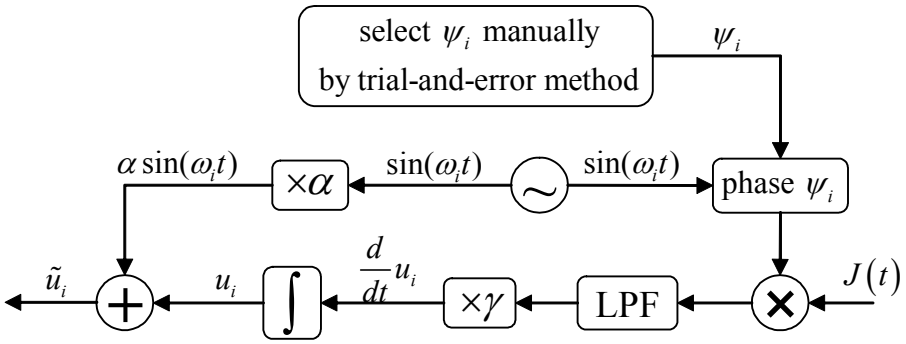

(b) Control channel implementation with trial-and-error method for introducing ψ_i

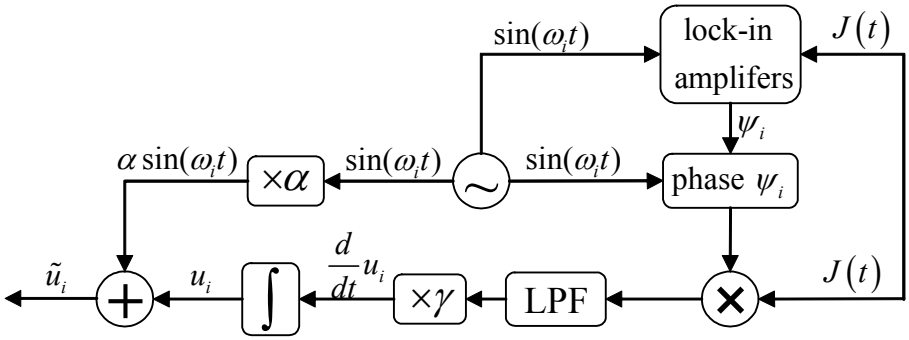

(c) Control channel implementation with improved trial-and-error method with lock-in amplifier pair for introducing ψ_i

Figure 4.6: Channel implementations in multi-dithering controller.

Notes: (a) synchronous detection is assumed; (b) round trip delay T is considered by introducing additional phase delay ψ_i to demodulation signal $\cos(\omega_i t)$ described in the caption of Figure 4.4 with trial-and-error method; (c) round trip delay T is considered by introducing additional phase delay ψ_i to demodulation signal $\cos(\omega_i t)$ with a pair of lock-in amplifiers. Methods using the trial-and-error method and the improved trial-and-error method with lock-in amplifier pair are addressed in text of this section.

4.8 Stochastic parallel gradient descent vs. multi-dithering: comparison

In the previous sections, stochastic parallel gradient descent (SPGD) and multi-dithering algorithms are discussed separately. In this section, a brief comparison of both approaches is provided. As indicated in Equations (4.2) and (4.3), both SPGD and multi-dithering algorithms estimate gradients of all control voltages in parallel, which is generally advantageous for the convergence speed over gradient descent algorithms, which estimate gradients in series. The SPGD algorithm is discrete in time, while the multi-dithering technique is continuous. This is from a practical point of view an advantage for the SPGD controller, because it can be implemented as software on PCs or firmware on digital electronic circuits, which makes debugging and improvement relatively easy, while the multi-dithering controller needs analog electronic circuits.

For estimating the gradients of the control voltages, the SPGD algorithm uses stochastic perturbations. More control channels can be added at the cost of convergence speed. The multi-dithering algorithm uses deterministic sinusoidal dithers at different frequencies for gradient estimations. In order to add more control channels, dither signals with higher frequencies need to be used. However, dither frequencies must satisfy Equations (4.31) and (4.32), which cause an upper limit for the total number of control channels N. Due to the nonsymmetrical nature of control channels with tags at different dither frequencies, contributions from individual control channels to the metric can be determined in multi-dithering systems. This feature could be used for optimizing of channel-specific control parameters.

Unknown or varying round trip delays T in target-in-the-loop applications can be a serious problem for the multi-dithering control approach as discussed in Section 4.7. The optimizing mode (maximizing or minimizing system metric $J(t)$) cannot be determined using the multi-dithering algorithm itself, but requires an external supervisory control loop that implements an trial-and-error method for determining the required additional phase shifts $\{\psi_i\}$ for the sinusoidal demodulation signals $\{\sin(\omega_i t)\}$. Since frequent, potentially time-consuming parameter searches are not feasible, multi-dithering controllers can work well only in stationary or quasi-stationary target-in-the-loop applications. The optimizing mode of SPGD algorithm is relatively insensitive to roundtrip time delay T as long as it is shorter than the time between subsequent control parameter perturbations, because the perturbed control voltages are held at discrete constant values instead of continuously varying values in this period T. If the round trip delay T becomes larger than the perturbation period, the timing sequences of SPGD algorithm is no longer valid. Hence, the iteration rate of SPGD algorithm cannot be made arbitrarily high. For the two implemented microprocessor-based SPGD controllers described in Section 4.4, perturbation periods can be as short as ~5 μs, which is equivalent to free-space beam round trip propagation distance of ~1.5km. In order to accommodate for larger propagation distance in target-in-the-loop (TIL) applications, the SPGD iteration rate need be slowed down. If the round trip delay T is negligibly small in localized applications, then iteration rate of SPGD controller can be made correspondingly higher.

If the round trip delay T is known all times or is at a fixed value for a given application setup, then the multi-dithering controller has an obvious advantage over SPGD controller:

In the state-of-the-art controller implementations described in Sections 4.4 and 4.7, the dither frequencies of the multi-dithering controller based on mixed signal VLSI technology can be made much larger (up to 200MHz) than the iteration rate of the SPGD controller based on microprocessors (up to ~180,000 iterations per second). When both controllers work properly, the compensation bandwidth of the multi-dithering controller is thus expected to be much higher than that of the SPGD controller.

Chapter 5 Experimental demonstration of phase-locking compensation with fiber-based experimental setup

Beam combining using conformal adaptive phase-locked fiber collimator arrays described in Sections 3.1 and 3.2 requires precise optical alignment of all subapertures. This involves sub-micrometer precision making the overall task challenging and time consuming. In order to overcome this difficulty, a first set of experiments to demonstrate phase-locking feasibility is performed without any free-space propagation; the testbeds used are equipped with optical fibers to realize all wave propagations. This chapter is organized as follows. A simplified fiber-based beam combining testbed is described in Section 5.1. In Section 5.2, beam combining and phase locking issues are addressed. Section 5.3 introduces an advanced fiber-based beam combining testbed for beam counter-propagation. In Section 5.4, the reciprocity principle in beam combining (see Section 3.6) is illustrated experimentally. Finally, the technical feasibility of phase-locking control for an optical communication link with intensity modulation is investigated in Section 5.5.

5.1 Basic fiber-based experimental setup for beam combining

In this section, a simplified version of the fiber-based testbed for coherent beam combining as shown in Figure 3.11 is described. The basic testbed is shown in Figure 5.1 and Figure 5.2. A DFB diode laser with a linewidth of 5MHz and a polarization-maintaining fiber-coupled linearly-polarized output is used. Then a dual-stage polarization-maintaining optical isolator is connected to the source laser through a polarization-maintaining fiber. After the optical isolator, a 1×8 integrated lithium niobate polarization-maintaining phase modulator array is connected through a polarization maintaining fiber. After necessary amplification, the control voltage from the phase-locking controller

is fed to the specific phase shifter. The output polarization-maintaining fibers are connected to a similar 8×8 polarization-maintaining phase modulator. The 8×8 phase modulator is used to simulate phase distortions. Although modeling of atmospheric aberrations in this way is far from accurate, it is good enough to experimentally demonstrate the technical feasibility of phase locking. A distortion generator array is composed of eight independent sinusoidal signal generators. The eight optical fiber outputs are then combined by an integrated polarization-maintaining beam combiner. The beam combiner is used to replace the receiver aperture or the target in the free-space adaptive optics architecture. After combination, the light goes to a photo detector, from which the system performance metric (the power of the received signal) is obtained for the feedback control. The phase-locking controllers described in Section 4.4 and Section 4.7 are implemented and tested separately using this all-fiber configuration testbed.

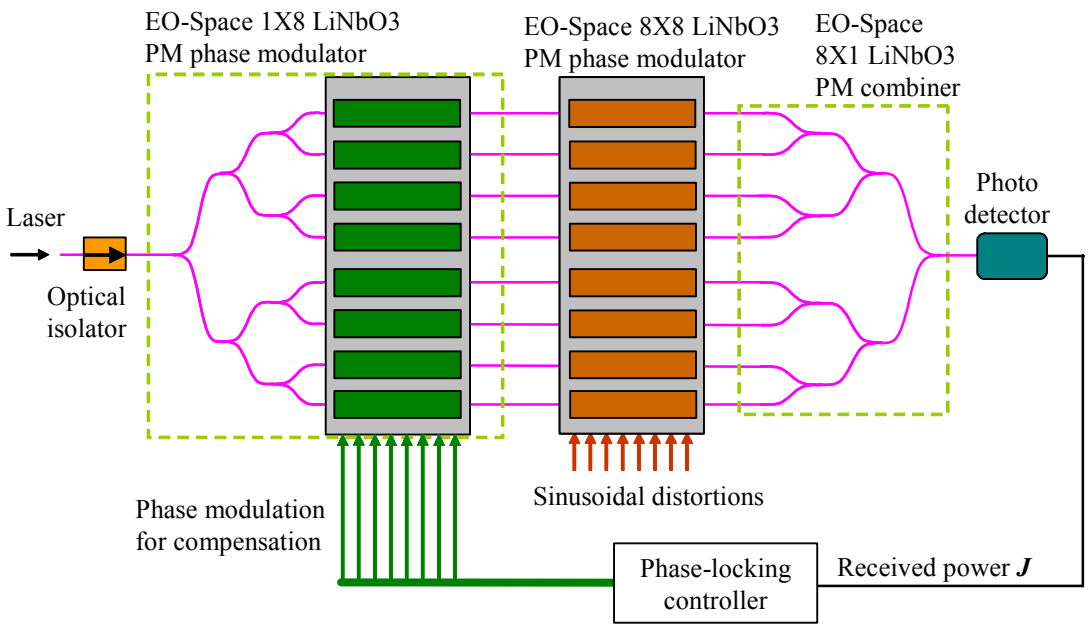

Figure 5.1 Schematic of the basic fiber-based testbed with phase-locking compensation

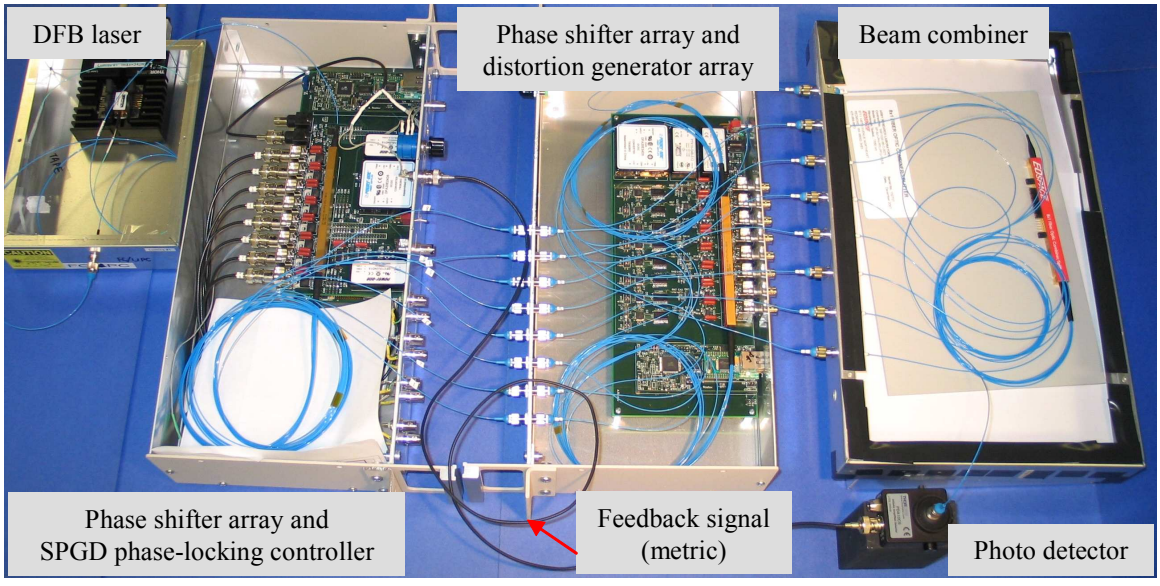

Figure 5.2: Picture of the basic fiber-based testbed with phase-locking compensation

5.2 Phase-locking experiments with basic fiber-based setup

In this section, experiments of phase-locking compensation for coherent beam combining with the basic all-fiber testbed given in the previous section are described. Three different phase-locking controllers are tested. These controllers are the PC-based SPGD controller, the AVR microprocessor-based SPGD controller and the multi-dithering controller based on mixed-signal VLSI technology. These phase-locking controllers are described in Section 4.4 and Section 4.7.

The computer-based software SPGD controller works in the following manner. The system performance metric obtained through a photo detector is fed into the SPGD controller through a built-in A/D converter board (PCI-DAS1602/12). The SPGD control algorithm generates update control voltages, and then outputs the voltages through a built-in D/A converter board (PCI-DDA08/12). The control voltage signals are amplified by multi-channel amplifiers with tunable gains. The gains are usually tuned to about 2~5 to keep the phase-locking system working in a stable and efficient manner. After amplification, the analog control voltages are applied to the 1×8 polarization maintaining phase modulator to compensate for phase distortions introduced by the simulated atmospheric aberrations introduced by the 8×8 phase modulator. The CPU speed of the computer in use is 3.4GHz.

Figure 5.3 shows transition curves from a destructive interference state (minimization) to a constructive interference state (maximization) of the system performance metric using the computer-based SPGD controller. The average curve (circle-dotted blue curve) is obtained by averaging over 2000 real-time transition curves. The normalized metric for a

specific curve or the average curve is the ratio of the specific real-time curve or the average curve to the global maximum in all the real-time metric samples in this experiment. A few selected real-time transition curves are shown as well (thin solid curves). The average transition time is ~7.81ms. On average, the number of iterations for seven channels needed for convergence is ~125. The number of iterations per channel needed for convergence is ~17.8. The iteration rate of the PC-based SPGD controller is about 16,000 iterations per second.

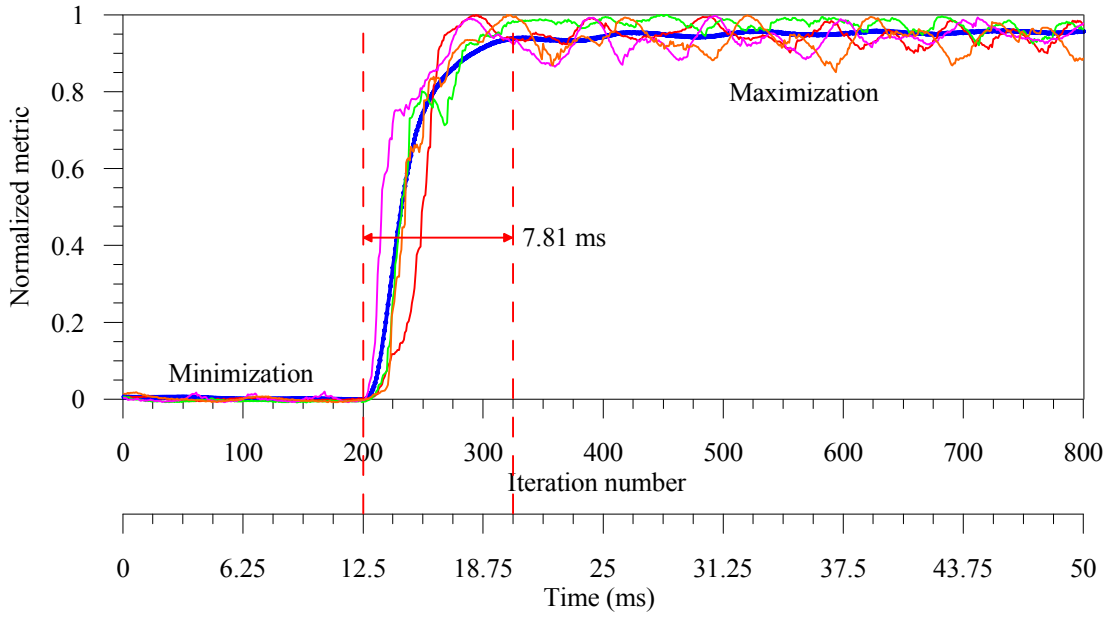

Figure 5.3: Transition curves from a destructive interference state (minimization) to a constructive interference state (maximization) of the system performance metric using computer-based SPGD controller.

The average curve (circle-dotted blue curve) is obtained by averaging over 2000 real-time transition curves. A few selected real-time transition curves are shown as well (thin solid curves). The average transition time is ~7.81ms. On average, the number of iterations for seven channels needed for convergence is ~125. The number of iterations per channel needed for convergence is ~17.8. The iteration rate of the PC-based SPGD controller is about 16,000 iterations per second.

A performance metric degradation curve with respect to the distortion frequencies for seven-channel fiber array phase-locking system is shown in Figure 5.4. To acquire this curve, the distortion magnitudes for all channels are fixed at 1.55V corresponding to π-radian phase shift for the phase shifter array for simulating atmospheric turbulence. The distortion frequencies are increased from dc to ~2000Hz. The curve shows that phase locking compensation system using the PC-based SPGD controller has a compensation bandwidth about 100Hz where the normalized metric is 0.80, a compensation bandwidth about 300Hz where the normalized metric is 0.50, and a compensation bandwidth larger than 2000Hz where there is any improvement of normalized metric from its incoherent combining state of normalized metric $\frac{1}{N} = \frac{1}{7} \approx 0.14$.

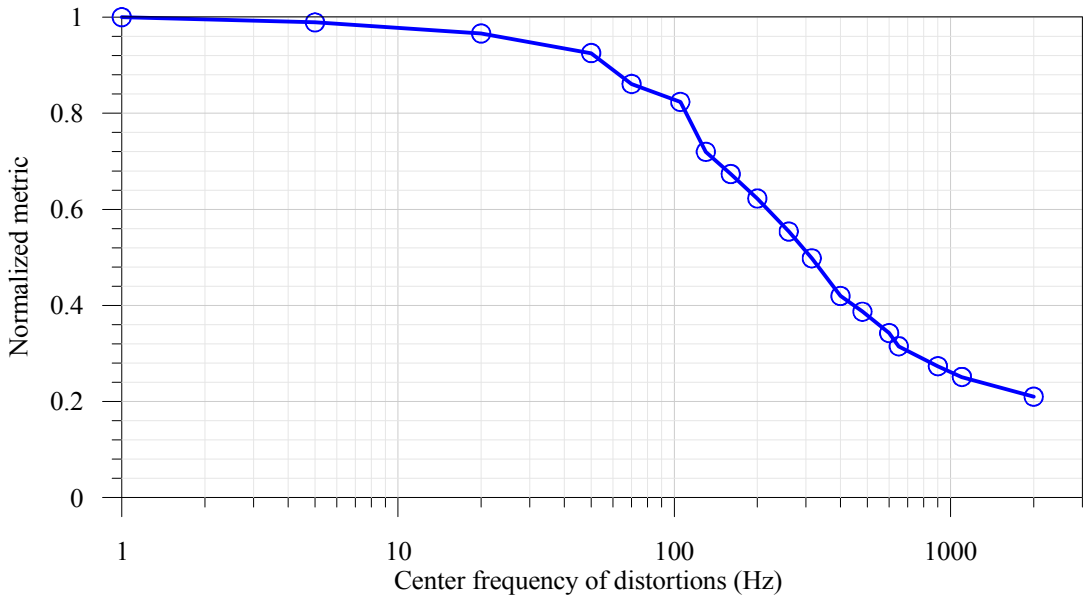

Figure 5.4: System metric degradation curve with respect to distortion frequencies for seven-channel fiber array phase-locking system using computer-based SPGD controller.

The distortion magnitudes for all channels are fixed at π-radian phase shift. The phase-locking compensation bandwidth is 100Hz where normalized metric is 0.80.

To verify the gain effect of coherent beam combining over incoherent beam combining as shown in Equation (2.50), the following experiment is performed. First, the output powers of all seven individual fiber channels are measured individually. For a given number of control channels, the following steps are taken. Sum the measured values, channel by channel algebraically, which results in the so-called "incoherent combining" power (not real combining, but algebraic sum). See the data points on the pink curve in the upper part of Figure 5.5. The small discrepancies between these calculated gains and ideal gains are mainly due to different power losses between different fiber channels.

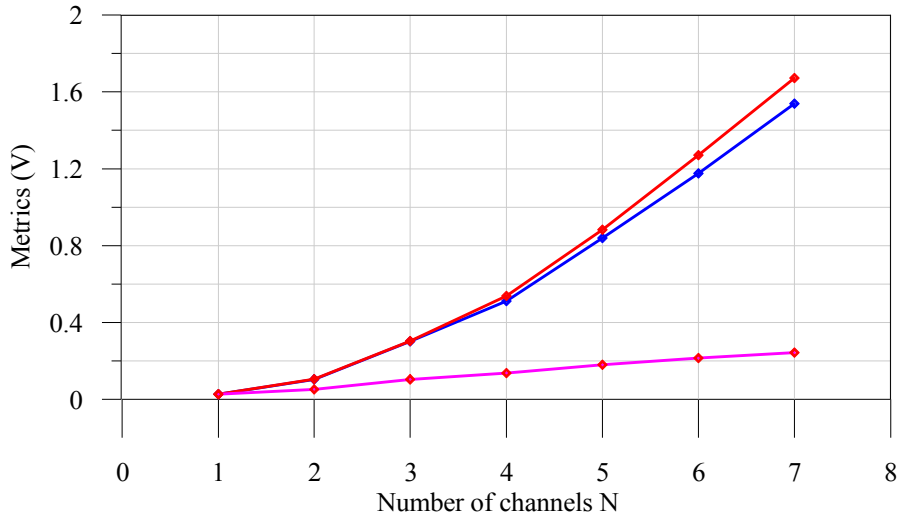

(a) Calculated incoherent metric, calculated coherent metric, and measured coherent metrics vs. number of control channels for constructive interference

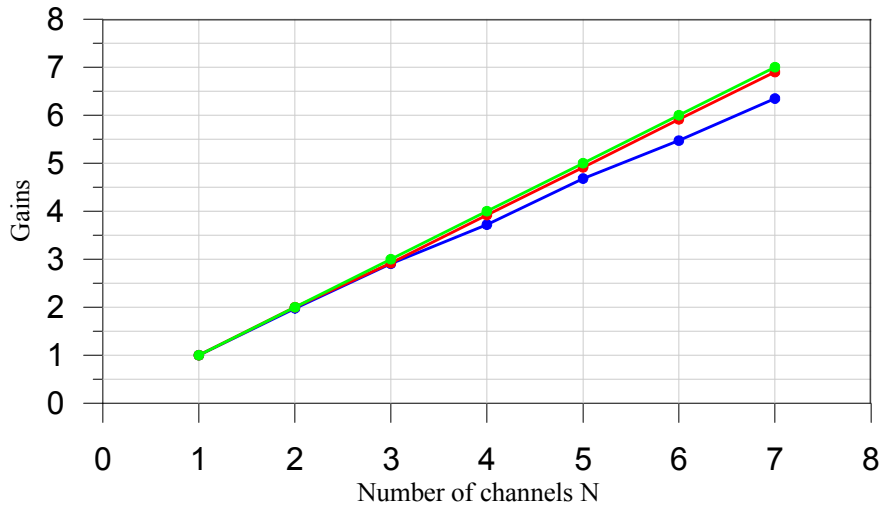

(b) Calculated gains, measured gains and ideal gains vs. number of control channels

Figure 5.5: Gain effect of all-fiber coherent beam combining over incoherent beam combining.

(a) Calculated incoherent combined powers (pink), calculated coherent combined powers (red), measured coherent combined powers (blue). (b) Calculated gains (red), measured gains (blue), ideal gains (green).

The all-fiber phase-locking experiment is also performed with the AVR microprocessor-based SPGD controller (see Figure 4.2). The performance metric degradation curve with respect to distortion frequencies for the seven-channel fiber array phase-locking system is shown in Figure 5.6.

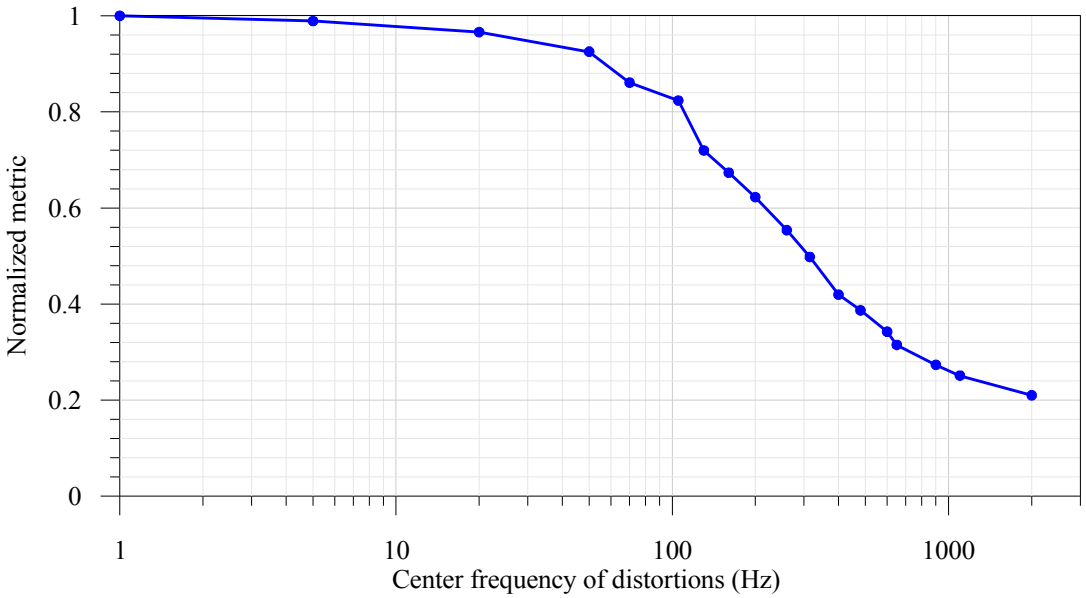

Figure 5.6: System metric degradation curve with respect to the distortion frequencies for the seven-channel fiber array phase-locking system using the AVR microprocessor based SPGD controller. The distortion magnitudes for all channels are fixed at π-radian phase shift. The phase-locking compensation bandwidth is 200Hz where the normalized metric is 0.80.

It can be seen that the compensation bandwidth using AVR microprocessor-based SPGD controller shown Figure 5.6 is approximately three times as large as the compensation bandwidth using the PC-based SPGD controller. The improvement of compensation bandwidth is due to the increase of the iteration rate. The iteration rate of the AVR microprocessor-based SPGD controller is about 95,000 iterations per second. The iteration rate of the PC-based software SPGD controller is about 16,000 iterations per second. The ratio of the two iteration rates is approximately six. In the PC-based software SPGD controller, adaptive control parameters such as adaptive update gain and adaptive

troller, adaptive control parameters such as adaptive update gain and adaptive perturbations are used. In the AVR microprocessor-based SPGD controller, constant control parameters are not used. This is a good reason why compensation bandwidth improvement factor is smaller than the ratio of the iteration rates.

The all-fiber phase-locking experiment is also performed with the multi-dithering controller based on mixed-signal VLSI technology (see Figure 4.5). Only three fiber channels are used for the phase-locking experiment here. A couple of examples of comparison for phase-locking control-off state and phase-locking control-on state are given in Figure 5.7. Three fiber channels are used in the setup as shown in Figure 5.2. The photo detector PDA-400 is replaced with PDA-10CF that has a bandwidth of 150MHz to accommodate for faster dither frequencies of the multi-dithering controller. In the upper part of Figure 5.7, three phase distortions are sinusoidal with frequencies 290kHz, 295kHz and 300kHz. The distortion amplitudes correspond to 0.5π-radian phase shifts. The dither frequencies of three control channels are 41MHz, 63MHz and 88MHz. Two instantaneous phase-locking control-off states and one instantaneous phase-locking control-on state of metric signal are given for this example. In the lower part of Figure 5.7, three phase distortions are triangular with frequencies 110kHz, 115kHz and 120kHz. Distortion amplitudes correspond to π-radian phase shifts. The dither frequencies of three control channels are 41MHz, 63MHz and 88MHz. Two instantaneous phase-locking control-off states and one instantaneous phase-locking control-on state of metric signal are given for this example. These two examples indicate system performance metric degradation that when distortion amplitudes increase, phase-locking compensation bandwidths decrease. The examples also show that the phase-locking compensation bandwidth can be up to hundred kilo-

hertz. The much larger phase-locking compensation bandwidth of this multi-dithering controller than that of the two previous SPGD controllers is due to its much higher dithering frequencies in the range of tens of megahertz. In general, the multi-dithering controller can be used to do the phase-locking control. This specific hardware implementation, however, need be improved further.

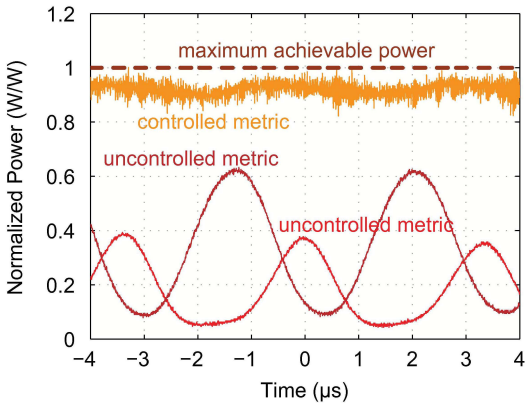

(a) Three phase distortions are sinusoidal with frequencies 290kHz, 295kHz and 300kHz; distortion amplitudes correspond to 0.5π-radian phase shifts; the dither frequencies of three control channels are 41MHz, 63MHz and 88MHz.

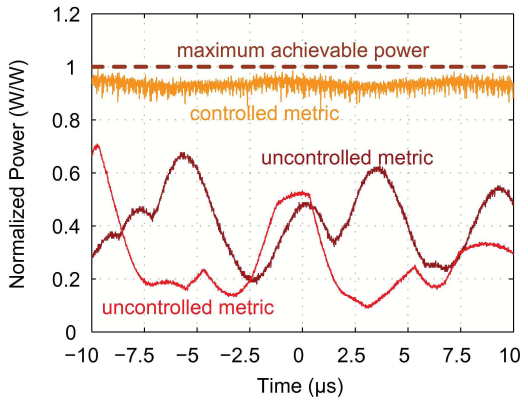

(b) Three phase distortions are triangular with frequencies 110kHz, 115kHz and 120kHz; distortion amplitudes correspond to π-radian phase shifts; the dither frequencies of three control channels are 41MHz, 63MHz and 88MHz.

Figure 5.7 Compensation effect of all-fiber phase-locking using VLSI multi-dithering controller.

Three fiber channels are used in the testbed as shown in Figure 5.2. The photo detector PDA-400 is replaced with PDA-10CF that has a bandwidth of 150MHz. Two instantaneous phase-locking control-off states and one instantaneous phase-locking control-on state of metric signal are given for each example. (Experimental work performed in collaboration with Loizos et al. as shown in [107, 109])

5.3 Fiber-based beam combining setup for counter-propagating beams

In this section, an advanced fiber-based beam combining testbed is described. This testbed is similar to the basic testbed as described in Section 5.1 and can be used to demonstrate phase-locking compensation for coherent beam combining. This testbed is better characterized than the basic testbed in beam polarization extinction ratio (PER), polarization crosstalk elimination, optical intensity balancing between different channels through intensity control and lower optical power losses. In addition, this testbed is intentionally designed and implemented for phase-locking experiments with counter-propagating transmitting and receiving. Application of the reciprocity principle in phase-locking compensation for counter-propagating beams through identical propagation paths is addressed in Section 5.4.

The testbed is shown in Figure 5.8. All pink lines in the schematic indicate polarization-maintaining fibers for C-band with the electric field vector of optical beams aligned to the slow axes of the fibers. The first part of the testbed is the transmitting optical link originating from a DFB laser diode (denoted as LD#1). This DFB laser diode has a nominal wavelength 1549.72nm, a spectral linewidth 1MHz, output optical power rating 80mW, and >20dB polarization extinction ratio. The DFB laser diode is driven by laser diode controller LDC205 and temperature controller TED200. The output of the transmitting laser diode is fed into a 1×2 50/50 fiber coupler. One output of the 50/50 fiber coupler is fed into port #1 and routed to port #2 of a fiber circulator. The output from port #2 of the circulator is fed to a 1×8 lithium-niobate fiber-coupled beam splitter with integrated phase modulation and intensity control for each channel. This 1×8 beam splitter has a

halfwave voltage $V_{\pi}^{phc} = 3.10\text{V}$ for each phase shifter and a halfwave voltage $V_{\pi}^{amp} = 4.10\text{V}$ for each Mach-Zehnder interferometer. The bias control voltage point of maximum intensity for each Mach-Zehnder interferometer is built to be $\pm 2\text{mV}$ around ground level. The insertion losses of these channels are within the range from 12.2dB to 12.6dB. This 1×8 beam splitter can be used to precompensate relative phase mismatches and optical intensity mismatches for all eight beams. Phase-locking compensation is performed by the SPGD controller (Figure 4.3) based on Atmel 32-bit ARM-based microcontroller AT91SAM9260. Then the eight outputs of the 1×8 beam splitter are fed into the eight inputs of an 8×8 lithium-niobate phase shifter array that has halfwave voltage $V_{\pi}^{phd} = 1.70\text{V}$ for each channel. This 8×8 phase shifter array modulated with sinusoidal generator array is used to simulate atmospheric turbulence as described in Section 5.1. The eight optical outputs of the 8×8 phase shifter array are combined by an 8×1 fiber-coupled beam combiner. The output of 8×1 fiber-coupled beam combiner is fed to port #2 and routed to port #3 of a second but identical fiber circulator then to a photo detector PD#1 (PDA-10CS, Thorlabs). The output voltage of this photo detector PD#1 is denoted as $J1$ and recognized as transmitting system performance metric. The 1×8 beam splitter with integrated phase modulation and amplitude control, the 8×8 phase shifter array and the 8×1 fiber combiner are developed at EO-Space Inc.

The second part is the receiving optical link. As shown in Figure 5.8, the counter-propagating receiving beam originates from a DFB laser LD#2 that has the same optical characteristics such as nominal wavelength, spectral linewidth, output optical power rating, and polarization extinction ratio as laser diode LD#1. By counter-propagating

through the same optical path, the receiving beam is split and then combined and then fed to photo detector PD#2 that is identical to PD#1. The output voltage of this photo detector PD#2 is denoted as $J2$ and recognized as receiving system performance metric. For convenience, the output powers of the two laser sources are tuned such that the transmitting metric $J1$ and the receiving metric $J2$ are roughly identical when they are used as feedback signal of the SPGD phase-locking controller and maximized, respectively. The third part is mainly composed of an optical spectrum analyzer Agilent 86143B and a 1×2 fiber coupler. This fiber coupler is not necessarily to be polarization-maintaining. Ordinary single-model fiber coupler is okay. This part is used to monitor the optical spectra of the two laser sources LD#1 and LD#2. In this monitoring part, only wavelengths of the two laser sources are of concerns.

Although the two laser sources LD #1 and LD #2 are nominally identical, they do not necessarily have identical wavelengths simultaneously because they are two independent laser sources. Denote the vacuum wavelength of LD #1 as λ_1 and the vacuum wavelength of LD #2 as λ_2. Denote the their nominal vacuum wavelength as

$$\lambda \approx \lambda_1 \approx \lambda_2 \tag{5.1}$$

Denote the wavelength difference between the two laser sources as

$$\delta\lambda = \lambda_1 - \lambda_2 \tag{5.2}$$

To make the following description more general, the number of total channels is denoted by N. For all $N = 8$ channels, they do not have exactly equal optical path lengths that are denoted as $l_1 \cdots l_N$. For convenience of description, $\{\bullet\}$ is used to represent an ensem-

ble. For example, $\{l_i\}$ represents $l_1 \cdots l_N$. The transmitting metric and the receiving metric can be respectively written as

$$\begin{cases} J1(t) = A_1^2 \left(N + \sum_{1 \le i \ne k \le N} \cos\left[\Phi_{i1}(t) - \Phi_{k1}(t) \right] \right) \\ J2(t) = A_2^2 \left(N + \sum_{1 \le i \ne k \le N} \cos\left[\Phi_{i2}(t) - \Phi_{k2}(t) \right] \right) \end{cases} \tag{5.3}$$

where A_1 is the identical complex amplitude for all N transmitting beamlets, A_2 is the identical complex amplitude for all N receiving beamlets, $\{\Phi_{i1}(t)\}$ are the relative phases of N transmitting beamlets and $\{\Phi_{i2}(t)\}$ are the relative phases of N receiving beamlets. These phase terms can be further written as

$$\begin{cases} \Phi_{i1}(t) = 2\pi \left[\dfrac{u_i(t)}{2V_\pi^{phc}} + \dfrac{\Delta_i(t)}{2V_\pi^{phd}} + \dfrac{nl_i}{\lambda_1} \right] \\ \Phi_{i2}(t) = 2\pi \left[\dfrac{u_i(t)}{2V_\pi^{phc}} + \dfrac{\Delta_i(t)}{2V_\pi^{phd}} + \dfrac{nl_i}{\lambda_2} \right] \end{cases} \tag{5.4}$$

where $\{u_i(t)\}$ are the N phase-locking control voltages, $\{\Delta_i(t)\}$ are the N distorting voltages, V_π^{phc} is the halfwave voltage of 1×8 phase shifter array for compensation, V_π^{phd} is the halfwave voltage of the 8×8 phase shifter array for simulating atmospheric turbulence and n is the nominal refractive index of glass fiber. The negligible difference of V_π^{phc} (or V_π^{phd}) for the two wavelengths λ_1 and λ_2 due to wavelength dependence as shown by Equations (3.7) and (3.8) do not affect much in phase-locking compensation experiments for counter-propagating beams and are assumed to be independent of wave-

lengths around 1550nm. The differences of the optical path lengths $\{l_i\}$ are of major concerns due to interference between different channels and are written as

$$l_{ik} = l_i - l_k \tag{5.5}$$

for $1 \le i \ne k \le N$. The transmitting metric and the receiving metric can be further written as

$$\begin{cases} J1(t) = A_1^2 \left(N + \sum\limits_{1 \le i \ne k \le N} \cos\left[2\pi \left(\dfrac{u_i(t) - u_k(t)}{2V_\pi^{phc}} + \dfrac{\Delta_i(t) - \Delta_k(t)}{2V_\pi^{phd}} + \dfrac{nl_{ik}}{\lambda_1} \right) \right] \right) \\ J2(t) = A_2^2 \left(N + \sum\limits_{1 \le i \ne k \le N} \cos\left[2\pi \left(\dfrac{u_i(t) - u_k(t)}{2V_\pi^{phc}} + \dfrac{\Delta_i(t) - \Delta_k(t)}{2V_\pi^{phd}} + \dfrac{nl_{ik}}{\lambda_2} \right) \right] \right) \end{cases} \tag{5.6}$$

It can be seen that these two metrics can be made correlated in phase by tuning wavelengths of the two laser diodes. Either of them can be used as the feedback signal for phase-locking controller. Without loss of generality, the receiving metric $J2$ is selected as the feedback signal. When the N receiving beamlets are constructively phase-locked such that phase terms in $J2$ vanish, the receiving metric

$$J2 = A_2^2 N^2 \tag{5.7}$$

The transmitting metric is

$$\begin{aligned} J1 &= A_1^2 \left(N + \sum_{1 \le i \ne k \le N} \cos\left[2\pi n l_{ik} \left(\frac{1}{\lambda_1} - \frac{1}{\lambda_2} \right) \right] \right) \\ &\approx A_1^2 \left(N + \sum_{1 \le i \ne k \le N} \cos\left[2\pi \left(\frac{nl_{ik}}{\lambda^2} \right) \delta\lambda \right] \right) \end{aligned} \tag{5.8}$$

It can be seen that transmitting metric $J1$ is the sum of the dc term and periodic functions of $\delta\lambda$. Consider the case $N = 2$. Transmitting metric $J1$ can be written as

$$J1(\delta\lambda) \approx 2A_1^2\left(1+\cos\left[2\pi\left(\frac{nl_{12}}{\lambda^2}\right)\delta\lambda\right]\right) \tag{5.9}$$

By sweeping $\delta\lambda$, a plot of period function $J1$ versus $\delta\lambda$ can be obtained. The pitch of this periodic function is equal to $\frac{\lambda^2}{nl_{12}}$. This is a potential method to estimate optical path length mismatches of different fiber channels in a pairwise manner.

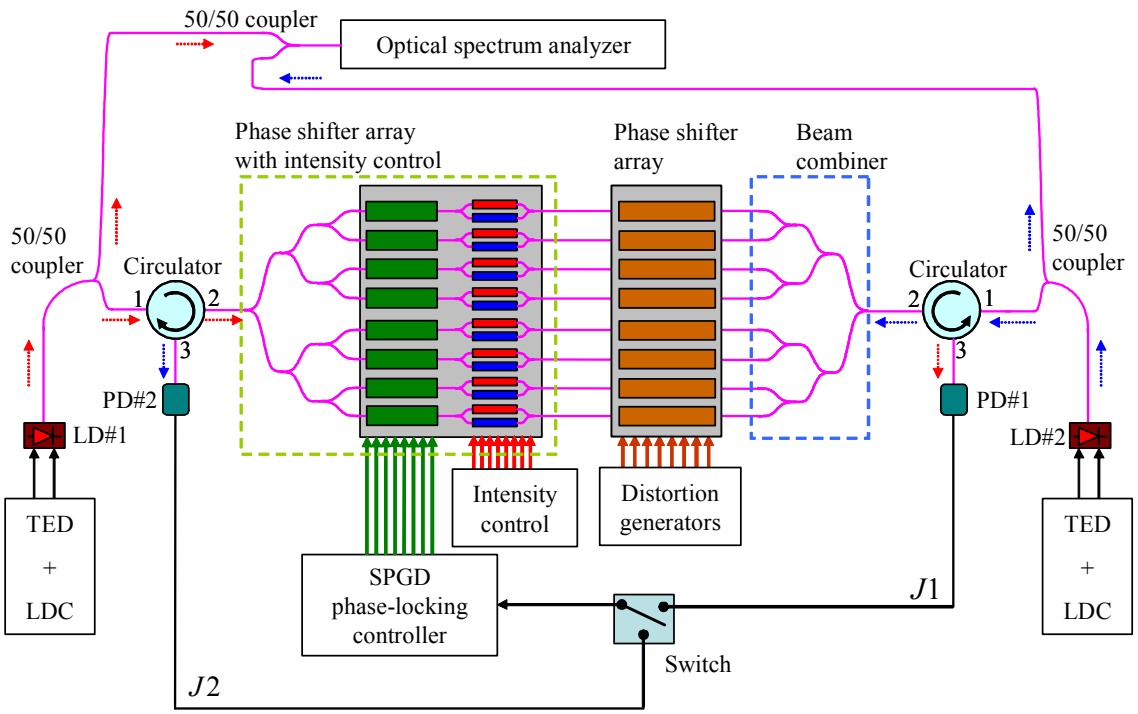

Figure 5.8: Advanced fiber-based phase-locking testbed with counter-propagating beams.

Both DFB laser sources LD #1 for transmitting beamlets (indicated by red dotted arrows) and LD #2 for receiving beamlets (indicated by blue dotted arrows) have nominal wavelength 1549.72nm, spectral linewidth 1MHz, output optical power rating 80mW, and >20dB polarization extinction ratio. Both laser diodes are controlled by Thorlabs LDC205 and TED200, respectively. Either transmitting or receiving optical propagation path includes a 50/50 fiber coupler, a fiber circulator, a 1×8 fiber splitter with integrated phase shifters and intensity controls for phase-locking compensation, an 8×8 phase shifter array for simulating atmospheric turbulence, a 1×8 fiber combiner, a circulator and a photo detector PDA-10CS. All fibers are polarization-maintaining fibers. SPGD phase-locking controller is shown in Figure 4.3. Wavelengths of both laser sources are monitored by Agilent 86143B optical spectrum analyzer.

5.4 Application of reciprocity principle in phase-locking compensation

In phase-locking compensation experiments performed on the testbed as shown in Figure 5.8, there are counter-propagating transmitting beamlets and receiving beamlets. In this research, the reciprocity principle means that when either transmitting metric or receiving metric is optimized (maximized or minimized), the other is optimized in the same manner simultaneously. Before the feasibility investigation of application of the reciprocity principle, the compensation bandwidth of phase-locking experiments performed on testbed as shown in Figure 5.8 using the SPGD controller based on Atmel 32-bit ARM-based microcontroller AT91SAM9260 as shown in Figure 4.3 is given in Figure 5.9. Figure 5.9(a) and Figure 5.9(b) are plotted in different ways from the same set of data points. Each data point of the compensation bandwidth is for normalized metric 0.50. Figure 5.9(a) shows curves of the compensation bandwidth vs. amplitude of sinusoidal distortions for a given number of control channels from two to eight. It can be seen that for a given number of control channels, the phase-locking compensation bandwidth decreases as distortion amplitude increases. For the same distortion amplitude, the compensation bandwidth decreases as the number of control channels increases. This is shown in Figure 5.9(b). By comparing the measured compensation bandwidth with characteristic frequencies of typical atmospheric turbulence as stated in Section 4.1, we claim that the SPGD controller as shown in Figure 4.3 is sufficiently fast for phase-locking compensation.

As described in Section 5.3, the feasibility of application of the reciprocity principle in phase-locking compensation for counter-propagating beams depends on the transmitting and receiving wavelengths and their difference. Both the transmitting and receiving laser sources are characterized. Characteristics of wavelength vs. temperature control resis-

tance for the two laser diodes are given in Figure 5.10. The driving currents for these two laser diodes are fixed. Driving current 47mA for transmitting laser diode and driving current 100mA for receiving laser diode are selected such that the detected phase-locked transmitting metric and receiving metric are roughly equal when their wavelength difference is zero and different power losses along optical paths are considered. An arbitrary available wavelength 1549.495nm is selected as the matched working point of the transmitting and receiving wavelengths. At wavelength 1549.495 with given driving currents, the temperature control resistance is 11.443KΩ for the transmitting laser diode and is 11.619KΩ for the receiving laser diode. Characteristics of wavelength vs. driving current for the two laser diodes are given in Figure 5.11. The temperature control resistance is fixed at 11.443KΩ for the transmitting laser diode. The temperature control resistance is fixed at 11.619KΩ for the receiving laser diode. It can be seen that wavelength of a DFB laser diode can be tuned through a variation of temperature control resistance or driving current. A variation of the driving current also introduces a variation of output optical power. In the following experiments for the feasibility investigation of application of the reciprocity principle, wavelength tuning of the transmitting laser diode is performed through variation of the temperature control resistance while keeping driving current unchanged. Wavelength of the receiving laser diode is fixed at 1549.495nm by keeping temperature control resistance and driving current unchanged during the measurement.

Typical waveforms of instantaneous samples of transmitting metric (blue), receiving metric (yellow) and their difference (red) are given in Figure 5.12. The receiving metric is used as the feedback signal for the phase-locking compensation system. The sinusoidal

distortion amplitude for all channels corresponds to π-radian phase shift. Distortion frequencies are 7, 37, 67, 97, 127, 157, 187, and 217 hertz for eight channels, respectively. The iteration rate of the SPGD controller is ~100,000 iterations per second. The case with a wavelength deviation $\delta\lambda = 0$ is shown in Figure 5.12(a, c, e) for phase-locking control ON (maximizing), phase-locking control OFF and phase-locking control ON (minimizing), respectively. The transmitting metric is optimized and fluctuates along with the receiving metric in the same manner. The case with a wavelength deviation $\delta\lambda = 25\text{pm}$ is shown in Figure 5.12(b, d, f) for phase-locking control ON (maximizing), phase-locking control OFF and phase-locking control ON (minimizing), respectively. With the given transmitting laser wavelength deviation, the transmitting metric is optimized along with the receiving metric in the same manner but has relatively smaller average value. The degradation of the transmitting metric is due to the uncompensated residual phases as shown in Equation (5.8). Two factors contribute to the uncompensated residual phases for the transmitting beamlets, the wavelength deviation $\delta\lambda$ and the optical path length difference l_{ik} for $1 \le i \ne k \le N$.

Experiments as described above are performed by sweeping the transmitting laser wavelength in a certain range. The receiving laser wavelength is fixed at 1549.495nm. The transmitting laser wavelength is swept from 1549.495nm to 1549.375nm by tuning the temperature control resistance from 11.443KΩ to 12.083KΩ. Equivalently, the wavelength deviation $\delta\lambda$ changes from zero to 120pm. This is shown in Figure 5.13. For each value of wavelength deviation $\delta\lambda$, the average and standard deviation of 2500 transmitting metric samples are plotted for three cases, six-channel beam combining, seven-channel beam combining and eight-channel beam combining. The results are shown in Figure 5.14. The local maxima of transmitting metric of these plots appear

Figure 5.14. The local maxima of transmitting metric of these plots appear "periodically" due to the periodic nature of terms as shown in Equation (5.8). The wavelength deviation between adjacent local maxima is about 35pm and is referred to as wavelength deviation pitch denoted as $(\delta\lambda)_p$. It is wanted for the transmitting metric to stay around the zeroth order maximum with $\delta\lambda = 0$. The uncompensated residual phase terms in Equation (5.8) must be much smaller less than 2π radians in order to get the transmitting metric less degraded and simultaneously optimized along with the receiving metric. Denote the maximum optical path length difference as

$$(\Delta l)_{\max} = \max_{1 \le i \ne k \le N} (l_{ik}) \tag{5.10}$$

With the measured wavelength deviation pitch $(\delta\lambda)_p$, $(\Delta l)_{\max}$ can be estimated as

$$(\Delta l)_{\max} \approx \frac{\lambda^2}{n(\delta\lambda)_p} \approx 46\text{mm} \tag{5.11}$$

with $\lambda = 1549.720\text{nm}$, $n = 1.50$ and $(\delta\lambda)_p \approx 35\text{pm}$. Equation (5.11) demonstrates that with a larger $(\Delta l)_{\max}$, $(\delta\lambda)_p$ must be smaller; with a smaller $(\Delta l)_{\max}$, $(\delta\lambda)_p$ must be larger. The wavelength deviation when the transmitting metric degrades by 50% is ~45pm for the given testbed. The wavelength deviation when the transmitting metric degrades to its incoherent state ($J1 = (1/N)$) is ~80pm for the given testbed.

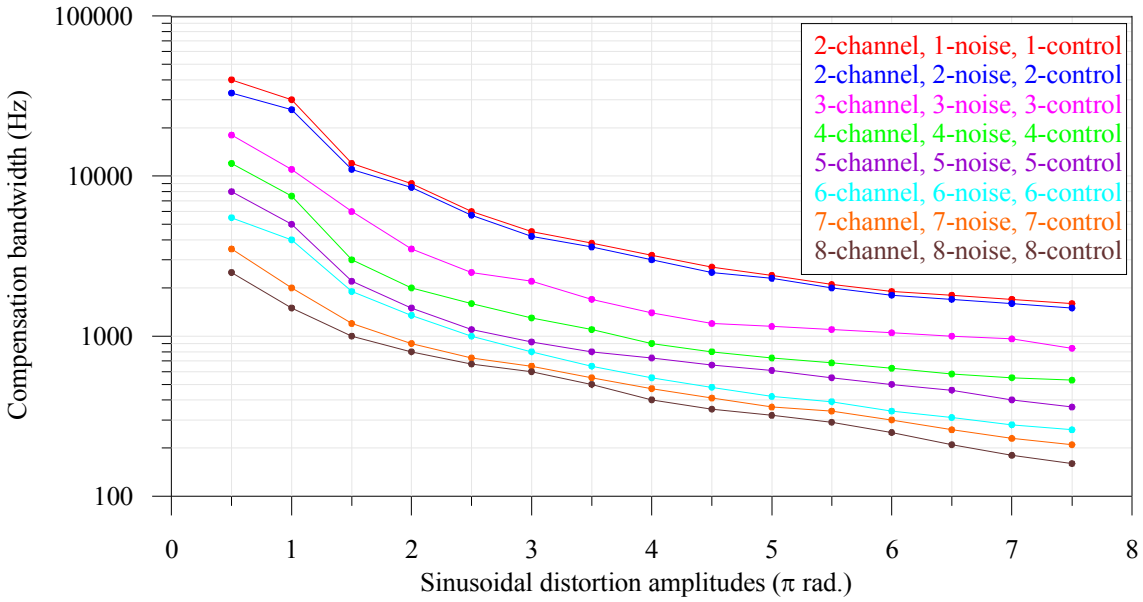

(a) compensation bandwidth vs. amplitude of sinusoidal distortions for a given number of control channels

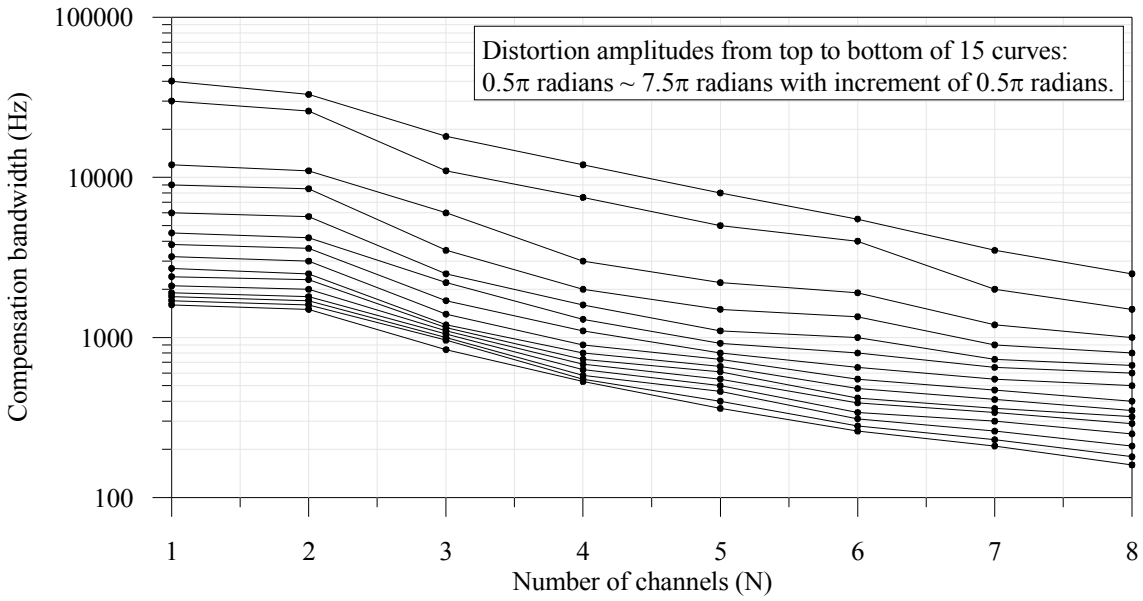

(b) compensation bandwidth vs. number of control channels for a given sinusoidal distortion amplitude

Figure 5.9: Compensation bandwidth of phase-locking experiments performed on testbed as shown in Figure 5.8 using the SPGD controller based on Atmel 32-bit ARM-based microcontroller AT91SAM9260 as shown in Figure 4.3.

Each data point of compensation bandwidth is for normalized metric 0.50. Notes: (a) and (b) are plotted in different ways from the same set of data points.

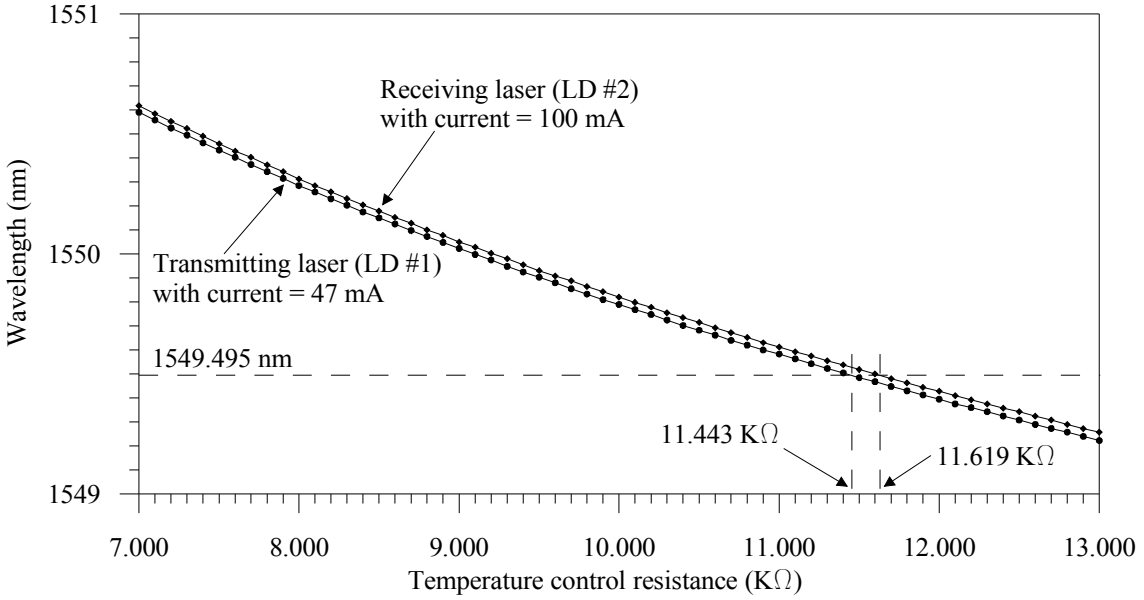

Figure 5.10: Characteristic curves of the transmitting and receiving laser diodes: wavelength vs. temperature control resistance with a fixed given driving current.

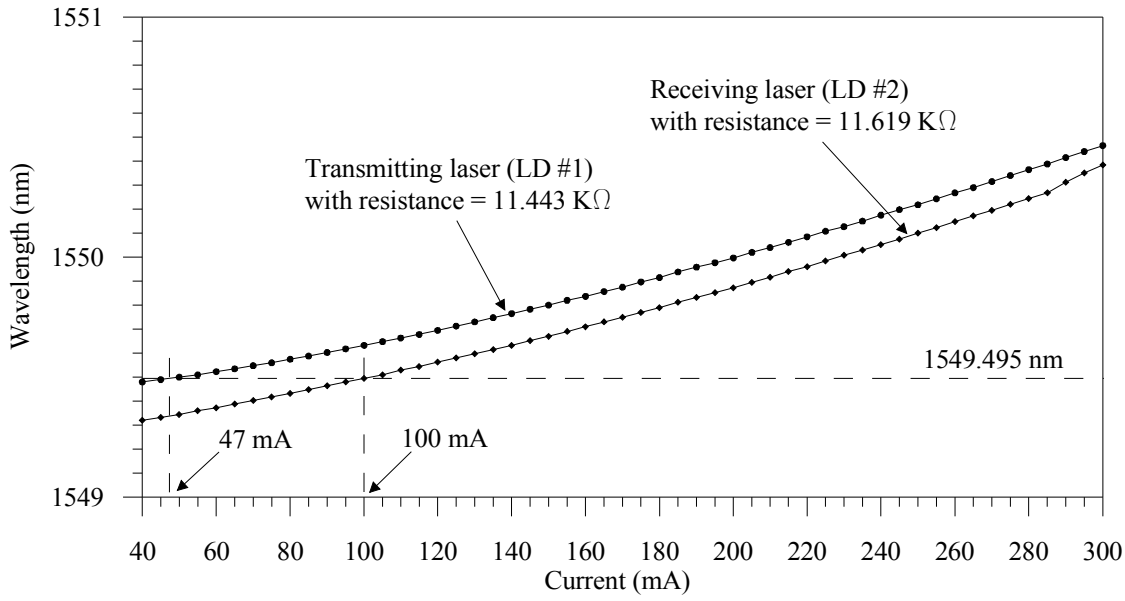

Figure 5.11: Characteristic curves of the transmitting and receiving laser diodes: wavelength vs. driving current with a fixed temperature control resistance.

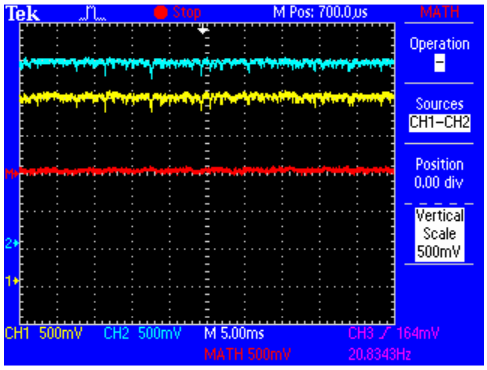

(a) phase-locking ON (maximizing), $\delta\lambda = 0$

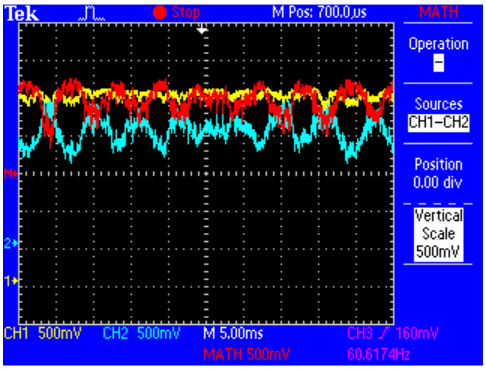

(b) phase-locking ON (maximizing), $\delta\lambda = 25\text{pm}$

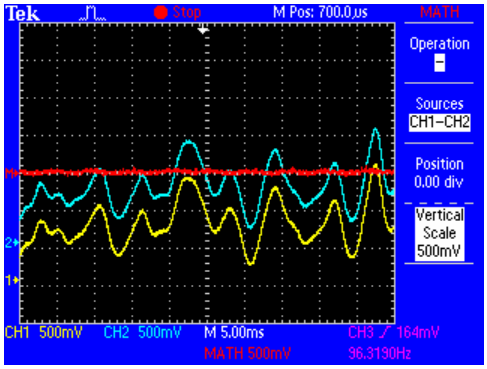

(c) phase-locking control OFF, $\delta\lambda = 0$

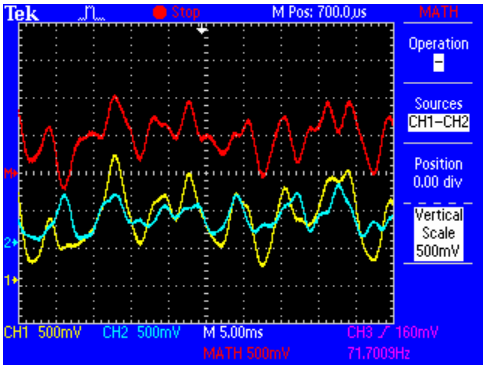

(d) phase-locking control OFF, $\delta\lambda = 25\text{pm}$

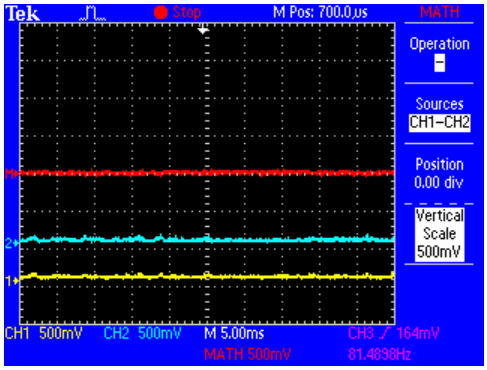

(e) phase-locking ON (minimizing), $\delta\lambda = 0$

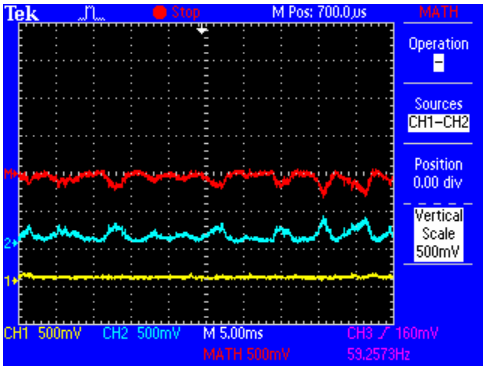

(f) phase-locking ON (minimizing), $\delta\lambda = 25\text{pm}$

Figure 5.12: Typical waveforms of instantaneous samples of the transmitting and receiving metric. The transmitting metric (blue), receiving metric (yellow) and their difference (red). The receiving metric is used as the feedback signal for the phase-locking compensation system. The sinusoidal distortion amplitude for all channels corresponds to a π-radian phase shift. Distortion frequencies are 7, 37, 67, 97, 127, 157, 187, and 217 hertz. The iteration rate of the SPGD controller is ~100, 000 iterations per second.

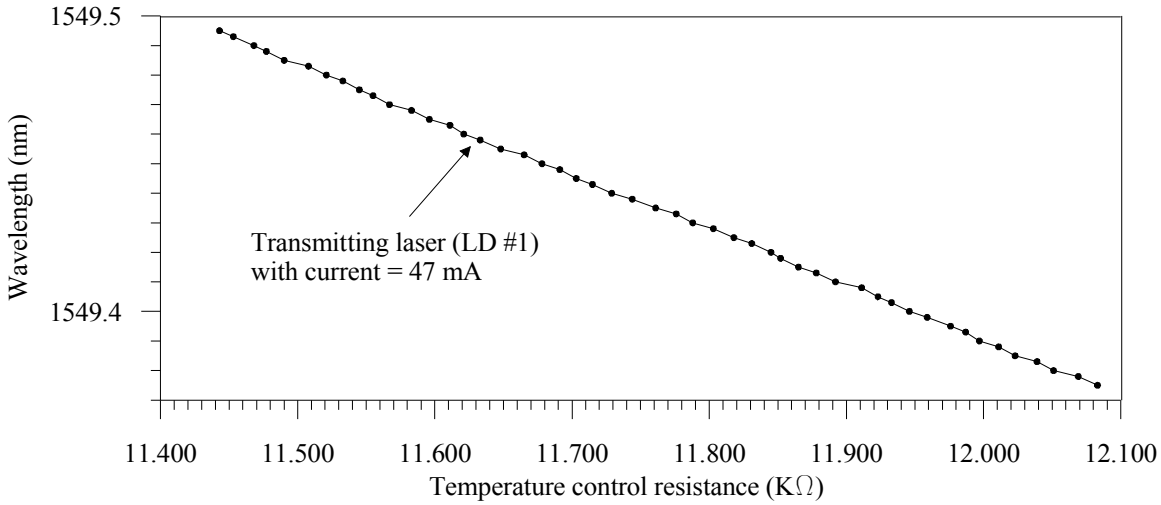

Figure 5.13: Used wavelength values of transmitting laser diode vs. temperature control resistance with a fixed driving current in phase-locking experiments with the counter-propagating beams. Wavelength of receiving laser diode is fixed at 1549.495nm.

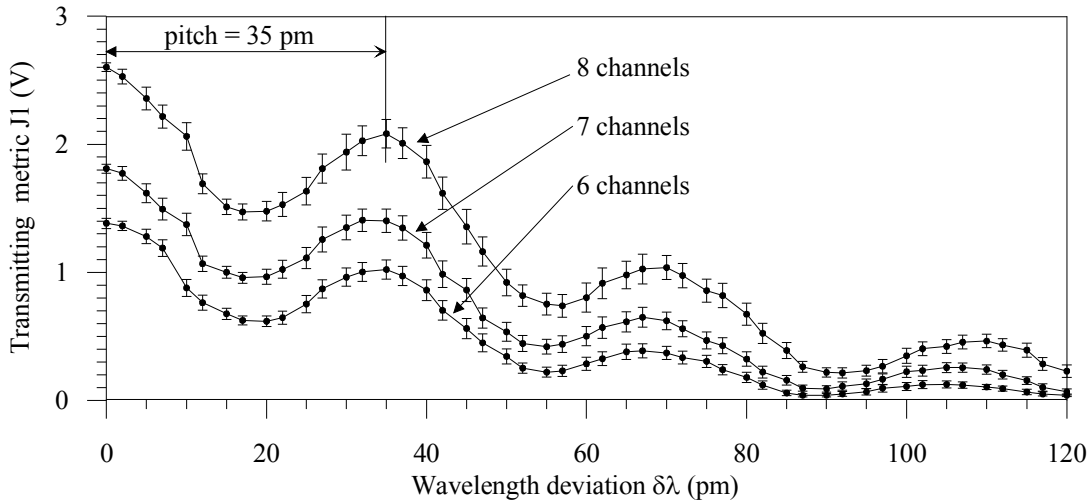

Figure 5.14: Transmitting metric degradation vs. wavelength deviation when the receiving metric is used as the feedback signal of the phase-locking compensation system and is maximized. The wavelength deviation (pitch) between zeroth order maximum and first order maximum is ~35pm, which corresponds to the largest optical path length difference ~46mm. Wavelength deviation when the transmitting metric degrades to its incoherent state ($J1 = (1/N)$) is ~80pm for the given testbed.

5.5 Phase-locking compensation in optical communication link

In the previous sections, phase-locking compensation for coherent beam combining is experimentally demonstrated with the fiber-based testbeds. In these experiments, there is no telecommunication intensity modulation signal added to the propagating beams. In this section, phase-locking compensation is investigated for a communication link in which an intensity modulation signal is involved. The fiber-based testbed as shown in Figure 5.8 is adapted for this purpose and is shown in Figure 5.15. A Mach-Zehnder interferometer, which is not optimized to be a high frequency up to gigahertz communication modulator, is used as an intensity modulator and is inserted between the DFB laser output and the optical input of the 1×8 fiber beam splitter with integrated phase shifters and amplitude controls. The two optical path lengths of the Mach-Zehnder interferometer (EO-Space, Inc.) are carefully balanced such that no bias control circuit is required. The output signal of a bit-error-rate (BER) analyzer (Agilent 86130A) is amplified by an amplifier (Picosecond 5866, 10GHz bandwidth) and is applied to the electrical input of intensity modulator. The main part of the eight-channel optical fiber network is kept unchanged. The combined beam output from the 8×1 fiber beam splitter is fed to the input of a 1×2 fiber coupler. One output of the fiber coupler goes to a photo detector (PDA-10CS, 17MHz bandwidth) for phase-locking feedback control. The other output of the fiber coupler is connected to the optical input of an optical oscilloscope (Agilent 86100A with module 86105A, 20GHz). A clocking trigger signal synchronized to the modulation signal from BER analyzer is connected to the electrical input of the optical oscilloscope. The optical oscilloscope is used to monitor the received optical communication signal.

As stated in Section 5.3, $l_1 \cdots l_N$ are the respective optical path lengths for N channels. The shortest path length is denoted as $l_{\min} = \min_{1 \le i \le M} (l_i)$. The largest path length difference $(\Delta l)_{\max}$ is denoted in Equation (5.10). Considering the optical communication intensity modulation, the transmitting metric (or simply metric) as described in Equation (5.3) can be written as

$$J(t) = \sum_{i=1}^{N} \left| A_i(t) \right|^2 + \sum_{1 \le i \ne k \le N} \left[A_i^*(t) \bullet A_k(t) \right] \cos\left[\Phi_i(t) - \Phi_k(t) \right] \tag{5.12}$$

where $A_i(t)$ is the complex amplitude of the i th beamlet, $\Phi_i(t)$ is the optical carrier relative phase of the i th beamlet, '*' indicates the operation of complex conjugate. The complex amplitude of the i th beamlet can be further written as

$$A_i(t) = A\left(t + \frac{n(l_i - l_{\max})}{c} \right) \tag{5.13}$$

where $A(t)$ is the complex amplitude for all N beamlets at time t if all N optical path lengths are identical, n is the nominal refractive index of glass fiber and c is the speed of light in vacuum.

For the multiple intensity modulated beamlets, if the intensity modulation in pulse format is thought to be an intensity fluctuation instead of communication signal, then proper detection of modulation signal is not a requirement for phase-locking compensation and the laser communication link becomes a pure beam projection system. The phase-locking compensation for a pure beam projection system has been demonstrated successfully with previous experiments. From this point of view, phase-locking compensation and commu-

nication modulation are separate from each other as long as communication intensity modulation does not lead phase-locking control system into its instability region. As can be seen from Equation (5.12), phase-locking compensation system tunes relative phases of optical carrier for all N beamlets. This is performed in frequency range around ~100 kilohertz depending on the iteration rate of the used SPGD phase-locking controller. Phase-locking control system for coherent beam combining must be turned on in order to eliminate phase distortions and increase the average received optical power before the intensity modulation is applied. The communication intensity modulation changes the complex amplitude of beamlets at a much higher frequency range, available commercially from tens of Mb/s to 40Gb/s. It is clear that phase-locking control and communication intensity modulation work in distinct frequency ranges. Phase-locking control system takes the metric value averaged over a characteristic time ~10μs depending on the iteration rate of the used SPGD phase-locking controller. Equation (5.12) can be rewritten for phase-locking control as

$$J^{pl}(t) = \frac{(1+\rho)}{2} A^2 \left(N + \sum_{1 \le i \ne k \le N} \cos\left[\Phi_i(t) - \Phi_k(t) \right] \right) \tag{5.14}$$

where A is the identical complex amplitude for all beamlets before the intensity modulation signal is applied, ρ is the relative intensity level for logic "0" defined as the ratio of the optical power representing logic "0" to the optical power representing logic "1". In Equation (5.14), the radio frequency intensity modulation is only represented by the relative intensity level ρ. Phase-locking compensation system cannot tell the difference between this communication modulation system and a pure beam projection system without any intensity modulation but with an appropriate reduced optical power level. It is con-

cluded that the communication intensity modulation is virtually invisible to phase-locking compensation. On the other end, phase-locking compensation looks "frozen" to communication intensity modulation.

For proper detection at the receiver end of the intensity modulation pulse signal that is applied at the transmitter end, pulses containing the same information must arrive at the receiver at the same time or they must well overlap with each other after they propagate through different optical channels. How well these pulses overlap with each other at the receiver end depends on the relative time delay terms $\left\{\frac{n\left(l_i - l_{\max}\right)}{c}\right\}$ as shown in Equation (5.13). Define an overlapping coefficient η of these optical pulses as the ratio of the minimum spatial duration overlapping when a proper detection can be made to the spatial duration of the optical pulse in glass fiber. Suppose that on-off keying (OOK) modulation with non-return-to-zero (NRZ) coding is used in the communication link. The spatial duration of the optical pulse in glass fiber can be written as $\frac{c}{nR}$, where R is the modulation rate. It can be verified that for proper detection of the modulation signal, the following relation must hold

$$\left(\Delta l\right)_{\max} \le \left(1-\eta\right)\frac{c}{nR} \tag{5.15}$$

$\left(\Delta l\right)_{\max}$ can be estimated through the experiments as described in Section 5.4 when the multi-channel optical communication link is physically built. The highest modulation rate $R_{\max}$ can be obtained through experiments using the testbed as shown in Figure 5.15 for a

specified criterion such as bit-error-rate (BER) or an overlapping coefficient η. If $\eta = 0.95$, $c = 3\times10^8$ m/s, $n \approx 1.50$, $(\Delta l)_{\max} \approx 46$mm, for instance, then $R_{\max} \approx 217$Mb/s.

The technical feasibility of applying phase-locking control to a multi-channel optical communication system as shown in Figure 5.15 is qualitatively verified by checking the eye diagrams as shown in Figure 5.16. Sinusoidal phase distortion amplitude for all channels corresponds to 0.25π-radian phase shift. Distortion frequencies are 7, 37, 67, 97, 127, 157, 187, and 217 hertz for eight channels, respectively. The eye diagrams of the intensity modulated transmitting beam immediately after the intensity modulation Mach-Zehnder interferometer are given in Figure 5.16(a, b) for two modulating rates, 100Mb/s and 200Mb/s, respectively. The deviation of these two eye diagrams away from their ideal situation are probably due to the non-idealness of the intensity modulator and the mismatch between the output impedance of the radio frequency amplifier and the input impedance of the intensity modulator. When the phase-locking control system is turned off, the eyes close in the eye diagrams of the receiving combined beam as given in Figure 5.16(c, d) for the two modulation rates, respectively. When the phase-locking control system is turned on, the eyes start to open in the eye diagrams of the receiving combined beam as given in Figure 5.16(e, f) for the two modulation rates, respectively. The improvement due to phase-locking compensation can be clearly seen from these eye diagrams. The eyes are not completely open when phase-locking control is on are probably due to the SPGD phase-locking controller 2π-reset process as described in Section 4.4. It can be also seen that as the modulation rate increases from 100MHz to 200MHz, the system performance degrades.

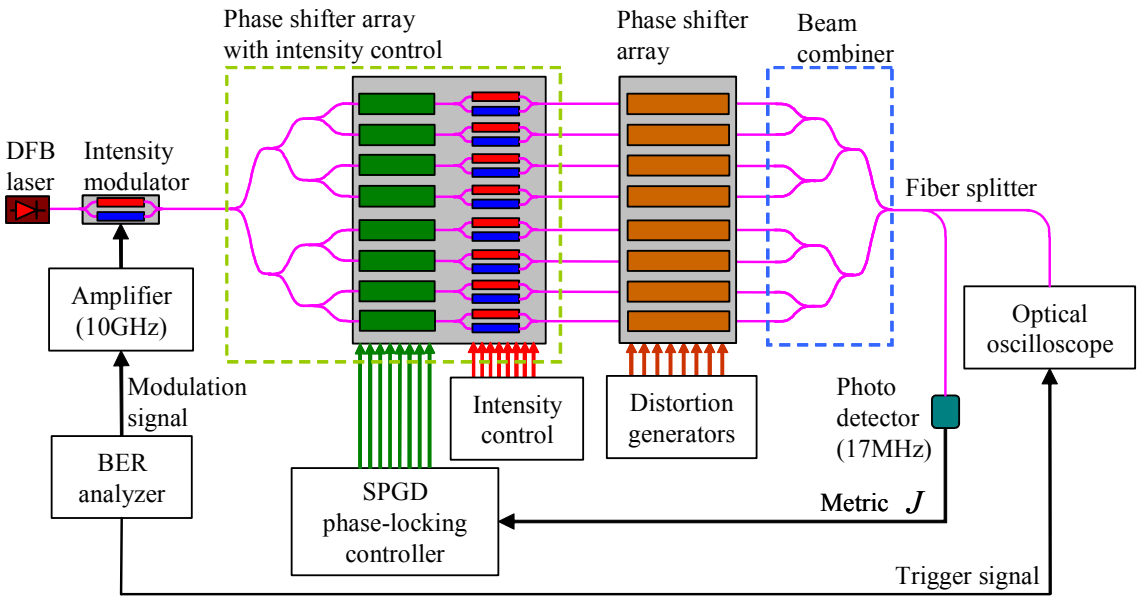

Figure 5.15: Fiber-based optical communication testbed with phase-locking compensation.

This testbed is adapted from the fiber-based testbed as shown in Figure 5.8 A Mach-Zehnder interferometer, which is not optimized to be a high frequency up to gigahertz communication modulator, is used as an intensity modulator and is inserted between the DFB laser output and the optical input of 1×8 a fiber beam splitter with integrated phase shifters and amplitude controls. The two optical path lengths of the Mach-Zehnder interferometer (EO-Space, Inc.) are carefully balanced such that no bias control circuit is required. The output signal of a bit-error-rate (BER) analyzer (Agilent 86130A) is amplified by an amplifier (Picosecond 5866, 10GHz bandwidth) and is applied to the electrical input of the intensity modulator. The combined beam output from 8×1 fiber beam splitter is fed to the input of a 1×2 fiber coupler. One output of the fiber coupler goes to a photo detector (PDA-10CS, 17MHz bandwidth) for phase-locking feedback control. The other output of the fiber coupler is connected to the optical input of an optical oscilloscope (Agilent 86100A with module 86105A, 20GHz). A clocking trigger signal synchronized to the modulation signal from BER analyzer is connected to the electrical input of an optical oscilloscope. The optical oscilloscope is used to monitor the received optical communication signal.

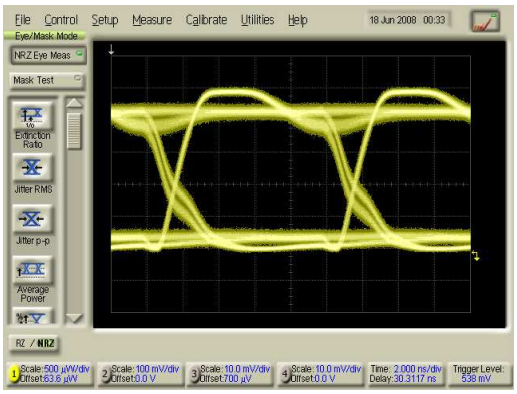

(a) transmitting beam before splitting into beamlets (modulation rate 100MHz)

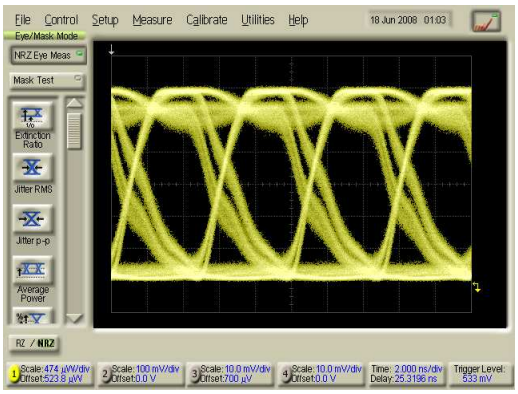

(b) transmitting beam before splitting into beamlets (modulation rate 200MHz)

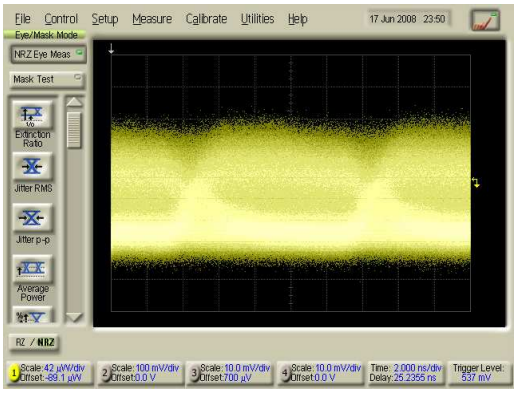

(c) receiving combined beam, modulation rate 100MHz, phase-locking control OFF

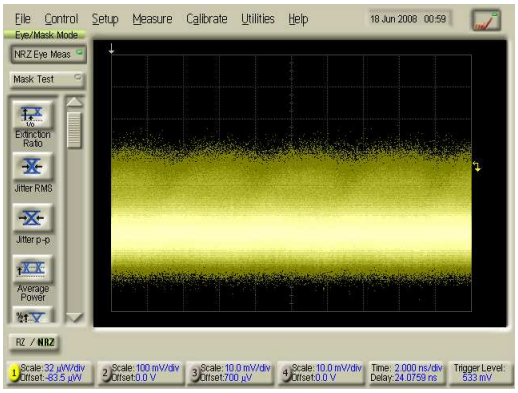

(d) receiving combined beam, modulation rate 200MHz, phase-locking control OFF

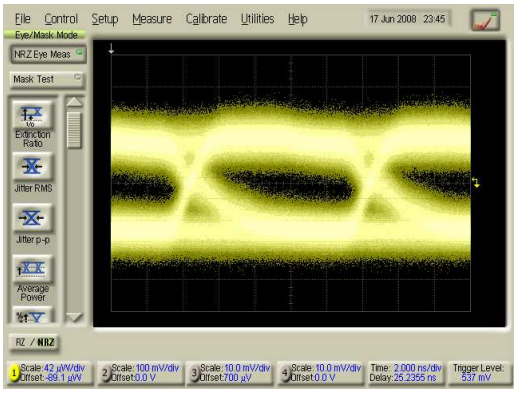

(e) receiving combined beam, modulation rate 100MHz, phase-locking control ON

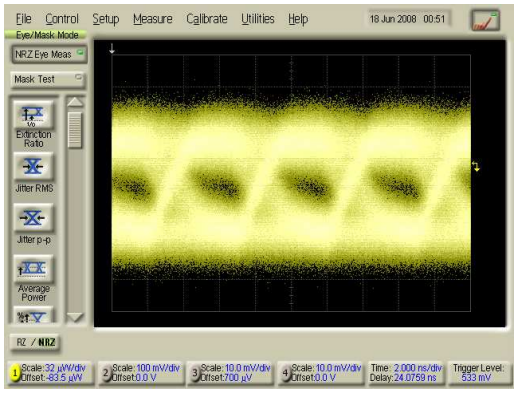

(f) receiving combined beam, modulation rate 200MHz, phase-locking control ON

Figure 5.16: Eye diagrams of intensity modulated transmitting and receiving signal.

Transmitting beam before splitting into beamlets is shown in (a, b) and receiving combined beam when phase-locking control OFF is shown in (c, d) and phase-locking control ON is shown in (e, f).

Chapter 6 Experimental demonstration of free-space beam combining using conformal adaptive phase-locked fiber array

This chapter addresses laboratory experimental work of free-space beam combining using our conformal adaptive phase-locked fiber array as introduced in Chapter 3. Successful integration of the optical transmitter based on conformal adaptive phase-locked fiber array is critical to the success of the following beam combining experiments. In Section 6.1, the integration efforts of conformal adaptive phase-locked fiber array are outlined. In Section 6.2, a free-space beam combining testbed using a conformal adaptive phase-locked fiber array is described. In Section 6.3, phase-locking compensation for static phase noise is demonstrated. In Section 6.4, phase-locking compensation using either AVR microprocessor-based SPGD controller or VLSI multi-dithering controller for dynamic phase noise is demonstrated and characterized. In Section 6.5, subaperture wavefront phase tip-tilt compensation using piezoelectric fiber positioners is demonstrated and characterized. In Section 6.6, beam combining with phase-locking control and subaperture wavefront phase tip-tilt compensation when simulating phase distortions or jitters are present in the propagation path of the three beamlets. In Section 6.7, free-space beam combining experiment with a non-cooperative extended target in the feedback control loop is demonstrated.

6.1 Integration of conformal adaptive phase-locked fiber array

The most critical part in the integration of the conformal adaptive phase-locked fiber array is the beam alignment procedure. Primary steps in the beam coarse alignment procedure are outlined in Figure 6.1, Figure 6.2, Figure 6.3 and Figure 6.4.

As shown in Figure 3.10, there are six degrees of freedom (DOF) to be adjusted for each beamlet in the coarse alignment procedure. First, the polarization angles of three linearly polarized beamlets are matched to each other. This is performed in two steps. The polarization direction (the direction of electric field of the beamlet) is first within ±2° tolerance aligned to one of the two bars of the cross of the fiber positioner (X-Y distributor of the fiber positioner, see Figure 3.7). This is done by twisting the fiber with respect to the fiber positioner central tube, then fixing the fiber to the tube with epoxy. The same steps are repeated for all three beamlets. Then the polarization angles of the three beamlets are matched to each other within ±0.5° tolerance and all are aligned horizontally by rotating the fiber positioner mount tubes with respect to the respective fiber collimator tubes. Here we assume that the three fiber collimator tubes are already mounted to the collimator mount as shown in Figure 3.5. Then the polarization angles are fixed by tightening the relevant screws. The polarization matching steps are depicted in Figure 6.1. The bidirectional rotational arrows in blue show the appropriate rotations of fibers or fiber positioners. An appropriate polarizer plate and a powermeter are used to determine the polarization orientation for each beamlet in both steps.

Second, a shearing interferometer is used for a preliminary check whether individual beamlets are collimated. As shown in Figure 3.10, three degrees of freedom of each beamlet need to be adjusted. Two DOFs are for the fiber-tip orientation, and one DOF is for the focus/defocus adjustment. The fiber-tip orientation is adjusted by two screws, and the focus/defocus can be adjusted by a picomotor. When an individual beamlet is well collimated, large parallel straight interference fringes can be observed either directly on the shearing interferometer screen or through a CCD camera focused on the shearing in-

terferometer screen. This step is depicted in Figure 6.2. The arrows in blue show the focus/defocus motion and the fiber tip orientation tilts.

In the next step the three beamlets are aligned in parallel to each other. There are two major steps for this involving the use of an interferometer. First, the reference mirror of the conformal transmitter (see Figure 3.5) is adjusted perpendicular to the optical axis of the interferometer (MINIFIZ-150). The optical axes of the three collimating lenses are assumed perpendicular to the reference mirror surface. This requirement was secured at manufacturing by using diamond-cutting mechanical manufacturing technique. In the ideal case, the zeroth order interference fringes (uniform pattern everywhere) should be observed when the reference mirror surface is measured using the interferometer. However, the reference mirror surface is not absolutely flat and smooth. Thus, the largest fringe pattern is observed in the best situation. Second, the internal lens and internal camera of the interferometer are used to check whether the three beamlets are focused at the same point as the back-reflected light from reference mirror was focused on when this reference mirror was illuminated by the beam of the interferometer. This corresponds to the adjustment of two DOFs of each fiber tip. They are performed through picomotors (either electrically driven or manually driven) for the rough x-adjustment and y-adjustment. This is depicted in Figure 6.3. The arrows in blue show the x-motion and y-motion for each fiber tip.

The last step of the initial alignment of three beamlets is a test of the alignment by installing a mirror in front of the beamlets parallel to the reference mirror surface. The test is done by measuring the back-reflection powers at the ports $P1$, $P2$, $P3$ (see Figure 6.6) for the three beamlets and determine whether the left-side focal points of the collimating

lenses are located in the center area of the dynamic range of the respective fiber positioners. This is performed by driving the fiber tip to every point (scanning) in the dynamic range of the fiber positioner and recording the detected power for the corresponding point. An image is formed by assigning the detected powers to the respective points. An example image is shown in the illustration of this step. For the three beamlets, there will be three corresponding images. If the brightest spots in these images are all in the center area, the test is passed. This step is depicted in Figure 6.4. The arrows in blue show the tilts due to scanning of the fiber tips driven by the fiber positioners.

Because multiple optical beamlets are involved, high precision up to submicrometer is required even for beam coarse alignment. The alignment precision of the fiber tip in the fiber positioner can be roughly estimated in the following way. In the aligned state, the fiber tip deviation should be such that the introduced steering angle as shown in Equation (3.1) is less than half of the full divergence angle for coherent beam combining. For example, the fiber tip alignment precision for the developed conformal transmitter as shown in Figure 3.5 is approximately $<1.17\ \mu m$. In this estimate, the fiber tip surface is assumed to be cleaved with a right angle exactly perpendicular to the axis of the fiber. Thus, the submicrometer high precision alignment of the beamlets is required.

The above outlined major steps for the beam coarse alignment procedure are more or less coupled to each other. Therefore, in general, the initial coarse alignment is an iterative procedure and the above steps need to be repeated until a good alignment state is achieved. After the initial coarse alignment, the three beamlets are in good positions and can be dynamically steered and accurately aligned by the fiber positioners in the experiments to perform the subaperture wavefront phase tip-tilt compensation for distortions.

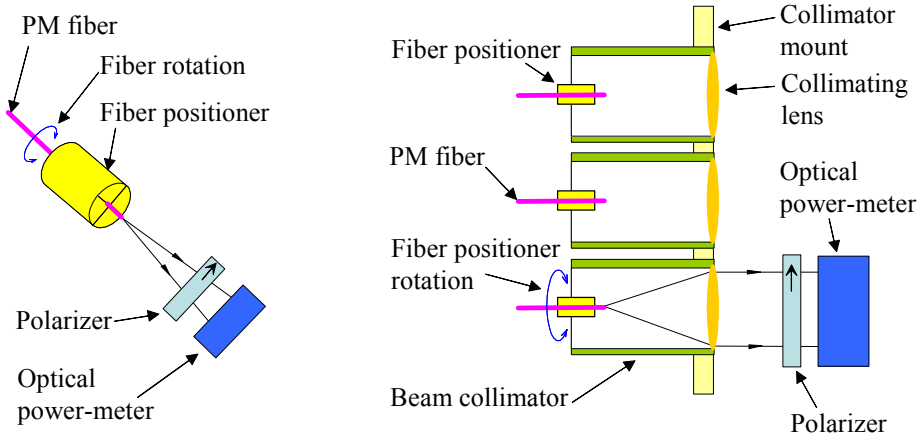

Figure 6.1 Schematic of adjustment for polarization states of three beamlets.

Left: the linear polarization of individual beamlet is aligned with the X-Y distributor of the corresponding fiber positioner (see Figure 3.7) within ±2° tolerance; Right: polarization angles of three beamlets are matched to each other within ±0.5° tolerance.

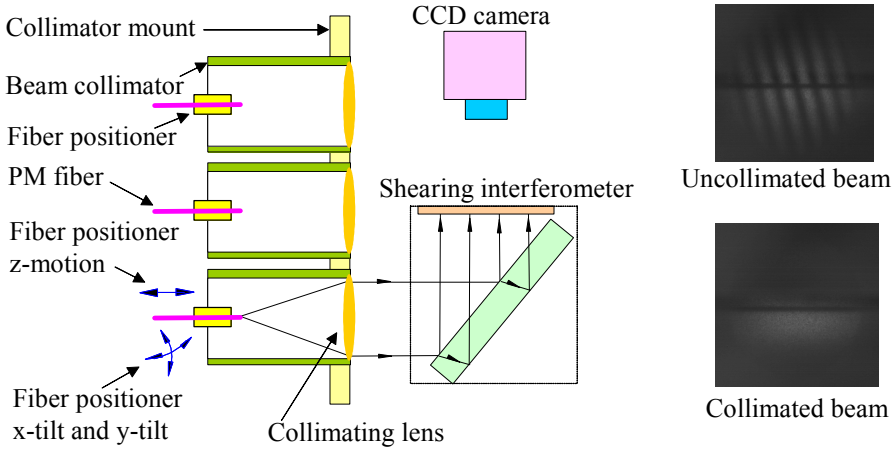

Figure 6.2: Schematic of collimation and static deaberration for three beamlets.

Collimation and static deaberration are coupled and must be performed iteratively. Two images on the right, which are captured through a CCD camera focusing on the screen of a shearing interferometer, show two cases of uncollimated and collimated beamlets. If there is static aberration, the interference fringes of the collimated beam are curved.

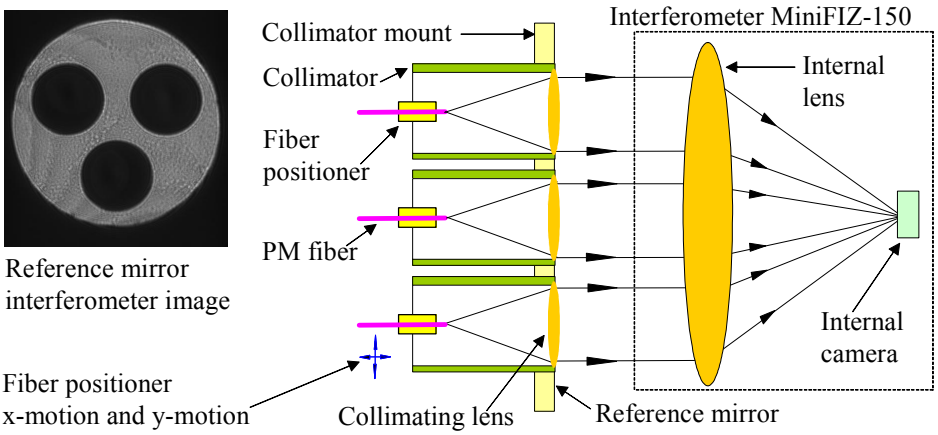

Figure 6.3: Schematic of the coarse alignment of the three beamlets.

In the first step the reference mirror of the conformal transmitter (see Figure 3.5) is made perpendicular to the optical axis of the interferometer MINIFIZ-150. Left is the reference mirror image captured by the interferometer. The right illustration shows how it was secured that the three beamlets are aligned relative to the surface of the reference mirror. This was done by using the internal lens and the internal camera of the interferometer and check whether all beamlets are focused at the same point as the reference mirror does if it is illuminated by the interferometer.

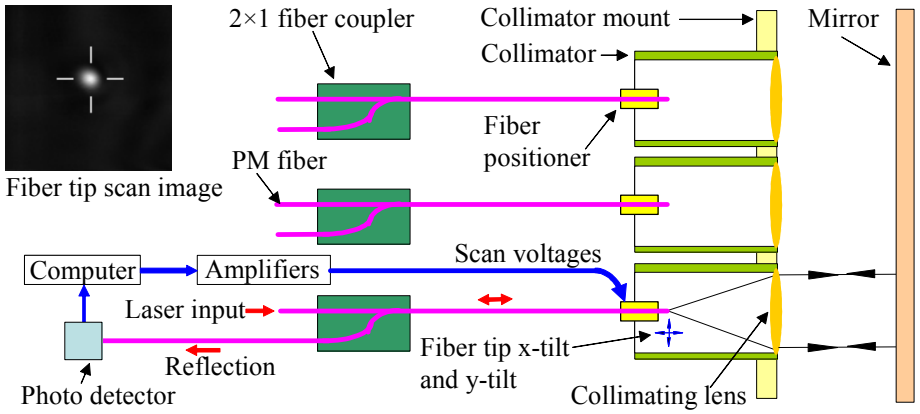

Figure 6.4: Schematic of the alignment-check for the three beamlets.

By scanning the control voltages for each individual fiber positioner and measuring the back-reflection power for the corresponding beamlet, it can be checked that the maximum back-reflected power is in the center of the dynamic range of the fiber positioner for each fiber-positioner.

6.2 Free-space beam combining experimental setup using conformal adaptive phase-locked fiber array

Section 3.1 describes the general system architecture using conformal adaptive phase-locked fiber arrays. Since the far-field distance is usually too large to perform actual free-space experiments in laboratory a far-field conversion lens is used to simulate the actual far field. A picture of the experimental optical setup in laboratory is given in Figure 6.5. The red arrowed lines show the propagation paths of the three beamlets. More details of the experimental setup including feedback control systems are given in Figure 6.6. The diode seed laser with wavelength 1064nm is used in the experiments. The laser output has a spectral linewidth of ~2MHz and a coherence length of ~100m by referring to Equation (3.2). The length differences between different fiber optical paths (~10m) for each beamlet are <0.20m. The output power grating of the diode seed laser used is ~100mW. If the laser output is not well linearly polarized, a fiber-coupled polarizer can be inserted in-line. The three outgoing beamlets into free space are correlated in phase after passing through optical fiber paths. The conformal optical system works in this low power range in the present experimental demonstrations. If high power fiber amplifiers, along with appropriate high power grating fibers are used, similar results for coherent beam combining are expected as long as the nonlinear effects such as stimulated Brillouin scattering (SBS) are suppressed sufficiently and the coherence length of seed laser is long enough.

All optical fibers used in the experiments are Panda-type polarization-maintaining single-mode fibers with design wavelength λ=1064nm. All fiber connectors are FC/APC in order to reduce back-reflections in the fiber-to-fiber couplings. The 1×8 polarization-

maintaining fiber beam splitter with phase shifters and amplitude controls is presented in Figure 3.13. Three channels of this fiber beam splitter are used for the three correlated beamlets, respectively. For the three channels used, amplitude control voltages (denoted by $A1$, $A2$ and $A3$) are tuned to appropriate dc values (usually ±0.05V) in order to balance optical powers of the three beamlets. The phase shifts for the three beamlets are modulated by control voltages (denoted by $U1$, $U2$ and $U3$) generated by SPGD or multi-dithering phase-locking controllers. In the schematic of experimental setup, three identical 2×1 fiber couplers are inserted in-line for each channel, respectively. The purpose is to measure the respective back-reflection powers at the port $P1$, $P2$ or $P3$ in the initial coarse alignment procedure for the three beamlets.

For each channel, there is a polarization-maintaining fiber-coupled beam collimator with a built-in piezoelectric fiber positioner. Each fiber positioner has two pairs of high voltage control terminals for the two pairs of fiber actuators (see Figure 3.7). Thus in total, there are six high-voltage control signals (denoted by $Ux1, Uy1$, $Ux2, Uy2$, and $Ux3, Uy3$). The high voltage amplifiers are made with Apex amplifier chips (PA15A). In the experiments, control voltages $(Ux1, Ux2, Ux3)$, $(Uy1, Uy2, Uy3)$ can be more or less coupled and synchronized in two groups through software programming. The coupling strength can be adjusted in software. Virtually only two control signals ($Ux1 \approx Ux2 \approx Ux3$, $Uy1 \approx Uy2 \approx Uy3$) are independent controllable voltages. How strong these control signals are coupled depends on requirements such as stability and convergence speed of the subaperture wavefront tip-tilt SPGD control system implemented through software on PC. In general, strong coupling between the control voltages for the

three fiber positioners affords relatively faster convergence speed, while weak coupling between them affords relatively better stability.

The three collimated beamlets pass the far-field conversion lens, are reflected by a large planar mirror, and then are reflected again by a piezoelectric tip-tilt mirror to a polarization-independent cubic beam splitter. The tip-tilt mirror can be used to generate tilts such that the focal spot of the combined beam is displaced in the target plane when additional jitters are needed. In this case, two harmonic modulating voltages (Utx, Uty) with random phases within the range of ±10V are applied to the tip-tilt mirror to generate jitter swing angle within the range of ±100μrad. Here the jitter swing angle is the focal spot deviation angle viewed from the aperture pupil plane of conformal optical transmitter.

Beyond the cubic beam splitter, a part of the power of the beamlets is transmitted to the target pinhole of diameter 50μm and a part of the power of the beam is reflected through an attenuator wheel to the CCD camera focused at the target focal plane. A photo detector (PDA-10CF, 150MHz bandwidth) and a wideband amplifier (DHPVA-100, 100MHz bandwidth, 10~60dB gain) are located immediately behind the target pinhole. The bandwidth of the combination of the given photo detector and amplifier is from dc to 100MHz for the used wavelength $\lambda = 1064\text{nm}$. The feedback metric signal J is shared between the phase-locking controller, which uses either SPGD or multi-dithering techniques, and the subaperture tip-tilt SPGD controller implemented on a PC. A lowpass filter (denoted by LPF) with cutoff frequency 10kHz is inserted in front of the PC to suppress the high frequency perturbations of the metric signal due to phase-locking controls. PC-based subaperture wavefront tip-tilt control works at a relatively slow perturbation rate

(~950Hz) to accommodate for the bandwidth of piezoelectric fiber positioners as shown in Figure 3.8.

The three beamlets propagate in free space from the conformal optical transmitter pupil to the target pinhole. In this propagation path, wavefront phase distortions can be introduced with the hotplate and the cooling fan as shown in Figure 6.5. Jitters can be introduced through the piezoelectric tip-tilt mirror. In the characterizing procedure for the phase-locking control using either SPGD or multi-dithering techniques, high frequency phase distortions are simulated by applying a harmonic voltage to one of the phase shifters in use. This is because the phase distortions generated through the hotplate and the cooling fan have only low frequency (<100Hz) components. Phase distortions up to 100kHz can be introduced to one beamlet relative to the others.

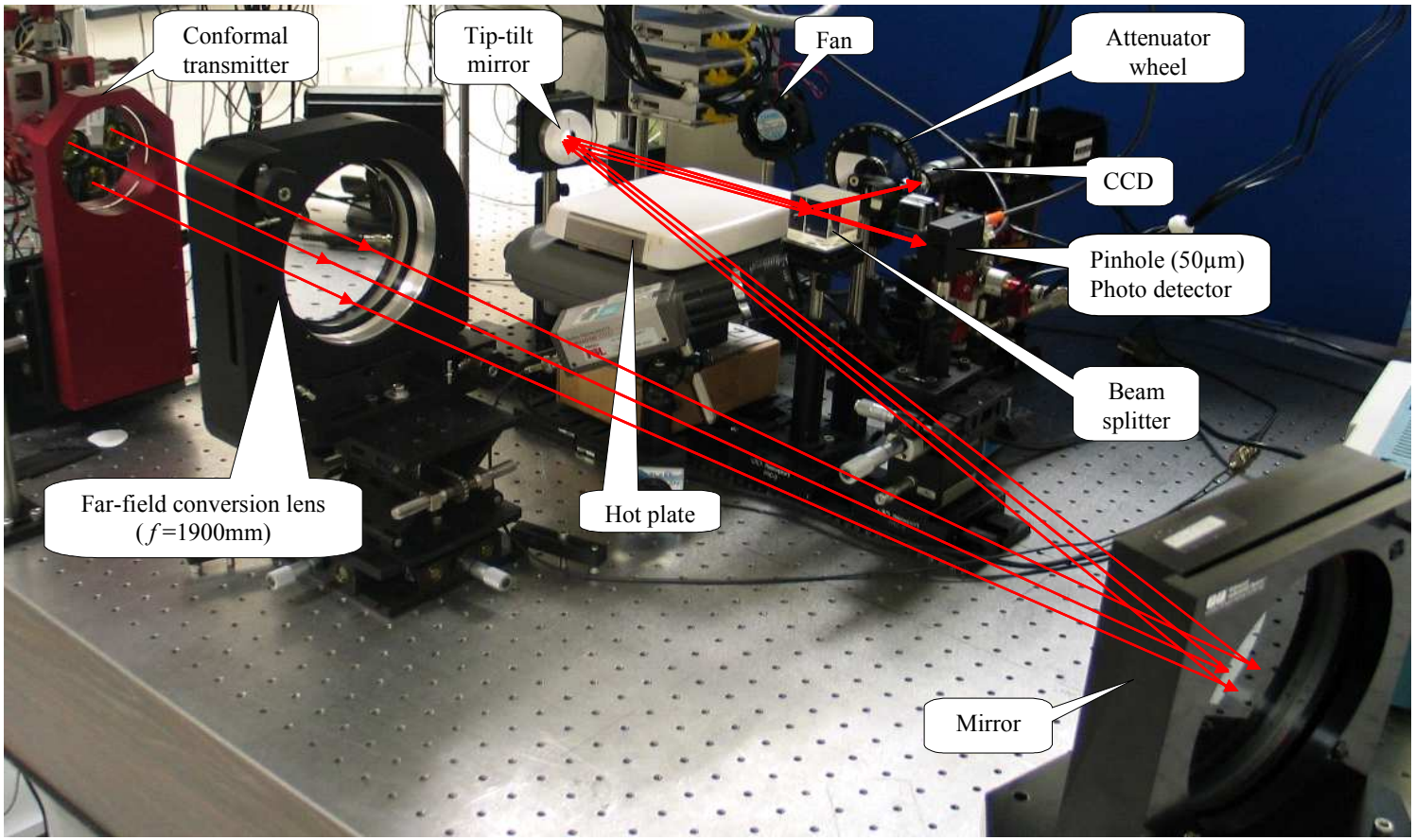

Figure 6.5: Free-space beam combining testbed (optical part) using conformal adaptive phase-locked fiber array with three subaperture elements. The red arrowed lines show the propagation paths of three beamlets. The tip-tilt mirror is used to generate wavefront tilts. The hotplate between the tip-tilt mirror and the cubic beam splitter is used to generate phase distortions. A cooling fan is used to generate airflow.

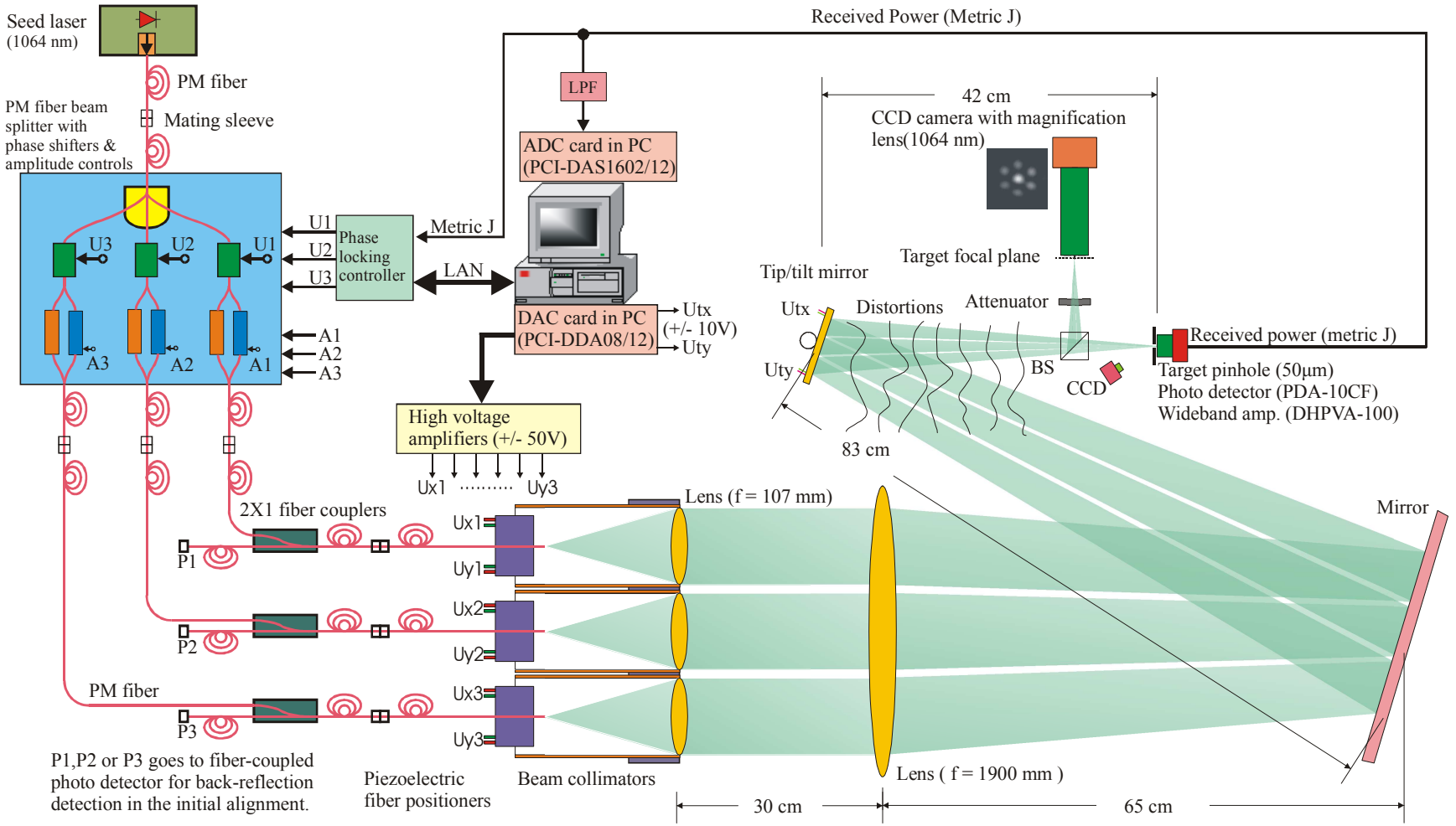

Figure 6.6: Schematic of free-space beam combining testbed using conformal adaptive phase-locked fiber array.

6.3 Phase-locking compensation using phase shifters for static phase noise

In a first step only compensation for static phase distortions by phase-locking was investigated with the free-space beam combining testbed. Static or quasi-static phase noise is slow-varying phase noise due to optical path differences or temperature variations (see Section 3.4). In the following experiments, three beamlets are aligned and focused at the same point of target pinhole one by one in advance. The used phase-locking controller was the AVR microprocessor-based SPGD controller described in Figure 4.2.

Figure 6.7 shows the target plane intensity distributions for incoherent beam combining and several different cases of coherent beam combining. Due to finite response speed of CCD camera these images are the time-averaged (instead of instantaneous) intensity distributions seen on monitor. In pseudo-incoherent beam combining, the relative phases of the three beamlets are scrambled by fiber phase shifters with different high frequency sinusoidal signals to be sufficiently random. The three beamlets look incoherent in phase to the CCD camera even though they are in reality correlated in phase. In the coherent beam combining cases, phase-locking control and subaperture wavefront tip-tilt control are on while no phase distortions or jitters are present. The images (a-e) are easily distinguished from each other. For these five cases, the instantaneous intensity distributions have similar patterns compared to the averaged distributions here. There are strong sidelobes present in these images. The strong sidelobes are due to the relatively small fill factor $\left(f_{con}\right)^2 \approx 0.37$ of the conformal transmitter with three subapertures. The beamlet identifications are defined in Figure 3.5. In the case (f) for coherent beam combining by destructive phase-locking control, the control system tries to minimize the received power in the bucket (pinhole). It can be seen that in constructive coherent beam combin-

bucket (pinhole). It can be seen that in constructive coherent beam combining cases, the size of central focal spot is much smaller than in the incoherent beam combining case.

The images in Figure 6.7 are captured by the CCD camera with magnification lens as shown in Figure 6.5 and Figure 6.6. The absolute sizes of central focal spots in these images are estimated in the following way. A known size object such as a stripped, cleaved single mode fiber tip with cladding diameter 125μm can be placed in front of the magnification lens. An image can be obtained for this fiber tip. This image can be used as a reference. Then the absolute sizes of images captured by the same imaging system composed of the CCD camera and magnification lens can be estimated. In Figure 6.8, the image of the single mode fiber tip is given on the left. The image of target plane intensity distribution of three constructively phase-locked beamlets as shown in Figure 6.7(e) is duplicated as well for comparison. The scale 50μm is shown in Figure 6.7 because it is equal to the pinhole diameter.

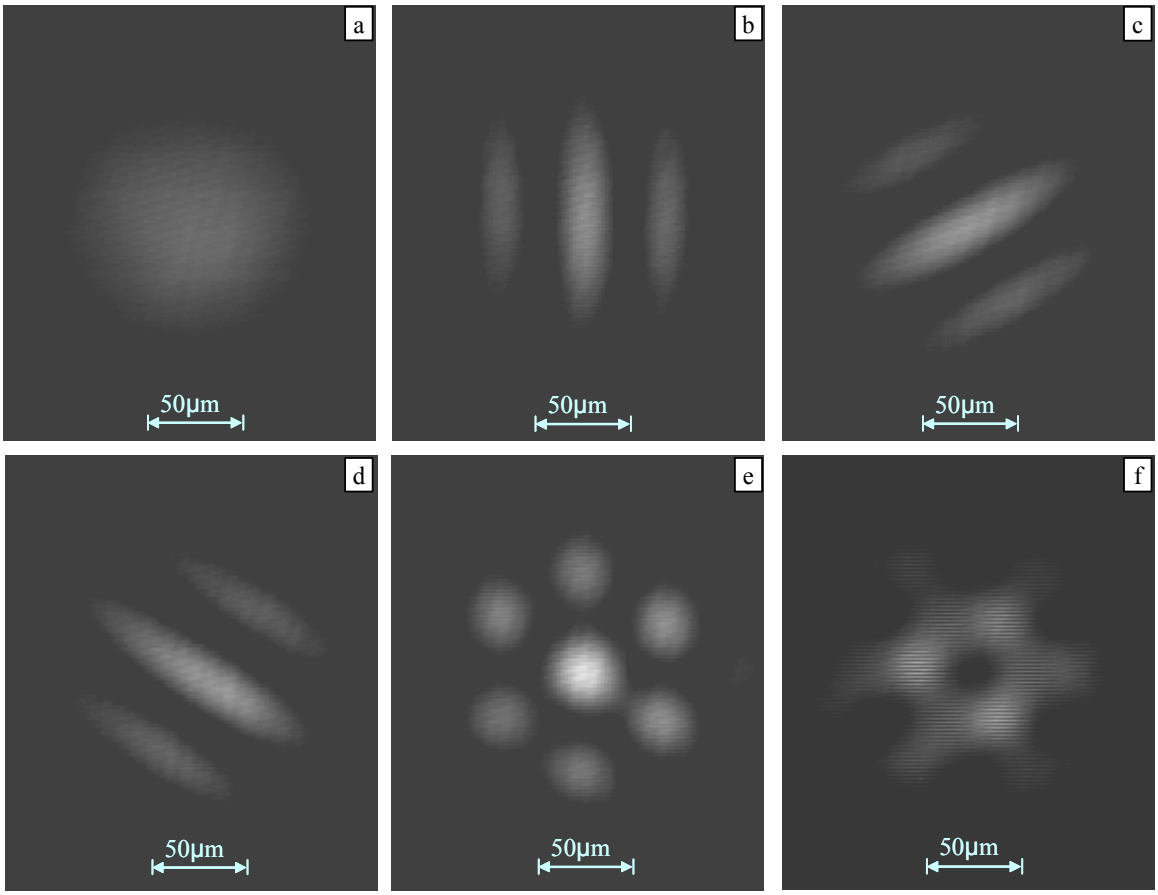

Figure 6.7: Target plane intensity distributions for incoherent and coherent beam combining.

Only quasi-static phase noise is present in the propagation path of the beamlets. In these experiments, three beamlets are aligned and focused at the same point of target pinhole one by one in advance. The used phase-locking controller is the AVR microprocessor-based SPGD controller described in Figure 4.2. (a) incoherent combining of 3 beamlets, (b) coherent combining of 2 beamlets (#1 and #2), (c) coherent combining of 2 beamlets (#2 and #3), (d) coherent combining of 2 beamlets (#1 and #3), (e) coherent combining of 3 beamlets (constructively phase-locked), (f) coherent combining of 3 beamlets (destructively phase-locked). The images are the time-averaged (instead of instantaneous) intensity distributions seen on monitor due to finite response speed of CCD camera. The beamlet identifications are defined in Figure 3.5.

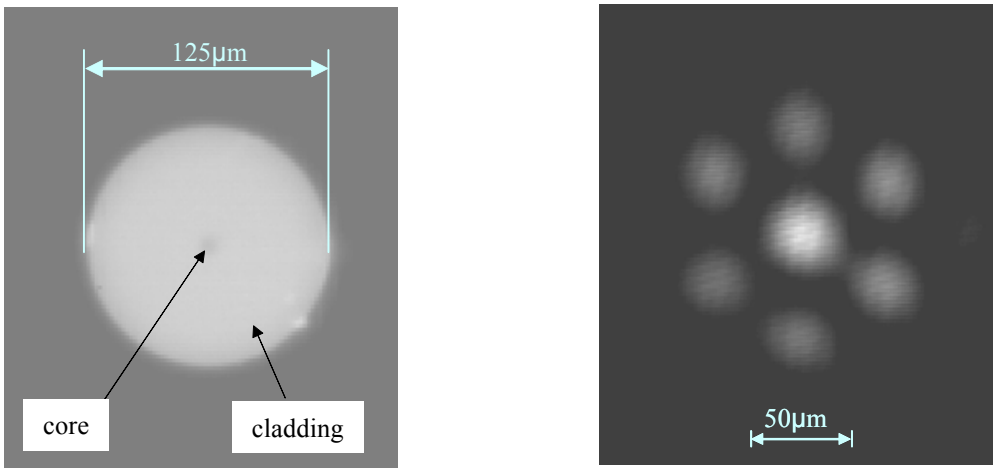

Figure 6.8: Target plane focal spot size estimation.

A stripped, cleaved single mode fiber tip with cladding diameter 125µm is placed in front of the imaging system with a magnification lens and a CCD camera as shown in Figure 6.5 and Figure 6.6. An image is obtained for this fiber tip. This image is used as a reference. The absolute sizes of images, as shown in Figure 6.7, captured by the same imaging system composed of the CCD camera and magnification lens can be estimated by comparison.

6.4 Characterization of phase-locking compensation using phase shifters for dynamic phase noise

In order to characterize the phase-locking compensation efficiency fiber phase shifters were used to introduce dynamic phase noise. With either the SPGD controller described in Figure 4.2 or multi-dithering controller described in Figure 4.5 as compensation controller, the following experiments have been performed. All three beamlets are well aligned using piezoelectric fiber positioners and their intensities are well balanced using the built-in amplitude controls along with the fiber phase shifters. There are no jitters introduced by the piezoceramic tip-tilt mirror. The beamlet identifications are defined in Figure 3.5. Other parts for an individual channel are also identified with the same number accordingly. These are described in the following six experiments.

Experiment #1: phase-locking of two beamlets (#1 and #2) using the AVR microprocessor-based SPGD controller. Beamlet #3 is blocked. The phase of beamlet #1 is distorted by applying a sinusoidal voltage to the phase control electrode of fiber phase shifter #1. The phase of beamlet #2 is controlled by one channel output of the SPGD controller. The distortion phase-shift amplitude and the compensation bandwidth are recorded. Here the phase-locking compensation bandwidth for a given distortion phase-shift amplitude is defined as the cutoff frequency (the highest frequency of the sinusoidal distorting voltage) at which the normalized metric is 0.80. The normalized metric in a phase-locking state is calculated by dividing the averaged metric signal when distortion is present by the averaged metric signal when distortion is absent. This experiment corresponds to the curve in red in Figure 6.9(a).

Experiment #2: phase-locking of three beamlets using the AVR microprocessor-based SPGD controller. The phase of beamlet #1 is distorted by applying a sinusoidal voltage to the phase control electrode of fiber phase shifter #1. The phases of the other two beamlets (#2 and #3) are actively controlled by two channel outputs of the SPGD controller. The distortion phase-shift amplitude and the compensation bandwidth are recorded. This experiment corresponds to the curve in blue in Figure 6.9(a).

Experiment #3: phase-locking of two beamlets (#1 and #2) using the VLSI multi-dithering controller. Beamlet #3 is blocked. The phase of beamlet #1 is distorted by applying a sinusoidal voltage to the phase control electrode of fiber phase shifter #1. The phase of beamlet #2 is controlled by one channel output of the multi-dithering controller. The distortion phase-shift amplitude and the compensation bandwidth are recorded. This experiment corresponds to the curve in red in Figure 6.9(b).

Experiment #4: phase-locking of three beamlets using the VLSI multi-dithering controller. The phase of beamlet #1 is distorted by applying a sinusoidal voltage to the phase control electrode of fiber phase shifter #1. The phases of the other two beamlets (#2 and #3) are controlled by two channel outputs of the multi-dithering controller. The distortion phase-shift amplitude and the compensation bandwidth are recorded. This experiment corresponds to the curve in blue in Figure 6.9(b).

In the experiments #1 and #2, the iteration rate of the SPGD controller is ~95,000 iterations per second. This corresponds to a perturbation rate of ~190,000 perturbations per second. In the experiments #3 and #4, the used highest dithering frequency is ~70MHz and the low pass cutoff frequency ω_{cut} defined in Equation (4.25) is set to be ~4.7MHz.

The following conclusions can be drawn from Figure 6.9. For a given distortion phase-shift amplitude, the compensation bandwidth for phase-locking of two beamlets is generally higher than the compensation bandwidth for phase-locking of three beamlets. This is true for the cases using either SPGD controller or using multi-dithering controller because the phase-locking of more beamlets is more difficult than the phase-locking of fewer beamlets. Also for a given distortion phase-shift amplitude, the compensation bandwidth using multi-dithering controller is approximately much higher than the compensation bandwidth using SPGD controller is. This is because the dithering frequencies of the multi-dithering controller are much higher than the perturbation rate of the SPGD controller. Here we assume the number of perturbations for SPGD control to converge is at the same order of magnitude as the number of dither cycles for multi-dithering control to converge. This fact is verified in the following experiments.

Experiment #5: transition from phase-unlocked state to phase-locked state using AVR microprocessor based SPGD phase-locking controller. Here phase-unlocked state means the state where phase-locking control and the subaperture wavefront tip-tilt controls are off while atmospheric turbulence generated by the hotplate and the cooling fan is present. The phase-locked state means the stable convergence state while the same atmospheric turbulence is present. All three beamlets are combined together. All three beamlets are phase-modulated by the respective fiber phase shifters with three channel outputs of the SPGD controller. The transition process is defined starting at the moment the control systems are turned on and ending at the moment the normalized metric reaches 95% of the value in its stable convergence state. This is plotted in Figure 6.10(a). This plot is averaged over 128 curves and is obtained on oscilloscope automatically because the data acquisition board PCI-DAS1602/12 for the metric signal is not able to sample the metric

quisition board PCI-DAS1602/12 for the metric signal is not able to sample the metric fast enough.

Experiment #6: transition from phase-unlocked state to phase-locked state using VLSI multi-dithering phase-locking controller. All three beamlets are combined together. This is plotted in Figure 6.10(b). The plot is also averaged over 128 curves and is obtained automatically on oscilloscope for the same reason as in the experiment #5. The periodic ripples along with the plot are due to the additional phase noise introduced by 2π-reset process of the multi-dithering controller.

In the experiments #5 and #6, the perturbation rate of the SPGD controller and the highest dithering frequency, the internal lowpass cutoff frequency of the multi-dithering controller are kept the same as in the experiments #1, #2, #3 and #4. The convergence time using AVR microprocessor based SPGD controller is ~0.825ms. The needed number of perturbations to converge is 157 for three beamlets. The system needs 52 perturbations (26 iterations) per beamlet to converge. The convergence time using VLSI multi-dithering controller is ~1.90μs. The needed number of dither cycles is 133 for three beamlets. The system needs 44 dither cycles per beamlet to converge.

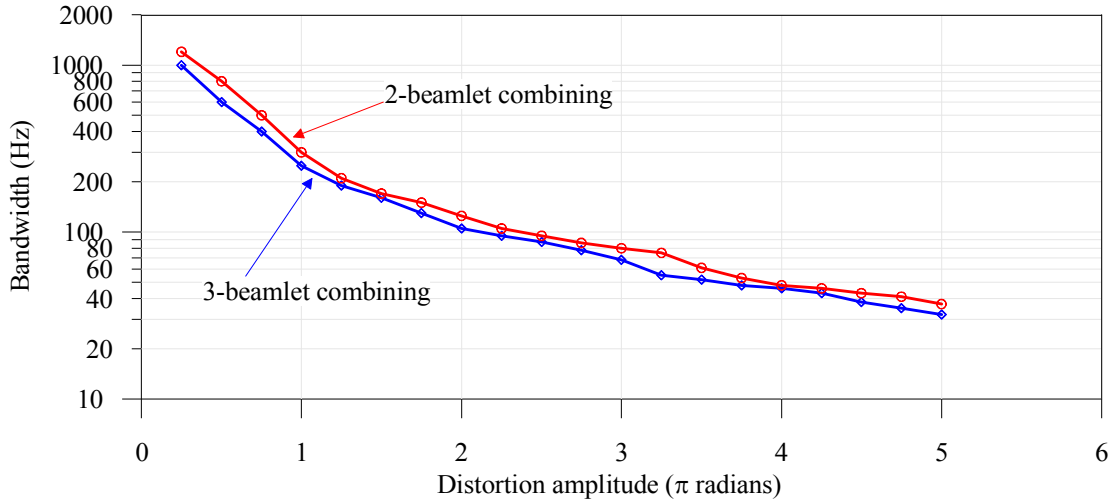

(a) phase-locking compensation using AVR microprocessor-based SPGD controller shown in Figure 4.2

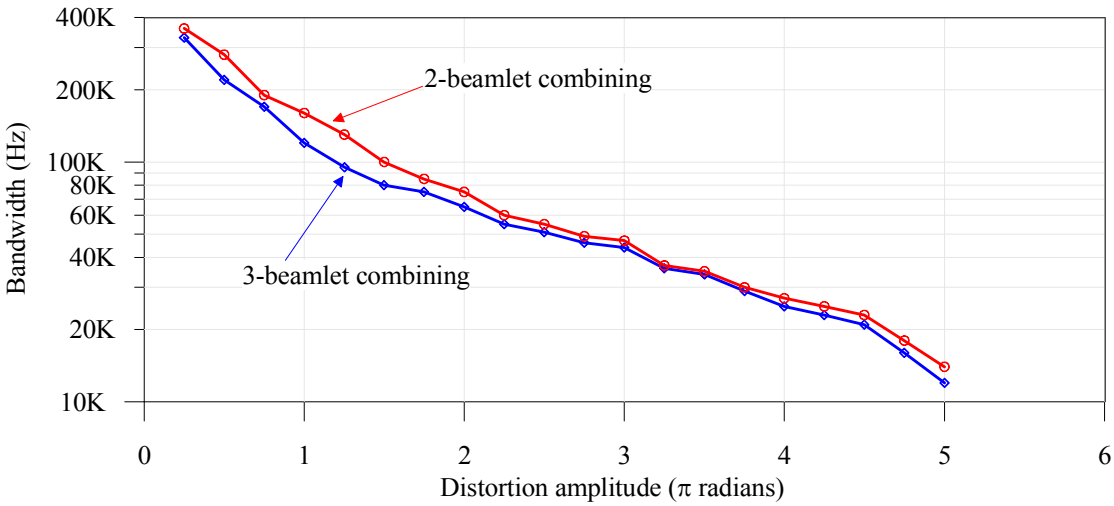

(b) phase-locking compensation using VLSI multi-dithering controller shown in Figure 4.5. The periodic ripples along with the plot are due to the additional phase noise introduced by 2π-reset process of the multi-dithering controller.

Figure 6.9 Free-space beam combining with phase-locking compensation using phase shifters for dynamic phase noise.

These curves correspond to the normalized metric 0.80. The iteration rate of the SPGD controller is ~95,000 iterations per second. The used highest dithering frequency of multi-dithering controller is ~70MHz. In each case, the distortion is generated by applying sinusoidal voltage to the phase modulating terminal of the fiber phase shifter #1. No jitters or atmospheric turbulence is present.

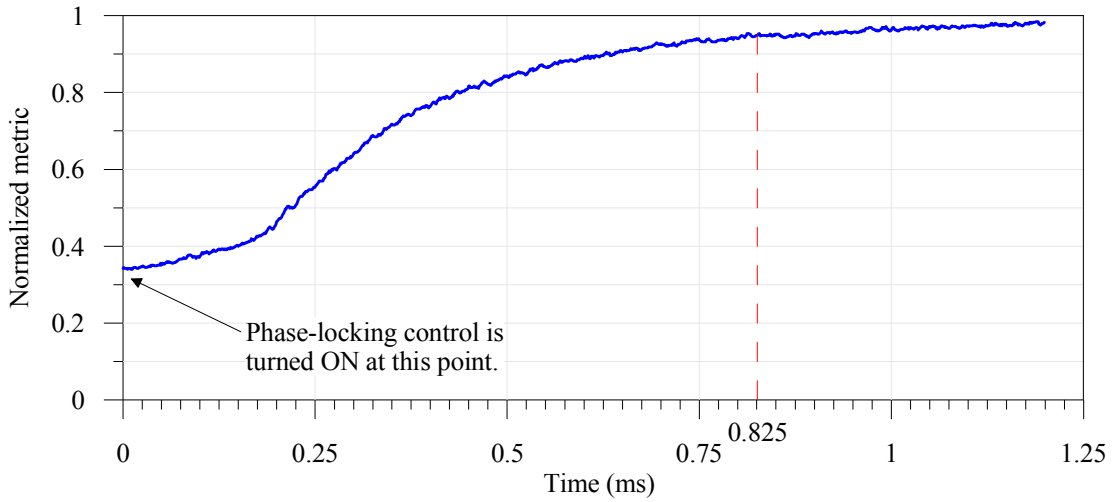

(a) phase-locking compensation using AVR microprocessor-based SPGD controller shown in Figure 4.2

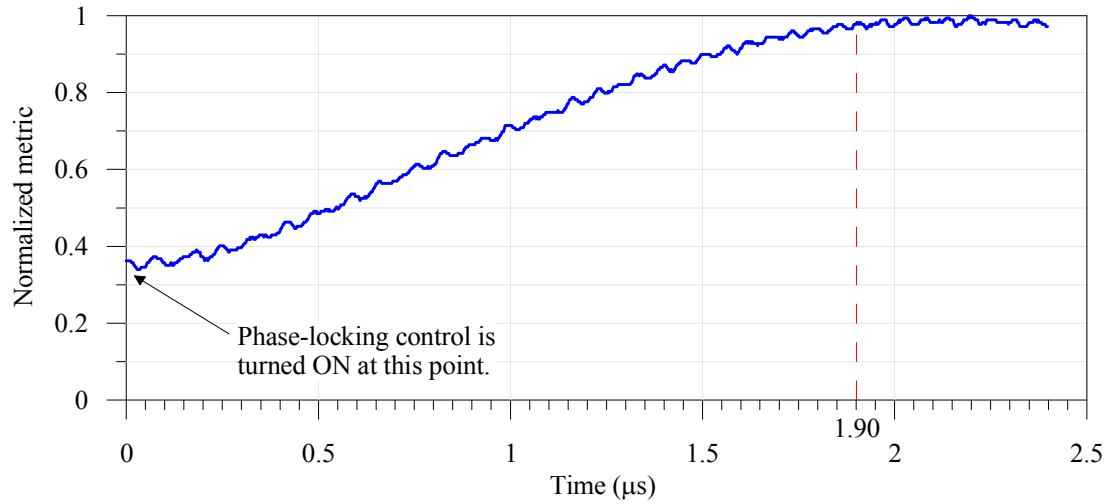

(b) phase-locking compensation using VLSI multi-dithering controller shown in Figure 4.5

Figure 6.10 Three-beamlet phase-locking compensation transition curves.

The iteration rate of the SPGD controller is ~95,000 iterations (or ~190,000 perturbations) per second. The convergence time is ~0.825ms. The needed number of perturbations to converge is 157 for three beamlets. The used highest dithering frequency of multi-dithering controller is ~70MHz. The convergence time is ~1.90μs. The needed number of dither cycles is 133 for three beamlets. Atmospheric turbulence generated by the hotplate and the cooling fan is present. No jitters are present.

6.5 Characterization of subaperture wavefront tip-tilt compensation using piezoelectric fiber positioners

In this section, the subaperture wavefront tip-tilt compensation efficiency using piezoelectric fiber positioners is characterized experimentally. Here all three beamlets are combined coherently. The AVR microprocessor-based SPGD controller for phase-locking control is kept on whenever subaperture wavefront tip-tilt control is on. The piezoceramic tip-tilt mirror is driven by two computer-generated sinusoidal voltages with random phases to introduce jitters to the three beamlets. The frequencies (denoted by f_x and f_y) of the two sinusoidal voltages with random phases are separated by an arbitrary factor around unity such as $f_x = 1.1345 f_y$ to avoid possible resonances to the mechanical-electrical fiber actuators. For convenience, here the jitters are referred to as x-jitter (or horizontal jitter) and y-jitter (or vertical jitter). The three fiber positioners are used to compensate the wavefront distortion due to the jitters. The fiber positioners are driven by the control voltages generated through PC-based SPGD controller as described in Section 4.4 and in the experimental setup. This SPGD controller has an iteration rate ~ 950 iterations per second. The six high voltage control signals are coupled into two groups ($Ux1 \approx Ux2 \approx Ux3$, $Uy1 \approx Uy2 \approx Uy3$) and thus virtually only two control signals are updated by the PC-based SPGD controller. Different jitter amplitudes and jitter frequencies are applied to the piezoceramic tip-tilt mirror and the resulted normalized metric data are recorded as shown in Figure 6.11. The subaperture wavefront phase tip-tilt compensation bandwidth is defined here as the cutoff frequency (the highest frequency of the sinusoidal jitter voltage) at which the normalized metric is 0.80 for a given sinusoidal jitter amplitude. The amplitude of the jitters is characterized by the target plane focal spot deviation

angle viewed from the conformal transmitter aperture pupil plane as described in section Figure 3.5. In general, when the target pinhole becomes larger, the combined beam focal spot falls into the pinhole with a larger probability and thus the subaperture wavefront tip-tilt compensation power is expected to be higher. It can be seen from the plot that the compensation bandwidth is about 80Hz for sinusoidal swing angle of 10μrad that might be due to fast but slight transceiver vibrations. In this region, subaperture wavefront tip-tilt control can be used to stabilize optical links for applications such as laser pointing. The compensation bandwidth is about 1Hz for relatively larger sinusoidal swing angle up to 90μrad. In this region, subaperture wavefront tip-tilt control can be used to track an object or transceiver in slow motion for applications such as laser communications or laser tracking. It is generally thought here that the subaperture wavefront tip-tilt compensation system is sufficiently fast and powerful for actual tilt aberration in atmospheric turbulence.

The subaperture wavefront tip-tilt compensation using fiber positioners is further characterized by the transition curve of normalized metric signal in the experiment. The transition curve is shown in Figure 6.12. For this specific experiment, the jitter swing angle is 60μrad, the horizontal jitter frequency is 1.16Hz, and the vertical jitter frequency is 1.32Hz. Horizontal and vertical jitters have random phases. The transition time is about 42ms. The number of iterations to converge is 40 iterations for virtually two control voltages ($Ux1 \approx Ux2 \approx Ux3$, $Uy1 \approx Uy2 \approx Uy3$). The number of iterations to converge is 20 iterations per controllable variable by using the PC-based SPGD controller. Remember that the number of iterations to converge is 26 iterations per beamlet in the phase-locking control by using the AVR microprocessor-based SPGD controller. The difference is due to

the following fact. In the PC-based SPGD controller for subaperture wavefront tip-tilt compensation, the update gain coefficients and the perturbation amplitudes are adaptive with respect to the feedback metric signal J. The update gain coefficients and perturbation amplitudes in the AVR microprocessor-based SPGD controller for phase-locking control are manually tunable but not dynamically adaptive with respect to the metric signal J. These results verify the statement that using adaptive update gain coefficients and adaptive perturbations can increase the convergence speed characterized by the number of iterations required to converge per controllable variable. From the viewpoint of controller design, the PC-based SPGD controller implementation with an iteration rate of ~950 iterations per second is fast enough and well compatible with the response characteristics of the piezoelectric fiber positioners as shown in Figure 3.8.

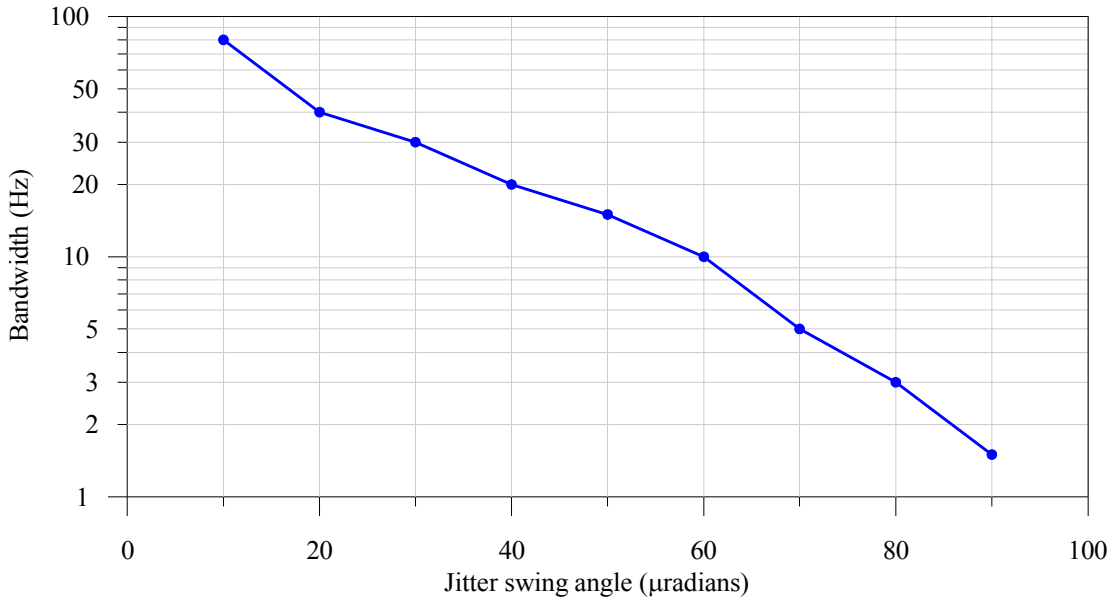

Figure 6.11 Subaperture wavefront tip-tilt compensation bandwidth using fiber positioners.

All three beamlets are combined coherently here. The AVR microprocessor-based SPGD controller for phase-locking control is kept on whenever subaperture wavefront tip-tilt control is on. The piezoceramic tip-tilt mirror is driven by two computer-generated sinusoidal voltages with random phases to introduce jitters to the three beamlets. The frequencies (denoted by f_x and f_y) of the two sinusoidal voltages with random phases are separated by an arbitrary factor around unity such as $f_x = 1.1345 f_y$ to avoid possible resonances to the mechanical-electrical fiber actuators. The SPGD controller has iteration rate ~950 iterations per second. The subaperture wavefront tip-tilt compensation bandwidth is defined here as the cutoff frequency (the highest frequency of the sinusoidal jitter voltage) at which the normalized metric is 0.80 for a given sinusoidal jitter amplitude. The amplitude of the jitters is characterized by the target plane focal spot deviation angle viewed from the conformal transmitter aperture pupil plane as described in section Figure 3.5.

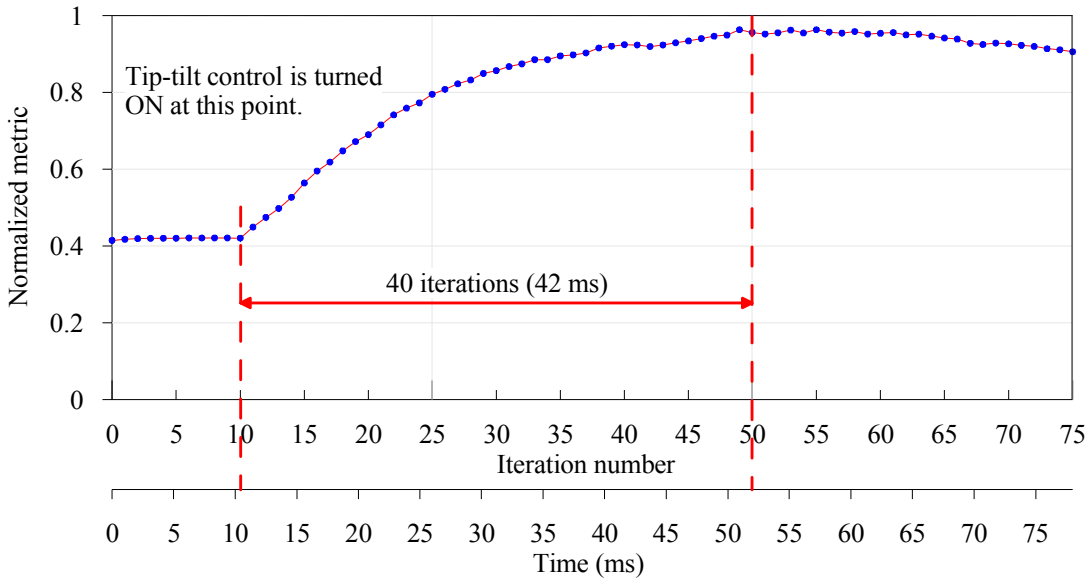

Figure 6.12 Transition curve of subaperture wavefront tip-tilt compensation using piezoelectric fiber positioners with PC-based SPGD controller.

Phase-locking control using AVR microprocessor-based SPGD controller is kept on whenever subaperture wavefront tip-tilt control is on. The iteration rate of the SPGD controller is ~950 iterations per second. The update gain coefficients and the perturbation amplitudes for subaperture wavefront tip-tilt compensation are adaptive with respect to the feedback metric signal. The jitter swing angle is 60μrad. The horizontal jitter frequency is 1.16Hz. The vertical jitter frequency is 1.32Hz. Both jitters have random phases. The transition time is ~42ms. The number of iterations to converge is 40 iterations for virtually two control voltages ($Ux1 \approx Ux2 \approx Ux3$, $Uy1 \approx Uy2 \approx Uy3$). The number of iterations to converge is 20 iterations per controllable variable by using the PC-based SPGD controller.

6.6 Phase-locking control and subaperture wavefront tip-tilt compensation for free-space beam combining

The compensation effects of phase-locking control and subaperture wavefront tip-tilt control are compared in the following eight cases of beam combining experiments of three beamlets when atmospheric turbulence generated by the hotplate and the cooling fan is present. The first four cases (a-d) are the cases where no jitters are present. The second four cases (e-h) are the cases where jitters are present. The horizontal jitter is sinusoidal with amplitude 60μrad and frequency 1.16Hz. The vertical jitter is sinusoidal with amplitude 60μrad and frequency 1.32Hz. These jitters are introduced into the system through the piezoelectric tip-tilt mirror. The eight cases are shown in Figure 6.13. In case (a), phase-locking control is off, tip-tilt control is off, atmospheric turbulence is present, and jitters are absent. In case (b), phase-locking control is on, tip-tilt control is off, atmospheric turbulence is present, and jitters are absent. In case (c), phase-locking control is off, tip-tilt control is on, atmospheric turbulence is present, and jitters are absent. In case (d), phase-locking control is on, tip-tilt control is on, atmospheric turbulence is present, and jitters are absent. In case (e), phase-locking control is off, tip-tilt control is off, atmospheric turbulence is present, and jitters are present. In case (f), phase-locking control is on, tip-tilt control is off, atmospheric turbulence is present, and jitters are present. In case (g), phase-locking control is off, tip-tilt control is on, atmospheric turbulence is present, and jitters are present. In case (h), phase-locking control is on, tip-tilt control is on, atmospheric turbulence is present, and jitters are present.

Eight short movie clips for the target plane intensity distributions are recorded for the respective eight cases. Each movie clip contains 139 frames (4.6-second long) and each

frame contains 400×400 pixels. The peak intensity in each frame of the movie clips is assumed the peak intensity of the central diffraction lobe of the combined beam focal spot in the target plane. The locations of the pixels with the maximum intensities of the individual frames within a movie clip are plotted for each case. The following conclusions can be drawn from Figure 6.13. If there are no jitters present (top row), the beamlets can be efficiently combined coherently by using the phase-locking control only when the beamlets are initially aligned and focused to the same point in the target plane. In this situation, the subaperture wavefront tip-tilt control does not contribute much because there are not strong wavefront tilt aberrations to be compensated. However, if there are jitters present (bottom row), using phase-locking control only is not sufficient to combine the beamlets successfully. In this situation, the subaperture wavefront tip-tilt control must be used along with the phase-locking control in order to coherently combine the beamlets efficiently. The subaperture wavefront tip-tilt control actually contributes much to the coherent beam combining. Here the phase-locking control is realized by using the AVR microprocessor-based SPGD controller.

Statistics for the same beam combining experiments as described in the above eight cases are given in Figure 6.14 when no jitters are present and in Figure 6.15 when jitters are present. The atmospheric turbulence generated by the hotplate and the cooling fan is always present. Two hundred metric data frames are collected for each of the two situations when jitters are absent and when jitters are present, respectively. For both Figure 6.14 and Figure 6.15, in the first quarter (in red) of the duration of each data frame, phase-locking control is off and local tip-tilt control is off. In the second quarter (in blue) of the duration of each data frame, phase-locking control is on and local tip-tilt control is off. In

the third quarter (in green) of the duration of each data frame, phase-locking control is off and local tip-tilt control is on. In the fourth quarter (in black) of the duration of each data frame, phase-locking control is on and local tip-tilt control is on. For each case, the averaged metric vs. time (top graphs in Figure 6.14 and Figure 6.15), the probability distribution vs. metric (middle graphs in Figure 6.14 and Figure 6.15), and the frequency spectra of the metric signal (bottom graphs in Figure 6.14 and Figure 6.15) are plotted.

For the situation (Figure 6.14) when there are no jitters present, phase-locking control solely can do rather good job and subaperture wavefront tip-tilt control does not contribute much. For the situation (Figure 6.15) when there are jitters present, phase-locking control solely are not capable to compensate the wavefront phase distortions sufficiently and subaperture wavefront tip-tilt control must be used as well in order to combine the three beamlets together. These conclusions are similar to the conclusions drawn from the results in Figure 6.13. In addition, from the plots for the frequency spectra of the metric signal, it is seen that when the low frequency components (>0.5Hz but <20Hz) of the phase distortions are suppressed by the phase-locking control and local tip-tilt control, the even lower frequency components (dc to 0.5Hz) and higher frequency components (>100Hz) appear. The increase of the subhertz components are expected because in the ideal situation of coherent beam combining, only the dc component is present. On contrary, the higher frequency components are not wanted. However, these higher frequency components are 20dB weaker than the low frequency components (>0.5Hz but <20Hz) and can be ignored. They are primarily generated due to the perturbations of the control systems based on SPGD algorithm.

The frequency spectra for the situation with jitters present clearly show the jitters (see red curve and blue curve in Figure 6.15, bottom graph) before the subaperture wavefront tip-tilt control is applied. The peaks immediately beyond 1Hz in the red plot and the blue plot of the frequency spectra represent the applied horizontal jitter at 1.16Hz and vertical jitter at 1.32Hz, respectively. The peaks between 2Hz and 3Hz in the red plot and the blue plot of the frequency spectra are the second order harmonics of the jitters.

From the top graph of Figure 6.14, it can be seen that when the phase-locking control is off at time zero and at time=18s, the metric does not drop abruptly on average. There is a short time delay. A new term referred to as interbeam phase correlation time is introduced for this time delay in Figure 6.14. The interbeam phase correlation time indicates how long the phases of the three beamlets can still be in a correlated state after the phase-locking control is turned off. When jitters or strong wavefront phase aberrations such as tilts are absent, the interbeam phase correlation time is not very small (~240ms). When jitters or strong wavefront phase aberrations are present, the interbeam phase correlation time is negligibly short (see sudden drop of the averaged metric at the very beginning of the top graph in Figure 6.15). This is because an initial phase-locked state without phase-locking control can be easily destroyed by jitters or strong wavefront phase aberrations such as tilts. In coherent beam combining applications, steering of beamlets with subaperture wavefront tip-tilt control is a prerequisite for successful phase-locking control. If these beamlets are not focused to the same area in the target plane, it seems impossible to phase-lock them.

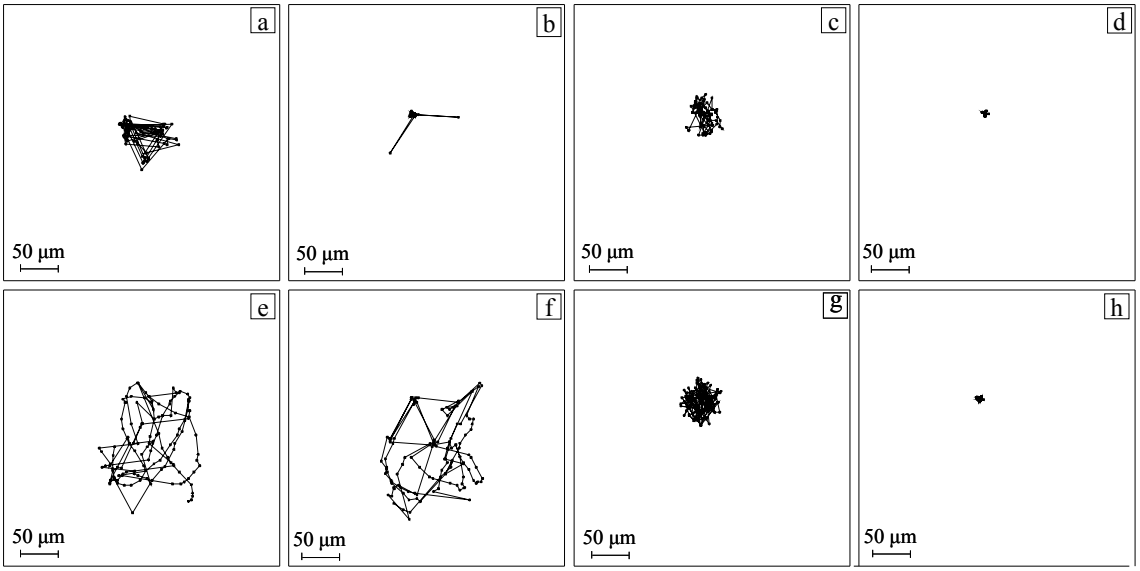

Figure 6.13 Loci of the target plane peak intensity of combining of three beamlets when atmospheric turbulence generated by a hotplate and airflow is present.

Top row is for the cases where no jitters are present. Bottom row is for the cases where jitters are present. Horizontal jitter: 60μrad, 1.16Hz. Vertical jitter: 60μrad, 1.32Hz. Both jitters are sinusoidal and have random phases. Notes: in cases (a) and (e), phase-locking control is off, local tip-tilt control is off; in cases (b) and (f), phase-locking control is on, local tip-tilt control is off; in cases (c) and (g), phase-locking control is off, local tip-tilt control is on; in cases (d) and (h), phase-locking control is on, local tip-tilt control is on. In case (b), the maximum intensities of 2 out of 139 frames jump from the central lobe to the side lobes.

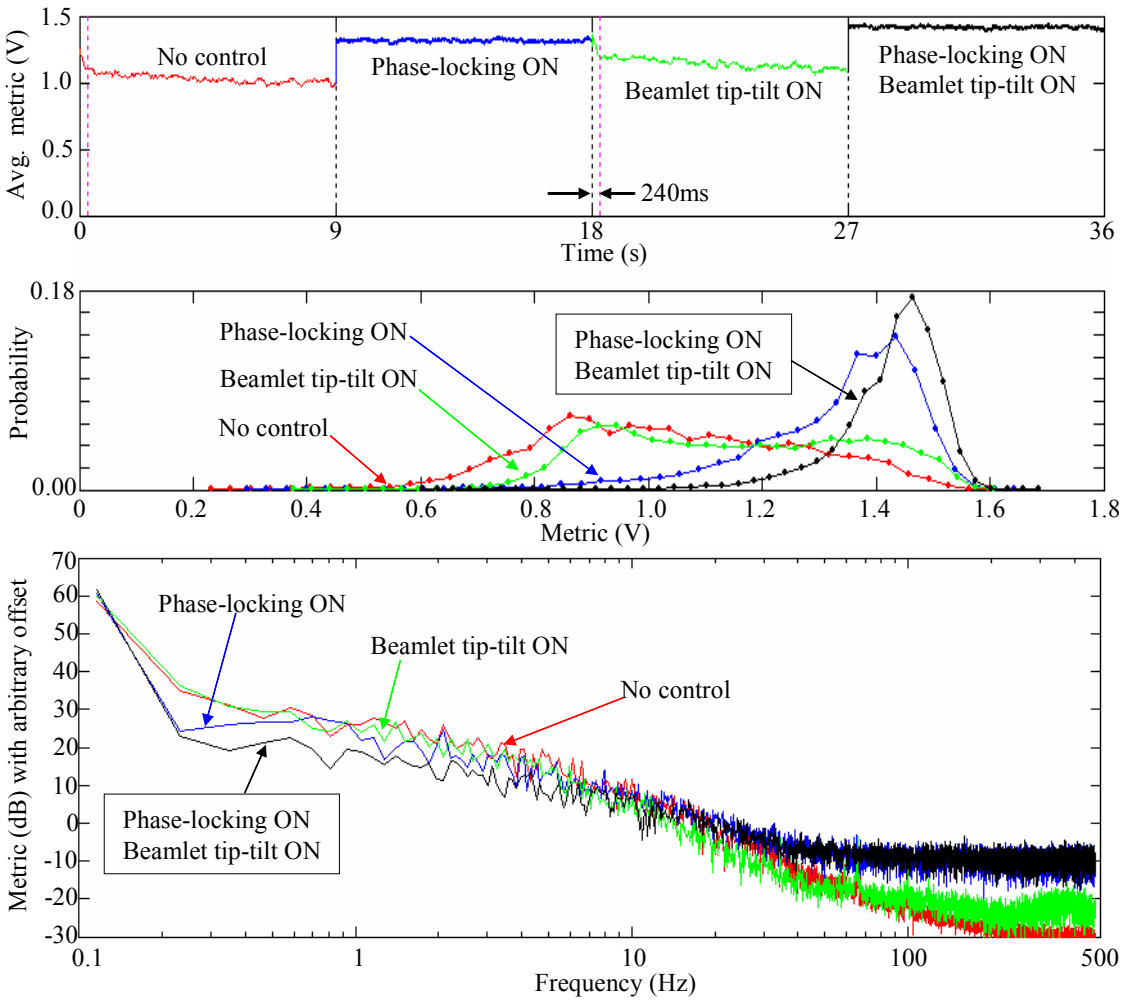

Figure 6.14 Statistics of phase-locking control and tip-tilt control without jitters present.

Top graph: averaged metric vs. time (or iteration number) within frame. Middle graph: probability distributions of metric with different controls. Bottom graph: averaged frequency spectra of the real-time metric with different controls. In all graphs (top, middle, bottom), red indicates that phase-locking control is off and local tip-tilt control is off; blue indicates that phase-locking control is on and local tip-tilt control is off; green indicates that phase-locking control is off and local tip-tilt control is on; black indicates that phase-locking control is on and local tip-tilt control is on. The inter-beam phase correlation time is ~240ms as shown in top graph.

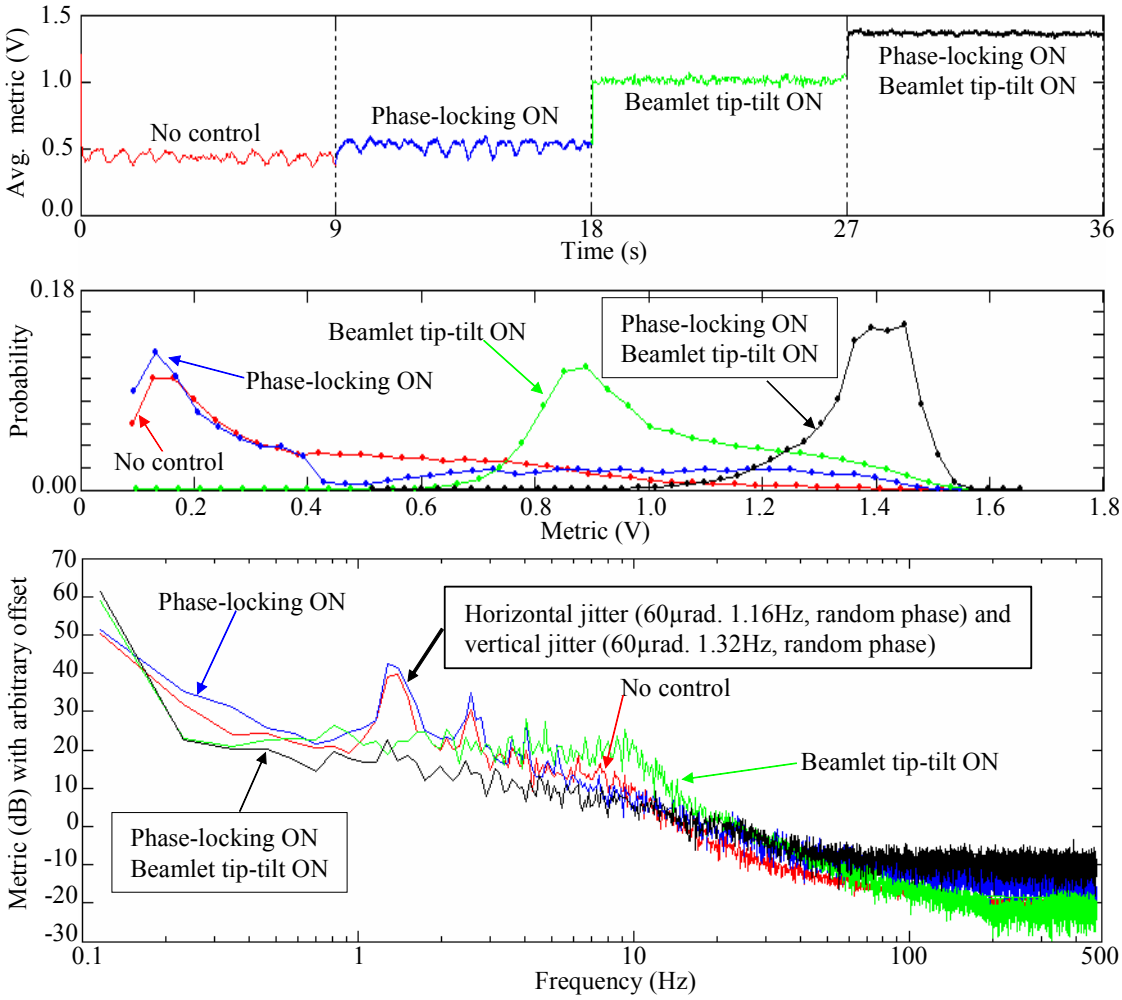

Figure 6.15 Statistics of phase-locking control and tip-tilt control with jitters present.

Top graph: averaged metric vs. time (or iteration number) within frame. Middle graph: probability distributions of metric with different controls. Bottom graph: averaged frequency spectra of the real-time metrics with different controls. In all graphs (top, middle, bottom), red indicates that phase-locking control is off and local tip-tilt control is off; blue indicates that phase-locking control is on and local tip-tilt control is off; green indicates that phase-locking control is off and local tip-tilt control is on; black indicates that phase-locking control is on and local tip-tilt control is on. The inter-beam phase correlation time is negligible due to jitters.

6.7 Free-space beam combining with non-cooperative extended target

In the free-space beam combining experiments described in previous sections, metric signal for phase-locking control system and subaperture wavefront tip-tilt compensation system is obtained by directly wiring back the output signal of a photo detector with a pinhole in front. The photo detector can in this case be regarded as a cooperative target. In Section 3.6, general working mechanism of feedback control systems with target-in-the-loop configuration is outlined. In this section, technical feasibility of applying phase-locking control and subaperture wavefront tip-tilt control to conformal optical beam projection system with non-cooperative extended target is investigated.

The free-space beam combining testbed as described in Section 6.2 (see Figure 6.5 and Figure 6.6) is adapted to the requirements for experiments in this section. The modified testbed is shown in Figure 6.16 and Figure 6.17. An aluminium disc of diameter 51mm with a rough surface acts as a non-cooperative extended target. The photo detector with a pinhole in front in Figure 6.5 and Figure 6.6 for feedback metric collection is moved to another position. This photo detector and the CCD camera with the magnification lens for the target plane focal spot are kept in order to be able to perform beam combining experiments as described in the previous sections. This optional part is for simplicity not shown in the schematic as shown in Figure 6.17. The reflected radiation from the focal spot of the combined beam on the non-cooperative extended target is present in a wide angle following Lambert's cosine law. A high-sensitivity CCD camera (WAT-902HS) in front of and ~105mm away from the target is used to detect scatter speckle field. This CCD camera has an active sensor area about 7mm×5mm. An ordinary CCD camera is used to image the focal spot of combined beam on target. A lens with diameter 152mm

and focal length ~600mm is used to collect optical power of scatter speckle field. The focal spot of combined beam on target is imaged through this lens and a mirror to high dynamic range photo detector (NewFocus model 2103, logarithmic detector) with a pinhole (50μm) in front. The basic idea here is to image the diffraction limit of the focal spot of the combined beam on target onto the logarithmic detector by using the pinhole. The multi-channel fiber system, phase-locking control system and subaperture wavefront tip-tilt system are kept unchanged except that the SPGD phase-locking controller as shown in Figure 4.3 is used instead. This SPGD phase-locking controller is characterized in compensation bandwidth in Section 5.4.

There are three primary steps to perform the free-space beam combining experiments with the non-cooperative extended target in the feedback control loop. The first step is to focus the three illuminating beamlets on the target surface. Focal spot size on target for each beamlet is adjusted by tuning its fiber-tip z-displacement through the focus/defocus adjustment picomotor as shown in Figure 3.10. A high sensitivity CCD camera (WAT-902HS) without objective is used to detect speckle field of the focal spot. When a beamlet is focused on the target, the largest speckles can be observed from a fixed point in scatter speckle field. Scatter field speckles of non-cooperative extended target illuminated by beamlet #3, for example, are given in Figure 6.18(a-h). The largest speckles are seen in Figure 6.18(a) where this beamlet is thought to be focused on the target and the z-position is assumed to be zero or reference position. There is an increment of 30μm (or 1000 steps × 30nm per step of picomotor motion) for the z-displacement of fiber-tip in each of the remaining seven cases. As the z-displacement of fiber-tip increases, the

speckle sizes decrease. It can be seen that the speckle sizes do not change much in fiber-tip z-displacement range of ±60μm considering bidirectional z-displacement.

The second step is to prealign the three beamlets such that their focal spots on the target overlap each other. The prealignment of the three beamlets is performed by scanning control voltages for piezoelectric fiber positioners while synchronously detect collected optical power through the logarithmic photo detector with a pinhole in front for feedback control as shown in Figure 6.16 and Figure 6.17. Focal spots of illuminating beamlets on the target for a few different cases and their respective speckle images are shown in Figure 6.19. When the three beamlets are focused on the target individually but not aligned as shown in Figure 6.19(a, b), hexagonal interference pattern due to the three separate focal spots can be seen in the speckle image. When beamlets #1 and #2 are focused and aligned while beamlet #3 is focused but misaligned from the other two beamlets as shown in Figure 6.19(c, d), there are virtually only two focal spots on the target. Long interference fringes can be seen in the speckle image. When the three beamlets are focused individually on the target and aligned as shown in Figure 6.19(e, f), there is virtually only one focal spot on the target. The speckle image looks similar to the speckle image as shown in Figure 6.18(a). Based on the case where the three beamlets are focused and aligned, the target is moved a little bit along the beamlet propagation path to defocus the three beamlets as shown in Figure 6.19(g, h), the speckle sizes become smaller. Before starting next step, the target is moved back to its original position.

The third step is to investigate the technical feasibility of applying feedback wavefront control systems especially the phase-locking control system to free-space beam combining with non-cooperative extended target in the feedback control loop. Two experiments

are performed for this purpose. In each experiment, subaperture wavefront tip-tilt compensation system is running. Phase-locking control system is off in one experiment and on in the other experiment. No atmospheric turbulence or jitter is present. Figure 6.20 shows the speckle images when the three beamlets are (a) not phase-locked and (b) phase-locked. When the three beamlets are phase-locked, the focal spot on the extended target becomes smaller and correspondingly the mean speckle size becomes larger. Further experiments are performed when phase noise are introduced by rigorously shaking the fibers manually for the three beamlets. It can be seen that phase-locking control helps stabilize the target focal spot of the combined beam and thus stabilize the corresponding speckle field. In the above experiments, the target is stationary to the illuminating beamlets. Related work using speckle field for wavefront compensation with moving target and single illuminating beam can be found in [25, 27]. More general discussions of using speckle field in wavefront control is given in Section 3.6.

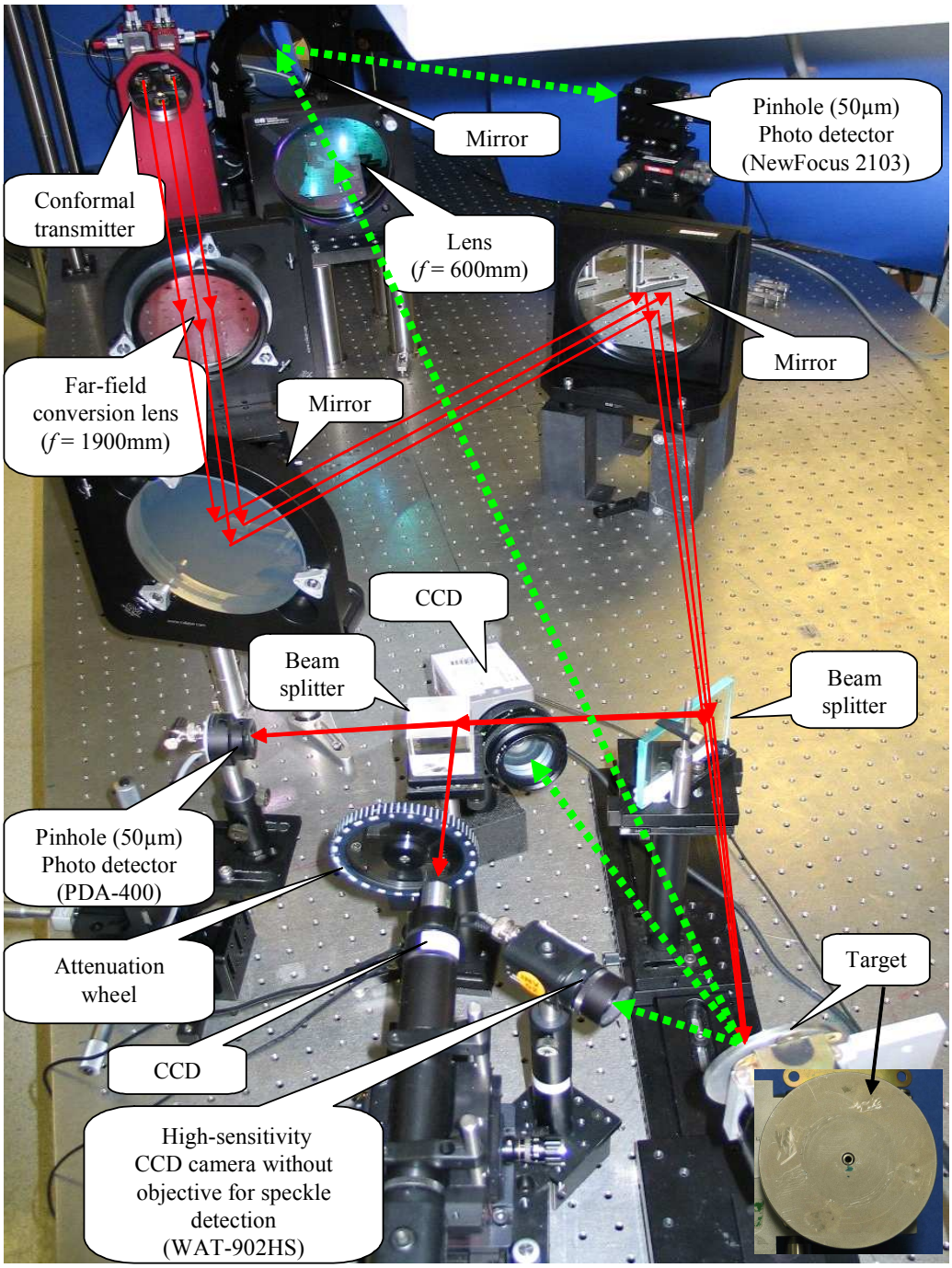

Figure 6.16: Free-space beam combining testbed (optical part) with target-in-the-loop configuration. The red arrowed solid lines indicate the three outgoing beamlets. The green arrowed dashed lines indicate scatter speckle field.

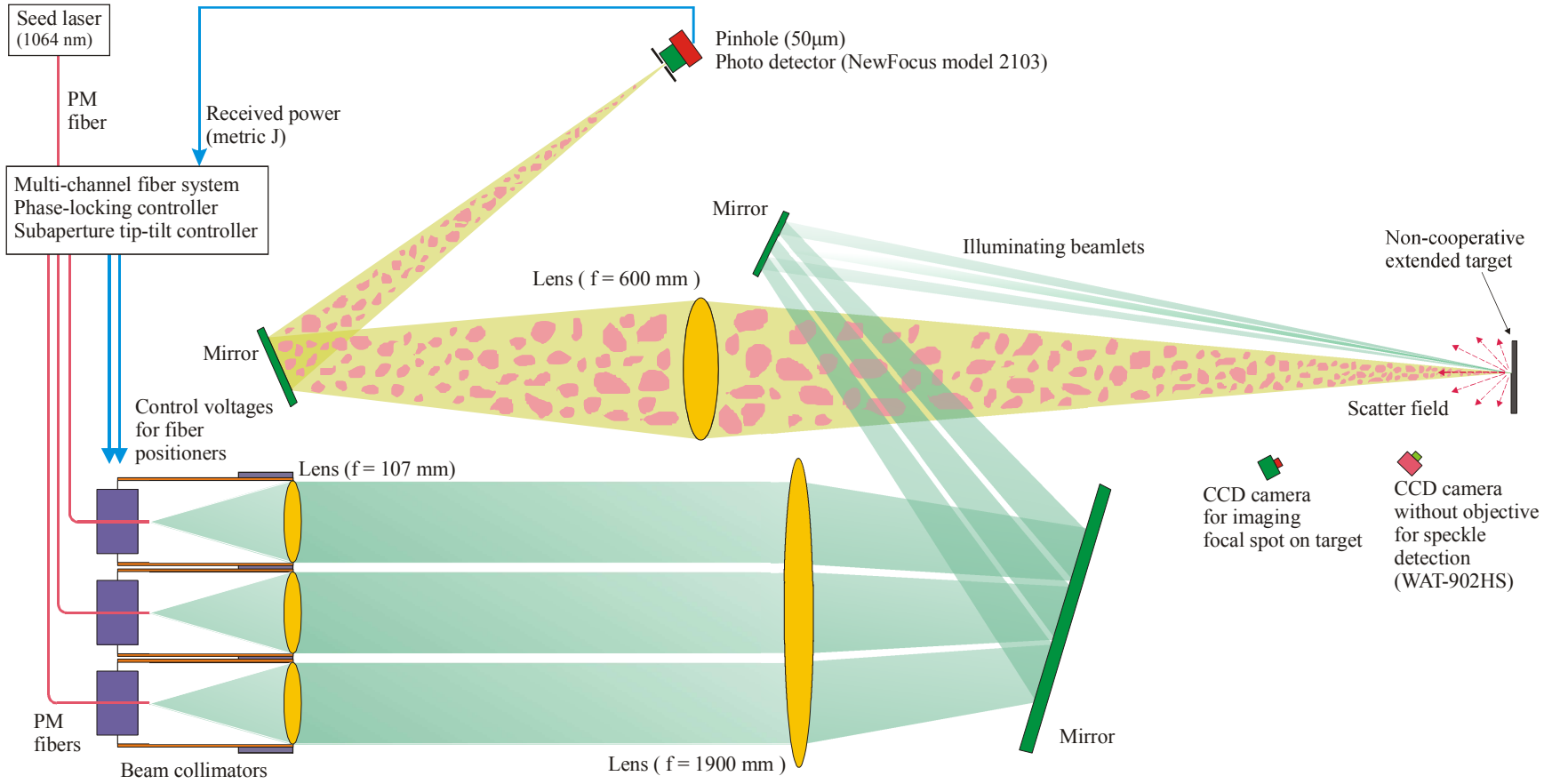

Figure 6.17: Schematic of free-space beam combining testbed (see Figure 6.16) with target-in-the-loop configuration.

Multi-channel fiber system, phase-locking control system, subaperture wavefront tip-tilt control system are represented by a textbox for simplification. These subsystems are the same as shown in Figure 6.6.

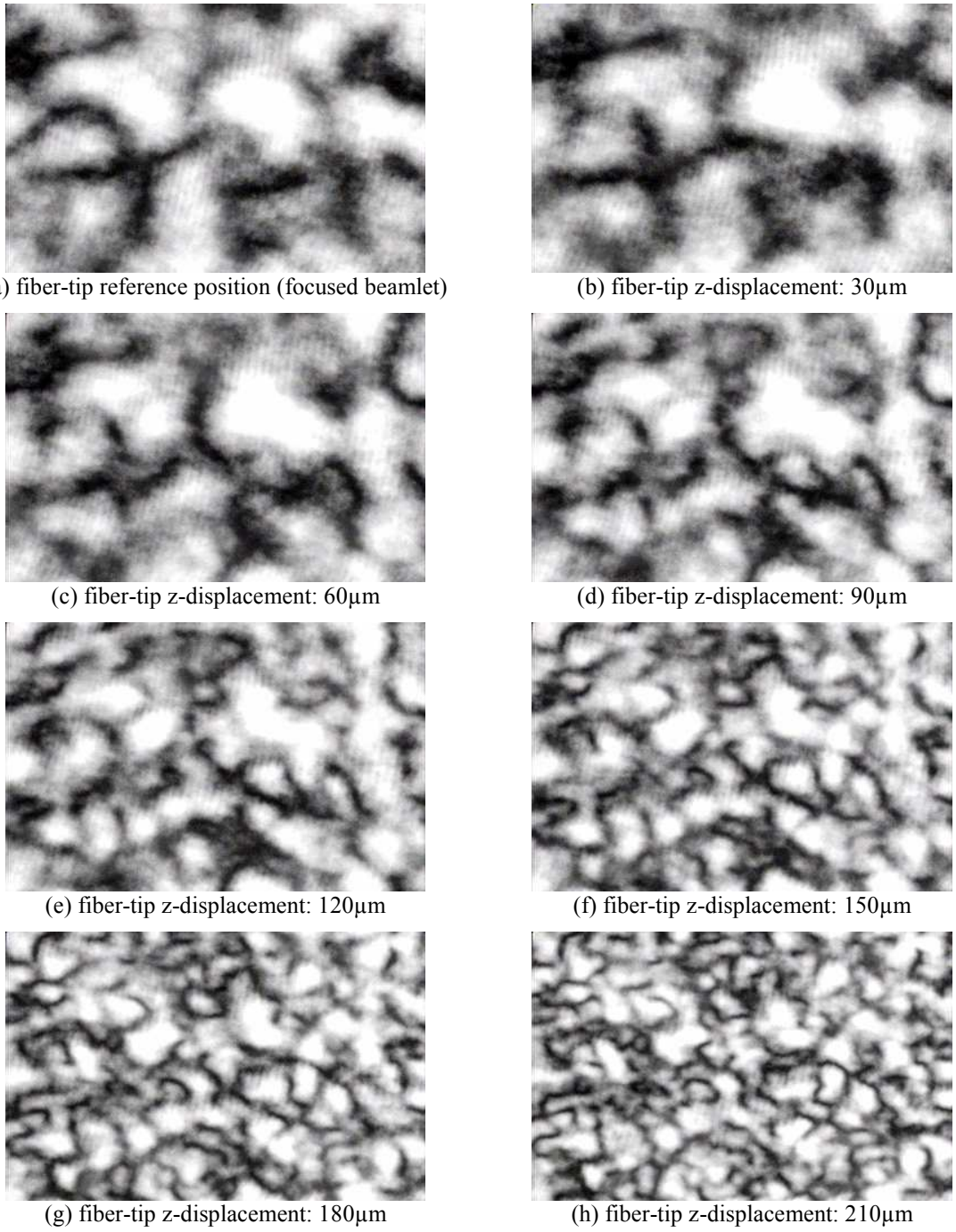

(a) fiber-tip reference position (focused beamlet)
(b) fiber-tip z-displacement: 30μm
(c) fiber-tip z-displacement: 60μm
(d) fiber-tip z-displacement: 90μm
(e) fiber-tip z-displacement: 120μm
(f) fiber-tip z-displacement: 150μm
(g) fiber-tip z-displacement: 180μm
(h) fiber-tip z-displacement: 210μm

Figure 6.18: Scatter field speckles of focal spot on a non-cooperative extended target.

Beamlet #3 is used. The focal spot size on target is adjusted by tuning fiber-tip z-displacement through the focus/defocus adjustment picomotor as shown in Figure 3.10. High sensitivity CCD camera (WAT-902HS) without objective is used.

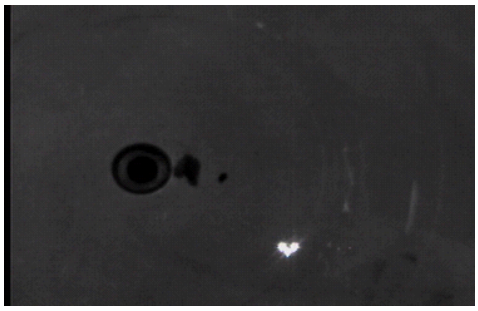

(a) three beamlets are focused but misaligned from one another.

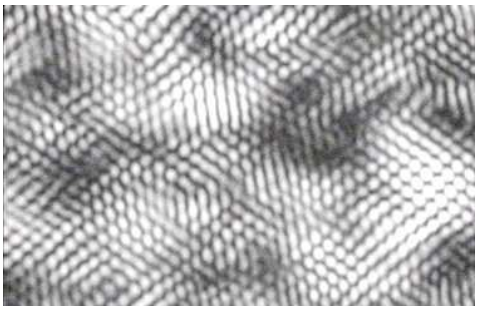

(b) scatter field speckles of focal spots in (a)

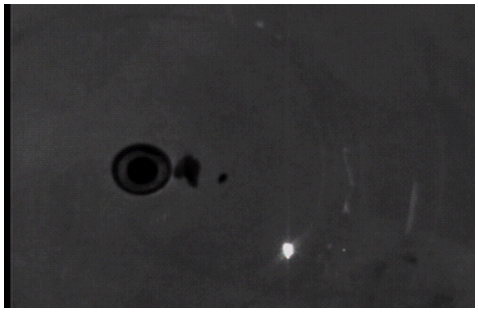

(c) beamlets #1 and #2 are focused and aligned, beamlet #3 is focused but misaligned.

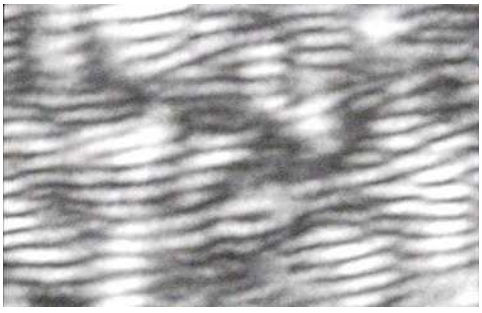

(d) scatter field speckles of focal spots in (c)

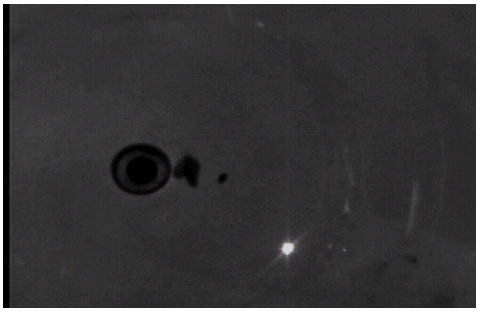

(e) three beamlets are focused and aligned.

(f) scatter field speckles of focal spots in (e)

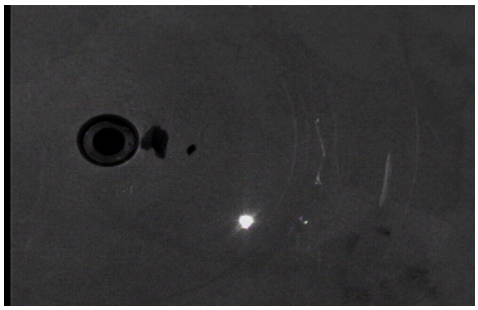

(g) three beamlets are out-of-focus but aligned.

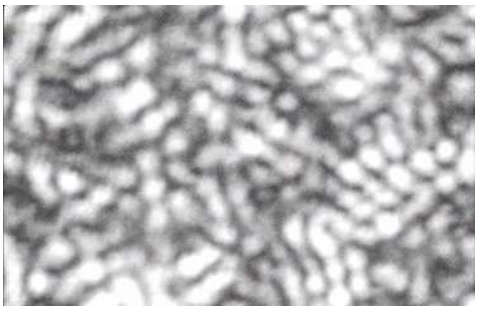

(h) scatter field speckles of focal spots in (g)

Figure 6.19: Illuminating beamlet spots on non-cooperative extended target and their corresponding scatter field speckles.

(a) aligned but not phase-locked

(b) aligned and phase-locked

Figure 6.20: Speckles images when the three beamlets are (a) not phase-locked and (b) phase-locked. When the three beamlets are phase-locked, the focal spot on the extended target becomes smaller and correspondingly the mean speckle size becomes larger.

Chapter 7 Summary and further work

In the previous chapters, a conformal adaptive phase-locked fiber collimator array was theoretically and numerically analyzed as well as experimentally demonstrated. To our knowledge, this system is the first reported conformal system with both phase-locking and subaperture wavefront phase tip-tilt control.The dissertation content and primary results are the following:

(1) An optical beam projection system composed of an array of fiber collimators (subapertures) was theoretically analyzed for both coherent and incoherent beam combining operation regimes. The impact of fill factors and the power scalability were evaluated through theoretical and numerical analyses. (Chapter 2)

(2) Various system architectures for a conformal adaptive phase-locked fiber array were investigated. Principal system components, e.g., integrated fiber-based phase shifters, were evaluated with respect to system integration. (Chapter 3)

(3) Feedback controllers based on the stochastic parallel gradient descent (SPGD) algorithm and the multi-dithering technique for wavefront correction were designed and built. Features and limitations of the controllers as well as considerations for control parameter optimization were discussed. (Chapter 4)

(4) All-fiber beam combining testbeds were built to demonstrate the technical feasibility of phase locking and to investigate the distortion compensation efficiency of SPGD and multi-dithering controllers. In addition, the reciprocity principle of phase-locking control for counter-propagating transmitting/receiving beams was investigated using these test-

beds. Phase-locking compensation was further investigated when optical communication modulation was present. (Chapter 5)

(5) System integration and evaluation was completed for an adaptive array with three fiber collimators. This included the installation of all major components: opto-electronic and fiber-optic hardware, controllers, and computer interfaces as well as the development of supervisory control software. (Section 6.1)

(6) Coherent beam combining with phase-locking and subaperture wavefront phase tip-tilt control were demonstrated when laboratory-simulated atmospheric turbulence and wavefront jitters were present in the propagation path. The compensation bandwidth of both phase-locking control and subaperture wavefront phase tip-tilt compensation were determined experimentally. In addition, coherent beam combining with a non-cooperative extended target in the feedback control loop was demonstrated. (Sections 6.2-6.7)

The research work as summarized above was performed in collaboration with colleagues in Prof. Vorontsov's research group at both University of Maryland and Army Research Laboratory. The major personal contributions include:

(1) Numerical analyses of the impact of fill factors and the power scalability for both incoherent and coherent fiber arrays; (Section 2.3 and Section 2.4)

(2) Evaluation of the response characteristics of the multi-channel polarization-maintaining $LiNbO_3$ phase-shifters with amplitude controls; (Section 3.4 and Section 3.5)

(3) Development (including software) and evaluation of the microprocessor-based SPGD phase-locking controllers; (Section 4.4)

(4) Integration and evaluation of the VLSI multi-dithering phase-locking controller developed at JHU; (Section 4.7)

(5) Integration of an all-fiber phase-locking system, data collection and analyses for phase-locking compensation using SPGD and multi-dithering techniques; (Section 5.1 and Section 5.2)

(6) Investigation of the phase relationship in counter-propagating beams in a phase-locked fiber array; (Section 5.3 and Section 5.4)

(7) Demonstration of a laser communication link based on a phase-locked fiber array (Section 5.5)

(8) Integration of a conformal adaptive phase-locked fiber array with three-subaperture elements; (Section 6.1 and Section 6.2)

(9) Experimental demonstration, data collection and analyses of phase-locking and on-subaperture wavefront tip-tilt controls in conformal beam projection using an adaptive phase-locked fiber array composed of three subapertures; (Sections 6.3 - 6.6)

(10) Experimental demonstration and analyses of conformal beam projection onto an extended rough surface with an adaptive phase-locked fiber array; (Section 6.7)

The obtained results demonstrate the theoretical and technical feasibility for using conformal adaptive phase-locked fiber array in free-space laser communications and beam projection applications. The following further changes and developments can be consid-

ered based on the lessons learned from the described development and evaluation of the adaptive fiber array system with three subapertures:

(1) Besides tip-tilt compensation, the subapertures of fiber array system should include capabilities for higher order aberration compensation. This can be achieved, e.g., by integrating multi-element liquid crystal spatial phase modulator into each fiber collimator subaperture.

(2) The use of non-polarization maintaining fiber systems (lasers, amplifiers, etc.) would allow for increasing the output power and reduction of the entire system cost. This requires the incorporation of polarization state control in each subaperture in order to obtain the identical polarization states for all beamlets required for efficient coherent beam combining.

(3) Atmospheric propagation experiments should be performed to investigate the performance of wavefront distortion compensation with the conformal adaptive phase-locked fiber array under conditions that resemble both laser communication and target-in-the-loop application scenarios.

Appendix: publications

(1) L. Beresnev, T. Weyrauch, M. Vorontsov, L. Liu and G. Carhart, "Development of adaptive fiber collimators for conformal fiber-based beam projection systems, " Proc. of SPIE V. 7090, 2008

In this paper, we describe bimorph piezoelectric fiber actuators, which enable tip and tilt control in fiber collimators, as well as their integration into a fiber-array based beam-projection system. A mechanism for alignment of individual fiber actuators within the array was developed. It provides six degrees of freedom and allows for high subaperture density. The alignment procedures for a seven-subaperture prototype system as well as first results from evaluation experiments are presented.

(2) L. Liu, M. Vorontsov, E. Polnau, T. Weyrauch, and L. Beresnev, "Adaptive phase-locked fiber array with wavefront tip-tilt compensation," Proc. of SPIE V. 6708, 2007

In this paper, we present the recent development of a conformal optical system with three adaptive phase-locked fiber elements. The coherent beam combining based on stochastic parallel gradient descent (SPGD) algorithm is investigated. We implement both phase-locking control and wavefront phase tip-tilt control in our conformal optical system. The phase-locking control is performed with fiber-coupled lithium niobate phase shifters which are modulated by an AVR micro-processor based SPGD controller. The perturbation rate of this SPGD controller is ~95,000 iterations per second. Phase-locking compensation bandwidth for phase distortion amplitude of 2π-radian phase shift is >100Hz. The tip-tilt control is realized with piezoelectric fiber positioners which are modulated by a computer-based software SPGD controller. The perturbation rate of the tip-tilt SPGD controller is up to ~950 iterations per second. The tip-tilt compensation bandwidth using fiber positioners is ~10Hz at 60-μrad. jitter swing angle.

(3) L. Liu, D. Loizos, M. Vorontsov, P. Sotiriadis, and G. Cauwenberghs, "Coherent combining of multiple beams with multi-dithering technique: 100 KHz closed-loop compensation demonstration", Proc. of SPIE V. 6708, 2007

In this paper, we demonstrate the coherent combining of three beams with a phase-locking controller using VLSI multi-dithering technique. Three fiber-coupled phase shifters are used to compensate phase distortions in the beam propagation path. The highest dither frequency in our system is ~70MHz. The achieved closed-loop compensation bandwidth of three beamlets is up to 100KHz.

(4) D. Loizos, L. Liu, P. Sotiriadis, G. Cauwenbergs, and M. Vorontsov, "Integrated multi-dithering controller for adaptive optics," Proc. of SPIE V. 6708, 2007

In this paper, we present an analog, continuous-time, high-speed VLSI (Very Large Scale Integration) controller implementing multi-dithering perturbative gradient de-

scent optimization of a direct measure of optical performance. This controller can be used to introduce effective compensation of phase noise in laser communication through adaptive wavefront control. The system applies parallel sinusoidal perturbations to the wavefront over a range of frequencies, and performs parallel synchronous detection of the metric signal to derive the gradient components over each frequency band. The system operates over a wide range of frequencies, supporting applications of model-free adaptive optics extending from compensation of slow atmospheric turbulence to compensation of fast random phase fluctuations in the actuators and laser amplifiers. The system has been tested as a phase controller for a multiple laser beam wavefront propagating through a highly turbulent medium. The results indicate a compensation bandwidth exceeding 300 kHz matching the turbulence bandwidth.

(5) L. Liu and M. Vorontsov, "Phase-locking of tiled fiber array using SPGD feedback controller," Proc. of SPIE V. 5895, 2005

In this paper, we present the laboratory experiments of phase locking of a multi-channel tiled fiber array using a stochastic parallel gradient descent (SPGD) feedback controller demonstrating the compensation effect of the simulating phase-induced distortions based on the model-free optimization of the received signal strength. An all-polarization-maintaining (PM)-fiber optical configuration is used to simplify the free-space transceiver system. The atmospheric aberrations are simulated by a multi-channel integrated optical phase modulator which obtains input control voltages from an array of multi-channel independent sinusoidal signal generators. A similar multi-channel phase modulator which obtains input control voltages from a computer-based SPGD controller is used to compensate the simulating phase distortions. The experimental results show that the constructive interference state is reached through phase locking of the multi-channel tiled fiber array for phase distortions up to 180 hertz for each channel. The update rate of the computer-based SPGD controller is ~16,000 iterations per second. The average compensation bandwidth is about 310 Hz.

(6) T. Weyrauch, M. Vorontsov, L. Beresnev, and L. Liu, "Atmospheric compensation over a 2.3 km propagation path with a multi-conjugate (piston-MEMS/modal DM) adaptive system," Proc. of SPIE V. 5552, 2004

In this paper, we discuss the expansion of wavefront distortion compensation based on stochastic parallel gradient descent (SPGD) optimization to the control of several wavefront correctors. We describe then a SPGD adaptive optics system that uses a low-order deformable mirror with modal control and a high-resolution (either 132 or 320 control channels) piston-type MEMS mirror. The system was installed at a 2.3km near-horizontal propagation and used for atmospheric compensation experiments. Results obtained for different system configurations are presented.

Bibliography

1. M. Vorontsov, "Adaptive photonics phase-locked elements (APPLE): system architecture and wavefront control concept," in *Target-in-the-Loop: Atmospheric Tracking, Imaging, and Compensation II*, 2005, San Diego, CA, USA, SPIE

2. R.K. Tyson, Book: "The principles of adaptive optics," 2nd ed, 1998, Academic Press

3. J.W. Hardy, Book: "Adaptive Optics for Astronomical Telescopes," Vol. 16 of *Oxford Series in Optical and Imaging Sciences* (Oxford University Press, 1998)

4. F. Roddier, Book: "Adaptive Optics in Astronomy," Cambridge University Press, 1999

5. T. Weyrauch and M.A. Vorontsov, "Atmospheric compensation with a speckle beacon in strong scintillation conditions: directed energy and laser communication applications," *Applied Optics*, 2005, 44(30): p. 6388-6401

6. T. Weyrauch and M.A. Vorontsov, "Free-space laser communications with adaptive optics: Atmospheric compensation experiments," *Journal of Optical and Fiber Communications Reports*, 2004, 1(4): p. 355-379

7. M.A. Vorontsov, "Chapter 7: wavefront control algorithms," in *Wavefront controllers in optics (manuscript)*, 2006

8. D.L. Fried, "Optical resolution through a randomly inhomogeneous-medium for very long and very short exposures," *Journal of the Optical Society of America*, 1966, 56(10): p. 1372-1379

9. D.L. Fried, "Optical resolution through a randomly inhomogeneous-medium for very long and very short exposures," *Current Contents/Engineering Technology & Applied Sciences*, 1980(7): p. 12-12

10. L.C. Andrews and R.L. Phillips, Book: "Laser Beam Propagation through Random Media," 2nd ed. SPIE Press Monograph Vol. PM152, 1998

11. J.W. Hardy, "Active optics: a new technology for the control of light," in *Proc. IEEE V. 66*, 1978

12. M. Born and E. Wolf, Book: "Principles of optics," 7th ed, Cambridge University Press, Cambridge, United Kingdom, 1999

13. R.J. Noll, "Zernike polynomials and atmospheric-turbulence," *Journal of the Optical Society of America*, 1976, 66(3): p. 207-211

14. W.B. Matkin, "Steered agile beams program support for army requirements," in *Free-Space Laser Communication and Laser Imaging*, 2002, San Diego, CA, USA, SPIE

15. V.W.S. Chan, "Optical space communications and networks," in *Free-Space Laser Communications VI*, 2006, San Diego, CA, USA, SPIE

16. A. Yaniv, V. Krupkin, A. Abitbol, J. Stern, E. Lurie, A. German, S. Solomonovich, B. Lubashitz, Y. Harel, S. Engart, Y. Shimoni, S. Hezy, S. Biltz, E. Kaminetsky, A. Goldberg, J. Chocron, N. Zuntz, and A. Zajdman, "Laser development for optimal helicopter obstacle warning system LADAR performance," in *Fiber Lasers II: Technology, Systems, and Applications*, 2005, San Jose, CA, USA, SPIE

17. A. Gibson, "Laser pointing technology," in *Laser Weapons Technology*, 2000, Orlando, FL, USA, SPIE

18. J.F. Riker, "Air force research laboratory program in active tracking," in *Free-Space Laser Communication and Active Laser Illumination III*, 2004, San Diego, CA, USA, SPIE

19. J.F. Riker, R.Q. Fugate, T. Holcomb, J.L. Kann, W.H. Lowrey, A.C. Slavin, J.M. Spinhirne, A.L. Tuffli, and J.M. Brown Ii, "Active tracking with moderate power lasers," in *Target-in-the-Loop: Atmospheric Tracking, Imaging, and Compensation*, 2004, Denver, CO, USA, SPIE

20. J.F. Riker, "Overview of the space-based laser (SBL) program," in *Laser and Beam Control Technologies*, 2002, San Jose, CA, USA, SPIE

21. S.E. Lamberson, "Airborne laser," in *Laser and Beam Control Technologies*, 2002, San Jose, CA, USA, SPIE

22. J. Shwartz, G.T. Wilson, and J.M. Avidor, "Tactical high-energy laser," in *Laser and Beam Control Technologies*, 2002, San Jose, CA, USA, SPIE

23. T. Weyrauch, M.A. Vorontsov, G.W. Carhart, G.V. Simonova, L.A. Beresnev, and E.E. Polnau, "Adaptive optical antennas: design and evaluation," in *Atmospheric Optics: Models, Measurements, and Target-in-the-Loop Propagation*, 2007, San Diego, CA, USA, SPIE

24. M.A. Vorontsov, G.W. Carhart, L.A. Beresnev, and J. Gowens II, "Adaptive WDM free-space laser communication system: low-order aberration compensation experiments," in *International Symposium on Optical Science and Technology, Conference 5550: Free-Space Laser Communications IV*, 2-6 August 2004, Denver, Colorado

25. M.A. Vorontsov, J.F. Riker, E. Polnau, S.L. Lachinova, and V.S. Rao Gudimetla, "Adaptive beam director for a tiled fiber array," in *AMOS Conference*, 2006

26. M.A. Vorontsov, G.W. Carhart, D.V. Pruidze, J.C. Ricklin, and D.G. Voelz, "Image quality criteria for an adaptive imaging system based on statistical analysis of the speckle field," *Journal of the Optical Society of America A-Optics Image Science and Vision*, 1996, 13(7): p. 1456-1466

27. Y. Deng, G. Cauwenberghs, E. Polnau, G. Carhart, and M. Vorontsov, "Integrated analog filter bank for adaptive optics speckle field statistical analysis," in *Target-in-the-Loop: Atmospheric Tracking, Imaging, and Compensation II*, 2005, San Diego, CA, USA, SPIE

28. M.A. Vorontsov and G.W. Carhart, "Adaptive phase distortion correction in strong speckle-modulation conditions," *Optics Letters*, 2002, 27(24): p. 2155-2157

29. M.A. Vorontsov and V. Kolosov, "Target-in-the-loop beam control: basic considerations for analysis and wave-front sensing," *Journal of the Optical Society of America A-Optics Image Science and Vision*, 2005, 22(1): p. 126-141

30. L. Li, A. Schulzgen, V.L. Temyanko, H. Li, J.V. Moloney, and N. Peyghambarian, "An all-fiber approach for in-phase supermode phase-locked operation of multicore fiber lasers," in *Fiber Lasers IV: Technology, Systems, and Applications*, 2007, San Jose, CA, USA, SPIE

31. R.J. Beach, M.D. Feit, S.C. Mitchell, K.P. Cutter, J.W. Dawson, S.A. Payne, R.W. Mead, J.S. Hayden, D. Krashkevich, and D.A. Alunni, "Ribbon fiber with multiple antiguided phase-locked gain cores," in *Advances in Fiber Lasers*, 2003, San Jose, CA, USA, SPIE

32. M. Wrage, P. Glas, D. Fischer, M. Leitner, N.N. Elkin, D.V. Vysotsky, A.P. Napartovich, and V.N. Troshchieva, "Phase-locking of a multicore fiber laser by wave propagation through an annular waveguide," *Optics Communications*, 2002, 205(4-6): p. 367-375

33. M. Wrage, P. Glas, and M. Leitner, "Combined phase locking and beam shaping of a multicore fiber laser by structured mirrors," *Optics Letters*, 2001, 26(13): p. 980-982

34. M. Wrage, P. Glas, M. Leitner, D.V. Vysotsky, and A.P. Napartovich, "Phase-locking and self-imaging properties of a Talbot resonator applied to circular structures," *Optics Communications*, 2001, 191(3-6): p. 149-159

35. M. Wrage, P. Glas, D. Fischer, M. Leitner, D.V. Vysotsky, and A.P. Napartovich, "Phase locking in a multicore fiber laser by means of a Talbot resonator," *Optics Letters*, 2000, 25(19): p. 1436-1438

36. E.J. Bochove, P.K. Cheo, and G.G. King, "Self-organization in a multicore fiber laser array," *Optics Letters*, 2003, 28(14): p. 1200-1202

37. P.L. Cheo, A. Liu, and G.G. King, "A high-brightness laser beam from a phase-locked multicore Yb-doped fiber laser array," *Ieee Photonics Technology Letters*, 2001, 13(5): p. 439-441

38. A. Shirakawa, K. Matsuo, and K.-i. Ueda, "Fiber laser coherent array for power scaling of single-mode fiber laser," in *Fifth International Symposium on Laser Precision Microfabrication*, 2004, SPIE

39. A. Shirakawa, K. Matsuo, and K.-i. Ueda, "Fiber laser coherent array for power scaling, bandwidth narrowing, and coherent beam direction control," in *Fiber Lasers II: Technology, Systems, and Applications*, 2005, San Jose, CA, USA, SPIE

40. A. Shirakawa, T. Saitou, T. Sekiguchi, and K. Ueda, "Coherent addition of fiber lasers by use of a fiber coupler," *Optics Express*, 2002, 10(21): p. 1167-1172

41. T.B. Simpson, F. Doft, P.R. Peterson, and A. Gavrielides, "Coherent combining of spectrally broadened fiber lasers," *Optics Express*, 2007, 15(18): p. 11731-11740

42. T.B. Simpson, A. Gavrielides, and P. Peterson, "Extraction characteristics of a dual fiber compound cavity," *Optics Express*, 2002, 10(20): p. 1060-1073

43. V.A. Kozlov, J. Hernandez-Cordero, and T.F. Morse, "All-fiber coherent beam combining of fiber lasers," *Optics Letters*, 1999, 24(24): p. 1814-1816

44. S. Akira, M. Keigo, and U. Ken-ichi, "Fiber laser coherent array for power scaling, bandwidth narrowing, and beam direction control," in *Advanced Solid-State Photonics (TOPS)*, 2005, Optical Society of America

45. S. Akira, S. Tomoki, M. Keigo, and U. Ken-ichi, "Scalable coherent beam combining of fiber lasers," in *Advanced Solid-State Photonics*, 2003, Optical Society of America

46. S. Akira, S. Tomoki, and U. Ken-ichi, "Scalable coherent beam combining of fiber lasers," in *Conference on Lasers and Electro-Optics/Quantum Electronics and Laser Science Conference*, 2003, Optical Society of America

47. D. Sabourdy, V. Kermene, A. Desfarges-Berthelemot, L. Lefort, A. Barthelemy, P. Even, and D. Pureur, "Efficient coherent combining of widely tunable fiber lasers," *Optics Express*, 2003, 11(2): p. 87-97

48. D. Sabourdy, V. Kermene, A. Desfarges-Berthelemot, L. Lefort, A. Barthelemy, C. Mahodaux, and D. Pureur, "Power scaling of fibre lasers with all-fibre interferometric cavity," *Electronics Letters*, 2002, 38(14): p. 692-693

49. M. Fridman, V. Eckhouse, N. Davidson, and A.A. Friesem, "Simultaneous coherent and spectral addition of fiber lasers," *Opt. Lett.*, 2008, 33(7): p. 648-650

50. A.S. Sami, C. Bill, N. Burke, S. Yuji, M.B. George, and W.H. Jerry, "System response in passively phased fiber amplifier arrays, 2008, SPIE

51. A.S. Sami, C. Bill, N. Burke, S. Yuji, M.B. George, and W.H. Jerry, "Power scaling of passively phased fiber amplifier arrays, 2008, SPIE

52. M.L. Minden, "Passive coherent combining of fiber oscillators," in *Fiber Lasers IV: Technology, Systems, and Applications*, 2007, San Jose, CA, USA, SPIE

53. M.L. Minden, H.W. Bruesselbach, J.L. Rogers, M.S. Mangir, D.C. Jones, G.J. Dunning, D.L. Hammon, A.J. Solis, and L. Vaughan, "Self-organized coherence in fiber laser arrays," in *Fiber Lasers: Technology, Systems, and Applications*, 2004, San Jose, Ca, USA, SPIE

54. H. Bruesselbach, D.C. Jones, M.S. Mangir, M. Minden, and J.L. Rogers, "Self-organized coherence in fiber laser arrays," *Optics Letters*, 2005, 30(11): p. 1339-1341

55. M. Minden, "Coherent coupling of a fiber amplifier array," in *Thirteenth Annual Solid State and Diode Laser Technology Review , SSDLTR 2000 Tech. Digest* 2000, Air Force Research Laboratory, Albuquerque, N.M.

56. B. Hans, M. Monica, L.R. Jeff, D.C. Jones, and S.M. Metin, "200W self-organized coherent fiber arrays," in *Conference on Lasers and Electro-Optics/Quantum Electronics and Laser Science and Photonic Applications Systems Technologies*, 2005, Optical Society of America

57. S.M. Metin, M.L. Minden, B. Hans, J.L. Rogers, D.C. Jones, D.L. Hammon, and A.J. Solis, "Self-organized coherence in fiber lasers," in *Nonlinear Optics: Materials, Fundamentals and Applications*, 2004, Optical Society of America

58. M.A. Culpepper, "Coherent combination of fiber laser beams," in *Laser Resonators and Beam Control V*, 2002, San Jose, CA, USA, SPIE

59. J. Anderegg, S. Brosnan, E. Cheung, P. Epp, D. Hammons, H. Komine, M. Weber, and M. Wickham, "Coherently coupled high-power fiber arrays," in *Fiber Lasers III: Technology, Systems, and Applications*, 2006, San Jose, CA, USA, SPIE

60. J. Anderegg, S.J. Brosnan, M.E. Weber, H. Komine, and M.G. Wickham, "8-W coherently phased 4-element fiber array," in *Advances in Fiber Lasers*, 2003, San Jose, CA, USA, SPIE

61. S.J. Augst, J.K. Ranka, T.Y. Fan, and A. Sanchez, "Beam combining of ytterbium fiber amplifiers (Invited)," *Journal of the Optical Society of America B-Optical Physics*, 2007, 24(8): p. 1707-1715

62. S.J. Augst, T.Y. Fan, and A. Sanchez, "Coherent beam combining and phase noise measurements of ytterbium fiber amplifiers," *Optics Letters*, 2004, 29(5): p. 474-476

63. D.C. Jones, A.M. Scott, S. Clark, C. Stace, and R.G. Clarke, "Beam steering of a fiber-bundle laser output using phased array techniques," in *Fiber Lasers: Technology, Systems, and Applications*, 2004, San Jose, Ca, USA, SPIE

64. T.M. Shay, "Theory of electronic phase locking of an optical array without a reference beam," in *Free-Space Laser Communications VI*, 2006, San Diego, CA, USA, SPIE

65. T.M. Shay, V. Benham, J. Spring, B. Ward, F. Ghebremichael, M.A. Culpepper, A.D. Sanchez, J.T. Baker, D. Pilkington, and R. Berdine, "Self-referenced locking of optical coherence by single-detector electronic-frequency tagging," in *Fiber Lasers III: Technology, Systems, and Applications*, 2006, San Jose, CA, USA, SPIE

66. T.M. Shay, V. Benham, J.T. Baker, A.D. Sanchez, D. Pilkington, D.J. Nelson, and C.A. Lu, "Narrow linewidth coherent beam combining of optical fiber amplifier arrays," in *Solid State Lasers XVI: Technology and Devices*, 2007, San Jose, CA, USA, SPIE

67. H. Bruesselbach, M.L. Minden, S. Wang, D.C. Jones, and M.S. Mangir, "A coherent fiber-array-based laser link for atmospheric aberration mitigation and power scaling," in *Free-Space Laser Communication Technologies XVI*, 2004, San Jose, Ca, USA, SPIE

68. H. Bruesselbach, S. Wang, M. Minden, D.C. Jones, and M. Mangir, "Power-scalable phase-compensating fiber-array transceiver for laser communications through the atmosphere," *J. Opt. Soc. Am. B*, 2005, 22(2): p. 347-353

69. W. Shuoqin, B. Hans, M. Monica, J. Cris, and M. Metin, "Coherent phase-locking of seven laser transmitters on a 408 meter outdoor range," in *Conference on Lasers and Electro-Optics/Quantum Electronics and Laser Science and Photonic Applications Systems Technologies*, 2005, Optical Society of America

70. J.E. Kansky, C.X. Yu, D.V. Murphy, S.E.J. Shaw, R.C. Lawrence, and C. Higgs, "Beam control of a 2D polarization maintaining fiber optic phased array with high-fiber count," in *Advanced Wavefront Control: Methods, Devices, and Applications IV*, 2006, San Diego, CA, USA, SPIE

71. X.Y. Charles, E.K. Jan, E.S. Scot, V.M. Daniel, and H. Charles, "Coherent beam combining of a large number of PM fibers in a 2D fiber array," in *Conference on Lasers and Electro-Optics/Quantum Electronics and Laser Science Conference and Photonic Applications Systems Technologies*, 2006, Optical Society of America

72. S.L. Lachinova and M.A. Vorontsov, "Performance analysis of an adaptive phase-locked tiled fiber array in atmospheric turbulence conditions," in *Target-in-the-Loop: Atmospheric Tracking, Imaging, and Compensation II*, 2005, San Diego, CA, USA, SPIE

73. M.A. Vorontsov and A. Kohnle, Book: "Optical waves in atmospheric turbulence." Vol. 2005/17, Dec. 8, 2005, FGAN-FOM

74. M.A. Vorontsov and S.L. Lachinova, "Laser beam projection with adaptive array of fiber collimators. I. Basic considerations for analysis," *J. Opt. Soc. Am. A*, 2008, 25(8): p. 1949-1959

75. S.L. Lachinova and M.A. Vorontsov, "Laser beam projection with adaptive array of fiber collimators. II. Analysis of atmospheric compensation efficiency," *J. Opt. Soc. Am. A*, 2008, 25(8): p. 1960-1973

76. B.E.A. Saleh and M.C. Teich, Book: "Fundamentals of photonics," 2nd ed, 1991, John Wiley & Sons, Inc.

77. W.L. Wolfe, Book: "Optical engineer's desk reference," 2003, Optical Society of America, Washington, DC

78. P. Sprangle, J. Penano, and A. Ting, "Incoherent combining of high-power fiber lasers for long-range directed energy applications--interim rept. May-Jun 2006, NRL/MR/6790-06-8963," 2006, Naval Research Lab., Washington, D.C.

79. J.W. Goodman, Book: "Introduction to Fourier Optics," 3rd ed, 2004, Roberts & Company Publishers

80. S.L. Lachinova and M.A. Vorontsov, "Adaptive tiled fiber array with coherent & incoherent beam combining: I. basic considerations for analysis," *Journal of the Optical Society of America*, 2007

81. L.A. Beresnev and M.A. Vorontsov, "Design of adaptive fiber optics collimator for free-space communication laser transceiver," in *Target-in-the-Loop: Atmospheric Tracking, Imaging, and Compensation II*, 2005, San Diego, CA, USA, SPIE

82. L.A. Beresnev, M.A. Vorontsov, and P. Wangsness, "Pocket deformable mirror for adaptive optics applications," in *Proc. AMOS Technical Conference*, September 10-14, 2006, Maui, Hawaii

83. G. Garcia-Torales, M. Strojnik, and G. Paez, "Risley prisms to control wave-front tilt and displacement in a vectorial shearing interferometer," *Appl. Opt.*, 2002, 41(7): p. 1380-1384

84. S.W. Sparrold, J.P. Mills, R.A. Paiva, T.D. Arndt, K.S. Ellis, and D.J. Knapp, "Beam steering optical arrangement using Risley prisms with surface contours for aberration correction," 2005, RAYTHEON CO (US)

85. P.F. McManamon, T.A. Dorschner, D.L. Corkum, L.J. Friedman, D.S. Hobbs, M. Holz, S. Liberman, H.Q. Nguyen, D.P. Resler, R.C. Sharp, and E.A. Watson, "Optical phased array technology," *Proceedings of the Ieee*, 1996, 84(2): p. 268-298

86. EOSPACE Inc., http://www.eospace.com

87. S. Thaniyavarn, "Wavelength-independent, optical-damage-immune z-propagation *LiNbO3* wave-guide polarization converter," *Applied Physics Letters*, 1985, 47(7): p. 674-677

88. S. Thaniyavarn, "Wavelength-independent, optical-damage-immune *LiNbO3* TE-TM mode converter," *Optics Letters*, 1986, 11(1): p. 39-41

89. J. Limpert, A. Liem, T. Schreiber, H. Zellmer, and A. Tuennermann, "Power and energy scaling of fiber laser systems based on ytterbium-doped large-mode-area fibers," in *Advances in Fiber Lasers*, 2003, San Jose, CA, USA, SPIE

90. J. Nilsson, J.K. Sahu, Y. Jeong, W.A. Clarkson, R. Selvas, A.B. Grudinin, and S. Alam, "High-power fiber lasers: new developments," in *Advances in Fiber Lasers*, 2003, San Jose, CA, USA, SPIE

91. I. Turek and N. Tarjanyi, "Investigation of symmetry of photorefractive effect in $LiNbO_3$," *Optics Express*, 2007, 15(17): p. 10782-10788

92. Y. Chen, S.W. Liu, D. Wang, T. Chen, and M. Xiao, "Measurement of laser-induced refractive index change of inverted ferroelectric domain $LiNbO_3$," *Applied Optics*, 2007, 46(31): p. 7693-7696

93. J. Soohoo and C.L. Hayes, "Phase locking of a multimode to a single-mode He-Ne-laser," *Optics Letters*, 1979, 4(7): p. 202-204

94. W.W. Chow, "Phase locking of lasers by an injected signal," *Optics Letters*, 1982, 7(9): p. 417-419

95. A. Yariv and P. Yeh, Book: "Optical waves in crystals: propagation and control of laser radiation," 2002, John Wiley & Sons Inc.

96. W. Charczenko, "Photonic multi-channel transmit/receive integrated phase and amplitude controller (TRIPAC)," Internal technical presentation, EOSPACE Inc., (2006)

97. C.M. Kim and R.V. Ramaswamy, "Overlap integral factors in integrated optic modulators and switches," *Journal of Lightwave Technology*, 1989, 7(7): p. 1063-1070

98. L.I. Goldfischer, "Autocorrelation function and power spectral density of laser-produced speckle patterns," *Journal of the Optical Society of America*, 1965, 55(3): p. 247-253

99. J.C. Dainty, Book: "Laser speckle and related phenomena," 1975, Springer-Verlag

100. M.A. Vorontsov, G.W. Carhart, and J.C. Ricklin, "Adaptive phase-distortion correction based on parallel gradient-descent optimization," *Optics Letters*, 1997, 22(12): p. 907-909

101. M.A. Vorontsov and V.P. Sivokon, "Stochastic parallel-gradient-descent technique for high-resolution wave-front phase-distortion correction," *Journal of the Optical Society of America A-Optics Image Science and Vision*, 1998, 15(10): p. 2745-2758

102. T. Weyrauch, M.A. Vorontsov, T.G. Bifano, J.A. Hammer, M. Cohen, and G. Cauwenberghs, "Microscale Adaptive Optics: Wave-Front Control with a μ-Mirror Array and a VLSI Stochastic Gradient Descent Controller," *Appl. Opt.*, 2001, 40(24): p. 4243-4253

103. G.W. Carhart, M.A. Vorontsov, L.A. Beresnev, P.S. Paicopolis, and F.K. Beil, "Atmospheric laser communication system with wide-angle tracking and adaptive compensation, 2005, SPIE

104. T.R. O'Meara, "Theory of multidither adaptive optical systems operating with zonal control of deformable mirrors," *J. Opt. Soc. Am.*, 1977, 67(3): p. 318-325

105. T.R. O'Meara, "The multidither principle in adaptive optics," *J. Opt. Soc. Am.*, 1977, 67(3): p. 306-314

106. T.R. O'Meara, "Stability of an N-loop ensemble-reference phase control system," *J. Opt. Soc. Am.*, 1977, 67(3): p. 315-318

107. D.N. Loizos, L. Liu, P.P. Sotiriadis, G. Cauwenberghs, and M.A. Vorontsov, "Integrated multi-dithering controller for adaptive optics," in *Atmospheric Optics: Models, Measurements, and Target-in-the-Loop Propagation*, 2007, San Diego, CA, USA, SPIE

108. D.N. Loizos, P.P. Sotiriadis, and G. Cauwenberghs, "A robust continuous-time multi-dithering technique for laser communications using adaptive optics," in *Circuits and Systems, 2006. ISCAS 2006. Proceedings. 2006 IEEE International Symposium on*, 2006

109. D.N. Loizos, "A multi-dithering controller with sub-microsecond response time: analysis and SiGe BiCMOS implementation," Ph.D. Dissertation, Department of Electrical and Computer Engineering, The Johns Hopkins University, Baltimore, Maryland, U.S.A (2007)